The Ground and Excited State Molecular Structure of Model Systems Undergoing Photochemical Processes and the Characterization of Active Agents by means of Vibrational Spectroscopy and Theoretical Calculations

Dissertation

zur Erlangung des
naturwissenschaftlichen Doktorgrades
der Bayerischen Iulius-Maximilans-Universität Würzburg

vorgelegt von

Adriana Viorica Szeghalmi
aus Oradea

Würzburg
2004

Eingereicht am: ……
bei der Fakultät für Chemie und Pharmazie

1. Gutachter: ……
2. Gutachter: ……
der Dissertation

1. Prüfer: ……
2. Prüfer: ……
3. Prüfer: ……
des Öffentlichen Promotionskolloquiums

Tag des Öffentlichen Promotionskolloquiums ……

Doktorurkunde ausgehändigt am: ……

Pentru mami, apunak
und meinen Professoren

Motto:

Listen to your heart

Contents

Chapter 1

Introduction

A major issue in the design of new materials and compounds for e.g. computer technologies, medicine and pharmacy is the understanding of their structural characteristics and the nature of their activity. The investigation of these systems on a molecular level is probably the most challenging aspect, and to accomplish this ambitious goal a variety of experimental and theoretical approaches have been developed. The development of various spectroscopic methods, such as e.g. NMR, X-ray, ESR, absorption, fluorescence or vibrational spectroscopy has played a decisive role in the technological progress. The development of theoretical methods, and in particular of quantum chemistry, allowed not only an interpretation of the experimental observations, but also made it possible to predict molecular properties, or even processes.

Especially vibrational spectroscopic techniques[1-4] like infrared (IR) and Raman spectroscopy represent one of the most useful tools for obtaining information about structure and properties of molecules[5-8]. Vibrational spectroscopy became over the last years a powerful, well established analytical tool in research and industry. These two different vibrational techniques, IR and Raman spectroscopy, are able to provide very similar, but often complementary information about the molecular structure in the gaseous,

liquid or solid state. The IR spectra supply data about the molecular vibrations based on an absorption process between the vibrational levels of the molecule, while the Raman process[9,10] corresponds to the measurement of the wavenumber and intensity of inelastically scattered light from molecules. Nevertheless, while the IR measurements are limited to a non-aqueous medium, the Raman process is characterized by a low intensity of the scattered light.

In the last decades, the Raman signal enhancement due to the resonance Raman or surface enhanced Raman scattering (SERS) effect has opened the possibility to investigate derivatives in solutions of low concentrations or in the gas phase. Moreover, resonance Raman and SERS spectra provide additional, very important information about the investigated system.

Resonance Raman spectroscopy has been widely applied to study biological, organic and inorganic molecules[11-16]. The resonance condition arises when the wavelength used to excite the Raman scattering lies within the electronic absorption band, causing the vibrations of the absorbing species to be selectively enhanced (by a factor of 10^6 compared to non-resonant excitation). The resonance Raman intensities and in particular the resonance Raman excitation profiles, carry vibrationally mode-specific information about the resonantly excited state potential energy surface. This information may be extracted from the RR spectra even if the absorption and emission spectra are completely diffuse[17,18]. The theoretical relationship between the RR intensities and excited-state structure has been known since the early work of Albrecht and coworkers[19-21]. The *sum over state*, *time-dependent* and *transform methods* have been developed to correlate the RR intensities[22] with the vibrational overlap integrals (Franck-Condon factors)[13,14,16,22]. These factors are a function of the excited state distortion (the displacement of the excited state potential surface along a normal mode coordinate relative to that of the ground state). The displacement parameters of the resonantly enhanced modes contain information about the symmetry, equilibrium geometry and dynamics of the excited electronic state[13,14,18]. Moreover, based on the theoretical work of Mukamel and co-workers[23], the effect of the solvent environment on the potential surfaces may be also examined. Myers Kelley and co-workers as well as other research groups, determined the solvent induced electronic spectral broadening via a quantitative analysis of the resonance Raman intensities for several systems, such as polyenes, push-pull chromophores, charge transfer systems[18,24], etc.

The SERS effect corresponds to the enhancement (by a factor of up to 10^{11-14}) of the Raman scattering of a molecule situated in the vicinity of a proper metal surface[25]. Substantial theoretical work was concerned with the understanding of the enhancement mechanisms responsible for this effect[25,26]. Moreover, since many chemical, physiological[27] and industrial processes take place at interfaces, it is of utmost importance to understand the molecular changes upon adsorption. Hence, SERS active metal surfaces serve as model substrates to investigate the type of interactions between a molecule and a substrate, the molecule's adsorption site[26] and if possible the new properties of such adsorbed molecules.

Quantum chemical calculations became indispensable for an analysis of molecular properties in both the ground and excited states[28-30]. Important molecular features like e.g. geometrical parameters, the prediction of stable conformations, orbital coefficients, charge distributions, dipole moments, polarizabilities or hyperpolarizabilities, excitation energies, interactions between molecules, reaction coordinates, transition states may be determined by theoretical calculations. In the work presented within this thesis, the possibility offered by computational chemistry to determine the vibrational wavenumbers, eigenmodes, IR intensities and Raman scattering activities was applied. To obtain a reliable vibrational assignment potential energy distribution (PED) calculations were applied[31]. Furthermore, a direct comparison between the optimized molecular geometries and charge distributions of the ground and excited state was also carried out to achieve a deeper understanding of the molecular changes upon electronic excitation.

The goal of the work presented within this study was to probe ground and excited state properties of photochemical active polyatomic molecules as well as to derive structure-activity relationship of various biologically or pharmaceutically relevant systems by means of vibrational spectroscopy in combination with theoretical calculations. The work is substantially motivated on the one hand by the fundamental theoretical importance of such systems, and also because of their relevant applicability and impact on our daily live. Photochemical processes, such as photo induced electron and hydrogen or proton transfer processes, are fundamental chemical and biological reactions. In order to understand these important processes on a molecular level, it is necessary to completely characterize the molecular modifications upon optical excitation of well defined small model systems. A detailed description of the investigated systems can be found in the corresponding chapters.

Chapter 2 provides a brief overview about the theoretical fundamentals of vibrational spectroscopy and quantum chemical calculations. The various experimental setups used to perform the experiments presented within this thesis, computational strategies and data analysis will be shortly presented in chapter 3.

Chapter 4 reports on the investigations of the initial dynamics of an intramolecular proton transfer model system, 1-hydroxy-2-acetonaphthone. Chapter 5 presents an IR, Raman and resonance-Raman spectroscopical study of the electronic structure of a triarylamine radical cation, being a simple model system to study the adiabatic electron transfer process. The following chapter describes first vibrational spectroscopic results obtained for a model photorefractive “push-pull” chromophore. The investigated thiophene derivative is a structural component of promising organic optically nonlinear systems. Mainly resonance Raman spectroscopy and in particular a resonance Raman intensity analysis with time dependent propagation methods and excited state calculations were applied to study the above mentioned photochemical active systems of the chapters 4-6.

The second major topic of this thesis, the characterization of active agents, can be found in Chapters 7 and 8. Chapter 7 presents the investigation of hydrogen bonding motifs in an aziridinyl peptide used as cysteine protease inhibitor by means of Raman spectroscopy, whereas chapter 8 discusses the adsorption characteristics of two anti-leukemia active agents on a silver substrate by means of SERS spectroscopy.

The last chapter of this thesis summarizes the main results obtained in these studies.

Chapter 2

Theoretical Fundamentals

This chapter, treating the theoretical fundamentals of vibrational spectroscopy and quantum chemical calculations, contains sections on IR and Raman, resonance Raman and surface enhanced Raman spectroscopy as well as ab-initio and density functional theory calculations. First, the IR and Raman spectroscopic methods, which provide in general equivalent structural information about the ground state, but are complementary when the molecule presents an inversion center, will be presented. Furthermore, the resonance Raman spectroscopy, which gives information about the resonantly excited molecular state, will be expatiated. For an in depth analysis of the resonance Raman excitation profiles in conjunction with the absorption spectra the time-dependent formalism will be described in detail. The SERS enhancement mechanisms and the SERS selection rules will be summarized. Second, some basic aspects of quantum chemical calculations will be treated. The Hartree-Fock approach for the optimization of the ground state molecular structure will be presented in more detail, and than procedures for the excited state calculations will be described. Finally, density functional calculations will be shortly discussed.

2.1 Vibrational Spectroscopy

Since the first *mid*-infrared spectrometers were constructed at the beginning of the twentieth century and the Raman effect was observed for the first time in 1928, IR and Raman spectroscopy became well established analytical techniques. The "fingerprint" IR and Raman spectra[1] allow the identification of compounds and provide information on their molecular structure in the gaseous, liquid or solid state[5-7,32]. The invention of cw and pulsed lasers, the observation of the resonance Raman and surface enhanced Raman scattering effects have contributed considerably to the development of Raman spectroscopy. Moreover, vibrational spectroscopy is undergoing a renaissance stimulated by new developments in infrared and Raman instrumentation and is gaining an increasing role in research, industry, medicine, pharmacy, etc. Besides UV/VIS/NIR, fluorescence, mass, X-ray, NMR spectroscopy and chromatography and other research techniques, vibrational spectroscopy brought a significant contribution to science and the improvement of our lives.

IR and Raman spectroscopy

Vibrational spectroscopy provides information on the structure of molecules based on the observation of the molecular vibrations[1,8]. The easiest way to imagine molecular vibrations is to consider a diatomic molecule being made up of two balls of masses m_1 and m_2 connected by a massless spring. According to Hook's law, the force F necessary to restore the spring is proportional to the displacement x from the equilibrium position

$$F = -kx \ , \tag{2.1}$$

where k (in N m^{-1}) is the force constant, which is a measure of the bond strength between the two atoms. The vibrational frequency n_0 (in Hz) of the harmonic oscillator is given by

$$n_0 = \frac{1}{2p}\sqrt{\frac{k}{m}} \ , \tag{2.2}$$

where m is the reduced mass (in kg), $m=m_1m_2/\ m_1+m_2$. The vibrational energy of a harmonic oscillator E_{vib} is defined according to quantum mechanics as

$$E_{vib} = hn_0\left(n+\frac{1}{2}\right), \tag{2.3}$$

where *h* is Planck's constant and *n* is the vibrational quantum number having the values 0, 1, 2, 3 etc. and characterizing the eigenstates of the harmonic oscillator. Although the harmonic oscillator model is a very useful approximation since it significantly simplifies the mathematics, it is not a realistic picture of the atomic motion in a vibrating molecule. Therefore, it is necessary to consider anharmonicity effects to describe molecular vibrations. The energy levels of such an anharmonic oscillator are approximately equal to

$$E_{vib} = hn_0\left[\left(n+\frac{1}{2}\right)-x_a\left(n+\frac{1}{2}\right)^2\right], \tag{2.4}$$

where x_a is the anharmonicity constant, and the higher order terms are omitted.

The vibrations of a polyatomic molecule can be considered as a system of coupled anharmonic oscillators[31]. A molecule consisting of *N* atomic nuclei will have a total of 3*N* degrees of freedom of motion for all the nuclear masses in the molecule. For non-linear molecules, there are (3*N*-6) vibrational degrees of freedom after subtracting the pure translations and rotations of the molecule, while linear molecules posses (3*N*-5) vibrational degrees of freedom. These internal degrees of freedom correspond to the number of independent normal modes of vibration. In each normal mode of vibration all the atoms of the molecule vibrate with the same frequency and pass through their equilibrium positions simultaneously. The determination of the form and the frequency of the normal modes of molecular vibrations will be presented in the following sections within the quantum chemical calculations (see Chapters 2.2 and 3.2).

The vibrational energy levels of the molecule[8], represented by an anharmonic oscillator, are depicted in Fig. 2.1. Under normal conditions, the molecule is in its vibrational ground state ($n=0$) of the electronic ground state. Its lowest energy, the so-called zero point energy is $E_{vib,0}=1/2hn_0$. Upon interaction with electromagnetic radiation, the molecule can be raised from its vibrational ground state in higher vibrational levels. The transition $n=0\rightarrow 1$ corresponds to the fundamental vibrational mode, while transitions in higher vibrational states are called overtones.

The energy of the absorbed quanta for a fundamental transition is given by

$$E_{0\rightarrow 1} = hn_0\left(1-2x_a\right) \tag{2.5}$$

in the case of an anharmonic oscillator. In vibrational spectroscopy, this energy is expressed in terms of wavenumbers (cm^{-1})

$$\tilde{n}_{(0\to1)} = \frac{n_0}{c}\left(1 - 2x_a\right), \tag{2.6}$$

where c is the light velocity in vacuum. The absorbed energy for polyatomic molecules lie in general in the range between 400 and 4000 cm^{-1}, corresponding to the *mid*-infrared spectral region.

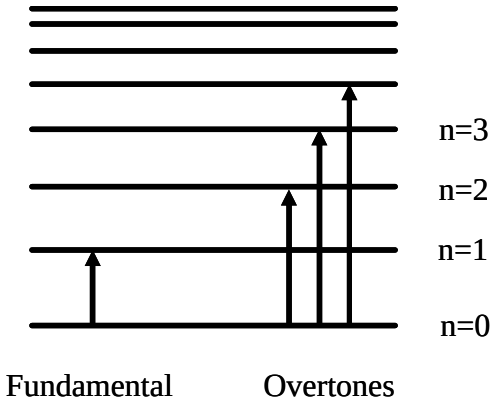

Figure 2.1 *The energy levels and transitions of an anharmonic oscillator.*

Hence, ***IR spectroscopy*** is based on the absorption of energy from the incident beam upon interaction of the electromagnetic radiation with the molecule inducing the molecular transition from the ground vibrational level in higher vibrational levels of the ground electronic state. The IR spectra represent the vibrational transitions for all molecular vibrations and give the characteristic vibrational wavenumbers, which depend on the force constants. The first-order IR absorption intensity of the *k*th mode is proportional to the square of the change of the dipole moment m caused by the normal mode coordinate q_k

$$I_k^{IR} = \frac{Np}{3c}\left|\frac{\partial m}{\partial q_k}\right|^2 \tag{2.7}$$

where N is the particle density. Since $\left|\partial m / \partial q_k\right|^2$ is the only molecular property, it is also referred to as the absolute infrared intensity. Therefore, a normal mode k will be IR active only if

$$\frac{\partial m}{\partial q_k} \neq 0 . \tag{2.8}$$

Fundamentals generally present strong IR intensity while overtones have very weak intensity. The overtones give rise to bands at about twice the wavenumber of a fundamental transition.

The ***Raman effect*** is an inelastic scattering of light by matter[7,9,10]. The energy level diagram of the spontaneous Raman effect is depicted in Fig. 2.2.

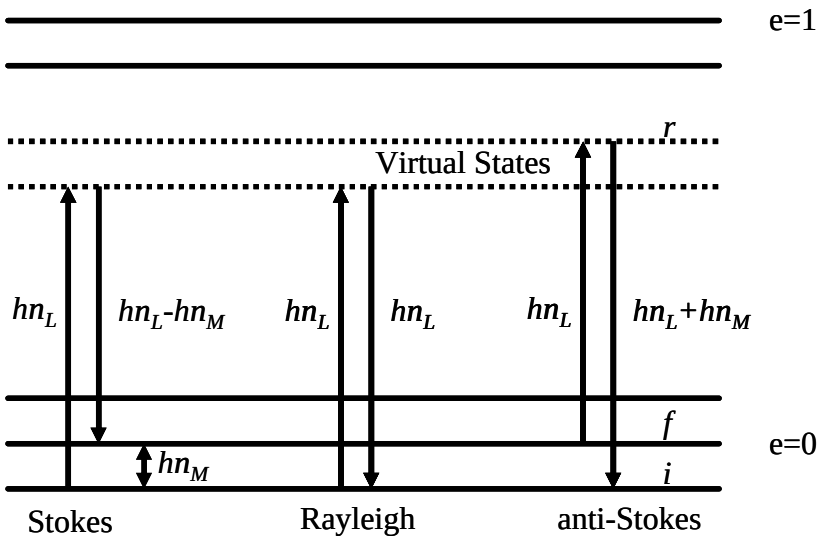

Figure 2.2 *The energy level diagram of the spontaneous Raman scattering.*

The Raman effect is a two photons effect[33]. The molecule is transferred to a virtual state by a light quantum of energy hn_L, where n_L is the frequency of the incident beam, and the scattered light is modulated by the molecular vibrational mode of frequency n_k. The Raman scattering of molecules in their vibrational ground state is referred to as Stokes lines, while the Raman scattering of molecules situated in higher vibrational states ($n \geq 1$) is called anti-Stokes scattering. The elastic scattering at a frequency equal to the frequency of the incident beam is called the Rayleigh scattering.

An electromagnetic field $\vec{E}$ interacting with a molecule induces a dipole moment given by

$$\vec{m}_{ind} = (a) \cdot \vec{E} \tag{2.9}$$

where (a) is the polarisability tensor of the molecule having the components

$$(a) = \begin{pmatrix} a_{xx} & a_{xy} & a_{xz} \\ a_{yx} & a_{yy} & a_{yz} \\ a_{zx} & a_{zy} & a_{zz} \end{pmatrix} \tag{2.10}$$

The polarizability tensor modulated by a vibrational mode of frequency n_k is given by

$$(a)_k = (a_0) + \left(\frac{\partial a}{\partial q_k}\right)_0 \cdot q_k{}^0 \cdot \cos 2\pi n_k t + \ldots . \tag{2.11}$$

The induced dipole moment becomes within this linear approximation

$$m_{ind} = (a_0) \cdot E_0 \cdot \cos 2\pi n_L t + \left(\frac{\partial a}{\partial q_k}\right)_0 \cdot q_k{}^0 \cdot \cos 2\pi n_k t \cdot E_0 \cdot \cos 2\pi n_L t + \ldots \tag{2.12}$$

Neglecting higher order terms and using trigonometric formula results in

$$\begin{aligned} m_{ind} &= (a_0) \cdot E_0 \cos 2\pi n_L t && \textit{Rayleigh-scattering} \\ &+ \frac{1}{2} \cdot \left(\frac{\partial a}{\partial q_k}\right)_0 \cdot q_k{}^0 \cdot E_o \cdot \cos 2\pi (n_L - n_k) t && \textit{Stokes-scattering} \\ &+ \frac{1}{2} \cdot \left(\frac{\partial a}{\partial q_k}\right)_0 \cdot q_k{}^0 \cdot E_o \cdot \cos 2\pi (n_L + n_k) t && \textit{anti-Stokes-scattering} \end{aligned} \tag{2.13}$$

From Eq. (2.13) becomes evident that a vibrational mode will be Raman active (which is similar to Eq. 2.8) only if

$$\left(\frac{\partial a}{\partial q_k}\right)_0 \neq 0 . \tag{2.14}$$

The evaluation of Raman scattering intensities is more complicated than in the case of IR spectroscopy. The observed radiant power is proportional to the square of the absolute differential Raman scattering cross-section $\partial s / \partial W$ (in $cm^2 \cdot sr^{-1}$) where s is the cross-section and W is the solid angle. The first-order differential Raman cross-section[34] for the Stokes component of the kth mode far from resonance is given by

$$\frac{\partial s_k}{\partial W} = \frac{(2\pi n_S)^4}{c^4} \left| \hat{e}_S \frac{\partial (a)}{\partial q_k} \hat{e}_L \right|^2 \frac{h(n_k{}^b + 1)}{8\pi^2 n_k}, \tag{2.15}$$

$$n_k{}^b = \left[\exp\left(\frac{h n_k}{kT}\right) - 1 \right]^{-1} . \tag{2.16}$$

In Eq. (2.15), $n_S = n_L - n_k$ is the frequency of the scattered light, $\hat{e}_S$ and $\hat{e}_L$ are the unit vectors of the electric-field direction (polarization) for the scattered and the incident light, and n_k^b is the Bose-Einstein statistical factor. Since molecules in the gas phase may be

oriented randomly, this expression has to be appropriately space averaged. The result of this averaging procedure depends on the relative orientations of the direction and the polarization of the incident and scattered beams. In most experiments, a plane-polarized incident laser beam is used. Further, the direction of the incident beam, the polarization of this beam and the direction of observation are perpendicular to each other. Under these circumstances, one yields a differential Raman cross section for the Stokes line *k* of

$$\frac{\partial s_k}{\partial W} = \frac{(2p n_S)^4}{c^4} \frac{h(n_k{}^b + 1)}{8p^2 n_k} \frac{I_k{}^{Ram}}{45} \quad , \tag{2.17}$$

where I_k^{Ram} is the Raman scattering activity[33] given by

$$I_k{}^{Ram} = 45\left(\frac{\partial \tilde{a}}{\partial q_k}\right) + 7\left(\frac{\partial g}{\partial q_k}\right) = 45\tilde{a}'^2 + 7g'^2 . \tag{2.18}$$

$\tilde{a}'$ is the mean polarizability derivative

$$\tilde{a}' = \frac{1}{3}\left(a'_{xx} + a'_{yy} + a'_{zz}\right) \tag{2.19}$$

and g'^2 the anisotropy of the polarizability tensor derivative for the *k*th mode

$$g'^2 = \frac{1}{2}\left[\left(a'_{xx} - a'_{yy}\right)^2 + \left(a'_{yy} - a'_{zz}\right)^2 + \left(a'_{zz} - a'_{xx}\right)^2 + 6\left(a'_{xy}{}^2 + a'_{yz}{}^2 + a'_{zx}{}^2\right)\right]. \tag{2.20}$$

Moreover, the depolarization ration r_k can be obtained if measurements with unpolarized light are additionally performed

$$r_k = \frac{6g'^2}{45a'^2 + 7g'^2} . \tag{2.21}$$

If the Raman signal is detected through a polarizer with its electric vector parallel to the one of the incident light[33], the depolarization ratio becomes

$$r_k = \frac{3g'^2}{45a'^2 + 4g'^2} \tag{2.21}$$

The Raman intensity of the anti-Stokes lines is very low at room temperature for higher wavenumber modes, since the molecules are mostly in their vibrational ground level. The intensity ratio of the Stokes and anti-Stokes lines is given by

$$\frac{I^{Stokes}}{I^{anti-Stokes}} = \left(\frac{n_L - n_k}{n_L + n_k}\right)^4 \cdot exp\left(hcn_k / kT\right) \tag{2.22}$$

and allows to determine the temperature of the sample.

IR and Raman spectroscopy are widely used techniques, both in the academic as well as in industrial fields. The development of very sensitive detectors, for e.g. charge-coupled devices (CCDs), laser excitation sources, step-scan techniques, interferometers and Fourier-transformation of the interferogram into a spectrum, light-fiber optics, the implementation of computer added on-line analysis, the advent of attenuated total reflectance (ATR), the possibility to combine an IR or Raman setup with a microscope to perform mapping and imaging experiments, have made vibrational spectroscopy a powerful experimental technique in chemistry, biochemistry and medicine. IR and Raman spectroscopy both have several advantages such as: they are fast, non-destructive, highly sensitive, relatively easy to automate, only small sample amounts are required and the measurements can be performed in all physical states. Often IR and Raman spectroscopy are complementary methods, since molecules with a center of symmetry possess IR inactive vibrational modes which are Raman allowed, and vice-versa. Nevertheless, there are also disadvantages: IR sample preparation can be difficult, water has very strong IR modes and therefore IR measurements in aqueous solutions are very difficult. Additionally, *mid*-IR spectra through glass plates cannot be recorded. Raman spectroscopy overcomes most of this difficulties, but unfortunately, the Raman signal of samples in diluted solution is generally very weak. When excited with visible light, many molecules or any present impurity may give rise to strong fluorescence, which masks the weak Raman signal. Nevertheless, the development of the NIR-FT Raman spectroscopy made it possible to obtain spectra free of fluorescence for most samples.

In the last decades, the Raman signal enhancement due to the resonance Raman and surface enhanced Raman scattering effects made it possible to obtain spectra in solution at low concentrations. Moreover, these techniques provide additional, valuable information about the molecular structure of the excited state or molecules adsorbed on different substrates, intermolecular interactions, etc. In the following, the theoretical fundamentals of these methods will be discussed.

Resonance Raman spectroscopy

General consideration

The resonance Raman (RR) effect was observed for the first time by Shorygin[35] in 1947. The resonance Raman effect occurs when the wavelength of the exciting electromagnetic field lies within an electronic absorption band[13,14]. For such a case, the molecule adsorbing an energy quantum will be raised to a higher electronic level ($e = 1$, see Fig. 2.2) and the transition probability for the two-photon Raman scattering process is significantly enhanced. The enhancement factor for the resulting RR signal is about 10^2 - 10^6 and the RR effect allows one to obtain well resolved Raman spectra in diluted solutions. The vibrational wavenumbers provide detailed information about the geometry and electronic structure of the ground state molecular structure. In addition, the intensities of the Raman lines give information about the symmetry, equilibrium geometry and dynamics of the resonantly excited electronic state[13,17].

Biological systems containing cromophoric groups such as hemoglobin, carotene, chlorophyll, rhodopsin, etc. were extensively investigated by means of RR spectroscopy[12]. These chromophores play crucial roles in many biological processes such as vision, photosynthesis, etc. The light induced molecular changes and the energetic of these photochemical processes can be investigated by RR spectroscopy, where the chromophores can be selectively excited.

According to the *Franck-Condon principle* the absorption process takes place without any changes of the positions of the nuclei (see Fig. 2.3). Nevertheless, the absorbed energy ($\hbar w_L$) promotes an electron from an orbital into an other with different bonding, non-bonding and anti-bonding properties. The promoting of an electron from a bonding into an anti-bonding orbital, for example, will lead to weaker bonding in the excited state and an increase of the bond length[16]. Therefore, the excited state equilibrium geometry differs from the ground state geometry of the molecule and the molecule will relax through radiationless deactivation to the equilibrium excited state geometry. The dimensionless displacement parameters, D_ks, (also referred to as Franck-Condon parameters) are a measure of how far along a particular normal mode the molecule in one state has to move in order to reach the geometry of the other state[14]. In a one-dimensional picture, the displacement parameter is the distance between the bottom of the parabolas of

the ground and excited state potentials (see Fig. 2.3). The reorganization energy is the increase in potential energy that results when one state is distorted to the geometry of the other state, and is equivalent to the energy which is set free through radiationless deactivation. In general this corresponds to the total vibrational energy and the energy which is taken over by the molecule's environment. The total vibrational energy is the sum of the contribution of each mode, $l_k = 0.5 w_k D_k^{\,2}$.

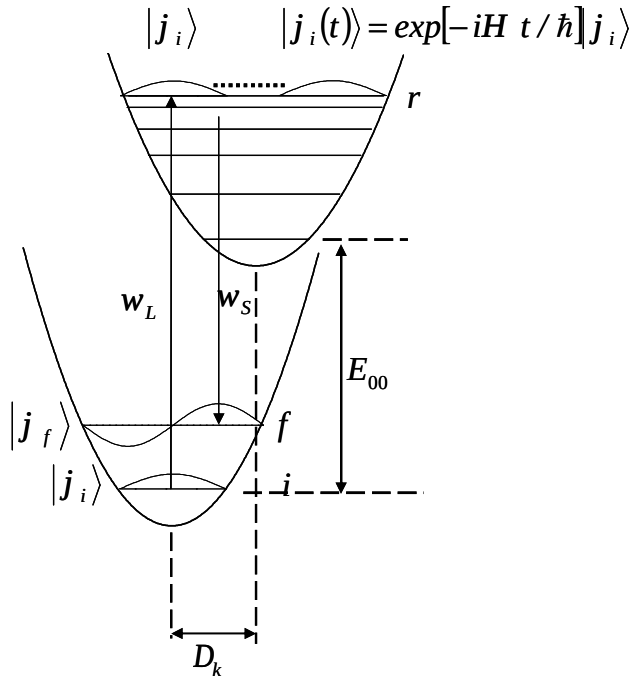

Figure 2.3 *Harmonic potential surfaces for the ground and resonant excited states.*

Quantitative analysis of the intensity of the bands in the resonance Raman spectra as function of the excitation wavelength gives the resonance Raman intensity profiles[14] (RR profiles). The intensity of the vibrational modes in the resonance Raman spectra as well as the absorption cross section depend on characteristics of the ground and excited state potential surfaces. Nevertheless, absorption spectra are in general diffuse, showing no vibronic structure due to fast photochemistry in the resonant state or severe solvent induced electronic spectral broadening, and therefore information about the excited state potential cannot be extracted. The resonance Raman intensities of transitions and their excitation profiles carry vibrational mode-specific information about the excited-state potential energy surface in the Franck-Condon region[17,36]. Several theoretical approaches[37] have been developed in order to extract information about the excited state potential

surface distortions from the resonance Raman spectra: the *sum-over-state* formalism, the *time-dependent* formalism[38-40] and *transform* methods[41,42]. The absorption spectrum depends on the same parameters as the resonance Raman profiles, and since electronic spectra can be easily measured very accurately, they provide a strong constraint in the resonance Raman intensity analysis. Hence, the resonance Raman intensity profiles of the vibrational modes in conjunction with the absorption spectrum provide detailed information about the displacement of the excited state potential surface along normal mode coordinates. Several review and book articles are describing these theoretical methods[16-18].

The traditional approach[6] to evaluate RR intensities is starting from the Kramers-Heisenberg-Dirac (KHD) dispersion formula originally derived using the time-dependent second-order perturbation theory. The KHD expression for the transition polarizability tensor components is

$$\left(a_{rs}\right)_{fi} = \sum_{r} \left\{ \frac{\left\langle e_f \left| m_r \right| e_r \right\rangle \left\langle e_r \left| m_s \right| e_i \right\rangle}{\hbar w_{ri} - \hbar w_L - iG} + \frac{\left\langle e_f \left| m_s \right| e_r \right\rangle \left\langle e_r \left| m_r \right| e_i \right\rangle}{\hbar w_{rf} + \hbar w_L - iG} \right\}, \tag{2.23}$$

where (r, s) refer to the molecule fixed cartesian coordinates (x, y, z), e_i and e_f refer to the initial and final states of the Raman transition, e_r is any state of the unperturbed molecule, m_r is the rth component of the transition dipole moment, Γ is a damping factor related to the lifetime of the state r, and w_{ri} is the angular frequency associated with the $r \leftarrow i$ transition. The summation involves all eigenstates r of the unperturbed molecule except i and f. The total Raman intensity scattered into the solid angle $4p$ is proportional to the third power of the scattered frequency w_S, the frequency of the incident beam and the square of the polarizability tensor components

$$I_{fi} \sim w_L w_S^{\,3} \sum_{r,s} \left| \left(a_{rs}\right)_{fi} \right|^2 . \tag{2.24}$$

When the angular frequency of the incident beam, w_L, approaches to the transition angular frequency for an absorption band of the molecule, w_{ri}, the denominator in the first term of Eq. (2.23) is getting small and this term begins to dominate[6]. The resonantly excited states dominate the *sum over states* of the Raman polarizability expression

$$\left(a_{rs}\right)_{fi} = \sum_{r} \left\{ \frac{\left\langle e_f \left| m_r \right| e_r \right\rangle \left\langle e_r \left| m_s \right| e_i \right\rangle}{\hbar w_{ri} - \hbar w_L - iG} \right\}. \tag{2.25}$$

In the *Born-Oppenheimer (adiabatic) approximation*, the electronic ($|g,e\rangle$), vibrational ($|j_{i,f,r}\rangle$) and rotational eigenstates of the unperturbed molecule may be separated. For the vibrational resonance Raman effect considering that the molecule is initially in its vibrational level *i* of the ground electronic state and the Raman transition terminates in the vibrational level *f* of the ground electronic state (see Fig. 2.3) one obtains

$$\begin{aligned} |e_i\rangle &= |g j_i\rangle = |g\rangle|j_i\rangle \\ |e_f\rangle &= |g j_f\rangle = |g\rangle|j_f\rangle \\ |e_r\rangle &= |e j_r\rangle = |e\rangle|j_r\rangle \ , \end{aligned} \tag{2.26}$$

where *e* is a resonantly excited electronic state and *r* represents vibrational states in the excited electronic state, respectively. The dipole transition moments in the numerator of Eq. (2.25) become

$$\begin{aligned} \langle e_f|m_r|e_r\rangle &= \langle j_f|M_r{}^e|j_r\rangle \\ \langle e_r|m_s|e_i\rangle &= \langle j_r|M_s{}^e|j_i\rangle \ , \end{aligned} \tag{2.27}$$

where only the vibrational wave functions are involved, while the electronic wave functions appear in the pure electronic transition moment M^e connecting the ground with the electronic excited state. M^e is a function of the nuclear coordinate and can be expanded into a Taylor series about the equilibrium position (Herzberg-Teller expansion)

$$M^e = M_0^e + \left(\frac{\partial M^e}{\partial q_k}\right)_0 q_k + \ldots \tag{2.28}$$

along the *k*th normal mode coordinate. Introducing the electronic transition dipole moment into the expression of the polarizability tensor components for resonant conditions given in Eq. (2.25) and separating the terms, one obtains[6,11]

$$\begin{aligned} (a_{rs})_{fi} = &\sum_{e,r} \frac{M_{0r}^e M_{0s}^e}{\hbar\omega_{ri} - \hbar\omega_L - iG}\langle j_f|j_r\rangle\langle j_r|j_i\rangle + \qquad A-Term \\ &\sum_{e,r} \frac{M_{0r}^e \left(\frac{\partial M_{0s}^e}{\partial q_k}\right)_0}{\hbar\omega_{ri} - \hbar\omega_L - iG}\langle j_f|j_r\rangle\langle j_r|q_k|j_i\rangle + \sum_{e,r} \frac{\left(\frac{\partial M_{0r}^e}{\partial q_k}\right)_0 M_{0s}^e}{\hbar\omega_{ri} - \hbar\omega_L - iG}\langle j_f|q_k|j_r\rangle\langle j_r|j_i\rangle \qquad B-Term. \end{aligned} \tag{2.29}$$

A- and *B*-terms are the so-called Albrecht's *A* and *B*-terms, respectively. The higher terms of the Taylor expansion in Eq. (2.28) would lead to additional terms (*C*, etc.).

The *A*-term represents the zero-order electronic transition. Since the electronic transition dipole moment $M_0{}^e$ is much larger than its derivative along the normal mode coordinate, the A-term scattering is dominant as long as the Franck-Condon overlaps (FC factors) $\langle j_f | j_r \rangle$ and $\langle j_r | j_i \rangle$ are not vanishing. This is usually the case for Raman transitions of totally symmetric vibrational modes along which the adiabatic potential minimum is displaced between the ground and excited electronic states (see Fig. 2.3). According to the relation given by Savin the preresonance Raman intensity is proportional to the square of the displacement parameters and the square of the vibrational wavenumber ($I_k{}^{RR} \sim D_k{}^2 w_k{}^2$). For very small displacements only the fundamental vibrational transition shows significant enhancement, while vibrational modes with large displacements give rise to overtone progressions and combination modes. In the case of a vibrational mode which is not totally symmetric, but antisymmetric with respect to a symmetry element, the product of the FC factors is zero. The assumption that the RR enhancement occurs only via the *A*-term is equivalent to the assumption that the electronic transition moment remains constant and does not depend on the normal mode coordinate. This is called the *Condon approximation*.

The *B*-term contribution is the so-called "borrowed intensity" or "the forbidden character" of the $|e\rangle \leftarrow |g\rangle$ transition[6,11]. In the Albrecht theory, the first-order expansion (Herzberg-Teller) expansion is used for $|e\rangle$

$$|e\rangle = |e_0\rangle + \sum_k \sum_{s \neq e} \frac{\langle e_0 | h_k | s_0 \rangle}{\hbar w_{e0} - \hbar w_{s0}} q_k |s_0\rangle \tag{2.30}$$

where $|s_0\rangle$ are excited electronic states, $\hbar w_{e0}$ and $\hbar w_{s0}$ are the pure electronic transition energies (the energy difference between the energy minima of the excited and ground electronic states, (E_{00} in Fig. 2.3), and h_k is the vibronic coupling operator given by the derivative of the interaction Hamiltonian H_{ev} with regard to q_k evaluated at $q_k = 0$, $h_k = (\partial H_{ev} / \partial q_k)$. Hence, *B*-term scattering requires the existence of a second excited state $|s_0\rangle$ for which the transition from the ground state is allowed and for which the vibronic coupling with $|e_0\rangle$ is significantly large. The vibronic coupling of two states takes place

only for a vibrational fundamental whose irreducible representation can be found in the direct product of the irreducible representations of the two states. Thus, *B*-term enhancement for a mode, *k*, requires that this mode couples two states of the same symmetry. This is the case for a few excited states which are close in energy. The integrals containing the derivative of the electronic transition moment are non vanishing for symmetric or antisymmetric modes even if the potential surfaces are not displaced. Therefore, the *B*-term can give intensity to the transitions concerned with an antisymmetrical vibrational mode. Contrary to the case of the *A*-term, transitions involving more than one vibrational quantum are not expected from the *B*-term. B-term scattering is in general significantly smaller than *A*-term scattering, but it can give rise to an asymmetric scattering tensor, $a_{rs} \neq a_{sr}$, leading to the phenomenon of "anomalous" polarization[43].

Concerning the *A*-term Raman scattering, only the Franck Condon integrals of the form $\langle j_f | j_r \rangle \langle j_r | j_i \rangle$ need to be calculated. In the absence of the *Duschinsky* effect, the normal modes of the ground and excited state can have a relative displacement of the coordinate system, but no rotation of the excited state coordinate system with respect to that of the ground state exists. The *Duschinsky* effect is similar to two Cartesian coordinate systems rotated and displaced with respect to each other, with the normal modes as axes[44]. When a one-dimensional slice of the potential surface is taken along a normal mode of one state, similarly to the example in Fig. 2.3, the slice does not correspond to a normal mode of the other state, but it goes along a linear combination of the normal modes of the second state. However, in the limit of no *Duschinsky* mixing, the multidimensional Franck-Condon integrals (3N-6, for a total number of vibrational modes) can be factored out into products of one-dimensional integrals[17,37]

$$\langle j_r | j_i \rangle_t = \langle j_{1r} j_{2r} j_{3r} \cdots | j_{1i} j_{2i} j_{3i} \cdots \rangle = \langle j_{1r} | j_{1i} \rangle \langle j_{2r} | j_{2i} \rangle \langle j_{3r} | j_{3i} \rangle \cdots . \qquad (2.31)$$

The one dimensional Franck-Condon integrals have the general form

$$\langle 0|0 \rangle = \left(\frac{2}{1+R} \right)^{1/2} R^{1/4} \, exp\left[\frac{-D^2}{2(1+R)} \right] \qquad (2.32)$$

$$\langle m|0 \rangle = \frac{\langle 0|0 \rangle}{\left(2^m m!\right)^{1/2}} \left(\frac{R-1}{R+1} \right)^{m/2} H_m \left[-\left(\frac{R}{R^2-1} \right)^{1/2} D \right] \qquad (2.33)$$

$$\langle 0|n \rangle = \frac{\langle 0|0 \rangle}{\left(2^n n!\right)^{1/2}} \left(\frac{1-R}{1+R} \right)^{n/2} H_n \left[\frac{D}{\left(1-R^2\right)^{1/2}} \right] \qquad (2.34)$$

$$\langle m|n\rangle = \langle 0|0\rangle^{-1} \sum_{r=0}^{min(m,n)} \left(\frac{2R^{1/2}}{1+R}\right)^{r} \frac{1}{r!} \times \left[\frac{m!\,n!}{(m-r)!\,(n-r)!}\right]^{1/2} \langle m-r|0\rangle\langle 0|n-r\rangle \ , \quad (2.35)$$

where $R = w_n / w_m$, w_n and w_m being the ground and excited state frequencies, $|n\rangle$ and $|m\rangle$ are vibrational levels of the ground and excited states, H_m is the mth Hermite polynomial and D is the displacement between the potential minima of the ground and excited states in ground-state dimensionless normal coordinates. For the case of equal ground and excited state wavenumbers (R = 1), the Franck-Condon integrals required to calculate the absorption spectrum and resonance Raman excitation profiles in the zero temperature limit (initial and final vibrational quantum numbers 0 and 1, respectively) are

$$\left|\langle r|0\rangle\right|^2 = exp\left(-\frac{1}{2}D^2\right) \cdot \left(\frac{1}{2}D^2\right)^{r} \cdot \frac{1}{r!} \quad (2.36)$$

$$\langle 1|r\rangle\langle r|0\rangle = exp\left(-\frac{1}{2}D^2\right) \cdot \sqrt{\frac{1}{2}}D \left[\frac{\left(\frac{1}{2}D^2\right)^{r}}{r!} - \frac{\left(\frac{1}{2}D^2\right)^{r-1}}{(r-1)!}\right]. \quad (2.37)$$

The summation for the polarizability components goes over the vibrational levels of the resonantly excited states, r, and in general the iteration is stopped when the absolute value of the Franck-Condon product for one vibrational mode drops below a chosen cutoff. However, this procedure can be applied only for small molecules with a few vibrational modes because of the very high computational demand. Therefore the *time-dependent* formalism has been introduced. Since this procedure was applied in the present RR studies, it will be described in detail in the following.

The *time-dependent* formalism

The *time-dependent* formalism to interpret the resonance Raman data is a powerful method. It allows the analysis of complicated molecules where the sum-over-state method would require too high computational effort. The *time-dependent* formalism of resonance Raman scattering was developed by Lee, Heller and coworkers. Several publications[37,38,40] are treating the theoretical background of this method. Several book articles[14,16,17] are describing in detail the handling of resonance Raman spectra based on this formalism and provide examples where the *time-dependent* analysis was successfully applied to investigate small molecules, photo dissociation processes, inorganic compounds, polyenes,

aromatic hydrocarbons, biological chromophores, electron transfer processes, to name only a few of them.

The *time-dependent* formalism can be derived[37] from the *sum-over-state* method presented above using the following mathematical relation

$$\frac{1}{s} = \frac{i}{\hbar}\int_0^\infty exp\left(-\frac{i}{\hbar}s\cdot t\right)dt \ , \tag{2.38}$$

where one replaces the denominator in the Albrecht's *A*-term by $s = \hbar w_{ri} - \hbar w_L - iG$. Introducing the explicit energy difference between the initial ground vibrational level and the excited state vibrational level $\hbar w_{ri} = \hbar w_r - \hbar w_i$, the Raman polarizability tensor components become

$$\begin{aligned}(a)_{fi} &= \sum_r \frac{\langle j_f | j_r\rangle\langle j_r | j_i\rangle}{\hbar w_r - \hbar w_i - \hbar w_L - iG} \\ &= \frac{i}{\hbar}\int_0^\infty \sum_r \langle j_f | j_r\rangle\langle j_r | j_i\rangle \cdot exp\left[-i(\hbar w_r - \hbar w_i - \hbar w_L - iG)t/\hbar\right]dt\end{aligned} \ , \tag{2.39}$$

where the sign $-iG$ is chosen for mathematical convenience. Then, with

$$exp\left[-i\hbar w_r t/\hbar\right] = exp\left[-iE_r t/\hbar\right] \tag{2.40}$$

and since

$$\langle j_r | exp\left[-iHt/\hbar\right] = \langle j_r | exp\left[-iE_r t/\hbar\right] \ , \tag{2.41}$$

where *H* is the excited state vibrational Hamiltonian propagating the ground state vibrational wavefunction $|i\rangle$ on the upper state potential surface

$$exp\left[-iHt/\hbar\right]|i\rangle = |i(t)\rangle \tag{2.42}$$

one obtains for the polarizability tensor components using the closure relation to remove the sum over *r*

$$(a)_{fi} = \frac{i}{\hbar}\int_0^\infty \langle j_f | j_i(t)\rangle exp\left[i(E_L + E_i)t/\hbar\right]\cdot exp\left[-Gt/\hbar\right]dt \ . \tag{2.43}$$

The complete expression[17] for the Raman cross section is

$$s_R(w_L) = \frac{8pM^4}{9\hbar^2 c^4} w_L w_S{}^3 \int_{-\infty}^{\infty} ddG(d)\left|\int_0^\infty dt\langle j_f | j_i(t)\rangle exp\left[i(w_L - w_0 - d + w_i)t - g(t)\right]\right|^2 \ , \tag{2.44}$$

where the transition dipole moment $M = eR$ is the transition length times the elemental charge, $\hbar w_0$ is the difference between the energy minima of the excited and ground state

potential surfaces, *d* is a static inhomogeneous broadening function of the zero-zero energy differences of the vibrational modes and $exp[-g(t)]$ is the damping function.

In the following, the *time-dependent* theory to calculate the absorption spectrum and the resonance Raman excitation profiles will be described in detail. The Franck Condon overlaps are estimated by use of wavepacket propagation techniques. These techniques are exact for harmonic potentials and are based on the analytic properties of Gaussians. In the case of anharmonic potentials, the integrals can be calculated numerically. Nevertheless, the parameters of the potential surfaces are required, which are in general difficult to obtain for larger molecules. The mathematical background[17] for the analytical calculations of the overlap factors will be skipped here and only the final formula will be given.

Although it is not necessary, since the time-dependent theory can treat generalized cases, some approximations will be considered. First, the potential surfaces are harmonic, second, the force constants are the same in both ground and excited state, third, the transition dipole moment, *M*, is constant and finally, the normal coordinates are not mixed in the excited state. Under these approximations, the *time-dependent* formalism is equivalent to the *Franck-Condon* analysis[16].

As mentioned previously, it is always necessary to simultaneously model the absorption and resonance Raman excitation profiles to determine the FC parameters[17]. The absorption cross section at the same level of theory is given by

$$s_A(w_L) = \frac{4p^2M^2}{3n\hbar c} w_L \int_{-\infty}^{\infty} ddG(d) \sum_i B_i \, Re \int_0^{\infty} dt \langle j_i | j_i(t) \rangle \cdot exp[i(w_L - w_0 - d + w_i)t - g(t)] \,, \tag{2.45}$$

where the *Re* signifies the real part of the integral and B_i is the Boltzmann population of the initial vibrational state.

In order to determine the absorption cross section it is necessary to evaluate the overlap of a propagating wavepacket $j(t)$, which is moving on the excited electronic potential surface, with itself at time zero. Under the assumptions mentioned above, the absorption overlap for one vibrational mode at the wavenumber w_k can be calculated[16,17] according to the following simple analytical formula:

$$\langle j_k | j_k(t) \rangle = exp\left[-\frac{D_k^2}{2}(1 - exp[-iw_k t]) - \frac{iw_k t}{2} \right] \tag{2.46}$$

where D_k is the dimensionless displacement parameter of the excited state potential surface along the *k*th mode. The total overlap in the case of a multimode system is the product of the overlap of each single mode and becomes:

$$\langle j \mid j(t) \rangle = exp\left[\sum_k \left[-\frac{D_k^{\,2}}{2}\left(1 - exp[-iw_k t]\right) - \frac{iw_k t}{2} \right] - iE_{00}t - G \cdot t \right], \qquad (2.47)$$

where $E_{00} = \hbar w_0$, the zero-zero energy and the damping factor G are taken into account. The role of E_{00} in the modeling process is to properly position the absorption spectrum.

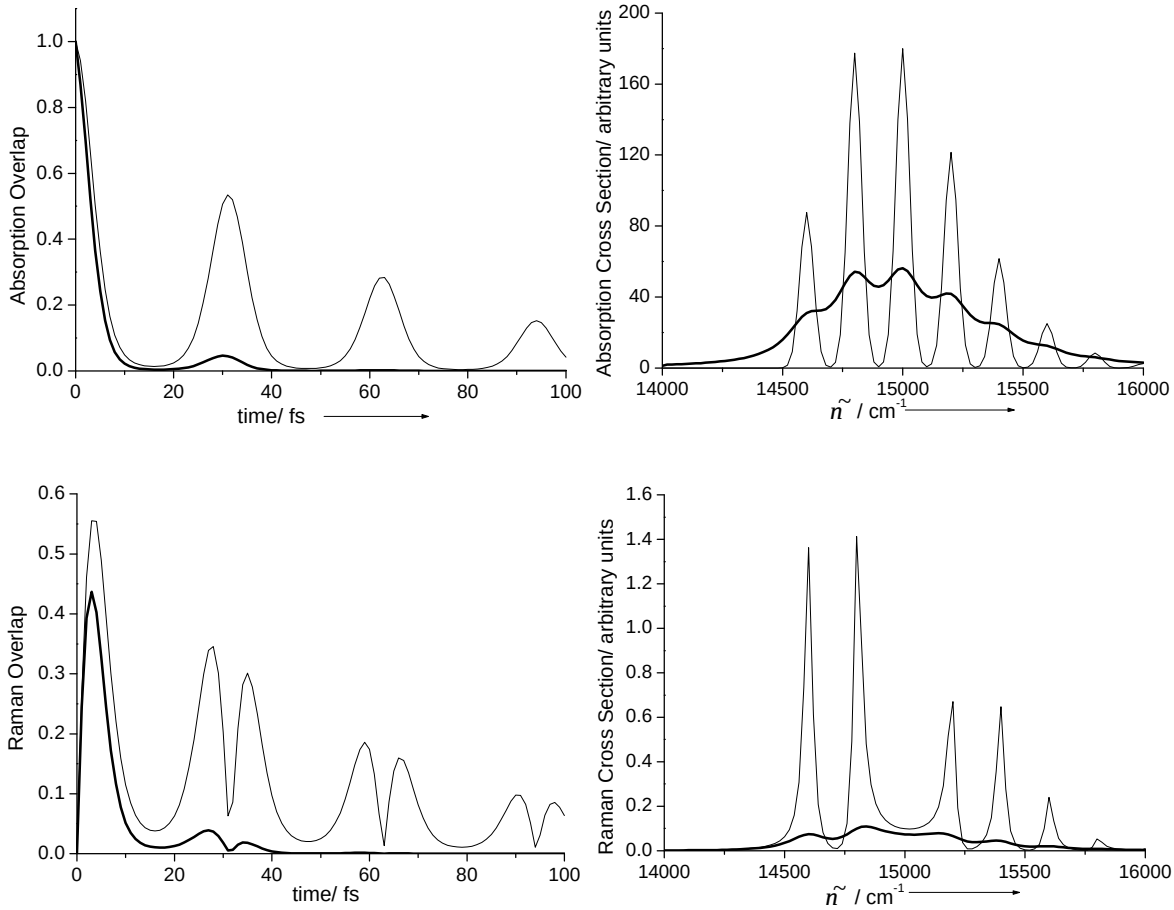

Figure 2.4 *The magnitude of the absorption and Raman overlap plotted for a vibrational mode at 200 cm^{-1}, displacement parameter D_k = 2, with E_{00} = 14500 cm^{-1} (689.6 nm) and G = 20 (thin line) and G = 100 (solid line). The corresponding absorption spectrum and RR excitation profiles obtained through Fourier transformation of the absorption overlap and half square Fourier transform of the Raman overlap are shown on the right side, respectively.*

The Raman cross section contains the overlap of the propagating wavepacket $j(t)$ with the wavefunction of the final vibrational level where the transition terminates, $j_f(t)$. The analytical expression[16,17] of this overlap factor for a symmetrical mode is given by

$$\left\langle j_{f,k} \middle| j_k(t) \right\rangle_s = exp\left[-\frac{D_k^{\,2}}{2}\left(1 - exp[-iw_k t]\right) - \frac{iw_k t}{2} \right] \cdot \left(1 - exp[-iw_k t]\right)^{n_k} \frac{(-1)^{n_k} D_k^{\,n_k}}{\sqrt{2^{n_k} n_k!}} \quad , \quad (2.48)$$

where n_k is the quantum number of the vibrational level f taking the value 1 for fundamentals, 2, 3, etc. for overtones.

A graphical representation of the Franck Condon overlaps as function of time and the resulting absorption spectrum and resonance Raman excitation profiles obtained through Fourier transformation and square of half-Fourier transformation of the functions for one vibrational mode are given in Fig. 2.4. For exemplification, a displacement parameter D_k of 2 was applied, the vibrational wavenumber w_k was 200 cm^{-1}, E_{00} was 14500 cm^{-1}, only the $1 \leftarrow 0$ transition was considered and two different values for the damping factor G were applied: 20 (thin line) and 100 (solid line), respectively.

Figure 2.4 visualizes the wave packet dynamics in the excited state for both absorption and Raman processes. In both types of spectroscopy, the initial vibrational wavepacket makes a vertical transition and propagates on the potential surface of the excited state. The displaced wavepacket is not a stationary state and evolves in time according to the Schrödinger equation, $\left| j_i(t) \right\rangle = exp[-iH\ t/\hbar] \left| j_i \right\rangle$. For the absorption cross section, the overlap of the propagating wavepacket $\left| j(t) \right\rangle$ with itself at time (t = 0) (with the wavefunction of the initial vibrational level of the ground state) is maximum (has a value of 1) for time zero. As the wavepacket is moving away from the Franck-Condon region, the overlap drops to zero. This time (about 15 fs for the example in Fig. 2.4) corresponds to the point when the wavepacket reached the other side of the excited state potential surface, and then it will return. The overlap will have a second maximum at the time t when the wavepacket has returned to its initial position. This time (about 30 fs, see Fig. 2.4) corresponds to one vibrational period. Due to the damping factor, the following maxima are smaller than the maximum at time zero.

In the case of the Raman transition, the overlap of the propagating wavepacket with the wavefunction of the final vibrational level is zero at $t = 0$, because the two functions are corresponding to orthogonal wavefunctions. At short times (a few fs) the overlap

reaches a maximum and than drops to zero when the wavepacket is far away from the Franck Condon region. The maximum overlap for overtones occurs at later times than for fundamentals. Afterwards, the wavepacket returns toward its initial point and before a vibrational period is completed a second maximum of the Raman overlap is reached, while at the initial point it is again zero. The repetition of this process leads to the pattern in the Raman overlap.

As can be seen in Fig. 2.4, for the case of a small damping factor, several maxima can be observed in the absorption and Raman overlaps, while for $G = 100$, the number of recurrences decreases. The absorption cross section and Raman cross section are smaller for large damping factors than for the lower one. Moreover, in the frequency domain, the spectra present less vibronic structure. For even larger damping factors, the spectra are completely diffuse. This fact can be correlated with the spectra obtained in the gas phase and in solution. In the gas phase, the interaction between the molecule and the "bath" is small, and each atom will return at the same time to its initial position, while in solution the molecule's vibrations are coupled with those of the solvent, and energy is transferred from the probe to the "bath".

The Brownian oscillator model

The quantitative analysis of the resonance Raman intensities is a valuable procedure, since the absolute Raman cross section exhibits different sensitivities to the homogeneous and inhomogeneous line widths as compared to the absorption cross section. If the integrands in Eqs. 2.44 and 2.45 decay rapidly in time, due to either a large G or to large excited state geometry changes in one or more vibrational modes, the absolute Raman cross sections are reduced and the absorption and excitation profiles are broadened. In contrast, an inhomogeneous distribution of zero-zero energies (the d function in these equations) does not affect the Raman amplitude. Hence, the absorption spectrum and excitation profiles are broadened by the inhomogeneous broadening without affecting the average Raman intensity. Hence, the simultaneous analysis of absorption and Raman cross sections allows one to determine the homogenous and inhomogeneous contributions to the spectral width[45]. In general, the inhomogeneous distribution of the zero-zero energy is taken to be a Gaussian function[46] of the form

$$G(E_0) = \frac{1}{d\sqrt{2p}} \int_0^{\infty} exp\left[\frac{-(E_{0,i} - E_0)^2}{2d^2} \right], \tag{2.49}$$

where $E_{0,i}$ is the electronic zero-zero energy whose average value is E_0 and d is the standard deviation of a Gaussian distribution.

The damping function $exp[-g(t)]$ takes into consideration the broadening of the absorption spectrum due to the lifetime decay of the excited state and due to the effect of the solvent molecules on the probe. The classical way of treating the effects of the solvent is in the stochastic, inhomogeneous limit. The stochastic model describes only the effect of the solvent on the solute and does not take into consideration effects on the solvent due to the change in the electronic state of the solute, which is responsible for the Stokes shift of the absorption relative to fluorescence. The Brownian oscillator model developed by Mukamel and co-workers considers the solvent mode as a damped oscillator[23,47]. It treats the solvent as one or more linearly coupled vibrational modes, each characterized by a wavenumber, a ground to excited state displacement and a frictional damping coefficient. For simplification, the solvent modes are considered to lump into one effective mode. The solvent contribution to the damping function in the high-temperature and high-friction limits ($\hbar w_k$, $g >> k_B T$, where g is the friction) is given by[23,48]

$$g(t) = \left(\frac{D}{L} \right)^2 [exp(-Lt/\hbar) - 1 + Lt/\hbar] + i \frac{l_S}{L} [1 - exp(-Lt/\hbar)], \tag{2.50}$$

where l_S is the solvent reorganization energy given by $l_S = D^2 / 2k_B T$. D represents the strength of the coupling between the solvation coordinate and the electronic transition, and L is the modulation frequency of the solvent oscillator and determines the characteristic solvent time scale. The time scale of the solvent induced width is usually expressed by the parameter $k = L / D$. Neglecting the imaginary part of Eq. 2.50 (corresponding to the infinite temperature limit), the Brownian oscillator model is equivalent to the stochastic broadening model. The real part in the damping function is responsible for the broadening of the optical line, and the imaginary part accounts for the solvent-induced Stokes shift of the emission spectrum.

Mukamel and co-workers[23] showed that D can be approximated with the following function

$$D = G_0\left[\frac{1+0.85k+0.88k^2}{2.355+1.76k}\right] \tag{2.51}$$

where G_0 is the so called "homogeneous" broadening. Thus, two parameters (G_0 and k) are used to describe the solvent induced broadening. In general, slow modulation is assumed, $k << 1$ (usually $k = 0.1$), which makes the solvent contribution to the line shape nearly Gaussian and the imaginary term of the damping function becomes[37]

$$i\frac{l_S}{L}\left[1-exp\left(-Lt/\hbar\right)\right] = i\left(\frac{D^2}{2k_BT}t/\hbar\right) \tag{2.52}$$

In the case of fast photochemistry in the excited state such as isomerization, proton transfer, etc. a pure exponential decay function is also taken into account which has in general Lorentzian shape ($exp\left[-Gt/\hbar\right]$). Gaussian line shapes, $exp\left(-G^2t^2/\hbar\right)$, were also considered if the damping is due to a dissociative channel.

Therefore, the quantitative relationship between Raman and absorption cross sections permits the partitioning of total vibronic linewidths into homogeneous and inhomogeneous components and provides information on the vibrational and solvent reorganization energies. These quantities are very useful, since they are involved in the calculation of the relaxation rates, charge transfer rates, etc. *Fermi's Golden Rule* provides the nonradiative rate constant expression[18,49]

$$k_{nr} = \left(2p/\hbar\right)\left|V\right|^2 \times FCWD \tag{2.53}$$

where V is the effective electronic coupling matrix element between two electronic states, depending on the distance and relative orientation of electron donor and acceptor, and *FCWD* is the Franck Condon weighted density of states, which depends on the vibrational wavenumbers and reorganization energies for both internal modes and the low-wavenumber intermolecular and solvent coordinates. *FCWD* is generally expressed as a sum over vibrational states and takes into account the solvent-induced broadening. Thus, the nonradiative rate constant is proportional to[50]

$$k_{nr} \sim \frac{1}{\sqrt{4p\,l_S k_B T}}. \tag{2.54}$$

l_S is the solvent induced reorganization energy, which is additionally including any low-wavenumber vibrational mode which cannot be observed directly in the resonance Raman spectra. Furthermore, *FCWD* was expressed[49] for both conceptual and computational purposes into an equivalent time-correlator expression

$$FCWD = \frac{1}{p}\sum_i B_i \, Re \int_0^\infty dt \langle i | exp(-iH_g t/\hbar) | i \rangle exp[i(w_0 + w_i)t - g(t)] \,, \qquad (2.55)$$

where B_i is the Boltzmann population of state $|i\rangle$ of $w_i = E_i/\hbar$ with E_i being the energy above the zero point of this state. H_g is the Hamiltonian for the final energy state. The contribution to the total reorganization energy from the high-wavenumber modes is contained in the correlation function, while the contribution from the low-wavenumber solvent and other classically behaving modes is given by the damping function $exp[-g(t)]$. The vibrational reorganization energy can be calculated according to

$$l_{V,k} = \frac{1}{2} D_k^{\,2} w_k \,. \qquad (2.56).$$

The expression of the *FCWD* is closely related to the expressions derived by the time-dependent formalism for the absorption and Raman cross sections.

Surface enhanced Raman scattering

Many chemical, pharmaceutical, physiological and industrial processes take place at interfaces[25-27]. Therefore the investigation of the interactions between the adsorbed molecule and the substrate, i.e. the molecular changes that occur upon adsorption, and the determination of the binding site of the adsorbate are an essential task in order to understand these processes. IR and Raman spectroscopy have proved to be valuable tools for studying the molecular structure and the reactivity of systems adsorbed onto surfaces. Nevertheless, while the analysis of aqueous solution-solid interfaces or polymer-modified surfaces is difficult by means of IR spectroscopy because of the strong IR absorbance of water or bulk phase, normal Raman spectroscopy suffers from the weakness of the Raman scattering process[6]. The discovery of the surface enhanced Raman scattering effect (SERS) has made it possible to investigate molecules from aqueous solutions at very low concentrations adsorbed on proper metal surfaces. Fleischmann et al.[25-27] observed high Raman signals from pyridine adsorbed onto roughened silver electrodes in 1974, and shortly after, two independent research groups showed that the Raman scattering cross section per molecule is enhanced by four to six orders of magnitude relative to that of the pyridine molecule in aqueous solution.

Enhancement mechanisms

Much experimental and theoretical work has been done to explain the SERS effect and to determine the factors that influence the enhancement mechanism as well as to develop SERS selection rules for an exact interpretation of the SERS spectra[26]. To describe the scattering behavior of a molecule in the vicinity of a metal substrate, the effect of the surface on the molecular characteristics, (a), as well as on the incident and scattered radiation must be taken into consideration. Moreover, in general, there is a field gradient ($\vec{E}'$) which contributes to the induced dipole moment through the quadrupole polarizablity A of the molecule

$$\vec{m}_{ind}{}^{S} = (a)^{S} \cdot \vec{E}^{S} + A^{S} \cdot \vec{E}'^{S} / 3 \,, \tag{2.57}$$

where the induced dipole moment (see Eq. 2.9) of the molecule adsorbed onto the surface involves parameters modified by the surface. In the following the enhancement through each of these factors will be discussed shortly.

The *surface electromagnetic field enhancement* has a very important contribution to the enhancement of the Raman signal of molecules adsorbed on adequate surfaces and the theoretical consideration of this effect explains several features observed in SERS spectroscopy. It has been determined experimentally that silver metal surfaces yield very high enhancement factors. Nevertheless, other metals such as gold, copper, alkali metals, aluminium and indium show comparable enhancement. Some other metals as well as some non-metallic surfaces served also as SERS surfaces, but the intensity of the signal was significantly lower than for silver. The SERS signal depends on the roughness of the substrates, the particle size of the metal clusters, but also on the excitation wavelength. Silver surfaces such as roughened electrodes, colloids, thin films, etc. are the most commonly used substrates in SERS studies[25-27]. The essential feature is that these silver surfaces are able to concentrate the electromagnetic field due to the incident light into the region of the surface. The electron gas composed of the conduction electrons of these essentially free-electron metals undergoes acoustic electron density oscillations (or *plasmons*) which, for the electrons of the bound particles or individual roughness features, may be resolved into localized normal modes of oscillation. In the case of nearly spherical particles, these oscillations have the form of spherical harmonics. The dipolar plasmons may be resonantly excited by the incident radiation resulting in an increase of the electromagnetic field in the vicinity of the surface. In the case of a spherical particle of

radius *a*, much smaller than the incident wavelength, the theoretical calculations are quite simple. The electromagnetic field inside the sphere is given by $3E_0/(e+2)$, where E_0 is the incident field and e is the complex dielectric constant of the material relative to the surrounding medium. In the vicinity of the sphere an additional electromagnetic field to E_0 is present, which is generated by a "hypothetical" induced dipole moment $a_S E_0$ at the centre of the sphere, with a_S, the polarizability of the sphere, given by

$$a_S = a^3 \frac{e-1}{e+2} \; . \tag{2.58}$$

The denominator in the above equation approaches zero if there is a wavelength for which the real part of the dielectric constant of the metal relative to the surrounding is approaching $Re(e) = -2$ and for which $Im(e)$ is small. This is the case for metals such as silver, gold, copper and alkali metals and therefore, these elements are utilized for SERS studies. Under this condition, the enhancement factor of the SERS signal can reach about 10^7. Moreover, the sphere is not only enhancing the incident light, but also the scattered radiation. Therefore, the theoretical calculations of the enhancement factors for small particles as a function of the excitation wavelength done by Kerker *et al.*[51] predicted a double maximum for the SERS signal. One maximum corresponds to the incident wavelength, where $Re(e) = -2$, and the other where the scattered radiation fulfills this condition. The enhancement factor of the SERS signal depends on the particle size and shape. In the case of spheroids, the maxima of the enhancement factors shift toward higher excitation wavelengths due to the shift of the longitudinal dipole resonance as the axial ratio is increased. Moreover, the shape of the metal surfaces is probably more complex, and for some particular surface shapes, such as in the vicinity of sharp points or edges or between near-contacting particles, in the so-called "hot spots" cluster structures, the local field nearby the surface is even more enhanced. Additionally, in such regions the electric field gradients are also significantly high and the contribution of the *quadrupole polarizability* to the induced dipole moment, according to the Eq. 2.57, may be significant. Hence, an electrochemical enhancement factor of up to 10^{10}-10^{11} has been reported.

The second model proposed to account for the enormous enhancement of the Raman signal of molecules adsorbed on metal surfaces is the *chemical (or adsorbate polarizability) enhancement* mechanism. At least two experimental observations showed that the electromagnetic field enhancement is not the only mechanism determining the

intensity of the SERS signal. One observation is that many molecules show no SERS activity even if they are undoubtedly adsorbed on proper metal substrates, and the second is that the SERS signal of molecules adsorbed on electrodes strongly depends on the potential of the electrodes in electrochemical experiments. Moreover, the potential where the SERS signal reaches a maximum also depends on the excitation wavelength, but the direction of the shift is determined by the molecular species. Furthermore, some substrates exhibit specific Raman enhancement for the first monolayer.

The above mentioned experimental observations can be explained by the fact that a resonance Raman process occurs when electrons from the HOMO of the molecule are excited into the Fermi level of the metal substrate or when free electrons of the metal are excited into the LUMO of the molecule. Therefore, the chemical enhancement is often referred to as the "*charge transfer*" enhancement, and called the surface enhanced resonance Raman scattering (SERRS) process. Moreover, the substrate particles lead to a quenching of the fluorescence signal which is of further benefit in the vibrational investigation of molecules.

Another aspect which must be taken into account is that a chemical bond between certain molecules and the metal particles may occur. Such a bond possibly modifies the polarizability tensor components of the molecule, its symmetry and other parameters similarly to bonding of ligands to metal atoms in metal complexes. The wavenumber shifts in the SERS spectra of adsorbed molecules with respect to the Raman spectra of the pure or solvated molecules may therefore be explained through the bonding of the molecule to the substrate and changes in the molecular identity of the adsorbate. Additionally, changes of the electron density in the molecule because of the molecular interaction with the substrate through the lone electron pairs or delocalized *p*-electrons lead also to significant band shifts. The lowering of the symmetry of the molecule upon adsorption on the metal substrate gives rise to the appearance of Raman-forbidden bands in the SERS spectra of highly symmetric molecules. However, the quadrupole polarizability mechanism may also be responsible for such an effect since the Raman-forbidden bands are quadrupole-allowed.

SERS Surface Selection Rules

As mentioned above, upon adsorption of the molecule onto the substrate, the vibrational modes of the molecule are usually shifted. Moreover, the relative intensities of the bands in the SERS spectra do not correspond to those in the normal Raman spectra[52-54].

Some vibrational modes are exceedingly enhanced while others do not appear in the SERS spectra. One of the goals of the SERS investigations is to determine the binding site and orientation of the molecule to the surface. The SERS "surface selection rules" were developed to extract this information from the spectral changes of molecules adsorbed on metal substrates. "Surface selection rules" were developed first for IR and electron energy loss (EELS) spectroscopy[26] to determine the orientation of molecules at metal surfaces. Metals have very high electrical conductivities for infrared excitation wavelengths, and as a consequence the parallel, but not the perpendicular electric field component of the radiation goes to zero at the surface. Therefore, only the vibrational modes modulating the component of the molecular dipole perpendicular to the surface (see Eq. 2.8) will be IR active for a molecule adsorbed on metal surfaces. Nevertheless, in the case of the SERS effect the "surface selection rules" are more complicated. The SERS intensities must be correlated with the respective enhancement mechanism, and in general many factors must be considered.

The chemical enhancement leads to frequency shifts of those modes involving atoms bonded to the surface. Moreover, it is expected that these modes are preferentially enhanced since the involved atoms are closest to the surface. In the case of the SERRS enhancement, the maximum of the SERS signal is expected at the resonance energy while in the case of dominant electromagnetic enhancement it is expected at the "plasmon resonance energy". The theoretical examination of the incident and scattered electromagnetic field components provides the rule explaining the selective SERS enhancement of the vibrational modes.

Creighton and co-workers[26] calculated the Raman intensity of a molecule in the vicinity of a sphere and generalized these results for aggregates, while Moskovits[52,53] and co-workers determined the Raman intensity for a molecule adsorbed on a flat metal surface. As shown in the previous section, the Raman intensity depends on the square of the polarizability tensor components. In the case of a spherical metal particle[26] the incident and scattered fields are enhanced and the *effective* polarizability tensor (a_{eff}) of the molecule adsorbed on the sphere can be written as

$$(a_{eff}) = \frac{9}{(e_i + 2)(e_s + 2)} \begin{pmatrix} a_{xx} & a_{xy} & e_s a_{xz} \\ a_{yx} & a_{yy} & e_s a_{yz} \\ e_i a_{zx} & e_i a_{zy} & e_i e_s a_{zz} \end{pmatrix} \tag{2.59}$$

with e_i and e_s being the complex dielectric constant of the metal relative to the surrounding at the incident and scattered wavelength, respectively. The presence of the prefactors for only some of the polarizability tensor components results in a differential enhancement effect, which favors Raman scattering by particular modes. Let us consider a molecule of high symmetry so that the off-diagonal elements of the polarizability tensor belong to different irreducible representations. The *z*-coordinate is along the surface normal. The non-totally symmetric modes of such a molecule which transform like a_{xz} or a_{yz} will be enhanced by a factor of $\approx e^2$ with respect to the modes which transform like a_{xy}. A totally symmetric mode for which a_{zz} is dominant, will exhibit an enhancement of about e^4. Nevertheless, totally symmetric modes usually contain all diagonal elements, but the two components whose subscripts define the plane in which the vibrational motion takes place are the largest. Hence, those A_1 vibrations whose motions are directed normal to the surface will be by far the most intense[53,54]. Therefore, the analysis of the relative intensity of the molecule's vibrational modes in the SERS spectra is useful to determine the orientation of the molecule on the metal surface. In the case of a molecule "standing up" on the metal surface stretching modes will be expected to have higher intensity, while for a molecule "lying down" on the metal surface the out-of-plane vibrations will be granted special enhancement compared with normal Raman spectra in solution or solid state.

2.2 Quantum Chemical Calculations

The ultimate goal of most quantum chemical approaches is the "approximate" solution of the Schrödinger equation[28]. Several methods have been developed and implemented in computational programs to solve the Schrödinger equation. Those methods which do not include empirical or semi-empirical parameters in their equations are called *ab-initio* methods. Some classes of *ab-initio* methods such as the Hartree-Fock, Møller-Plesset perturbation theory, configuration interaction, coupled cluster, reduced density matrices are widely applied in quantum chemistry. However, the application of density functional theory (DFT) calculations is gaining more and more interest. The basic principles applied in quantum chemistry will be presented in the following.

The Hartree-Fock approach

The time-independent Schrödinger equation[30] for a system containing *M* nuclei and *N* electrons is given by

$$\hat{H}Y_i\left(\vec{x}_1,\vec{x}_2,...,\vec{x}_N,\vec{R}_1,\vec{R}_2,...,\vec{R}_M\right)=E_iY_i\left(\vec{x}_1,\vec{x}_2,...,\vec{x}_N,\vec{R}_1,\vec{R}_2,...,\vec{R}_M\right), \qquad (2.60)$$

where $\hat{H}$ is the Hamilton operator in the absence of magnetic or electric fields and is representing the total energy, the wave function $Y_i\left(\vec{x}_1,\vec{x}_2,...,\vec{x}_N,\vec{R}_1,\vec{R}_2,...,\vec{R}_M\right)$ contains all information about the quantum system in the *i*th state depending on the vector coordinates of the electrons (3*N* spatial coordinates $\vec{r}_i$) and the N spin coordinates (s_i) of the electrons given by $\vec{x}_i$ and the 3*M* spatial coordinates of the nuclei, and E_i is the numerical value of the energy of the system.

The starting approximation applied in the calculation of the Schrödinger equation is the Born-Oppenheimer approximation (adiabatic approximation). Since the mass of nuclei is by far greater than the mass of electrons (for the H-atom by a factor of about 1800), the motion of electrons can be considered decoupled from the motion of nuclei. Moreover, the position of the nuclei may be considered fixed, and therefore their kinetic energy is zero and their potential energy constant. Hence, the electrons are moving in the field of fixed nuclei, and the complete Hamiltonian reduces to the electronic Hamiltonian given by the kinetic energy of the nuclei, the electron-nuclei and electron-electron potential interactions

$$\hat{H}_{elec} = -\frac{1}{2}\sum_{i=1}^{N}\nabla_i^2 - \sum_{i=1}^{N}\sum_{A=1}^{M}\frac{Z_A}{r_{iA}} + \sum_{i=1}^{N}\sum_{j>i}\frac{1}{r_{ij}} = \hat{T} + \hat{V}_{Ne} + \hat{V}_{ee} \quad . \tag{2.61}$$

The solution of the Schrödinger equation for the electronic Hamiltonian is the electronic wave function and the electronic energy. The electronic wave function must be *antisymmetric* with respect to interchange of the spatial and spin coordinates of any two electrons (Pauli's exclusion principle) and *normalized* (continuous everywhere and quadratic integrable). In order to solve the Schrödinger equation one has to set up the Hamilton operator for the system and than to find the eigenfunctions Y_i and the corresponding eigenvalues E_i. However, this cannot be accomplished exactly apart from a few simple cases. The *variational principle* states[28,30] that the expectation value of a Hamiltonian calculated from any guessed wave function, Y_{trial}, is never lower in value than the true ground state energy E_0 which is the expectation value of the Hamiltonian calculated using the true wave function

$$\left\langle Y_{trial} \middle| \hat{H} \middle| Y_{trial} \right\rangle = E_{trial} \geq E_0 = \left\langle Y_0 \middle| \hat{H} \middle| Y_0 \right\rangle \ , \tag{2.62}$$

where the equality holds if and only if Y_{trial} is identical to Y_0. Hence, the strategy of finding the ground state energy is to make a guess of a physically plausible trial wave function, which depends on several parameters. The parameters can be adjusted so that a minimal energy will be obtained leading to an accurate estimate of the ground state energy. In Eq. 2.62 the rule on the left hand side, which assigns a number (E_{trial}) to a function (Y_{trial}), is called a functional ($F(f) \rightarrow value$).

The Hartree-Fock approach is based on the approximation of the *N*-electron wave function by an antisymmetrized product of *N* one-electron wave functions given by the *Slater determinant* F_{SD}

$$Y_0 \approx F_{SD} = \frac{1}{\sqrt{N!}}\begin{vmatrix} c_1(\vec{x}_1) & c_2(\vec{x}_1) & \cdots & c_N(\vec{x}_1) \\ c_1(\vec{x}_2) & c_2(\vec{x}_2) & & c_N(\vec{x}_2) \\ \cdot & & & \cdot \\ \cdot & & & \cdot \\ c_1(\vec{x}_N) & c_2(\vec{x}_N) & & c_N(\vec{x}_N) \end{vmatrix} \ , \tag{2.63}$$

where the one electron wave functions $c_i(\vec{x}_i) = y_i(r_i)s(s)$ are called molecular *spin orbitals*, and are composed of a spatial orbital and a spin function. The spin functions are orthonormal and the spin orbitals themselves are usually chosen to be also orthonormal

$$\int c_j^*(\vec{x}) c_i(\vec{x}) d\vec{x} = \langle c_i \,|\, c_j \rangle = d_{ij} \ , \tag{2.64}$$

where d_{ij} is the Kronecker symbol equal 1 for $i = j$ and 0 for $i \neq j$. However, replacing the true *N*-electron wave function Y_{exact} by a single Slater determinant represents a fairly drastic approximation. Using the variational principle, the spin orbitals $\{c_i\}$ are varied to find the "best" Slater determinant for which the energy reaches a minimum under the given convergence criteria. The technique is the so-called *self-consistent field* (SCF) procedure which starts form a set of orbitals, with which the Hartree-Fock equations are solved. Iteratively, the resulting new set of orbitals is used in the next cycle until the input and output orbitals differ by less than a predetermined threshold.

The Hartree-Fock energy[28,30] is given by

$$E_{HF} = \langle F_{SD} | \hat{H} | F_{SD} \rangle = \sum_i^N \langle i | \hat{h} | i \rangle + \frac{1}{2} \sum_i^N \sum_j^N \langle ii \,|\, jj \rangle - \langle ij \,|\, ji \rangle \ , \tag{2.65}$$

where

$$\langle i | \hat{h} | i \rangle = \int c_i^*(\vec{x}_1) \left\{ -\frac{1}{2} \nabla^2 - \sum_A^M \frac{Z_A}{r_{1A}} \right\} c_i(\vec{x}_1) \ d\vec{x}_1 \tag{2.66}$$

corresponds to the kinetic energy of the electron with the spin orbital $\{c_i\}$ and the attraction between this electron and the nuclei.

$$\langle ii \,|\, jj \rangle = \iint |c_i(\vec{x}_1)|^2 \frac{1}{r_{12}} |c_j(\vec{x}_2)|^2 \, d\vec{x}_1 d\vec{x}_2 \tag{2.67}$$

$$\langle ij \,|\, ji \rangle = \iint c_i(\vec{x}_1) c_j^*(\vec{x}_1) \frac{1}{r_{12}} c_j(\vec{x}_2) c_i^*(\vec{x}_2) \ d\vec{x}_1 d\vec{x}_2 \tag{2.68}$$

are the *Coulomb* and *exchange* integrals, respectively. The summation of the *Coulomb* integrals in Eq. 2.65 describes the Coulomb interaction of an electron in spin orbital c_j with the average charge distribution of the other electrons. The *exchange* integral does not have a classical physical meaning and arises from the antisymmetry requirement of the wave function. If $\vec{x}_1 = \vec{x}_2$ the two integrals are equal, and thus, the interaction of an electron with itself is eliminated. The *Coulomb* and *exchange* operators ($\hat{J}_j$ and $\hat{K}_j$) are defined as

$$\hat{J}_j(\vec{x}_1) = \int |c_j(x_2)|^2 \frac{1}{r_{12}} d\vec{x}_2 \tag{2.69}$$

$$\hat{K}_j(\vec{x}_1)c_i(\vec{x}_1) = \int c_j^*(\vec{x}_2)\frac{1}{r_{12}}c_i(\vec{x}_2)d\vec{x}_2\, c_j(\vec{x}_1)\ , \tag{2.70}$$

where the *Coulomb* operator provides the average local potential at point x_1 due to the charge distribution from the electron in orbital c_j. The Fock operator can be written as

$$\hat{f}_i = \hat{h}(i) + \hat{V}_{HF}(i) = -\frac{1}{2}\nabla_i^2 - \sum_A^M \frac{Z_A}{r} + \sum_j^N \left(\hat{J}_j - \hat{K}_j\right), \tag{2.71}$$

where the Hartree-Fock potential represents the average repulsive potential experienced by the *i*th electron due to the remaining *N*-1 electrons. The Hartree-Fock energy is a functional of the spin orbitals, and because the spin orbitals has to be orthonormal one can derive the *Hartree-Fock equations*. Hence, a total of *N* equations (*Hartree-Fock equations*) given by

$$\hat{f}c_i = e_i c_i,\ i = 1, 2, \ldots, N \tag{2.72}$$

has to be solved to determine the *Lagrangian multipliers* e_i which are the eigenvalues of the Fock operator $\hat{f}$ and have the physical meaning of orbital energies. The *Koopmann*'s theorem states that the orbital energy e_i obtained from the Hartree-Fock theory is an approximation of minus the ionization energy associated with the removal of an electron from that particular orbital.

Basis sets

The molecular orbitals which arises in the Slater determinant are usually expanded in the form of a linear combination of a finite set *T* of one-electron functions known as basis functions j_m

$$y_i = \sum_{m=1}^{T} c_{m\,i} j_m\ , \tag{2.73}$$

where $c_{m\,i}$ are the molecular orbital expansion *coefficients*. Atomic orbitals of the constituent atoms are used as basis functions. Well known basis set types are the *Slater-type atomic orbitals* (STOs), which have an exponential radial part, and the *gaussian-type atomic functions* (GTOs), which are powers of *x*, *y*, *z* multiplied by $exp\left(-ar^2\right)$ with *a* determining the radial size of the function. The general form of the GTOs is

$$g_i(a, r) = N(a)\cdot x^l y^m z^n \cdot exp\left(-ar^2\right), \tag{2.74}$$

where the parameters depend on the nucleus. These functions, or combination of these functions, correspond to the angular symmetry of the *s*-, *p*-, *d*- and *f*-orbitals. Another possibility is the application of a combination of gaussian functions as basis set called *contracted gaussians*, while the individual terms are called *primitive gaussians*. The GTOs are computationally easier to handle than the STOs, and therefore they are widely applied. The *minimal basis set* contains that number of functions required to describe all of the electrons of the atom. Although it seems that only the occupied orbitals should be considered, practically also the energetically low lying unoccupied orbitals must be included.

The 6-31G and the 6-311G basis sets comprise inner-shell functions each written in terms of a linear combination of six gaussian functions and two or three valence shells corresponding to the numbering 31 and 311, respectively. The two valence shells are represented by a linear combination of three gaussians and one gaussian function for the 6-31 G basis set, while in the case of 6-311G the three valence shells are represented by a set composed of a linear combination of three gaussians, one gaussian and one gaussian function.

One property of the above functions is that they are constrained to be centered at the nuclear position, which is often not a realistic description of the molecular orbitals. In the case of highly polar systems, the charge is not uniformly distributed around the atomic nucleus. Therefore, *polarization basis sets* were developed which incorporate functions of higher angular quantum number than are needed by the atom in its ground electronic state. Polarization functions are depicted by d, p or f in the basis set, for example in the 6-31G(d) or 6-31G(d,p) (identical to 6-31G* and 6-311G**) notations. The polarization function d prescribes that a set of six second-order (*d*-type) gaussian primitives with different exponents will be included for each heavy atom (non-hydrogen atom) in the description of the *p*-type orbitals. The p symbol prescribes an additional set of *p*-type orbitals to each hydrogen atom.

Diffuse functions are normally *s*- and *p*-type gaussian functions and are usually denoted by + or ++, with the first + indicating a set of diffuse (larger) *s*- and *p*- functions on heavy atoms and the second + prescribes an additional diffuse *s*- type gaussian for the H-atoms. Diffuse functions are necessary when species with significant electron density far removed from the nuclear centers, such as in anionic compounds, are investigated.

Excited state calculations

Several methods have been implemented in quantum chemical programs to calculate the excitation energies, to determine the excited state molecular geometry and vibrational wavenumbers[28,30]. An excited state may be described in the orbital picture as a system where an electron from an occupied orbital has been moved to an unoccupied orbital. Therefore, the simplest method for calculating electronically excited states is the *configuration interaction singles* (CIS) which is limited to singly-excited states. Considering the solved Hartree-Fock problem, one has obtained the ground state single-determinant wave function written in the contracted form as

$$Y_0 = (N!)^{-1/2} \left| c_1 c_2 \cdots c_N \right| , \tag{2.75}$$

which is corresponding to Eq. 2.63. The next step is to excite one or more of these occupied spin orbitals by unoccupied or *virtual* orbitals. Hence, the wave function becomes

$$Y_{CIS} = a_0 Y_0 + \sum_i^{occ} \sum_a^{virt} a_i^a Y_i^a \ , \tag{2.76}$$

where the Y_i^a wave function contains occupied and virtual spin orbitals and the coefficients are determined by the linear variational method. Further improved methods allow double excitation like in the CID method or both single and double excitation like in the CISD method. However, the CI methods do not involve orbital optimizations and therefore the CI procedure is biased against the excited states.

The *Multi-configuration Self-consistent Field* (MCSCF) method can be considered as a CI method where not only the coefficients in front of the determinants are optimized by the variational principle, but also the *molecular orbitals* (MOs) used for constructing the determinants are made optimum (Jensen). Convergence of MCSCF wave functions is hard to reach and often converge to solutions which are no minima. This is usually checked by calculating the matrix of second derivatives of the energy with respect to the MO coefficients, and diagonalization gives the eigenvalues, which should be all positive.

The *Complete active space self-consistent field* (CASSCF) method is a type of MCSCF calculations in which the configurations are chosen to be all those obtainable using a specified number of electrons and a specified set of orbitals. The set of orbitals is called the "active space," and the specified electrons are called "active." Hence, one has to decide which molecular orbitals are involved in the electronic transition by analyzing the

molecular system and taking into consideration the computational effort needed to perform the calculation.

The choice of the active space is not always easy. In general, for each occupied orbital there will be a virtual orbital. The orbital energies and most important their shapes can be useful in deciding which MOs should be included in the active space. Hence, CASSCF calculations are not a “black box” method like for example HF calculations, and they require some experimentation and insight.

Density functional theory calculations

Until now the central quantity in the quantum chemical calculations was the wave function Y_0 which depends on the 3*N* spatial coordinates of the electrons and their spin functions. Hence, the wave function is a very complicated quantity and if the number of atoms and especially the number of the electrons is very large, the computational effort is tremendous and cannot be performed. The Hamiltonian operates simultaneously only on one or two particles at a time, and thus the complicated form of the wave function is not absolutely necessary. Moreover, if the wave function has a very complicated form, a descriptive understanding of it is difficult.[29]

The wave function itself is not an observable, but the square of the wave function

$$\left|Y\left(\vec{x}_1,\vec{x}_2,...,\vec{x}_N\right)\right|^2 d\vec{x}_1 d\vec{x}_2 ... d\vec{x}_N \tag{2.77}$$

represents the probability of simultaneously finding the N electrons in the volume elements $d\vec{x}_1 d\vec{x}_2 ... d\vec{x}_N$. The electron density is defined as the multiple integral over the spin coordinates of all electrons and over all with the exception of one spatial variables

$$r\left(\vec{r}\right) = N\int\cdots\int\left|Y\left(\vec{x}_1,\vec{x}_2,...,\vec{x}_N\right)\right|^2 ds_1 d\vec{x}_2 ... d\vec{x}_N \ , \tag{2.78}$$

where $d\vec{x}_i$ is containing the spin and spatial variables. The electron density represents the probability of finding any of the *N* electrons within the volume element $d\vec{r}_1$ but with arbitrary spin, while the other *N*-1 electrons have arbitrary positions and spins in the state represented by Y. The multiple integral represents the probability of finding one particular electron in this volume element, and since the electrons are indistinguishable the probability of finding any of the *N* electrons is obtained by multiplying Eq. 2.78 with *N*. The *Fermi* or *exchange correlation* corresponds to the fact that $r_2\left(\vec{x}_1,\vec{x}_1\right) = 0$, which means that the probability of finding two electrons with the same spin at the same point in

space is exactly zero. The *Coulomb correlation* corresponds to the electrostatic repulsion between electrons. The *conditional probability* given by

$$W(\vec{x}_2;\vec{x}_1)=\frac{r(\vec{x}_1,\vec{x}_2)}{r(\vec{x}_1)} \tag{2.79}$$

represents the probability of finding any electron at position 2 in the coordinate-spin space if there is one electron at position 1. The *exchange-correlation hole* defined as the difference between $W(\vec{x}_2;\vec{x}_1)$ and the uncorrelated probability of finding an electron at $d\vec{x}_2$

$$h_{XC}(\vec{x}_1;\vec{x}_2)=\frac{r(\vec{x}_1,\vec{x}_2)}{r(\vec{x}_1)}-r(\vec{x}_2) \tag{2.80}$$

describes the change in conditional probability caused by the correction for self-interaction, exchange and Coulomb correlation and can be split into the *Fermi hole* and the *Coulomb hole.* In the Hartree Fock approach, the Fermi hole is accounted for by the choice of the Slater determinant (due to the antisymmetry of the wave function), whereas the Coulomb hole is neglected.

The Schrödinger equation may be rewritten in terms of reduced one- or two-particle density matrices. The *Hohenberg-Kohn theorem* shows that the *ground state* electronic energy is determined completely by the electron density, and therefore it is "only" necessary to determine the functionals, which when applied on the density function, will give the energy. Nevertheless, it should be mentioned that Thomas and Fermi in 1927 and later Slater in 1951 were already concerned with the possibility of replacing the complicated wave function by the electron density. Similarly to the Hartree-Fock approach, the second *Hohenberg-Kohn theorem* states that the real ground state energy is obtained if and only if the real electron density is applied[29]

$$E_0 = E_{DFT}[r_0] \le E_{DFT}[r] \tag{2.81}$$

which is the basis for the application of the variational principle. Here $E_{DFT}[r]$ is the general DFT energy functional which can be partitioned similarly to the wave mechanics methods into

$$E_{DFT} = T[r]+E_{Ne}[r]+E_{ee}[r]\,, \tag{2.82}$$

where $T[r]$ corresponds to the kinetic energy of the electrons, $E_{Ne}[r]$ describes the Coulomb attraction between the nuclei and the electrons, while the electron-electron interaction is given by the final term which can be divided into a *Coulomb,* $J[r]$, and an *Exchange,* $K[r]$, part.

The electron density was first described as a non-interacting uniform electron gas, but this approach led to erroneous energies, and no bonding was predicted. The introduction of electron density gradients improved the results, but such methods were not viable. Not until the use of molecular orbitals by Kohn und Sham, DFT calculations started to obtain acceptance and become important, reliable and established methods. Moreover, the Kohn Sham formalism splits the kinetic energy into two parts, one of which can be calculated exactly, $T_S[r]$, and the second is a small correction term. Hence, the DFT energy functional becomes

$$E_{DFT} = T_S[r] + E_{Ne}[r] + J[r] + E_{XC}[r] , \tag{2.83}$$

where $E_{XC}[r]$ corresponds to

$$E_{XC} = (T[r] - T_S[r]) + (E_{ee}[r] - J[r]) \tag{2.84}$$

with the final parenthesis corresponding to both exchange and correlation energies. The exchange energy is dominating with respect to the correlation part. One aim of the density functional theory is to find proper functionals for the exchange and correlation energy. If the exact $E_{XC}[r]$ was known, DFT methods would provide the exact total energy including electron correlation, which was omitted in the uncorrelated HF method. Nevertheless, the computational effort for the DFT calculations is similar to that for the HF method only if some approximations of the $E_{XC}[r]$ are applied. The main difference between DFT methods is the appropriate choice of the functional form of the exchange-correlation energy.

The first DFT methods were the local density methods[29] (*local density approximation* and *local spin density approximation*, LDA and LSDA, respectively) considering the electron density as a slowly varying function, and thus treating it as a uniform electron gas. The *gradient corrected* or *generalized gradient approximation* (GGA) methods are an improvement over the LSDA methods since they take into consideration that the exchange and correlation energies depend not only on the electron density, but also on derivatives of the density. The exchange and correlation functionals are usually treated separately. There are several GGA functionals implemented in commercial quantum chemical programs. Some of the GGA functionals are corrections to the LDA methods while others have independent forms. The formula of the energy functionals was summarized by Jensen[29] and will not be given here. The gradient corrected correlation functional due to Lee, Yang and Parr (LYP) became very popular. Other

correlation functionals (corrections to the LSDA energy) are the P86 (proposed by Perdew in 1986) or the modification of this in 1991, the PW91 (Perdew and Wang) functional. A more recent correlation functional is due to Becke (B95) which has the advantage that it does not predict correlation energies for one-electron systems and the exchange energy cancels the Coulomb self-repulsion. Widely used exchange functionals are the Becke 88 (B88 or simply B) functional and the Becke 3 parameter hybrid functional (B3). The combination of the exchange and correlation functionals yields DFT methods associated with the acronyms BLYP, B3LYP, B3P86, BPW91 and B3PW91. These methods generally provide accurate geometries and vibrational frequencies as well as proton affinities and other energies. Another advantage of DFT methods based on unrestricted determinants for open-shell systems is that they are free of spin contamination.

Chapter 3

Experimental Details

This chapter shortly presents the various experimental setups for the absorption, Raman, RR and SERS measurements and provides an overview about the computational strategies of the quantum chemical and PED calculations. Finally, the handling of the experimental and theoretical data to determine the displacement parameters and the geometry of the resonantly excited state is presented.

3.1 Spectroscopical Methods

Materials and UV-VIS-NIR absorption measurements

1-Hydroxy-2-acetonaphthone, 6-Mercaptopurine and 6-Mercaptopurine-ribose were purchased from Sigma Aldrich Chemical Company and used without further purification. N,N,N',N'-tetraphenylphenylenediamine radical cation and the corresponding neutral species was synthesized in the group of Prof. C. Lambert. 2-(diethylamino)-5-(2',2'-dicyanovinyl)-thiophene was synthesized in the group of Prof. Würthner. The aziridinyl peptide EtO-Azi-Gly-Gly-OBn, the electrophilic building block EtO-Azi-OEt and the epoxide analogon BnO-Gly-Gly-Epo-Gly-Gly-OBn as well as the deuterated species were synthesized in the group of Prof. Schirmeister.

The electronic absorption spectra were recorded with an UV-VIS-NIR Perkin-Elmer Lambda 19 spectrometer with a scan speed of 240 nm/min.

Fourier-Transform-Raman measurements

The FT-Raman spectra were measured with a Brucker IFS 120-HR spectrometer equipped with an integrated Model 106 Raman module. The 1064 nm output from a Nd:YAG laser was used as excitation line and the scattered light was detected with a nitrogen cooled Ge detector.

Resonance Raman measurements

For the resonance Raman experiments, the samples were dissolved in solvents of analytical purity. The concentration of the solutions was optimized to obtain a maximum signal-to-noise ratio and was in the millimolar range.

For the resonance Raman experiments in the UV, the output of a Spectra Physics cw argon and krypton ion laser served for resonant excitation in the range of the S_0-S_1 absorption band at 363.8, 351.1, 334.5 and 356.5 nm, respectively. The output power was between 0.7 and 0.15 W for the different lines. For the resonance Raman spectra recorded in the visible, the 514.5, 501.7, 496, 488, 476.5, 472.7, 465.8 and 458.5 nm excitation lines of a cw argon ion laser were used. Measurements with excitation lines of a tunable dye laser were also carried out. Stilbene 3 pumped with the UV multiline output of the argon ion laser (ca. 3.8 W) yielded excitation lines in the 420-460 nm range.

The spectra were recorded in a 90° scattering arrangement. To avoid the heating of the sample a rotating cell was utilized, where possible. The scattered light was focused onto a Spex Model 1404 Double Monochromator equipped with 2400 grooves/mm gratings and detected with a CCD camera (Photometrics Model 9000).

The resonance Raman spectra excited at 830 and 785 nm were taken with a micro Raman setup (LabRam, Jobin-Yvon-Horiba). The spectrometer has a focal length of 300 mm and is equipped with 950 lines/mm grating. The applied laser power was about 1 mW for both wavelengths. The scattered light was detected by a CCD camera operating at 220 K. An Olympus MLPlanFL 50 objective focused the laser light on the sample solutions. For the measurements with 830 and 785 nm excitation a backscattering geometry was applied.

SERS measurements

The sodium-citrate reduced Ag colloid used in the SERS measurements was prepared as described in the literature[55]. All solutions were prepared with distilled and deionized water. NaCl solution (10^{-2} M) was added prior to the 6MP and 6MPR solutions to activate the colloid. HCl and NaOH solutions were used to adjust the pH value of the mixture which was measured with pH paper.

Micro-Raman spectra of ca. 10^{-1} M solutions of 6MP and 6MPR at pH = 13 and saturated solutions at pH = 1 were recorded using a LabRam (Jobin-Yvon-Horiba) system equipped with a Peltier cooled CCD camera. The spectrometer has a focal length of 300 mm and is equipped with a 1800 grooves·mm^{-1} grating and an Olympus BX40 optical microscope with a MLPlanFL X 100 objective. The SERS spectra were measured using a micro-Raman setup with an Olympus U-CMAD-2 optical microscope with two objectives: DPLAN 20 160/ 0.17 and ULWD MS-PLAN 80/ 0.75. The SERS spectra were recorded with a Spex Model 1404 Double Monochromator equipped with 2400 grooves·mm^{-1} grating and a liquid nitrogen cooled CCD camera. The 514.5 nm excitation line of a Spectra Physics Ar^+ laser with an output of 200 mW to 1 W was employed for the SERS measurements. The spectra were measured in back-scattering geometry.

3.2 Quantum Chemical Methods

Geometry optimization and vibrational analysis

The quantum chemical calculations were performed with the Gaussian 98[56] program package. The starting molecular description for the geometry optimization was generally carried out with the Molden program package or taken from the known crystal structure analysis. The ground state geometry optimizations correspond to an energy minimization according to the variational principle described in the previous section.

The vibrational wavenumber calculations were done analytically for the optimized molecular structures using the same functional and basis set as for the optimization calculation. These calculations deliver both the normal mode coordinates, the force constants and the vibrational wavenumbers, and are additionally a test if the predicted geometry corresponds to the minimum of the potential surface. If this is not the case, the wavenumber calculation ends with imaginary values, which are denoted by the minus sign, and the geometry corresponds to a transition state or a second minimum of higher energy.

IR intensity and Raman scattering activity

As mentioned in section 2.1, in order to obtain the Raman intensities one has to calculate the polarizability derivatives along the normal mode coordinate q_k, while for the IR intensities only the dipole moment derivatives are needed. Generally, the infrared intensity of the *k*th mode is proportional to the squared derivative of the dipole moment with respect to the normal mode coordinate q_k.

For a given geometry[57] the total energy of a molecule in a homogeneous electric field can be expanded in a power series:

$$E(F) = E^0 - \sum_i \mu_i F_i - \frac{1}{2}\sum_{jk} \alpha_{jk} F_j F_k - \dots , \tag{3.1}$$

where μ_i are the components of the permanent dipole moment vector, E^0 is the energy of the molecule in the absence of the electric field, and F_i, F_j and F_k represent the components of the applied external field. The dipole moment can be obtained as the first derivative of the energy

$$\mu_i = \frac{\partial E}{\partial F_i} . \tag{3.2}$$

The polarizability tensor has a more complicated form because it is given by the second derivative of the energy

$$a_{jk} = \left(\frac{\partial^2 E}{\partial F_j \partial F_k} \right). \tag{3.3}$$

Nonetheless, the polarizability and dipole moment derivatives can be evaluated first in the Cartesian coordinates instead of normal mode coordinates

$$\frac{\partial a_{ij}}{\partial R_k} = \frac{\partial^3 E}{\partial F_i \partial F_j \partial R_k} \tag{3.4}$$

and

$$\frac{\partial m_{ik}}{\partial R_k} = -\frac{\partial^2 E}{\partial F_i \partial R_k} \ , \tag{3.5}$$

where R_k is a component of the R vector which includes the Cartesian coordinates of all atoms of the molecule.

Usually, in order to obtain the normal coordinates, the force constant matrix is first constructed through the calculation of the Hessian (a 3Nx3N matrix, where N is the number of atoms) of the total energy

$$H_{ij} = \frac{\partial^2 E}{\partial R_i \partial R_j}. \tag{3.6}$$

After this, a transformation of the Hessian to atomic mass-weighted Cartesian coordinates is necessary. (The vibrational wavenumber calculations are performed by this procedure. It should be noted, that this transformation is only valid for a stationary point. Hence, it is meaningless to compute wavenumbers at any geometry other than a stationary point for the method used for the wavenumber determination).

$$H'_{ij} = \frac{H_{ij}}{\sqrt{m_i}\sqrt{m_j}} \ , \tag{3.7}$$

where $m_{i,j}$ are the atomic masses associated with the Cartesian coordinates. The polarizability derivative matrix must be transformed also to atomic mass-weighted Cartesian coordinates. The next step is to diagonalize H' to obtain the normal mode coordinates as the eigenvectors (q_k) while the eigenvalues correspond to the vibrational wavenumbers. In order to obtain the corresponding derivative matrices of the polarizability tensor components in terms of normal coordinates., one has to transform the mass-

weighted polarizability derivative matrix with the *Q* matrix. The *Q* matrix consists of the eigenvectors (q_k).

The derivatives in Eq. 3.4 and 3.5 can be evaluated analytically or by numerical differentiation. Analytical techniques are generally superior to numerical ones both in computational efficiency and in accuracy. However, their main disadvantage is the complex programming needed to implement these techniques, particularly if derivatives higher order are demanded. Thus, generally the vibrational wavenumbers and IR intensities are computed analytically, while the Raman intensities are obtained by numerical differentiation.

The computed intensities are very sensitive to the level of theory and implicitly depend on the chosen basis set. Inclusion of polarization functions allows the electronic wave function to respond to the presence of an electric field and will result in more accurate Raman intensities[58].

Potential energy distribution

The DFT calculations with the Gaussian[56] program delivers the set of vibrational modes in terms of the atomic displacement matrix in Cartesian coordinates for each mode (*file*.log). These vibrations can be visualized by variuos programs such as Molden, gOpenmol[59], HyperChem. However, an exact vibrational assignment is difficult. In order to obtain a detailed and exact vibrational assignment, *potential energy distribution* (PED)[60,61] calculations were performed. The potential energy calculations were conducted with the GAR2PED[62] freeware program, which is based on the Wilson GF matrixes[1] method.

The PED describes the molecular vibrations in terms of internal coordinates, this means as stretching modes, in-plane and out-of plane deformation and torsional modes localized on groups of the molecule[31]. A nonlinear molecule with *N* atoms has 3*N*-6 vibrational modes, and for such molecules 3*N*-6 internal coordinates are required. The difficulty consists in the fact that the internal coordinates must be defined manually. It should be mentioned that the number of internal coordinates, which may be defined, is larger than the number of degrees of freedom of the molecule. Nevertheless, there is a correlation between these internal coordinates given by the so called redundant relations between the internal coordinates. The problem is therefore, to define the non-redundant

internal coordinates. The most important characteristics of the PED analysis with the GAR2PED program will be shortly discussed in the following.

First of all, the atom numbering of the molecule in the Gaussian output had to be determined. The next step was to choose the internal coordinates. Some characteristic internal coordinates will be presented in the following.

1) The number of stretching modes is equal to the number of bonds in the molecule. 2) The in-plane and out-of-plane deformation modes are defined, for example, in the case of the XYC=O unit as the displacement of the O atom in the plane and out of the plane given by the XYC atoms, respectively. However, several deformation modes can be defined as a combination of modes localized on specific groups. 3) The methyl group presents beside the stretching modes, one symmetrical, two antisymmetrical and two rocking vibrations. Furthermore, an additional torsion mode between X-CH_3 must be defined. 4) The methylene moiety (X-CH_2-Y) shows also five deformation modes: the CH_2 scissoring, CXY scissoring, CH_2 rocking, wagging and twisting. In some cases, it proved better to define individual coordinates rather than combinations for the CH_2 group, and describe this group as two times an in-plane and an out-of-plane deformations of the XYC-H units (resulting four modes, which can be assigned to the CH_2 scissoring, rocking, wagging and twisting), and an in-plane and an out-of-plane deformation on the XCY atoms. 5) For the C-OH group there are the in-plane and out-of-plane deformation modes. 6) In the case of an *n*-membered ring, there are 3*n*-6 internal coordinates for the skeleton. The number of bond stretchings is *n*. Hence, for example for a five-membered ring, there are totally nine internal coordinates, five bond stretching and four deformation modes. Two of them are in-plane and two out-of-plane deformation vibrations. 7) In the case of a system containing many rings, as naphthalene, the butterfly vibration can be defined as a torsion around the bond connecting the rings.

Another possibility to obtain the non-redundant internal coordinates is to perform an analysis with the TurboMol program. This program can deliver automatically an output with the transformation of the Cartesian coordinates into internal coordinates, but it is quite tedious to apply this output to the PED analysis.

3.3 Data Analysis

Absorption cross section

The quantitative analysis of the absorption spectra requires the measurement of the molar extinction coefficient, $e(w)$ in L mol^{-1} cm^{-1}. This value was determined for the intervalence charge transfer radical cation presented in Chapter 5 by the group of Prof. C. Lambert through titration measurements. The extinction coefficients for the other solutions were determined from the absorption spectra according to the *Lambert-Beer*'s law by dilution of stock solutions. The absorption cross section (Å^2 molecule^{-1}) is related to the molar extinction coefficient through the relation

$$s_A(w) = 1000 \ln 10 e(w) / N_A \cdot 10^{16} , \tag{3.8}$$

where N_A is Avogadro's number. In general, the absorbance is recorded as function of the excitation wavelength (nm) and a transformation into units of wavenumbers (cm^{-1}) of the excitation energy is necessary for further calculations.

Moreover, the transition length (R) can also be evaluated from the molar extinction coefficient. R^2 determines the oscillator strength which is a measure of the intensity of a spectral band (giving the effective number of electrons taking part in a certain transition). R is proportional to the square root of the area of the absorption band. After evaluation of the constants, R is given by

$$R = 0.01998 \sqrt{\frac{\int e(w) dw}{w_{max}}} \tag{3.9}$$

with R in Å and w_{max} is the wavenumber of the maximum of the electronic transition. The square root of the refractive index of the solution is considered approximately 1.

Absolute differential Raman cross section

Absolute Raman cross section measurements are quite difficult, because of the experimental complexity. Nevertheless, the cross sections of the resonant enhanced modes can be easily determined relative to a standard band of known absolute differential cross section using the relation

$$\left(\frac{\partial s_R}{\partial W}\right)_k = \frac{I_k}{I_{standard}} \frac{[standard]}{[solute]} \left(\frac{\partial s_R}{\partial W}\right)_{standard} , \tag{3.10}$$

where I_k and $I_{standard}$ are the integrated band areas of the *k*th mode of the probe and of the standard's mode (usually the solvent line), respectively. The molar concentrations of the probe and of the standard are taken into consideration.

Trulson and Mathies[63] determined the absolute cross sections in the visible and ultraviolet for several standards (benzene, cyclohexane, cacodylate) using an integrating cavity according to the relation

$$s_R = \frac{8p}{3}\left(\frac{1+2r}{1+r}\right)\left(\frac{\partial s_R}{\partial W}\right), \tag{3.11}$$

where r denotes the depolarization ratio of the mode. They measured the cross sections for different excitation wavelengths and the following extrapolation function can be used assuming a single Albrecht's *A*-term active preresonant electronic state $|e\rangle$ of the standard

$$\left(\frac{\partial s_R}{\partial W}\right)_k = K w_L (w_L - w_k)^3 \left[\left(w_e^2 + w_L^2\right)/\left(w_e^2 - w_L^2\right)^2\right]^2 , \tag{3.12}$$

where w_L is the laser excitation wavenumber, w_k is the wavenumber of the vibration, w_e (in cm^{-1}) is the wavenumber of the resonant state, and K (in $Å^2/ sr^{-1}$) is a prefactor that scales the overall cross section. Trulson and Mathies[63] determined the w_e and K parameters through a fitting of the measured cross section according to this function. Moran and Myers[48] determined these parameters for other solvent bands such as methanol, acetonitrile, dichloromethane, dioxane, etc. relative to the experimentally determined parameters of cyclohexane. Additional measurements were performed in this study to determine the cross section of DMSO relative to dioxane, because of the good solubility of these two solvents and of no overlapping bands.

An important issue for a quantitative resonance Raman analysis is the intensity correction because of a wavelength dependent spectrometer sensitivity and self-absorption of the solution of probes under resonant conditions. This was in general accomplished by determining the relative intensities of the solvent bands (802 cm^{-1} and 1426 cm^{-1} for example in the case of cyclohexane) or the known response of the spectrometer as function of wavelength. The correction was very important for the measurements with 830 nm excitation line, because the spectrometer sensitivity of the CCD camera drops drastically in this spectral region. In the case of the other excitation wavelengths the correction led to about 5-15% deviation from the measured intensities.

In the back-scattering geometry the correction for self-absorption can be performed via the equation

$$I^k = \frac{I_0^{\,k}}{\frac{e^L + e^{Standard}}{e^L + e^k}}\ , \qquad (3.13)$$

where I^k is the corrected intensity, while $I_0^{\,k}$ is experimentally obtained intensity, e^L is the extinction coefficient of the investigated compound at the pump wavelength, $e^{Standard}$ at the wavenumber of the standard's mode, and e^k is the extinction coefficient at the wavenumber of the *k*th mode.

Displacement parameters

The one dimensional simulation of the absorption and Raman overlaps and the corresponding spectra in the wavenumber domain (see Fig. 2.4) were calculated with the Mathematica program. Nevertheless, the exact calculation of the integrals took about 1 minute.

The absorption and Raman excitation profiles for multimode systems were modeled using a FORTRAN code[64] kindly supplied by Professor Anne Myers Kelley and Dr. Andy Moran. A time cutoff was applied, where the convergence was accomplished, and hence, the calculations took only about 5 seconds (significant advantage of the Fortran code). The fitting procedure was described extensively by Professor Myers[37]. The fitting parameters are the displacement parameters D_k, the inhomogeneous broadening d, the time scale of the solvent modulation k, the solvent homogeneous broadening G_0, the lifetime decay of the excited state G for some compounds, the zero-zero energy E_{00}, the transition moment length R. In special cases, different wavenumbers for the excited state potential surface than the ground state wavenumbers were taken into consideration for a few vibrational modes.

The vibrational wavenumbers were obtained from the Raman spectra. A first estimate of the displacement parameters was accomplished using Savin's formula, where the preresonant to resonant Raman intensities are proportional to the square of the vibrational wavenumber and displacement parameters. The transition moment length and the zero-zero energy were estimated from the absorption spectrum.

The absolute scaling of the displacements was chosen to give the correct overall width of the absorption envelope, and the homogeneous linewidth G_0 was adjusted to yield

the correct absolute Raman cross sections, with the electronic transition length scaled to match the integrated absorption intensity. Finally, the inhomogeneous standard deviation was increased to reproduce the observed diffuseness of the absorption band, and all parameters were refined several times to obtain the best reproduction of the absorption cross sections and the resonance Raman excitation profiles[45].

Conversion from dimensionless normal to internal coordinates and vice-versa

The geometry bond length and angle changes of the excited state structure with respect to the ground state can be determined by conversion of the dimensionless displacement parameters to Cartesian coordinates. This can be accomplished if a normal mode analysis was performed. The formula to convert the dimensionless displacement parameters D_k into Å is[16]

$$\ell_i = 5.8065 \sum_{k=1} A_{k,i} \left(w_k m_k\right)^{-1/2} D_k \quad , \tag{3.14}$$

where the prefactor corresponds to

$$\sqrt{\frac{6.023 \cdot 10^{23} \hbar}{2pc}} \times 10^8 \tag{3.15}$$

with $\hbar = h / 2p$, h the Planck's constant in g cm^2 s^{-1}, c is the speed of light in cm s^{-1}, w_k is the vibrational wavenumber of the kth mode in cm^{-1}, m_k is the mass involved in the vibration in units of gram atomic weight as given by Gaussian, $A_{k,i}$ is the matrix of $k$the vibrational mode in Cartesian coordinates as written in the Gaussian output. The changes in bond lengths and angles between the ground and excited states are given by the ℓ_i matrix. Nevertheless, since the Raman intensities depend on the square of the displacement parameters, their sign cannot be determined through the resonance Raman intensity analysis. Therefore, the calculation of the bond length changes upon optical excitation according to the above equation is not straightforward. There are 2^k possible combinations of the signs of the displacement parameters where k is the number of enhanced modes in the resonance Raman spectra. After a careful consideration of the chemical process and/ or an analysis of the molecular valence orbitals, which can also be determined through HF calculations, one can conclude the probable signs of the displacement parameters, i.e. if the optical excitation will lead to the lengthening or the shortening of representative bonds, thus reducing the number of possible combinations.

The calculations were performed with the Mathematica program package. The molecular changes were evaluated with the Molden program. Therefore, the matrix ℓ_i and the matrix of the Cartesian coordinates of the ground state geometry were summed up and thus the molecular parameters of the excited state could be determined.

On the other side, the Franck Condon parameters can also be determined theoretically. This procedure involves the calculation of the excited and ground state molecular structures and the use of the vibrational analysis of the ground state vibrations. The displacement parameters are given by[65]

$$D_k = 0.1722(w_k m_k)^{1/2}\left[A_k{}^T \bullet F(X,G)\right], \qquad (3.16)$$

where F(X,G) is the column vector (Gaussian output is in the form of a 3xN matrix) containing the differences of the nuclear position vectors in the excited state X and the ground state G equilibrium geometries, which can be written in the form of a 3xN matrix of Cartesian coordinates. $A_k{}^T$ is the transposed matrix of the mass weighted Cartesian nuclear displacements in the *k*th mode (a Nx3 matrix). The trace of the dot product of the matrices multiplied with the square root of the vibrational wavenumber and reduced mass of the vibrational mode and a prefactor (0.1722 = 1/5.8065) gives the displacement parameter along this normal coordinate. These calculations were also carried out with the Mathematica program package.

Chapter 4

Excited State Intramolecular Proton Transfer in 1-Hydroxy-2-Acetonaphthone

Excited state inter- and intramolecular proton transfer (ESIPT) processes are fundamental chemical and biological reactions. In order to investigate the initial structural changes of ESIPT systems, it is of interest to select well defined model systems. 1-Hydroxy-2-acetonaphthone (HAN), an intramolecular proton transfer system, was investigated in the present study by means of quantum chemical calculations and resonance Raman spectroscopy. The DFT calculated vibrational wavenumbers and the Raman intensities for the enol tautomer are in excellent agreement with the experimental FT-Raman spectrum and constituted the basis for the vibrational analysis. To determine the Franck-Condon parameters a time-dependent approach for the analysis of the resonance Raman spectra was applied. About eighteen vibrational modes were found to be involved in the initial dynamics of HAN upon photo excitation. Moreover, the excited state geometry was optimized at the CASSCF level of theory and the displacement parameters were determined. A very good agreement between the theoretical and experimental parameters was obtained. The vibrations with the highest displacements correspond to stretching and in-plane deformation modes of the naphthalene ring and the conjugated carbonyl group, while the OH stretching mode exhibits no observable enhancement. Hence, a general molecular rearrangement takes place upon photo excitation, where the intramolecular oxygen-oxygen distance reduces corresponding to a redistribution of the electron density.

Motivation

Since the seminal work of Weller[66], the photo induced excited-state intramolecular proton or hydrogen transfer ESIPT reactions have been highly investigated[67-76]. ESIPT reactions are denoted by a highly-Stokes-shifted fluorescence (6000-10000 cm^{-1}) of the product tautomer[68,74]. The characterization of this process is of great importance not only from the point of view of spectroscopy, but also from the point of view of the reaction dynamics and relaxation pathway of the tautomer[68]. In most of the studied cases there is a reverse isomerization on the ground-state potential energy surface after the excited-state decays, so that the entire process is cyclic[74]. The intramolecular redistribution of electronic charge due to photon absorption induces an elementary and fast reorganization of the molecular structure[68].

Resonance Raman (RR) spectroscopy provides specific information on the molecular degrees of freedom involved in the initial structural changes of photochemically active systems. Moreover, it is a reliable tool for investigating the symmetry, equilibrium geometry and dynamics of the resonant excited electronic state[13,18,77]. RR studies for several intramolecular proton transfer systems can be found in the literature[46,78-82]. The RR spectrum of 2-hydroxyacetophenone[46] is dominated by a vibrational mode described as a combined symmetric expansion of the benzene ring and a shortening of the C-O bond. Thus, it has been concluded that a skeletal rearrangement occurs following optical excitation prior to proton transfer in this system[46]. The combined RR band assignment and transform analysis of four hydroxyantraquinones (HAQ's) and their deuterated derivatives showed that the proton transfer involves the hydrogen bonded cycle. High values of the displacement parameters for vibrations of the chelate pseudo-aromatic ring were found for all HAQ's, while for HAQ's undergoing ESIPT the displacement parameters of the OH stretching mode were also quite large[78]. Resonance Raman studies of heterocyclic aromatic compounds[79-82] which undergo intramolecular proton transfer reaction revealed 15 modes in the wavenumber range between 120 and 1600 cm^{-1} strongly coupled to the electronic transition. Moreover, combination modes of the strongest band below 500 cm^{-1} and the vibrations at higher wavenumbers could be also observed in two of the considered systems[80].

1-Hydroxy-2-acetonaphthone (HAN) is an extremely photostable intramolecular hydrogen bonded system used in polymer protection[83]. Several spectroscopic studies have

been reported in order to discern the photophysics of HAN[67,84-90]. Based on early fluorescence measurements of different HAN solutions and of the solid and gas phase forms, Catalan and del Valle[84] assumed that in this system the keto tautomer does not occur. Fluorescence excitation and dispersed emission spectra of HAN have been investigated in a free jet expansion[67]. The results were interpreted in terms of ESIPT from the initial enol form to the keto conformer through a small energy barrier between two closely lying local potential minima.

The goal of this study is to obtain a reliable picture of the initial structural changes induced by the electron density redistribution upon photoexcitation in this derivative. Therefore, a detailed resonance Raman study of HAN has been carried out. The RR spectra of HAN were recorded in cyclohexane solution and about fifteen vibrational modes were found to be resonantly enhanced. Density functional theory (DFT) calculations[56] of the vibrational wavenumbers, Raman scattering activities, and potential energy distribution (PED)[62] calculations were performed in order to get insight into the microscopic elongations of the molecule. Furthermore, CASSCF[91-93] optimizations for the first excited-state were carried out, indicating major changes of the geometry parameters of the naphthalene ring, the C-O and C=O bonds with respect to the ground-state molecular structure. The Franck Condon parameters were derived both from the experimental results through the time-dependent resonance Raman intensity analysis and from quantum chemical calculations. A very good agreement between the experimental and theoretical displacements was obtained, with the largest displacements corresponding to the vibrations of the naphthalene and chelate ring stretching and deformation modes.

Theoretical calculations of the ground and excited state molecular structures

The atom numbering scheme of the optimized enol and keto tautomer structures of 1-hydroxy-2-acetonaphthone is presented in Fig. 4.1 The molecular parameters (bond distances and selected bond angles) predicted for the optimized geometries of the enol species in the ground and first excited states are summarized in Table 4.1. The geometries were calculated applying all methods without geometry restrictions. The computations led to planar molecular structures of C_s symmetry for both ground (S_0) and first excited (S_1)-states. To the best of our knowledge no experimental X-ray structure data are available for HAN. Recent calculations for HAN have been performed by two research groups, at the HF/6-31G(d,p)[87] and B3LYP/6-31G(d,p)[86] levels of theory for the ground-state and at the

CIS/6-31G(d,p) level for the first excited-state[88]. Here, a direct comparison of the ground and first excited state geometries of HAN within the same quantum-mechanical method was possible for the first time on the basis of the CASSCF calculations. However CASSCF calculations require the choice of the active space.

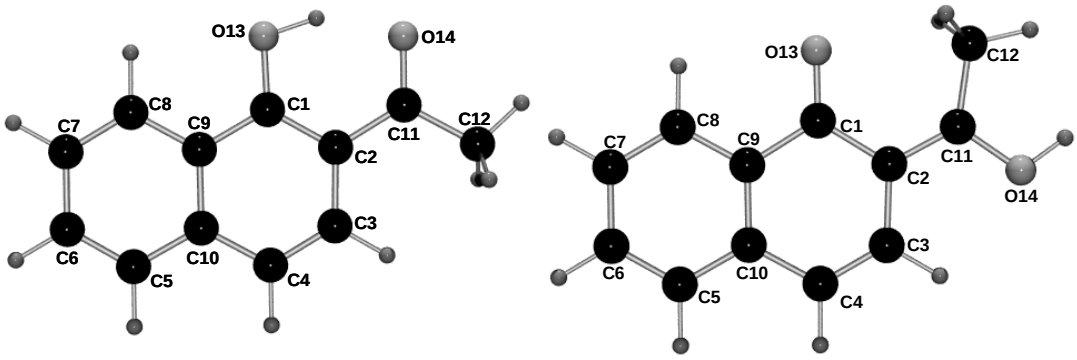

Figure 4.1 *Optimized molecular structure and atom numbering of HAN.*

In order to determine the molecular orbitals which are involved into the electronic transition, a preliminary HF calculation was performed (see Chapter 2.2). Figure 4.2 presents the π-type molecular orbitals selected for the active space. The total number of π-type orbitals is seven and three orbitals are occupied, and thus there are 6 electrons in 7 orbitals in the minimal active space. This active space was extended by the σ-type orbital (8 electrons in 8 orbitals), but the differences between the molecular structures computed with the small (6,7) and larger (8,8) active space were insignificant (Table 4.1).

The ground state parameters computed at the CASSCF level differ very slightly (0.01 Å) from the values obtained by means of the HF method[87]. The B3LYP and BPW91 functionals led to very similar structural parameters, which diverge from the results obtained within the HF[87] or CASSCF (see Table 4.1) methods maximally by 0.03 and 0.04 Å, respectively. However, DFT calculations tend to overestimate systematically[94] the bond lengths involving second row elements with respect to the X-ray spectroscopy data of the crystal structure and require for accurate results large basis sets by adding diffuse functions, hence implying higher computational costs. However, the DFT computed wavenumbers and Raman scattering activities are generally precise.

Concerning the selected basis sets, the computations at the CASSCF level showed that the inclusion of the polarization function for the hydrogen atom does not change significantly the structural parameters of HAN. Perceptible differences in the case of the

ground state occur only for the O-H bonds. In the case of the S_1 state, the intramolecular hydrogen bond is estimated to be shorter by 0.05 Å with the 6-31G(d,p) than with the 6-31G(d) basis set.

The bond lengths showing significant changes between the ground and excited states are depicted in bold in Table 4.1. It is noteworthy that, comparing the CASSCF computed ground state with the excited state geometry, the skeletal bond changes are even larger (about 0.1 Å) than when comparing the B3LYP or BPW91 ground state structure with the calculated excited state structure (about 0.08 Å). Nevertheless, the same tendency can be observed concerning the lengthening or shortening of the bond lengths. Interestingly, the O13-H bond length calculated with the CASSCF method for the ground state is only by 0.04 Å shorter than the excited state bond length, thus showing fewer changes than the skeletal bonds. However, it is obvious that the DFT calculations overestimate the O-H bonds, since the BPW91 method predicted even longer O13-H bond length than the value for the excited state. In contrast, the intramolecular O14-H bond length changes drastically and shows a shortening of about 0.23 Å in the excited state (within the CASSCF method). This feature can also be observed qualitatively in Fig. 4.3 which presents the superimposed molecular structure for the ground and excited states, both calculated within the CASSCF method. Moreover, comparing the O13-O14 distance in the two states (which changes by 0.13 Å) it becomes clear that the O14-H bond shortening is mainly due to the change in the relative position of the oxygen atoms.

Furthermore, it is important to take a closer look at the molecular orbitals involved into the electronic transition (see Fig. 4.2). The CIS and CASSCF calculations predicted a dominant transition from the HOMO into the LUMO, but the HOMO-1 and LUMO+1 orbitals are also involved (ca. 20%). The analysis of the HOMO and LUMO orbitals reflects very nicely the bond length changes predicted by the calculations. The C3-C4 bond shows the largest lengthening which is in accordance with the change of the bonding character of the HOMO localized on these atoms into a non-bonding orbital. The C1-C2 bond also changes according to the transfer of an electron from a bonding into an anti-bonding molecular orbital, while the C2-C11 bond shortens because the excitation of an electron into a bonding orbital localized on these atoms occurs, while the C11-O14 bond lengthens. Hence, although the analysis of the molecular orbitals cannot give quantitative information about the bond length changes, it is a very good approach to obtain a qualitative picture about the structural changes probably occurring upon photo excitation.

Table 4.1. *Calculated structural parameters of the ground- and excited-state optimized geometry of HAN.*

Bond lenghts (Å)	B3LYP 6-311+G(d)	BPW91 6-311+G(d)	CAS/6-31G(d,p) //S_0 (6,7)	CAS/6-31G(d,p) //S_0 (8,8)	CAS/6-31G(d,p) //**S_1** (6,7)	CAS/6-31G(d,p) //**S_1** (8,8)
C1-C2	**1.407**	**1.419**	**1.388**	**1.388**	**1.461**	**1.461**
C2-C3	**1.429**	**1.432**	**1.430**	**1.430**	**1.385**	**1.385**
C3-C4	**1.365**	**1.373**	**1.349**	**1.349**	**1.448**	**1.448**
C4-C10	1.426	1.430	1.426	1.426	1.431	1.431
C10-C5	1.416	1.420	1.426	1.426	1.394	1.394
C5-C6	1.378	1.385	1.354	1.354	1.379	1.379
C6-C7	1.412	1.415	1.421	1.421	1.398	1.398
C7-C8	1.377	1.385	1.353	1.353	1.374	1.374
C8-C9	1.416	1.419	1.428	1.428	1.406	1.406
C9-C10	1.425	1.434	1.403	1.403	1.416	1.416
C9-C1	1.432	1.437	1.432	1.432	1.428	1.428
C2-C11	**1.467**	**1.465**	**1.486**	**1.485**	**1.447**	**1.447**
C11-C12	1.514	1.516	1.511	1.511	1.509	1.509
C11-O13	**1.335**	**1.338**	**1.333**	**1.333**	**1.296**	**1.296**
C2-O14	**1.239**	**1.255**	**1.207**	**1.207**	**1.256**	**1.256**
O13-H15	0.990	1.013	0.953	0.952	0.991	0.991
O14-H15	**1.683**	**1.618**	**1.795**	**1.795**	**1.562**	**1.563**
O13-O14	**2.565**	**2.543**	**2.613**	**2.613**	**2.481**	**2.482**

Bond angles (°)	B3LYP/6-311+ G(d)	BPW91/6-311+ G(d)	CAS/6-31G(d,p) //S_0 (6,7)	CAS/6-31G(d,p) //S_0 (8,8)	CAS/6-31G(d,p) //$\mathbf{S_1}$ (6,7)	CAS/6-31G(d,p) //$\mathbf{S_1}$ (8,8)
C9-C1-C2	120.7	120.6	120.6	120.6	122.8	122.8
C1-C2-C3	118.5	118.5	118.4	118.4	115.7	115.7
C2-C3-C4	121.9	121.9	121.9	121.9	122.9	122.9
C3-C4-C10	120.5	120.5	120.3	120.3	120.6	120.6
C4-C10-C9	119.4	119.5	119.4	119.4	118.1	118.1
C10-C9-C1	119.1	119.0	119.3	119.3	120.1	120.1
C10-C5-C6	120.9	121.0	120.6	120.6	120.6	120.6
C5-C6-C7	120.4	120.4	120.5	120.5	119.8	119.9
C6-C7-C8	120.2	120.1	120.4	120.4	120.7	120.7
C7-C8-C9	120.4	120.4	120.2	120.2	120.3	120.3
C8-C9-C10	119.7	119.8	119.5	119.5	118.9	118.9
C9-C10-C5	118.4	118.3	118.8	118.8	119.7	119.7
C3-C2-C11	121.9	122.3	121.2	121.2	124.4	124.4
C2-C11-C12	120.0	120.3	119.6	119.6	120.6	120.5
C12-C11-O14	118.7	118.6	119.0	119.0	119.6	119.6
O14-C11-C2	121.2	121.1	121.4	121.4	119.8	119.8
C11-C2-C1	119.7	119.3	120.3	120.3	119.9	119.9
C2-C1-O13	122.5	122.0	123.6	123.6	118.6	118.6
O13-C1-C9	116.8	117.4	115.8	115.8	118.6	118.6
C1-C9-C8	121.2	121.2	121.2	121.2	121.0	121.0
C4-C10-C5	122.2	122.3	121.8	121.8	122.3	122.3
C1-O13-H15	107.6	106.0	109.5	109.5	107.6	107.6
O13-H15-O14	146.1	149.4	142.2	142.2	152.0	152.0
H15-O14-C11	102.8	102.3	103.0	103.0	102.1	102.1

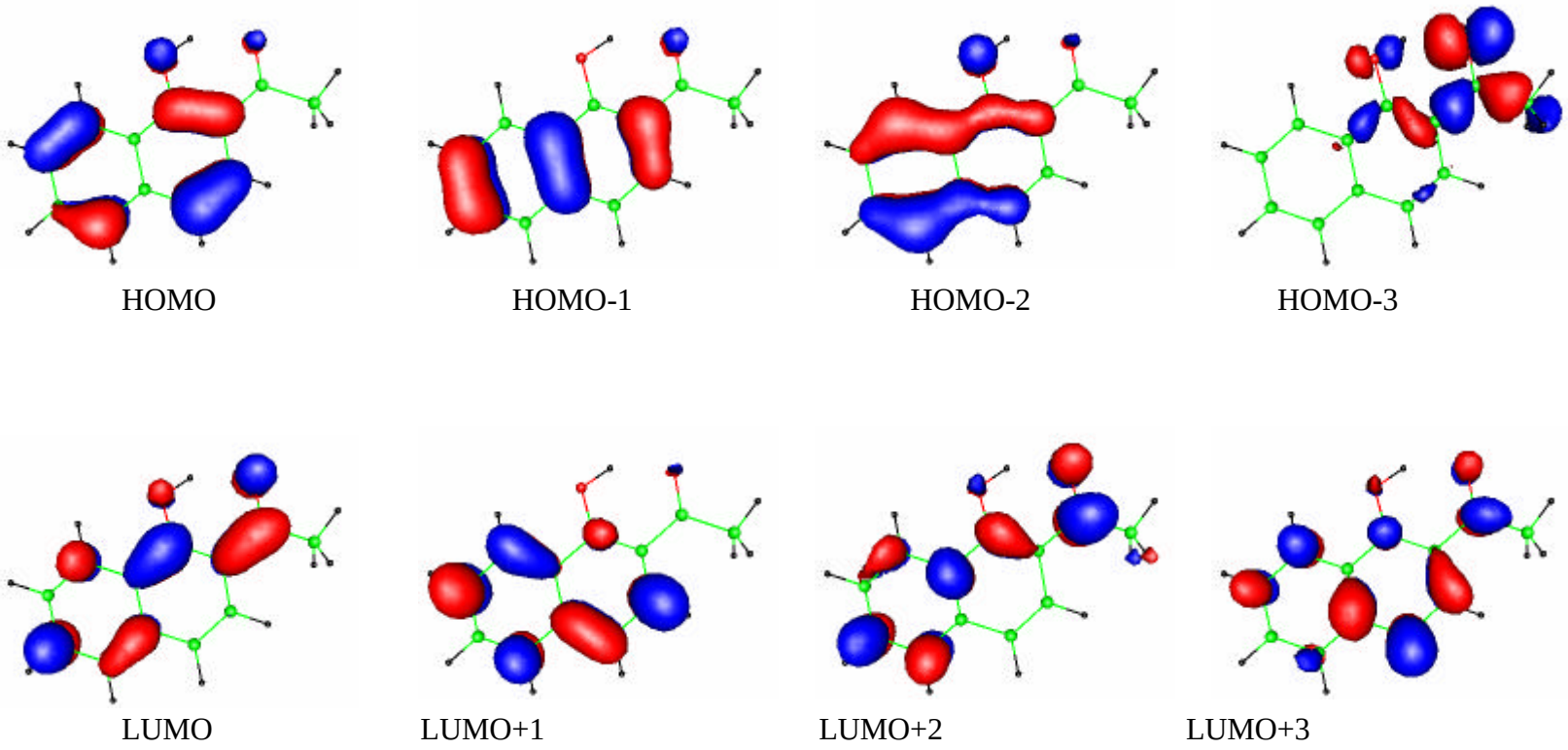

Figure 4.2 *Plot of the valence molecular orbitals of HAN for an isosurface value -0.05 to +0.05. The HOMO - 2 to LUMO + 3 orbitals are of p-type while the HOMO – 3 is of s-type.*

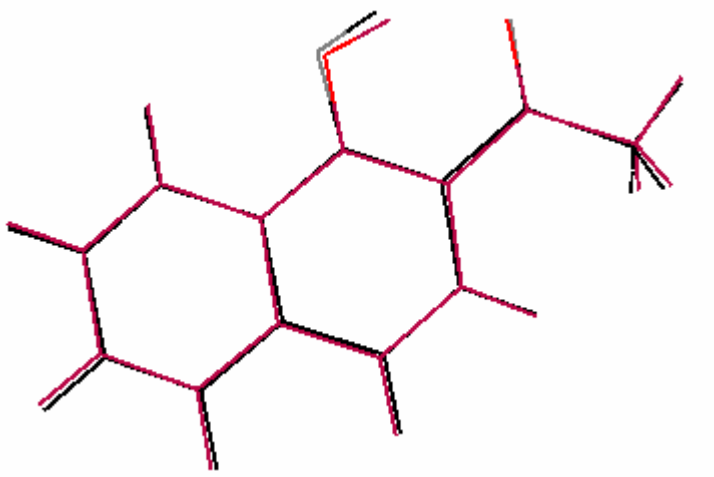

Figure 4.3 *Superimposed molecular structures of HAN. The ground state geometry is depicted grey and the excited state structure black.*

Table 4.2. *Partial electron charges (e) obtained within the natural population analysis (NPA) at the CASSCF level of theory.*

Atom	**S_0**	**S_1**
C1	**0.493**	**0.553**
C2	**-0.269**	**-0.186**
C3	**-0.200**	**-0.106**
C4	**-0.246**	**-0.071**
C5	-0.228	-0.193
C6	-0.206	-0.231
C7	-0.244	-0.223
C8	-0.189	-0.178
C9	-0.101	-0.151
C10	-0.013	-0.111
C11	**0.700**	**0.466**
C12	-0.739	-0.717
O13	**-0.781**	**-0.756**
O14	**-0.689**	**-0.790**
H15	0.550	0.574

Moreover, the examination of the HOMO and LUMO indicates that charge seems to move upon excitation from the naphthalene ring toward the carbonyl unit making the O14 more negative. The orbital coefficient on the O14 atom increases, while it slightly decreases on the O13 atom. This is further substantiated by the calculated partial electron charges obtained through the natural population analysis at the CASSCF level of theory. The partial electron charges are listed in Table 4.2. The electron charge significantly

increases on the O14 atom (by 0.1 e) and decreases on the hydroxyl O13 atom (by 0.025 e), thus favouring the ESIPT. These calculations also show that a severe reorganization of the electron density takes place.

In the following, the vibrational characteristic of HAN will be discussed and the experimental data of the excited state potential surface obtained through the resonance Raman analysis will be presented.

Spectroscopical data

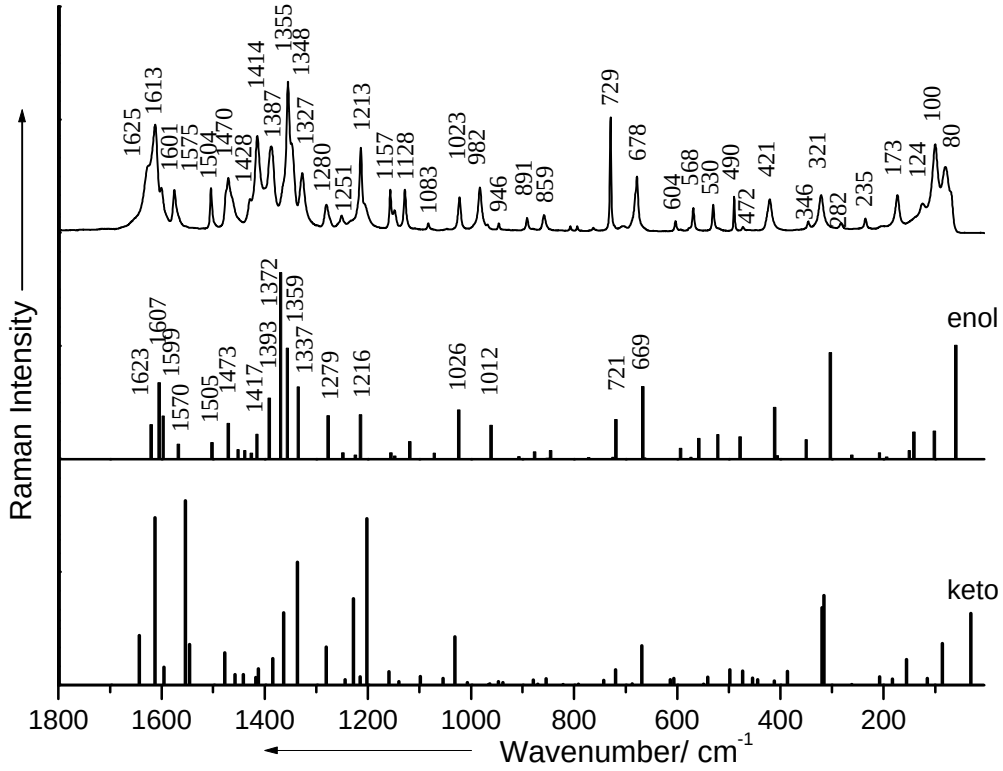

Figure 4.4 *FT-Raman spectrum of solid, neat HAN and the theoretical Raman intensities of the gas phase HAN enol and keto tautomers computed at the BPW91/6-311+G(d) level of theory presented as bar lines.*

The vibrational analysis of the FT-Raman spectrum of HAN has been performed on the basis of DFT and PED calculations in comparison to the vibrational assignments of related derivatives[4] as well as from previous spectroscopical data[67] of HAN. The FT-Raman spectrum of solid HAN is presented in Fig. 4.4 together with the Raman

intensities[34] of the vibrational modes calculated at the BPW91/6-311+G(d) level of theory for the enol and keto tautomers. Excellent agreement can be observed not only for the calculated wavenumbers, but also with respect to the relative Raman intensities between the enol species and the experimental Raman spectrum. Although, below 1000 cm^{-1} some discrepancies arise. Namely, the band at 729 cm^{-1} has higher intensity in the FT-Raman spectrum of HAN powder than it is predicted by the theoretical calculations. However, in the Raman spectrum of a saturated solution (not shown here) this band comes up with a similar intensity to the band at 678 cm^{-1}. Besides, the out-of-plane deformation modes of the naphthalene ring around 100 cm^{-1}, which have very low intensity in the theoretical spectrum, are probably overlapped by lattice vibrations of the crystal unit in the FT-Raman spectrum. Hence, these dissimilarities can be merely attributed to intermolecular interactions in the solid state.

Table 4.3 lists the observed bands in the FT-Raman spectrum of HAN with their vibrational assignment according to the PED calculations for the enol tautomer. The vibrational wavenumbers computed with different functionals have also been included.

The vibrational characteristics of HAN reveal very strong intramolecular hydrogen bonding. The OH stretching mode has been predicted by the DFT calculations to arise at lower wavenumbers than the CH_3 and CH stretching modes around 2900 cm^{-1} (Table 4.3). The Raman scattering activity of this mode is usually weak compared to the unsaturated CH moieties, and therefore the band at 2921 cm^{-1} was assigned to the OH stretching vibration. Generally, the stronger the intramolecular hydrogen bond, the more the OH stretching mode is shifted to a lower wavenumber[4]. The planar geometry favours the chelation, where the OH group is involved in the molecular resonance structure of a six-membered ring. The aromatic CH stretching modes give rise to the very intense band at 3070 cm^{-1}. The CH_3 symmetrical and antisymmetrical stretchings, which are in Fermi resonance with the CH_3 bending, regularly occur near 2872 and 2962 cm^{-1} and are probably responsible for several weak bands in this vibrational region.

The other group sensitive to the strength of the intramolecular hydrogen bond is the C=O moiety. Although the carbonyl stretching vibration usually arises around 1700 cm^{-1}, the PED calculations showed that in HAN two vibrations at 1613 and 1601 cm^{-1} have contributions from the C=O stretch (see Table 4.3). Moreover, the C=O stretching modes dominating the band at 1613 cm^{-1} arise at even lower wavenumbers than the aromatic ring stretching vibrations (see Table 4.3). This result can be explained through the fact that the

C=O unit is involved in the intramolecular hydrogen bond and because of a strong electron delocalization due to the conjugation with the aromatic ring system. The C=O bending comes up at 568 cm^{-1} and also contributes to the band at 678 cm^{-1} in the low wavenumber region.

The stretching modes of the C2-C11-C12 aceto group corresponding to the strong bands at 1355 and 1327 cm^{-1} (see Tab. 4.3) arise at higher wavenumbers than usually C-C stretching modes are expected, thus reflecting the partial double bond character of the C2-C11 bond (calculated 1.46 Å, see Table 4.1).

The asymmetric CH_3 deformation mode gives rise to a broad band at 1470 cm^{-1}, while the in-plane deformation modes of the aromatic CCH moieties couples with the ring stretching and deformation modes. The ring stretching modes appear in the FT-Raman spectrum of HAN as strong bands between 1000 and 1600 cm^{-1} and often couple with substituent groups. The in-plane and out-of-plane deformation modes of the ring give rise to bands below 1000 cm^{-1} (see Table 4.3).

Figure 4.5 shows the resonance Raman spectra of HAN in comparison to the off-resonant Raman spectrum excited at 488 nm in the 900-1700 cm^{-1} range. While the off-resonant spectrum was measured in a saturated solution, the concentration of HAN was only $2 \cdot 10^{-3}$ M in the case of the resonance Raman spectra. The position of the bands in the Raman spectrum recorded in solution is slightly shifted with respect to the band positions in the FT-Raman spectrum of polycrystalline HAN (see Table 4.3). The carbonyl stretching mode becomes a broad band in the solution Raman spectra and shifts to 1634 cm^{-1}. The resonance Raman spectra are dominated by vibrations corresponding to skeletal stretching and in-plane deformation modes of the naphthalene backbone and the conjugated aceto group (see Table 4.3 vibrations marked in bold). In the low wavenumber region (see Fig. 4.6) the most enhanced band is at 603 cm^{-1} whereas the modes at 565 cm^{-1}, 488 cm^{-1}, 414 cm^{-1}, 340 cm^{-1}, and 319 cm^{-1} experience a moderate enhancement. All of these modes lead to deformations of the H-chelate ring and of the naphthalene chromophore. However, the mode at 603 cm^{-1} exhibits in comparison with the other low wavenumber modes the strongest enhancement, while in the high wavenumber region the bands at 1355 and 1414 cm^{-1} are particularly enhanced.

Table 4.3. *Experimental and calculated vibrational wavenumbers (cm^{-1}) of HAN and their vibrational assignment. The Franck-Condon parameters obtained experimentally (bold) and through quantum chemical calculations (in parenthesis next to the calculated wavenumbers) are also listed.*

Raman	D **Exp**	BPW91/ 6-311+G(d)	BPW91/ 31+G	B3LYP/ 311+G	B3LYP/ 6-31+G(d)	Vibrational assignment with the PED (%) in parenthesis
3091		3143 (-0.18)	3159 (-0.24)	3274 (-0.16)	3230 (-0.05)	νC8H(90) + νC7H(8)
		3128 (-0.33)	3145 (-0.42)	3213 (-0.01)	3216 (-0.16)	νC3H(80) + νC4H(18)
3070		3121 (0.38)	3139 (0.49)	3198 (-0.07)	3206 (0.23)	νC6H(48) + νC7H(32) + νC5H(12) + νC8H(6)
		3108 (-0.27)	3126 (-0.31)	3187 (0.11)	3193 (-0.27)	νC7H(47) + νC5H(32) + νC6H(10) + νC4H(6)
		3105 (0.01)	3122 (0.07)	3175 (-0.23)	3190 (-0.02)	νC4H(74) + νC3H(16)
		3095 (-0.22)	3113 (-0.28)	3171 (-0.08)	3180 (-0.25)	νC5H(53) + νC6H(37) + νC7H(8)
3016		3092 (-0.15)	3108 (0.01)	3162 (-0.21)	3178 (-0.03)	$\nu^{asym}CH_3$(100)
		3041 (0)	3057 (0)	3148 (-0.36)	3164 (-0.23)	$\nu^{asym}CH_3$(100)
2972		2980 (-0.15)	2993 (-0.17)	3098 (0)	3113 (0)	$\nu^{sym}CH_3$(100)
2921		2907 (-0.16)	2806 (-0.28)	3042 (-0.05)	3054 (-0.08)	νOH(99)
1625sh	**0.29**	1623 (-0.53)	1628 (-0.43)	1677 (0.34)	1683 (0.48)	ν_{ring}(62) (asym) + δ_{ring}(19) + δOH(6)
1613s		1607 (1.02)	1615 (0.86)	1664 (1.20)	1671 (1.09)	νC=O(45) + δOH(11) + δCC-C11(6) + νC2-C11(5)
1601sh	**0.16**	1599 (-0.18)	1604 (-0.33)	1646 (0.66)	1652 (0.45)	ν_{ring}(22 C5-C6, 22 C3-C4, 8 C7-C8) + νC=O(12)
1575w	**0.20**	1570 (0.68)	1577 (0.50)	1609 (1.12)	1617 (0.94)	ν(43 unsub) + νC1-C2(10) + δOH(16)
1504w	**0.17**	1505 (0.42)	1511 (0.38)	1544 (-0.69)	1551 (-0.65)	ν(17 C6-C7, 14 C2-C3, 20 C4-C10-C5) + δCCH(7)
147x sh		1473 (0.80)	1478 (0.72)	1511 (0.92)	1517 (0.89)	δOH(17) + ν(19 C3-C4-C10) + δCCH(7)
1470m		1454 (0)	1461 (0)	1498 (0)	1503 (0)	$\delta^{asym}CH_3$(93)
		1441 (0.04)	1448 (0.13)	1485 (-0.07)	1491 (0.01)	$\delta^{asym}CH_3$(89)
1428sh		1428 (-0.08)	1436 (-0.11)	1463 (0.45)	1469 (-0.45)	ν(13 C3-C4, 17 C9-C10-C5, 10 C5-C6) + δOH(10) + δCCH(8)
1414ms	**0.67**	1417 (0.85)	1424 (-0.84)	1453 (-0.95)	1461 (0.92)	ν(33 trigonal ring) + δCCH(33)
1387ms	**0.28**	1393 (0.27)	1402 (-0.38)	1427 (0.12)	1436 (0.28)	ν(26 unsubstituted ring, 13 C1-C9) + νC-O(14) + δ_{ring}(13)
1355vs	**0.71**	1372 (0.13)	1379 (0.01)	1410 (-0.14)	1420 (-0.17)	ν^{asym}C2-C11-C12(27) + νC=O(7) + $\delta^{sym}CH_3$(22) + δOH(7)
1348sh		1359 (-0.50)	1368 (-0.64)	1389 (-1.12)	1400 (-1.01)	ν(36 unsubstitued ring, 13 C1-C9) + νC-O(8) + $\delta^{sym}CH_3$(18)

1327m	**0.42**	1337 (-0.52)	1348 (-0.47)	1362 (0.90)	1373 (0.88)	$\delta^{sym}CH_3(37) + \nu^{asym}C2\text{-}C11\text{-}C12(23) + \delta OH(9)$
1280w	**0.38**	1279 (-0.39)	1286 (-0.50)	1308 (-0.24)	1313 (-0.36)	ν(19 C9-C1, 13 C2-C11) + δCCH(12)
1251vw		1251 (-0.43)	1257 (-0.50)	1279 (0.30)	1285 (0.31)	ν(15 C2-C3, 11 C2-C11, 8 C5-C10) + δCCH(25) + νC-O(6)
sh		1227 (-0.08)	1233 (-0.04)	1252 (-0.29)	1260 (-0.24)	ν(26 C8-C9-C10-C4, 10 C2-C3) + νC-O(16) + δCCH(24)
1213ms		1216 (0.43)	1222 (0.41)	1239 (0.68)	1245 (0.65)	δCCH(29) + ν(29 C4-C10-C5, 6 C1-C9)
1157w		1157 (0.08)	1163 (0.06)	1184 (-0.01)	1187 (0.15)	δCCH(76)
1148sh	**0.34**	1151 (-0.06)	1155 (-0.04)	1183 (-0.22)	1190 (-0.04)	δCCH(67) + νC3-C4(10)
1128w	**0.30**	1121 (0.67)	1124 (0.63)	1152 (0.85)	1155 (0.76)	δCCH(32) + νC11-C12(9) + $\delta_{ring}(8)$ + νC2-C3(5)
1083vw	**0.23**	1074 (0.24)	1075 (0.12)	1105 (0.38)	1107 (0.26)	$\delta_{ring}(32)$ + δCCH(12) + νC5-C10(8) + νC1-C2(6) + $\delta^{rock}CH_3(7)$
1023w		1026 (-0.37)	1030 (-0.37)	1047 (-0.38)	1051 (-0.40)	ν(41 C6-C7, 9 C5-C6, 7 C7-C8) + δCCH(26)
982w		1012 (0)	1017 (0)	1051 (0)	1054 (0)	$\delta^{rock}CH_3(67) + \delta^{out}C{=}O(10) + \delta^{out}CC\text{-}C12(8) + \delta^{out}CC\text{-}C11(7)$
968sh		963 (0.39)	967 (0.27)	994 (0.53)	998 (0.43)	$\delta^{rock}CH_3(60) + \nu C11\text{-}C12(10)$
946vw		956 (0)	965 (0)	1000 (0)	1006 (0)	$\delta^{out}CCH(86) + \delta^{out}{}_{ring}(7)$
		932 (0)	945 (0)	974 (0)	981 (0)	$\delta^{out}CCH(90) + \delta^{out}{}_{ring}(8)$
891w		879 (0.80)	879 (0.81)	902 (-0.83)	902 (-0.88)	$\delta_{ring}(36) + \nu C8\text{-}C9\text{-}C10(15) + \nu C11\text{-}C12(8)$
		855 (0)	922 (0)	884 (0)	901 (0)	$\delta^{out}OH(92)$
		851 (0)	858 (0)	870 (0.86)	890 (0)	$\delta^{out}CCH(54) + \delta^{out}{}_{ring}(31)$
859w		848 (0.53)	848 (0.38)	819 (0)	870 (0.70)	$\delta_{ring}(46) + \nu C11\text{-}C12(13)$
807w		786 (0)	792 (0)	811 (0)	822 (0)	$\delta^{out}CCH(41) + \delta^{out}{}_{ring}(19) + \delta^{out}CC\text{-}C11(13) + \delta^{out}CC\text{-}O13(11)$
794w		774 (0)	779 (0)	801 (0)	805 (0)	$\delta^{out}{}_{ring}(59) + \delta^{out}CCH(13) + \delta^{out}CC\text{-}O13(7)$
		727 (0)	734 (0)	755 (0)	762 (0)	$\delta^{out}CCH(72) + \delta^{out}CC\text{-}C11(11) + \delta^{out}{}_{ring}(6)$
729s		722 (-0.53)	722 (-0.62)	740 (-0.39)	740 (-0.45)	$\delta_{ring}(37) + \nu C5\text{-}C10(9) + \nu C9\text{-}C10(8) + \nu C4\text{-}C10(6)$
678m		669 (0.48)	673 (0)	690 (0)	695 (0)	$\delta_{ring}(37) + \nu C11\text{-}C12(8) + \nu C9\text{-}C10(9) + \nu C2\text{-}C11(7) + \delta C{=}O(5)$
		666 (0)	670 (0.50)	686 (0.30)	686 (0.30)	$\delta^{out}{}_{ring}(77) + \delta^{out}CC\text{-}C11(6) + \delta^{out}CC\text{-}O13(5)$
604vw	**0.69**	596 (0.90)	596 (0.80)	612 (1.02)	613 (0.96)	$\delta^{in}{}_{ring}(51) + \delta^{in}CC\text{-}C11(7) + \delta^{in}CC\text{-}O13(6) + \nu C2\text{-}C3(12)$
		576 (0)	582 (0)	598 (0)	604 (0)	$\delta^{out}CC\text{-}C11(28) + \delta^{out}C{=}O(22) + \delta^{out}CC\text{-}O13(11) + \delta^{out}CC\text{-}C12(10)$
		562 (0)	568 (0)	584 (0)	585 (0)	$\delta^{out}{}_{ring}(80)$
568w	**0.44**	561 (0.17)	561 (0.02)	574 (0.27)	575 (0.12)	$\delta^{in}C{=}O(41) + \delta^{in}{}_{ring}(30)$
530w		524 (0.21)	523 (0.01)	541 (0.47)	540 (0.31)	$\delta^{in}{}_{ring}(52) + \delta^{in}CCH(14)$

490w	**0.78**	481 (0.30)	480 (0.24)	496 (0.37)	495 (0.34)	$\delta^{in}{}_{ring}(67) + \delta^{in}CC\text{-}C11(8)$
472vw		460 (0)	465 (0)	478 (0)	483 (0)	$\delta^{out}{}_{ring}(75) + \delta^{out}CC\text{-}C11(16)$
421w	**0.68**	414 (-0.08)	416 (0)	427 (0)	433 (0)	$\delta^{in}CC\text{-}O13(31) + \delta^{in}CC\text{-}O13(22) + \delta^{in}{}_{ring}(9)$
		409 (0)	415 (-0.09)	420 (0.07)	422 (0.04)	$\delta^{out}{}_{ring}(87) + \delta^{out}CC\text{-}C11(6)$
346vw	**0.71**	352 (-0.22)	350 (-0.30)	358 (-0.10)	358 (-0.21)	$\delta^{in}{}_{ring}(30) + \delta^{in}CC\text{-}O13(18) + \delta^{in}C{=}O(7)$
321w	**0.73**	305 (-0.45)	305 (-0.20)	317 (-0.85)	316 (-0.61)	$\delta^{in}CC\text{-}O13(22) + \delta^{in}CC\text{-}C12(19) + \delta^{in}{}_{ring}(15) + \delta^{in}CC\text{-}C11(7)$
282w		264 (0)	267 (0)	274 (0)	279 (0)	$\delta^{butterfyl}{}_{ring}(45) + \delta^{out}CC\text{-}O13(30) + \delta^{out}{}_{ring}(11)$
235w		211 (0)	215 (0)	218 (0)	224 (0)	$\delta^{out}{}_{ring}(73)$
		196 (0.81)	195 (0.68)	203 (1.02)	202 (0.90)	$\delta^{in}CC\text{-}C12(26) + \delta^{in}C{=}O(25) + \delta^{in}CC\text{-}C11(16) + \delta^{in}CCH(12)$
173w		153 (0)	151 (0)	163 (0)	158 (0)	$\tau C\text{-}CH_3(59) + \delta^{butterfyl}{}_{ring}(14) + \delta^{rock}CH_3(12)$
124w		143 (0)	147 (0)	147 (0)	150 (0)	$\delta^{butterfyl}{}_{ring}(60) + \delta^{out}{}_{ring}(22)$
100ms		104 (0)	107 (0)	102 (0)	106 (0)	$\delta^{butterfyl}{}_{ring}(39) + \delta^{out}{}_{ring}(30) + \delta^{out}CC\text{-}C12(10)$
80m		63 (0)	64 (0)	65 (0)	67 (0)	$\delta^{out}{}_{ring}(43) + \delta^{out}C{=}O(24) + \delta^{out}CC\text{-}C11(9) + \delta^{out}CCH(14)$

ν *stretching*, δ *deformation*, in *in-plane*, out *out-of-plane*

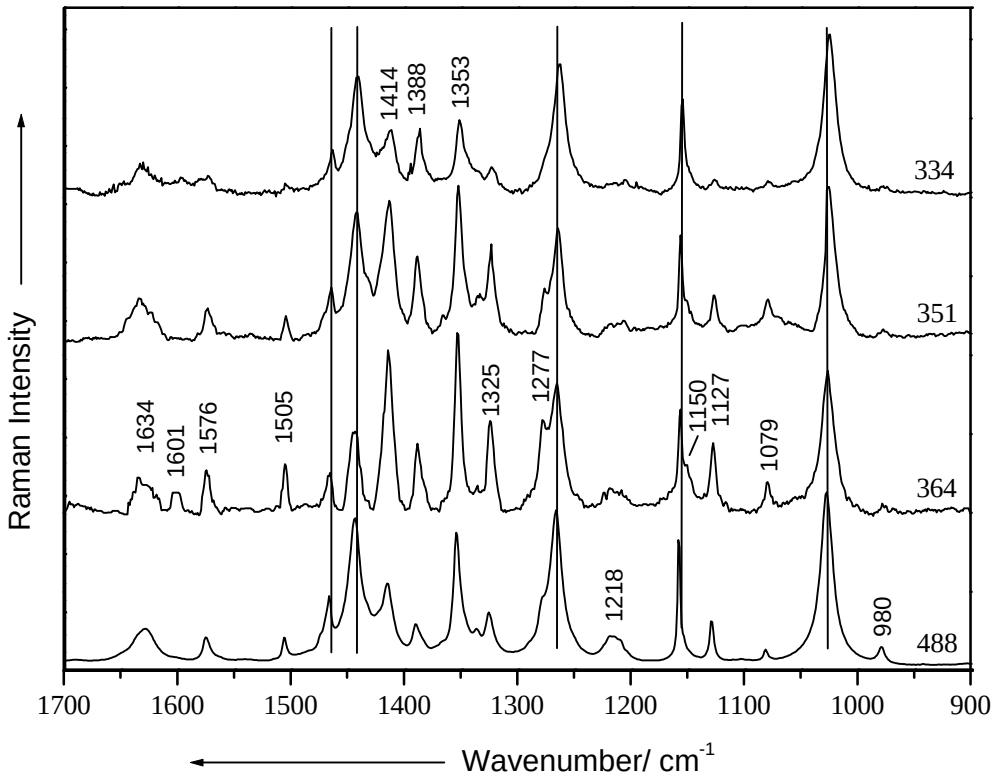

Figure 4.5 *The resonance Raman spectra of HAN in comparison to the off-resonance Raman spectrum recorded at 488 nm excitation. The solvent lines are marked with vertical lines. The concentration of the sample used for the measurement with 364 and 351 nm was 2×10^{-3} M and for 334 nm was 10^{-2} M, while the off-resonance spectrum was recorded in saturated solution (» 0.5 M).*

Interestingly, no enhancement of the O-H stretch motions could be observed. The keto fluorescence starts at the O-H stretch mode region in the Raman spectrum, i.e. vibrations within these wavenumber region are partially overlapped by the keto fluorescence. However the Raman spectrum of this region shows solvent bands sitting on top of the fluorescence band and no O-H stretching modes could be observed even for high concentrations. Similar findings were reported in the case of 2-hydroxy-acetophenone (OHAP), where no enhancement of the O-H stretching mode was observed[46]. This shows that directly after the optical excitation the hydrogen of the OH-group is still bound to the oxygen and does not directly move towards the oxygen of the acetyl group as one might expect for a PT molecule.

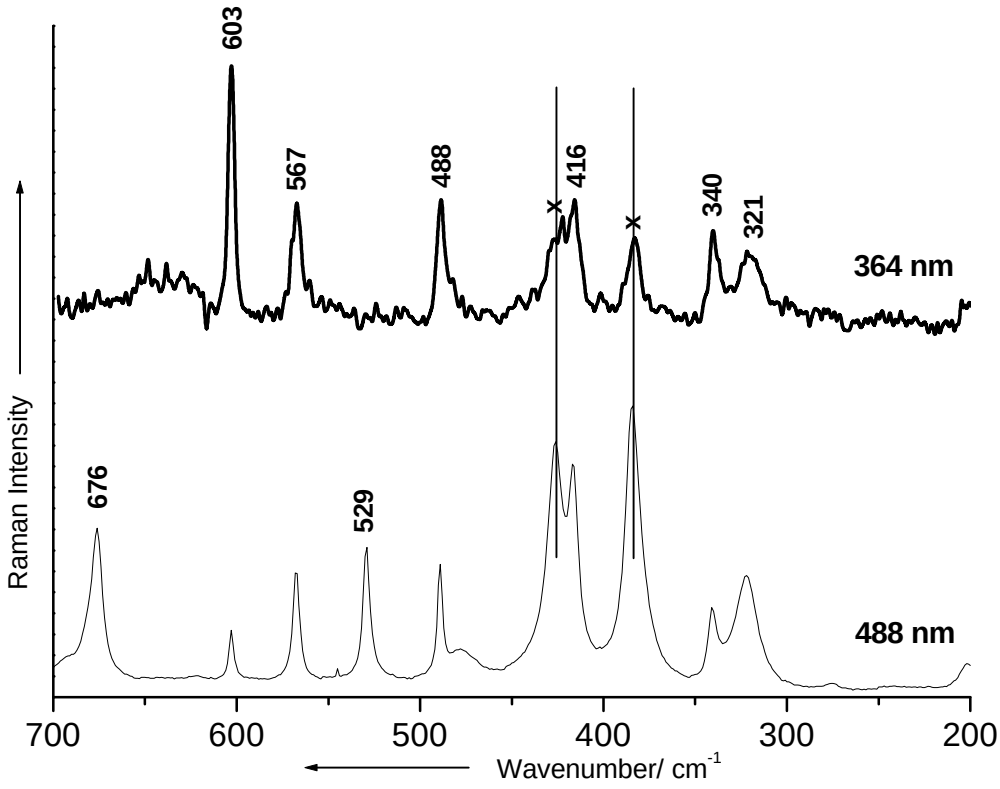

Figure 4.6 *Resonance Raman spectrum of HAN compared to the off-resonance spectrum in the low wavenumber region. The concentration of HAN in the resonantly excited spectrum was* 2×10^{-3} *M, while the off-resonance spectrum was recorded in saturated solution (» 0.5 M).*

Displacement parameters

The displacement parameters Δ of the excited state potentials along eighteen resonance Raman enhanced modes (see Table 4.3, the values marked in bold) were obtained through a simultaneous fit of the absorption and resonance Raman excitation profiles following the computational strategy described by Myers and coworkers[37] and summarized in Chapter 3.3. The absorption spectrum and resonance Raman profiles of HAN were calculated using the time-dependent formalism. Due to the fact that this treatment is described extensively in literature[13,16,18,77], little detail will be given here. Harmonic potential surfaces for the ground and excited states were considered with equal wavenumbers for most of the vibrational modes. In order to properly simulate the vibronic structure of the absorption spectrum, the wavenumbers of the vibrational modes at 1414

and 1355 cm^{-1} had to be reduced. For the excited state potentials of these modes wavenumbers values of 1300 and 1200 cm^{-1} were considered, respectively. Reducing the wavenumbers of these modes for the excited state significantly improved the fit of the absorption and resonance Raman profiles. The transition moment (0.69 Å) and zero-zero transition energy (25780 cm^{-1}) were evaluated from the absorption spectrum and slightly adjusted during the fit. A small amount of static inhomogeneous broadening of 150 cm^{-1} corresponding to zero-zero energy shifts had to be included. The solvent induced broadening was evaluated in terms of the Brownian oscillator model developed by Mukamel and coworkers[23,47]. The homogeneous broadening due to the interaction with the solvent amounts to 450 cm^{-1}. Furthermore, for a proper simultaneous fit of the absorption spectrum and resonance Raman profiles, a pure exponential lifetime decay (Γ = 400 cm^{-1}) was included. The solvent induced broadening is quite low and therefore the interaction of the molecule with the surrounding medium does not strongly affect the initial dynamics of the proton transfer process.

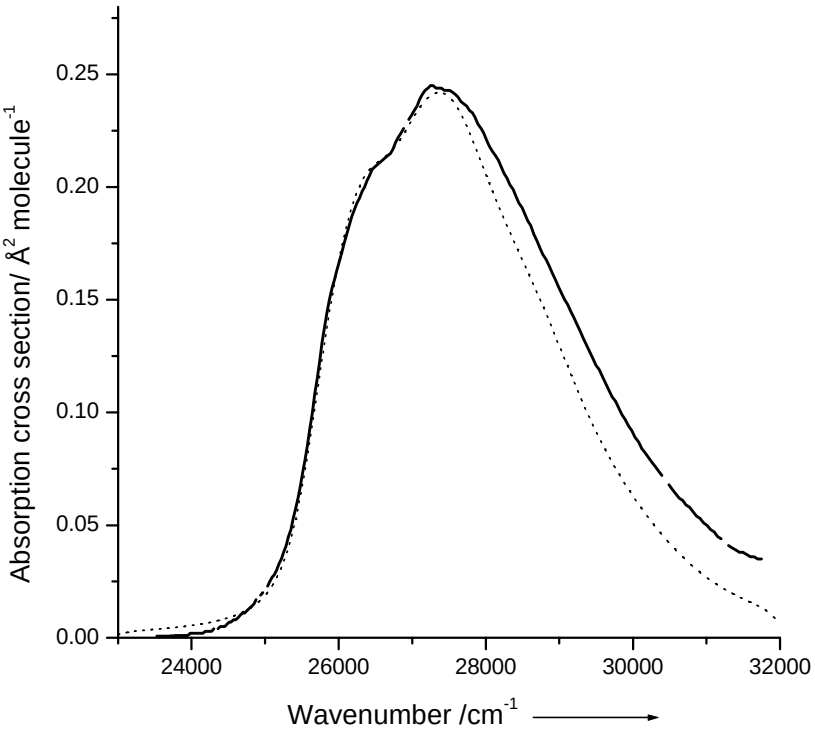

Figure 4.7 *The experimental and calculated absorption spectrum of HAN using the parameters listed in Table 4.3.*

Figure 4.7 (dashed line) shows that a reasonably good fit for the absorption band could be obtained. The UV absorption spectrum of HAN in cyclohexane solution at 297 K presents a broad band, which has an onset at ~ 400 nm, with a maximum at 367 nm and has been assigned to the p-p* electronic transition of the planar conjugated system including the pseudo-aromatic chelate ring.

The experimental and calculated absolute differential Raman intensities for the vibrational modes are presented in Fig. 4.8. The fitted values match the experimental data quite well, although several Raman bands strongly overlapped. In the low wavenumber region, the scattering due to the quartz glass is increasing when excitation in the UV is used, and the band at 414 cm^{-1} overlaps with the solvent band. Furthermore, the fluorescence of the keto photoproduct was steeply increasing from 1550 cm^{-1}, overlapping the bands at 1574, 1601 and 1634 cm^{-1}, and hence the displacement parameters for these modes are estimated to have the largest uncertainty.

The experimental displacement parameters determined through the time-dependent analysis are listed in Table 4.3 (bold values). The theoretical displacements are also included in Table 4.3 in parenthesis next to the calculated wavenumbers. The theoretical method additionally delivers the sign of the displacement parameters indicating if the vibrational mode will lead to a shortening or lengthening of the structural parameters. Unfortunately, this information cannot be extracted from the experimental data since the Raman intensity depends on the square of the displacements. Nonetheless, very good agreement between the experimentally determined displacement parameters and the absolute value of the theoretical ones can be observed. The different theoretical methods depending on the applied functional and basis set also led to similar parameters. Several modes mainly corresponding to out-of-plane deformation modes show zero displacements in accordance to the absence of these modes in the RR spectra. In the case of the carbonyl stretching mode, the quantum chemical calculations probably overestimate the displacement parameter, because the calculation is performed for the gas phase and does not take into account the effect of the solvent (a strong shift of this band upon solvation was observed). Moreover, the calculations predicted for the O-H stretching mode only a low displacement which is in agreement with the resonance Raman experiment and intensity analysis.

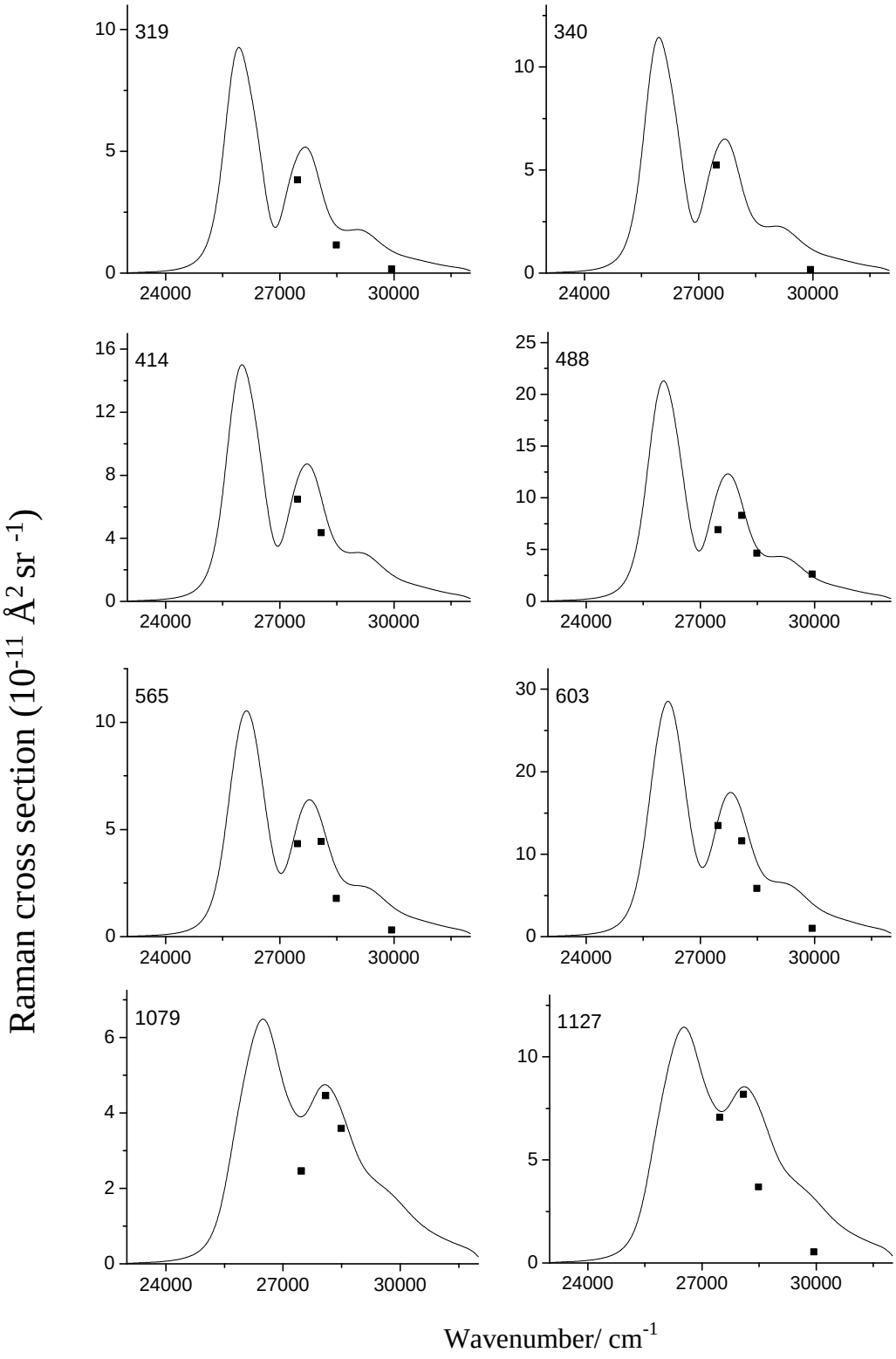
319
340
414
488
565
603
1079
1127
Raman cross section (10^{-11} Å^2 sr^{-1})
Wavenumber/ cm^{-1}

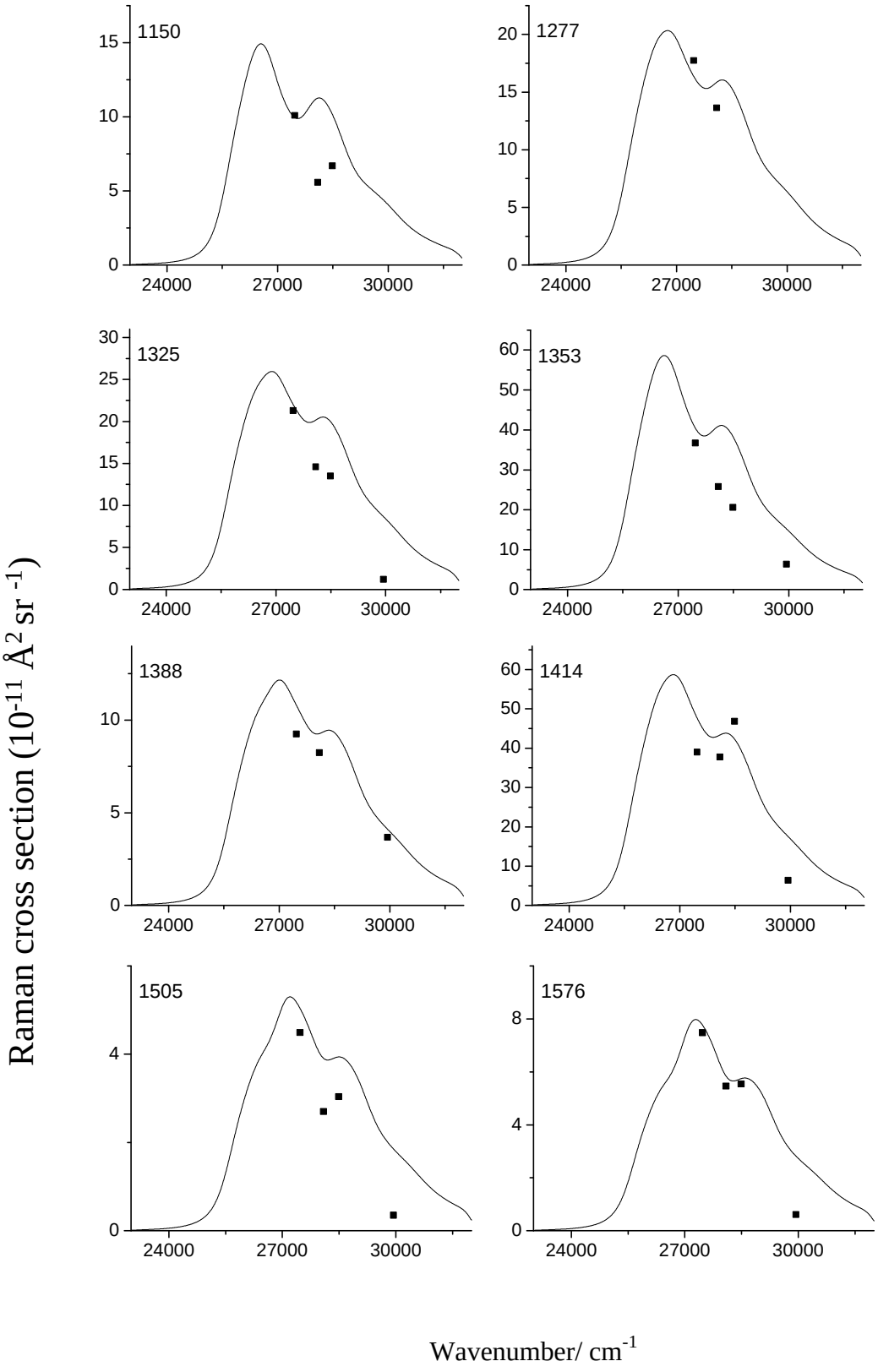
1150
1277
1325
1353
1388
1414
1505
1576
Raman cross section (10^{-11} Å^2 sr^{-1})
Wavenumber/ cm^{-1}

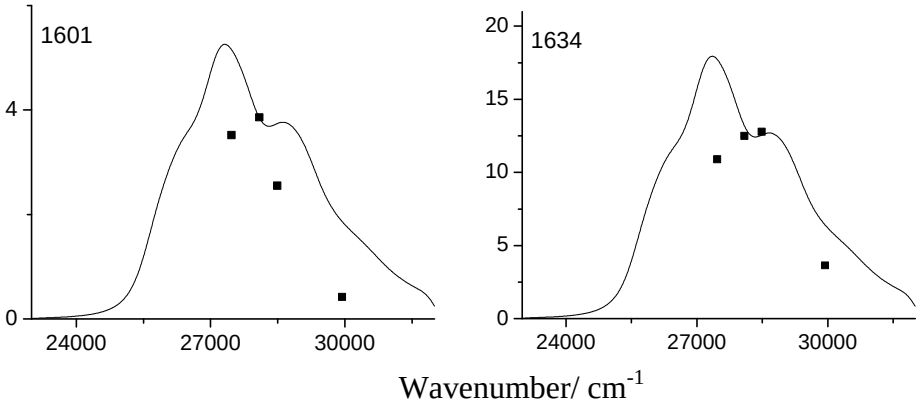

Figure 4.8 *The excitation profiles of HAN calculated with the experimental parameters listed in Table4.3. The experimentally obtained data are ploted as squares.*

The resonance enhancement of several stretching and deformation modes of the naphthalene chromophore and the conjugated aceto moiety indicates that the proton transfer mechanism is more consistent with a picture of the excited state of HAN in which a general molecular reorganization of the aromatic ring system together with conjugated aceto group takes place. In the high wavenumber region, the modes at 1414 and 1355 cm^{-1} exhibit the highest enhancement and Raman cross sections (see Fig. 4.8). The vibration at 1414 cm^{-1} is mainly localized on the substituted ring, and the band at 1353 cm^{-1} was assigned to a stretching motion of the aceto-moiety and naphthalene ring. The broad band at 1355 cm^{-1} probably corresponds to both vibrational modes calculated at 1372 and 1359 cm^{-1} with the BPW91/6-311+G(d) method, but it is difficult to experimentally determine the separate contribution of these vibrations to the displacement parameter. Nevertheless, the quantum chemical calculations showed that the band calculated at 1359 cm^{-1} has a higher displacement than the band at 1372 cm^{-1}. The modes at 1414 and 1353 cm^{-1} exhibit the highest displacement parameters Δ of all the stretching modes.

The deformation modes in the low wavenumber region (see Table 4.3) also show high displacement parameters. The highest displacement was predicted for the band calculated at 596 cm^{-1} (603 cm^{-1} in the Raman spectra), which also experience a conspicuous enhancement under resonant conditions in the RR spectrum (see Fig. 4.6). The bands at 321 and 346 cm^{-1} present comparable displacement parameters to the one at 603 cm^{-1}, although their intensity is lower. However, the Raman cross section is approximately proportional to the square of the vibrational wavenumber.

Unfortunately, it is very difficult to determine the changes in geometry using the experimental displacements, because the number of modes, which are enhanced, is too large. Nevertheless, the very good agreement between the theoretically calculated displacement parameters using the optimized excited state molecular structure and the experimental parameters is a proof that the CASCF method delivers a very good estimation of the excited state geometry.

Comparing the data obtained for HAN with related derivatives, one can observe that generally skeletal stretching and deformation modes of ESIPT systems are coupled to the proton transfer process. In the case of OHAP (1-hydroxy-2-acetophenone) a single exceedingly enhanced stretching mode (at 1324 cm^{-1}) corresponding to the symmetric ring stretching and C-O contraction vibration was observed[46]. However, about fifteen vibrational modes altogether are resonantly enhanced in OHAP. Thus, it has been concluded that for OHAP a skeletal rearrangement occurs upon optical excitation prior to proton transfer in this system. For HAN two modes at 1414 and 1355 cm^{-1} are especially enhanced in this high wavenumber region. This indicates that the electronic excitation in HAN is more complex than in OHAP and involves more nuclear degrees of freedom than in OHAP due to the presence of the second aromatic ring. Moreover, the displacement parameter of the mode at 1324 cm^{-1} in OHAP is much higher than the parameters of the deformation modes of OHAP[46]. In contrast, for HAN the displacement parameters of the deformation modes are even higher than the displacement parameters of the stretching modes, indicating that the structural changes are the result of cooperative deformation and stretching motions.

Conclusions

Resonance Raman spectroscopy in combination with quantum chemical methods was successfully applied to investigate the initial dynamics of the intramolecular proton transfer system 1-hydroxy-2-acetonaphthone upon photo excitation. Therefore, DFT calculations of the ground state geometry, vibrational wavenumbers, Raman intensities and PED calculations for the enol and keto tautomers were performed to assign the FT-Raman spectrum of HAN. Very good agreement with the experimental spectrum was obtained for the enol species. CASSCF calculations were done for the ground and first excited state showing that the excited state skeletal structural parameters significantly differ from the ground state ones. The analysis of the molecular orbitals and the NPA calculations show an

increase of the electron density on the carbonyl group in the excited state, which is probably the leading force for the proton transfer process.

About eighteen vibrational modes corresponding to skeletal stretching and in-plane deformation modes are resonantly enhanced, showing that a general structural rearrangement takes place upon excitation. The resonance Raman intensity analysis of these modes delivered the Franck-Condon parameters. The very good agreement between the experimental parameters and those calculated using pure quantum chemical data indicates that the optimized excited state geometry is a reliable picture for the molecular changes upon photo excitation.

Chapter 5

Inter-Valence Charge Transfer in Triarylamine-Radical Cation

*The electronic and molecular structure of N,N,N',N'-tetraphenylphenylenediamine radical cation (**1**$^+$) is in focus of this chapter. Resonance Raman experiments showed that at least eight vibrational modes are strongly coupled to the optical charge resonance band observed in the NIR. With the help of a DFT based vibrational analysis, these eight modes were assigned to symmetric vibrations. The contribution of these symmetric modes to the total vibrational reorganization energy is dominant. The solvent induced broadening is found to be low. These findings are in agreement with the conclusions from a simple two-state two-mode Marcus-Hush analysis carried out in the group of Prof. Lambert, which yields a tiny electron transfer barrier. The excellent agreement of the X-ray crystal structure analysis and the DFT computed molecular structure of **1**$^+$ on the one hand as well as the solvent and solid state IR spectra and the DFT calculated IR active vibrations on the other hand prove **1**$^+$ to adopt a symmetrical delocalised Robin-Day Class III structure both in the solid state and in solution. Moreover, the structural changes upon photo excitation were evaluated using the experimental displacement parameters determined through a time-dependent resonance Raman intensity analysis.*

Motivation

Mixed-valence (MV) species play a dominant role as simple model systems in the investigation of adiabatic electron transfer (ET) processes.[95-100] The usually employed one-dimensional MV systems consist of two redox centers (ligand coordinate metals or organic redox active moieties) that are connected via a bridge molecule. If the two redox centers have a different oxidation state an electron or a hole can be transferred either by optical excitation or thermally. Several structural parameters which control the electron (hole) transfer rate were varied and investigated such as the type of the redox centers (purely organic vs. ligand complexed metal ions), the bridge length, the nature of the bridge (conjugate vs. non-conjugate), the local bridge energy etc. The electronic coupling V of two diabatic (i.e. noninteracting) states in which the excess electron (or hole) is localized on the left-hand or right-hand redox center describes the communication between these centers (see Fig. 5.1).

According to Robin and Day,[101] MV species can be classified into three categories: Class I with practically no coupling between the different redox states, Class II with intermediate coupling and, Class III in which the excess electron (or hole) is delocalised over the two redox centers. The adiabatic potential energy surface (PES) for the one-dimensional degenerate case can be constructed by coupling two diabatic states which are represented by quadratic potentials in a 2 x 2 matrix where V (see Figure 5.1) is the electronic coupling and λ the reorganization energy of the diabatic potentials. The optical excitation from one energy minimum of the ground state surface to the excited state yields directly λ as long as $2V < \lambda$.[102,103] The absorption band associated with this optical excitation is usually found in the NIR and is called intervalence charge transfer band (IV-CT) in the case of Class II and charge resonance band in the case of Class III.[104] While for MV species of Class I or II there exists a barrier ΔG^* for the thermal ET this barrier vanishes for Class III compounds at $2V > \lambda$. If one seeks to use MV species as electronic switching or storage units for future optoelectronic devices on a molecular level, it is of utmost importance to assess the degree of delocalization in these MV species.[105] Thus, in particular the transition between Class II and Class III has attracted considerable interest in recent years.[103,106-115]

While for many MV compounds the electronic situation is quite clear (e.g. N,N,N',N'-tetraalkylphenylenediamine radical cations[116,117] belong to Class III), the

situation remained uncertain for others for many years (e.g. the Creutz-Taube salt)[107] or is still under debate (e.g. N,N,N',N'-tetraanisylphenylenediamine radical cation).[109,118,119] The confusion arises because Class III compounds are believed to have narrow charge resonance absorption lines with vibrational progression visible (e.g. in N,N,N',N'-tetraalkylphenylenediamine radical cations)[116,117] while typical Class II compounds show a broad featureless IV-CT band similar to the one observed in N,N,N',N'-tetraanisylphenylenediamine radical cation. The latter cation was thought to be weakly localised[109,118,119] but a recent vibrational coupling calculation showed it out to be delocalised.[109,118,119]

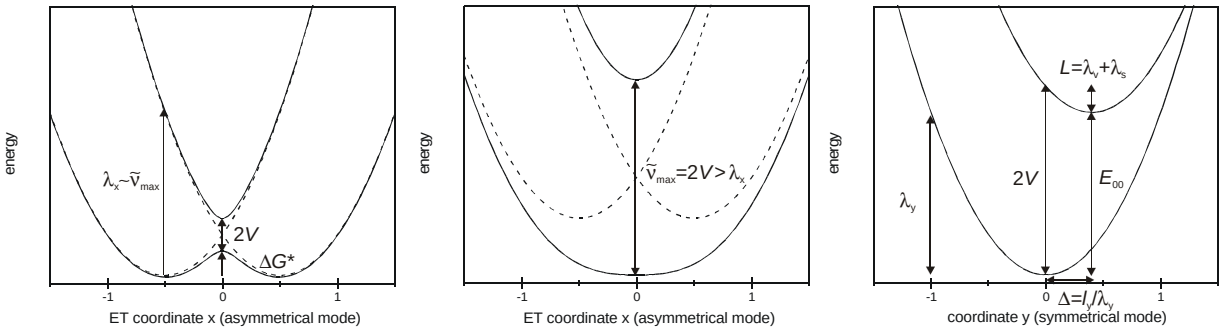

Figure 5.1 *Diabatic potentials (dashed lines) and adiabatic potentials (solid lines) for a Class II system (left diagram), a Class III system (center diagram) along the asymmetrical x mode and the corresponding section along the symmetrical y mode at x = 0 (right diagram) as derived from the solutions of eqn. (1).* l_v *and* l_s *refer to the vibrational and solvent reorganization energies as derived from the resonance Raman analysis, see below.*

However, mode-specific information is generally difficult to extract from the IV-CT or charge resonance absorption band shape due to severe solvent induced broadening and/or fast photochemistry in the excited state. Resonance Raman spectroscopy[17] (RR) provides specific information on the molecular degrees of freedom involved in the initial structural changes of photochemically active systems. Moreover, it is a reliable tool for investigating the symmetry, equilibrium geometry and dynamics of the resonantly excited electronic state (see Chapters 2.1 and 3.3). In order to gain more insight into the vibrations involved in the charge transfer of mixed valence systems, and thus into the absorption band shape, extensive resonance Raman spectroscopical studies were carried out previously by several research groups.[120-122] The time-dependent formalism[38-40] has been applied to interpret the RR scattering activities, absorption cross section and to determine the Franck-

Condon parameters of the vibrational modes coupled to the intensive charge transfer band in asymmetrical[123,124] and symmetrical inorganic mixed-valence compounds.[44,50,125-128] Recently, the attention has been directed also towards organic[116,129] charge transfer systems.

The special interest in triarylamine based radical cations and their electronic nature stems from their wide application as hole transport molecules in optoelectronic materials[130,131] and their use as high-spin compounds in organic magnets.[132,133]

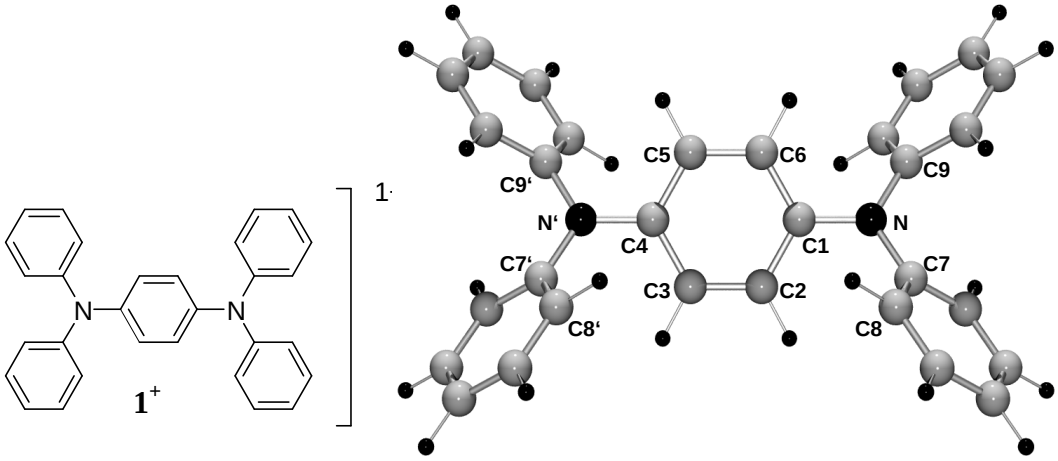

Scheme 5.1 *Chemical structure and the optimized molecular geometry of* ***1***$^{+}$ *for the* C_{2h} *symmetrical structure with the atom numbering.*

The smallest bis(triarylamine) MV species conceivable is N,N,N',N'-tetraphenylphenylenediamine radical cation **1**$^{+}$. The goal of this study is to collect and compare electronic, structural as well as spectroscopic data on **1**$^{+}$ in order to clarify the electronic situation. The accuracy of the structural parameters predicted for the gas phase of **1**$^{+}$ will be analyzed by comparison to the data derived from X-ray diffraction measurements done in the group of Prof. Stalke. The assignment of the IR and Raman spectra of 1^{+} by comparison with DFT calculated vibrations and the resonance Raman spectra, which give insight into the modes involved in the ET process, will be presented. A detailed resonance Raman intensity analysis within the time-dependent formalism[38-40] will be expatiated in order to determine the vibratioanal and solvent reorganization energies upon optical excitation. The structural changes in the excited state will be predicted based on the experimental displacement parameters.

Structural properties

The title compound was synthesized in the group of Prof. Lambert. The crystal structure analysis, which was performed in the group of Prof. Stalke,[134] shows two independent cations, both having a crystallographic inversion center which makes the point group C_i but with only little deviations from C_{2h}.

For comparison with the X-ray structure analysis DFT calculations for $\mathbf{1}^+$ and **1** with the Gaussian98[56] program package were performed. The structures, vibrational characteristics, IR intensities and Raman scattering activities of the radical cation were computed. The molecular structures were optimized at the UBPW91 level of theory requiring the Becke's 1988 exchange and Perdew and Wang's 1991 gradient-corrected correlation functionals. The 6-31G* split valence plus polarization basis set was used. Unlike UHF calculations which are highly spin contaminated, the DFT calculations are almost free of any spin contamination (S^2 = 0.753). The fully optimized molecular geometries correspond to minima on the ground state potential surface of $\mathbf{1}^+$ and **1**, as was proven by normal-mode analysis, employing the analytically calculated Hessian (see Chapter 3.2). The molecular structures of $\mathbf{1}^+$ and **1** computed with symmetry restrictions resulted in structural parameters almost identical to those calculated without symmetry restrictions. The bond lengths differences between the two procedures are smaller than 0.001 Å. For $\mathbf{1}^+$ two minima close in energy with D_2 and C_{2h} symmetry, the latter involving a center of inversion, were found. The X-ray structure analysis of $\mathbf{1}^+$ showed that the molecular structure in the solid state has C_{2h} symmetry. Moreover, the C_{2h} symmetric cation is predicted by the quantum chemical calculations to be more stable (by 2.6 kJ/mol) than the D_2 symmetric form. These two conformers differ in the relative helicity of the two triarylamine propellers.

Important distances and angles for $\mathbf{1}^+SbCl_6^-(dioxane)_{0.5}$ are collected in Table 5.1. The distances and angles of the in total four independent cations vary only little in the case of the X-ray analysis and the calculations without symmetry restrictions. The nitrogen centers are trigonal planar coordinate, the angle sum is 360°. The aryl rings are arranged in propeller form around the nitrogen centers as observed in other triarylamine radical cations.[135-137] Selected DFT computed parameters of the cation are included in Table 5.1 and are in good agreement with the experimentally observed values. The computed molecular parameters for the neutral species and the radical cation mainly differ in the

bonds and angles involving the central benzene and the nitrogen atoms. The C-N bond is significantly reduced in the cation, compared to the neutral form. As mentioned before, removing an electron from **1** stabilizes the C_{2h} symmetric cation $\mathbf{1}^+$ with respect to the D_2 symmetric form. However, in the case of the neutral compound **1** the D_2 symmetric form has been found to be slightly more stable (by 0.03 kJ/mol) than the C_{2h} symmetric isomer, but this is of course insignificant.

Table 5.1 *Selected distances (Å) and angles (°) of* ***1***$^+$ *and of* ***1*** *determined by X-ray crystallography as well as DFT calculated values.*

	1	BPW91 **1** (C_{2h})	**1**$^+$$SbCl_6^-$ $(dioxane)_{0.5}$	BPW91 **1**$^+$ (C_{2h})
Distances				
C2-C3	1.387(4)	1.396	1.351(2)	1.385
C6-C1	1.389(4)	1.412	1.416(2)	1.424
C1-C2	1.387(4)	1.412	1.418(2)	1.424
C1-N	1.433(3)	1.425	1.363(2)	1.397
N-C7	1.405(4)	1.425	1.444(2)	1.432
N-C9	1.426(3)	1.425	1.430(2)	1.432
Angles				
C9-N-C1	121.2(2)	119.93	120.90(15)	120.68
C9-N-C7	121.9(2)	120.12	116.53(14)	118.64
C7-N-C1	116.8(2)	119.93	122.54(15)	120.68
C7-N-N'-C9'	180	180	180	180
C7-N-N'-C7'	-3.3	0	-4.4	0
C2-C1-N-C7	-53.8	-40.99	-8.6	-29.97
C1-N-C7-C8	-55.7	-45.57	-64.0	-39.90

Both the X-ray structure analysis and the DFT calculations indicate a centrosymmetric structure of $\mathbf{1}^+$. However, the unambiguous conclusion of a delocalised Class III structure for $\mathbf{1}^+$ cannot be drawn from these investigations for several reasons: 1) the investigations refer to either the solid state or the gas phase and not to solution where time and density fluctuations of the solvent may induce a certain degree of asymmetry in $\mathbf{1}^+$. 2) Cation $\mathbf{1}^+$ might be slightly asymmetric in the solid state and the crystallographic symmetry is due to static or dynamic disorder. 3) The symmetry of $\mathbf{1}^+$ in the solid state might be induced by the position of the $SbCl_6^-$ gegenion which sits right above the middle of the cation. 4) DFT methods are known to overemphasize delocalization in radical ions.[138,139]

IR and Raman spectra and their DFT computation

In order to investigate the vibrational modes involved in the charge resonance excitations of $\mathbf{1}^+$ a detailed vibrational study was carried out. This involved the measurement of the IR, off resonance and resonance Raman spectra, the assignment of IR and Raman vibrational modes by comparison with DFT computed vibrations as well as the resonance Raman intensity analysis in order to determine the Franck-Condon parameters. The IR spectra in solution were recorded in the group of Prof. Lambert.

The vibrational spectroscopic techniques IR and Raman spectroscopy represent one of the most useful tools for obtaining information about the structure and properties of molecules from their vibrational transitions (see Chapter 2.1). However, the assignment of the infrared and Raman bands of polyatomic molecules is rather complicated[140]. Theoretical calculations, first of all DFT calculations, are therefore the appropriate approach to obtain a deeper insight into the microscopic atomic displacements of complicated molecules.

In order to obtain structural information of $\mathbf{1}^+$ IR and Raman spectra of $\mathbf{1}^+$ in CH_2Cl_2 solution were measured. The IR spectrum of $\mathbf{1}^+$ was recorded also in a KBr matrix.

The Raman scattering activities of $\mathbf{1}^+$ were calculated maintaining the symmetry restrictions (C_{2h} or D_2) because of the high computational costs. The Raman scattering activities were converted into Raman scattering intensities for the 514.5 nm off-resonant excitation line as described by Porezag and Pederson[34] (see Eq. 2.17).

The off-resonance Raman spectrum of $\mathbf{1}^+$ in CH_2Cl_2 solution is shown in Fig. 5.2 in comparison with the DFT calculated Raman scattering intensities. The IR spectra of $\mathbf{1}^+$ measured in a KBr matrix and in solution are presented in Fig. 5.3. The calculated vibrational wavenumbers (no scaling factors were applied) and IR intensities are in good agreement with the experimental data. For the Raman data, a general correspondence between the calculated and experimental intensities could be observed. However, the calculation of the polarizability derivatives, which is required to evaluate the Raman intensities, is very sensitive to the level of theory.[34] In order to get a better agreement between the experimentally observed Raman intensities and the calculated ones a higher level of theory is required, but then the numerical calculation of the Raman scattering activities would be extremely time consuming. Therefore, we refrained from applying a higher level of theory.

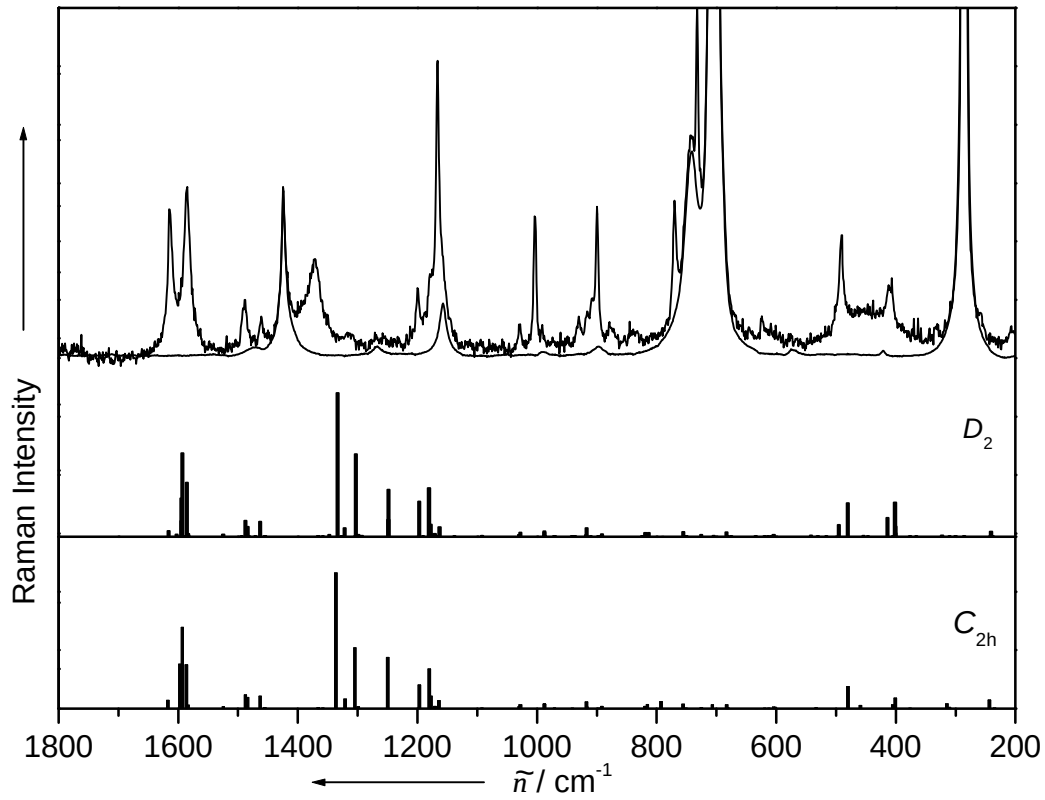

Figure 5.2 *Calculated Raman scattering intensities at the BPW91/6-31G(d) level for* ***1***$^+$ *and the off-resonance Raman spectrum in* CH_2Cl_2 *solution measured at 514.5 nm excitation. The spectrum of the pure* CH_2Cl_2 *solvent is also given as a thin solid line.*

The DFT calculations with D_2 and C_{2h} symmetry constraints yielded very similar results for the vibrational wavenumbers, infrared absorption intensities and Raman scattering intensities (Figs. 5.2 and 5.3). In the case of C_{2h} symmetry the IR active vibrational modes are forbidden in the Raman spectrum due to the center of inversion. However, the calculations with D_2 symmetry restrictions predicted a similar behavior. The IR active bands have almost zero Raman scattering activity, and vice versa. Thus, a definite conclusion about the symmetry of $\mathbf{1}^+$ (D_2 or C_{2h}) in solution cannot be drawn from our Raman and IR measurements, but the excellent agreement of the IR spectra in solution and in the solid state (KBr matrix) where the structure is known by the X-ray crystal structure analysis on the one hand and the good agreement of the calculated and computed

spectra on the other hand suggests a symmetric, and therefore a Class III structure of $\mathbf{1}^+$ in which both nitrogen atoms are equivalent.

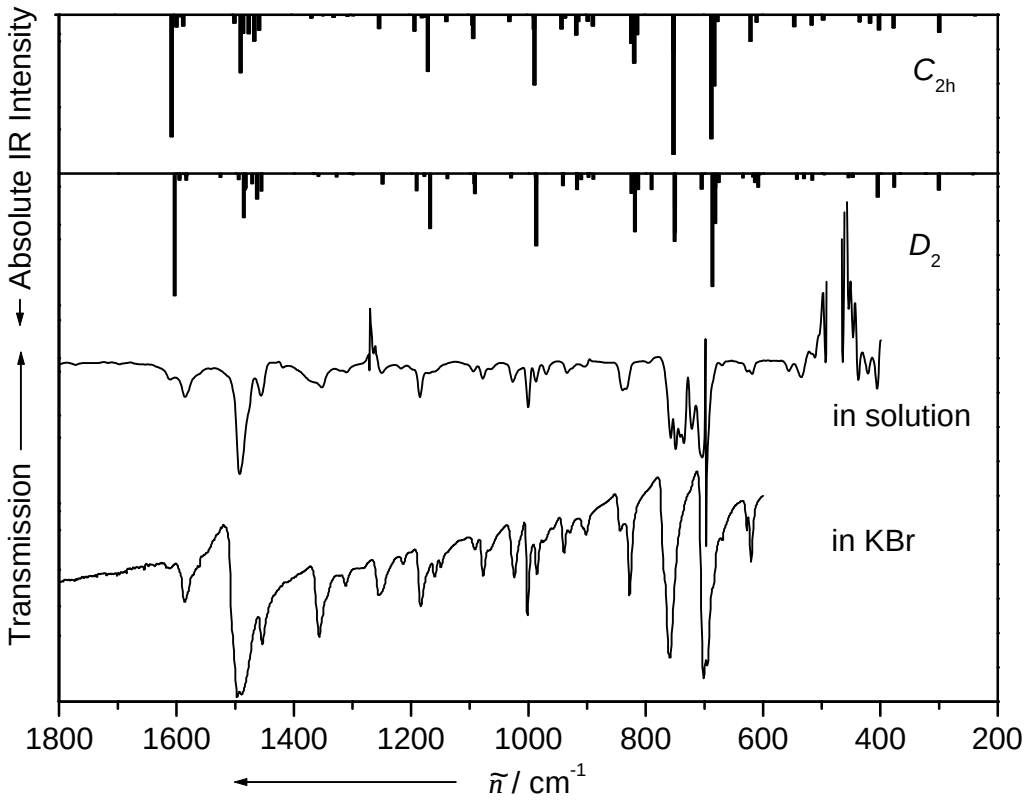

Figure 5.3 *Calculated IR intensities at the BPW91/6-31G(d) level for* $\mathbf{1}^+$ *and the IR spectrum recorded in* CH_2Cl_2 *solution and in KBr matrix.*

The vibrational analysis was carried out by comparing the computed vibrational modes with those obtained from the literature for benzene derivatives.[4] The vibrational assignment is given in Table 5.2. The corresponding computed wavenumbers are also listed. Upon substitution of the benzene molecule the symmetry is lowered and the degenerate vibrations are split into their counterparts.[4] A molecular structure of C_{2h} symmetry has a_g and b_g Raman and a_u and b_u IR active modes, while a molecular structure of D_2 symmetry has vibrational modes of a, b_1, b_2 and b_3 symmetry, which are Raman active. Only the a modes are IR inactive. The vibrational modes will be discussed in the following, taking into consideration a molecular structure of C_{2h} symmetry (see Table 5.2),

but a strong correspondence between the molecular vibrations of the two symmetries has been observed (Figs. 5.2 and 5.3).

Cation $\mathbf{1}^+$ consists of four identical monosubstituted (phenyl) benzene units and one disubstituted (phenylene) benzene unit. The computations showed that many vibrational modes involve only one type of the benzene rings, while others involve also the nitrogen atoms. Several vibrations are strongly coupled and involve the entire system. Scheme 5.2 presents selected vibrational modes and the corresponding Cartesian atomic displacements.

The splitting of the aromatic C=C stretch mode, which arises in the Raman spectrum of benzene[4] as a very strong band at 1596 cm^{-1} (Wilson numbers 8a and 8b, of e_{2g} symmetry) and in the IR spectrum at 1486 cm^{-1} (Wilson numbers 19a and 19b, of e_{1u} symmetry), due to the lowering of symmetry leads to several Raman or IR active vibrations in this spectral region. In the off-resonance Raman spectrum of $\mathbf{1}^+$ (Figure 5.2) two vibrational modes at 1613 and 1582 cm^{-1} can be observed. The calculations (see Table 5.2) predicted several intense modes (1617, 1595, 1593, 1586 cm^{-1}) in this spectral region. The strongest vibration calculated at 1593 cm^{-1} (Scheme 5.2) corresponds to the symmetric aromatic stretch of the phenyl and phenylene rings and also involves the C-N bond. Raman bands due to C=C stretch vibrations also arise at 1489 and 1461 cm^{-1}, but with very weak intensity (Fig. 5.2). The strong and broad band around 1490 cm^{-1} in the IR spectrum (Fig. 5.3) probably consists of several C=C vibrational modes. The C=C stretching vibration shows weak IR intensity around 1600 cm^{-1}.

The broad band at 1365 cm^{-1} in the off-resonance Raman spectrum of $\mathbf{1}^+$ can be assigned to a symmetric C-N stretching mode along the N-bridge-N axis. The largest atomic motions involved in this vibration are presented in Scheme 5.2.

The CCH deformation modes give rise to a strong Raman band (Fig. 5.2) at 1166 and a shoulder at 1177 cm^{-1}. The vibration at 1198 cm^{-1} can be assigned to a CCH deformation band strongly coupled to the C-N stretching mode. The weak bands in the IR spectrum around 1150 cm^{-1} and the medium strong band at 1024 cm^{-1} are due to the CCH deformation modes.

Scheme 5.2. *The Cartesian displacements of the atoms during the fundamental resonance enhanced vibrations of* ***1***$^{+}$*. Values given in brackets in cm*$^{-1}$ *units.*

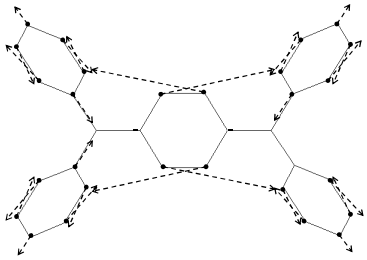

1613 cm^{-1} (calculated 1617)

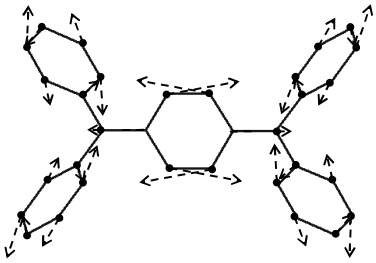

1582 cm^{-1} (calculated 1593)

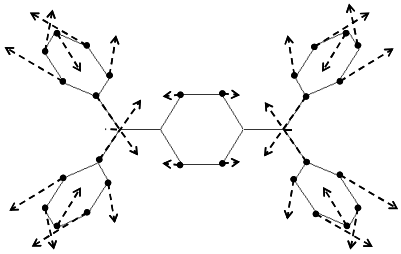

1489 cm^{-1} (calculated 1488)

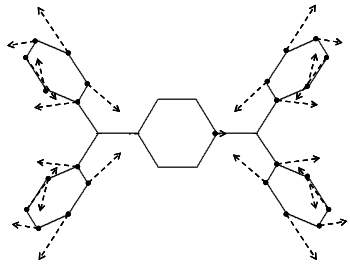

1461 cm^{-1} (calculated 1463)

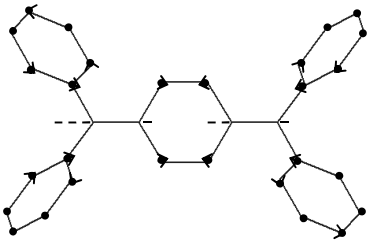

1365 cm^{-1} (calculated 1337)

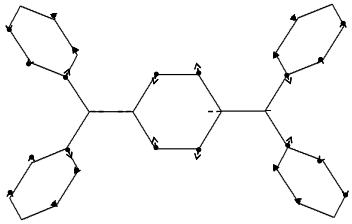

1310 cm^{-1} (calculated 1295)

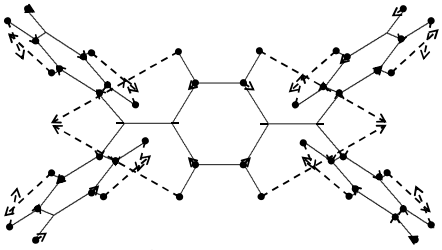

1198 cm^{-1} (calculated 1180)

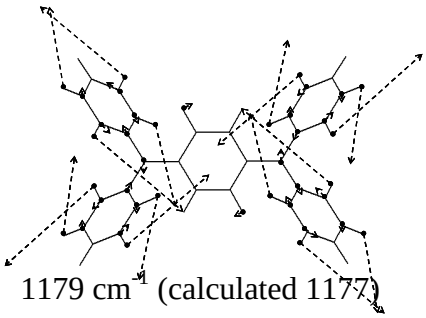

1179 cm^{-1} (calculated 1177)

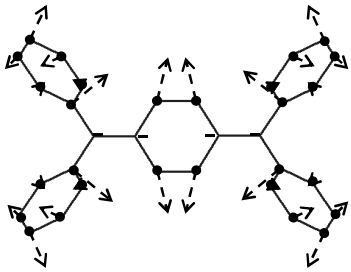

491 cm^{-1} (calculated 480)

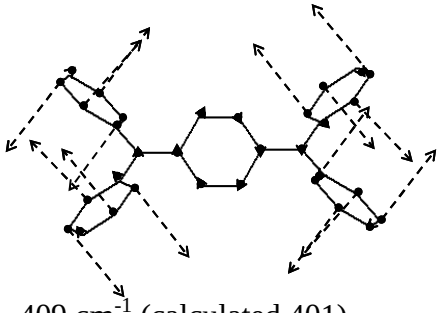

409 cm^{-1} (calculated 401)

Table 5.2. *Experimental and computed vibrational wavenumbers $\tilde{n}$, displacement parameters D, vibrational reorganization energies $l_{v,i}$ and tentative vibrational assignment with DFT results for the most prominent vibrations of* ***1***$^{+}$***.*** *Selected values for* ***2***$^{+}$ *are given in parentheses.*[116]

	$\tilde{n}$ /cm^{-1}	$\tilde{n}$ DFT /cm^{-1}	D	$l_{v,i}$ /cm^{-1}	Vibrational assignment[i]
IR	1585	1603 a_u			C=C stretch/ phenyl e_{2g}^{a}, phenylene e_{1u}^{a}
		1595 b_u			C=C stretch/ phenyl e_{2g}^{a}
		1588 a_u			C=C stretch/ phenyl e_{2g}^{b}
		1583 b_u			C=C stretch/ phenyl e_{2g}^{b}, phenylene e_{1u}^{b}
		1494 a_u			C=C stretch/ phenyl, phenylene e_{1u}^{a}
	1491	1486 b_u			C=C stretch/ phenyl e_{1u}^{a}, phenylene e_{1u}^{b} + C-N-C stretch
	1489	1482 a_u			C=C stretch/ phenyl, phenylene e_{1u}^{a} + sym C-N stretch
		1472 b_u			C=C stretch/ phenylene e_{1u}^{a} + asym C-N-C stretch
		1462 a_u			C=C stretch/ phenyl e_{1u}^{b},phenylene e_{1u}^{a} + asym C-N stretch
	1454	1454 b_u			C=C stretch/ phenyl, phenylene e_{1u}^{b}
	1356	1366 a_u			sym C-N-C stretch + C=C stretch/ phenyl e_{1u}^{b}
		1366 b_u			asym C-N-C + C=C stretch/ phenyl, phenylene e_{1u}^{b}
		1346 b_u			sym C-N-C stretch + C=C stretch/ phenylene e_{1u}^{b}
	sh	1328 a_u			CCH deformation + sym C-N-C stretch
	1254	1250 b_u			C-N-C stretch + CCH deformation/ phenylene e_{1u}^{b}
	1184	1190 a_u			CCH deformation/ phenyl e_{2g}^{a}, phenylene e_{1u}^{a}
		1178 b_u			CCH deformation/ phenyl e_{2g}^{a}, phenylene e_{1u}^{b}
	1161	1171 a_u			CCH deformation/ phenyl
	1150	1168 a_u			CCH deformation/ phenyl e_{2g}^{a}, phenylene e_{1u}^{a}
	1078	1092 a_u			CCH deformation/ phenyl e_{1u}^{b}
		1091 b_u			CCH deformation/ phenyl e_{1u}^{b}
	1024	1030 b_u			CCH deformation/ phenyl e_{1u}^{a}
	1001	987 a_u			phenyl trig. ring breathing + CCH deformation/ phenylene
	826	817 a_u			out-of-plane CCH deformation
	758	751 b_u			out-of-plane CCH deformation
	702	686 a_u			out-of-plane CCH deformation

Raman	**1613** (1620)	1617 a_g	0.42 (0.64)	142.3 (335)	C=C stretch/ phenyl, phenylene $e_{2g}{}^a$
		1595 b_g			C=C stretch/ phenyl $e_{2g}{}^a$
	1582	1593 a_g	0.56	248.1	C=C stretch/ phenyl $e_{2g}{}^b$, phenylene $e_{2g}{}^a$ + C-N stretch
		1586 a_g			C=C stretch/ phenyl $e_{2g}{}^b$, phenylene $e_{2g}{}^a$ + C-N stretch
		1583 b_g			C=C stretch/ phenyl, phenylene, $e_{2g}{}^b$
	1489	1488 a_g	0.25	46.5	C=C stretch/ phenyl $e_{1u}{}^a$, phenylene $e_{2g}{}^a$ + C-N-C stretch
		1484 b_g			C=C stretch/ phenyl $e_{1u}{}^a$ + C-N-C stretch
	1461	1463 a_g	0.22	35.4	C=C stretch/ phenyl $e_{1u}{}^b$ + C-N stretch + sym C-N-C stretch
		1455 b_g			C=C stretch/ phenyl $e_{1u}{}^b$, phenylene $e_{2g}{}^b$
	1365 (1368)	1337 a_g	1.20 (0.44)	982.8 (132)	sym N-Ar-N stretch
		1321 b_g			CCH deformation a_{2g} (Wilson 3, very weak usually)
		1305 a_g			sym N-Ar-N stretch
	1310 (1095)	1295 a_u			asym N-Ar-N stretch
		1197 a_g			CCH deformation/ phenyl, phenylene $e_{2g}{}^a$ + C-N stretch
	1198	1180 a_g	0.64	245.4	CCH deformation/ phenyl, phenylene $e_{2g}{}^a$ + C-N stretch
	1179	1177 a_g	0.43	109.0	CCH deformation/ phenyl $e_{2g}{}^a$
		1171 a_g			CCH deformation/ phenyl $e_{2g}{}^b$
	1166	1164 a_g			CCH deformation + phenylene ring stretch
	1030	1030 b_g			CCH deformation/ phenyl $e_{1u}{}^a$
		1028 a_g			CCH deformation/ phenyl $e_{1u}{}^a$
	1004	988 a_g			phenyl trig. ring breathing/ b_{1u}
		987 b_g			phenyl trig. ring breathing b_{1u}
	sh	971 a_g			out-of-plane CCH deformation
	928	917 a_g			phenylene ring breathing/ a_{1g} + C-N stretch
	898 (1014)	892 a_g	(0.47)	(112)	phenylene ring breathing/ a_{1g}
	839	820 a_g			out-of-plane CCH deformation
		815 b_g			out-of-plane CCH deformation
	800 RR	793 a_g			out-of-plane phenylene deformation
	770	756 a_g			ring deformation/ phenylene $e_{2g}{}^a$
	732	725 a_g			ring deformation/ phenyl, phenylene $e_{2g}{}^a$
	491 (505)	480 a_g	1.34 (0.72)	440.8 (132)	C-N-C twist + in-plane phenylene deformation

421	405 a_g			out-of-plane phenyl ring deformation
409 (405)	401 b_g	1.24 (1.07)	314.4 (232)	out-of-plane phenyl ring deformation
257	243 a_g	1.49	285.3	C-N-C (phenyl) twist + phenyl wagging
205	194 a_g			phenylene out-of-plane deformation + N-Ar-N deformation

[i] the benzene fundamentals from which the vibrational modes of **1**$^+$ are derived, [a,b] refer to the Wilson notation of the degenerate vibrations of the benzene molecule. The RR enhanced modes are marked as bold.

The medium strong band at 1004 cm^{-1} in the Raman spectrum corresponds to the trigonal phenyl ring breathing mode, which derives its intensity from the benzene ring stretch of b_{1u} symmetry. Nevertheless, this mode is Raman allowed in $\mathbf{1}^+$ since the overall symmetry of the mode is a_g or b_g (see Table 5.2) as predicted by the calculations. A shoulder at higher wavenumbers can usually be observed in monosubstituted benzene derivatives and is attributed to CCH deformation. The benzene ring breathing of a_{1g} symmetry of the phenylene unit arises as a band of comparable intensity to the trigonale ring breathing mode at 898 cm^{-1}. The shoulder at 928 cm^{-1} has been attributed based on our DFT calculations also to a phenylene ring breathing mode, but coupled to a C-N stretch vibration.

The vibrational bands at 732 cm^{-1} in the Raman spectrum and at 758 cm^{-1} in the IR spectrum have been attributed to out-of-plane CCH deformation modes. The broad band in the IR spectrum of the solid form of $\mathbf{1}^+$ at 702 cm^{-1} has been accurately predicted by the computations and is also corresponding to an out-of-plane CCH deformation mode.

The Raman spectrum could be also recorded in the low wavenumber region. The CCN deformation mode arises at 491 cm^{-1}. The band at 409 cm^{-1} is mainly due to the out-of-plane deformation of the phenyl rings.

Resonance Raman intensity analysis and the excited state molecular structure

Figure 5.4 presents the resonance Raman spectra of $\mathbf{1}^+$ in CH_2Cl_2 solution measured at 1064, 830 and 785 nm in comparison with the off-resonance spectrum recorded at 514.5 nm. Raman measurements for the neutral form **1** were also performed. These control experiments together with the non-resonant Raman measurements of $\mathbf{1}^+$ confirmed that scattering from the radical is strongly resonance enhanced if excitation wavelengths within the charge resonance band (see Fig. 5.5) are applied. Moreover, changes in the relative intensities of several bands could be observed. The vibrational mode most enhanced is the C-N stretching vibration around 1370 cm^{-1}. Other vibrational modes, including the bands at 1198, 1178, 491 (see Scheme 5.2) and 409 cm^{-1}, which highly involve the C-N stretching- and CCN deformation-motion are also significantly enhanced (Table 5.2). The symmetrical C=C stretching modes around 1600 cm^{-1} are also enhanced under resonant excitation conditions. Additionally, a vibrational mode at 1310 cm^{-1}, which was assigned to an *asymmetric* C-N stretching mode (Table 5.2, calculated at 1295 cm^{-1}), can be observed in the resonance Raman spectra, although it cannot be found in the off-resonance Raman

spectrum. Nevertheless, the assignment of this band is disputable since the DFT calculations predicted a medium strong symmetric C-N stretch vibration at 1305 cm^{-1}, which is, however, similar to the mode most enhanced under resonant excitation predicted at 1337 cm^{-1} (a_g symmetry). So far, we can conclude that the charge transfer excited-state potential surface is displaced along the above mentioned normal mode coordinates.

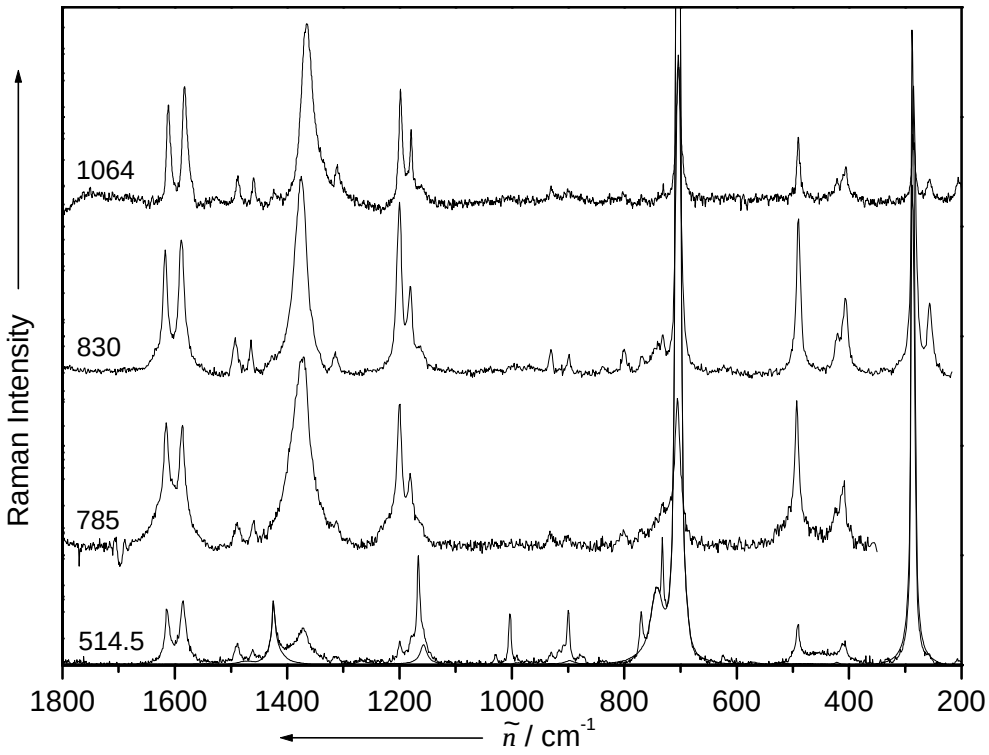

Figure 5.4. *Resonance Raman spectra of 1^+ in CH_2Cl_2 solution measured at 1064, 830 and 785 nm excitation lines (top to bottom) in comparison with the off-resonance Raman spectrum at 514.5 nm.*

Both the absorption spectra and resonance Raman spectra contain information about the excited state potentials. The time-dependent treatment[38-40] of electronic and vibrational spectroscopy quantifies the absorption and resonance Raman cross sections, and thus the quantitative analysis of the absorption and resonance Raman spectra allows the dimensionless displacement parameters *D* to be determined (see Chapters 2.1 and 3.3). The displacements are a measure of how far along a particular normal mode the molecule in one electronic state has to move in order to reach the geometry of the excited electronic state.[44] Generally, these are illustrated in one-dimensional representations of the potential

energy surfaces along a normal mode where the distance between the minima of the parabolas is *D* (see Fig. 2.3).

The absorption and resonance Raman cross sections are given within the time-dependent theory[38-40] as a full Fourier transform and a half Fourier transform of the Franck-Condon factor, respectively[16-18,24,36] (see Chapter 2.1 for a detailed discussion). Mode specific information about the vibrational modes involved in the electronic transition can be obtained by simultaneously modeling both the resonance Raman intensity profiles and the absorption spectrum. Knowing the vibrational characteristics (from theoretical vibrational analysis; see Table 5.2) and the dimensionless displacement parameters *D* of the resonance enhanced vibrational modes, the latter can be converted into absolute bond distorsions[48,141-143] (see Eq. 3.17). However, these depend on the sign of *D*, while the vibrational reorganization energies can be calculated directly from the *D*s and the corresponding wavenumbers (see Eq. 2.56).

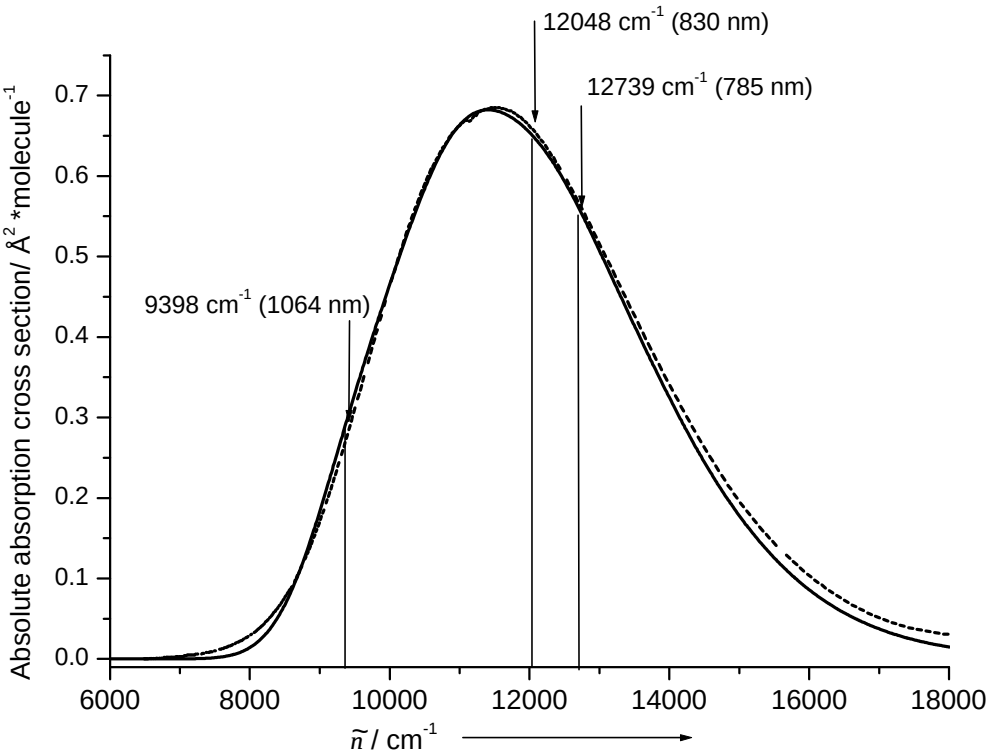

Figure 5.5. *Absorption cross section of 1^+ (dashed line) and the calculated spectrum (solid line). The excitation lines used in the resonance Raman measurements are marked.*

Raman cross sections for the most RR enhanced vibrational modes (see Table 5.2) were determined by integrating over the respective bands and calculating the ratio of this value and the area of the CH_2Cl_2 band at 702 cm^{-1} of known cross section[48,63] which was used as an internal standard (see Eq. 3.10). Band deconvolution was performed where necessary.

Correction for self-absorption was made as described in Chapter 3.3 for the back-scattering geometry[50,144]. Following the general computational strategy described by Myers[14,17] and outlined in Chapter 2.1 and 3.3, the absorption and differential Raman cross sections of the symmetrical RR enhanced modes marked in bold in Table 5.2 were simulated. The mode of very low intensity at 1310 cm^{-1}, which is most likely an asymmetrical N-Ar-N stretching vibration has not been considered for the calculations since we lack the machinery to treat asymmetrical modes. The theoretical absorption and Raman cross sections for the symmetrical modes were calculated using the same input parameters. Harmonic ground and excited state potentials with equal force constants were considered. Within the Condon approximation, the derivatives of the transition dipole moment with respect to the vibrational coordinates were set to zero. A temperature of 298 K and no thermal population of higher vibrational levels of the electronic ground state were assumed. The electronic zero-zero energy as defined in Fig. 2.3 for a symmetrical mode, E_{00}, which was estimated from the absorption spectrum and slightly modified during the fitting procedure, amounts 8300 cm^{-1}. A small amount of static inhomogeneous broadening (250 cm^{-1}) corresponding to the zero-zero energy shifts had to be included, in order to suppress any vibrational feature in the absorption spectrum (see Chapter 2.1).

The solvent induced broadening was taken into account in terms of a single overdamped Brownian oscillator model[23,47] (see Chapter 2.1) and no damping due to the lifetime decay has been taken into account. The solvent induced "homogeneous" broadening G_0 amounts 1180 cm^{-1}, which corresponds[23,48] to a classical reorganization energy of l_s = 628 cm^{-1} (see Eqs. 2.50 and 2.51). The displacement parameters for the RR enhanced symmetrical modes are summarized in Table 5.2. The calculated vibrational reorganization energies for these vibrational modes are also listed.

Figure 5.5 shows that an excellent fit for the charge resonance absorption band shape could be obtained. The resonance Raman excitation profiles obtained for the most enhanced symmetrical modes with the parameters listed in Table 5.2 are presented in Figure 5.6. The absolute differential Raman cross section of the mode at 1365 cm^{-1} is the

largest. This mode presents an intensity larger by a factor of 3 up to 10 compared to the other vibrational modes under resonant conditions. Several points concerning the resonance Raman data are worth noting (see Table 5.2): A recent resonance Raman study of an organic mixed-valence system performed by Williams *et al.*[129] based on the same procedure like the one applied in the study presented here, reported very good simulations for both the absorption and the relative Raman cross sections. However, the absolute Raman scattering cross sections were roughly an order of magnitude higher than those measured experimentally. The calculations were done on the diabatic surfaces of a symmetrical, localized charge-transfer system. In order to gain insight into the underlying Raman cross section problem, Williams *et al.*[129] approximated the upper and lower adiabatic surfaces with inequivalent, vertically displaced parabolic surfaces. However, under these conditions they found that the upper state wavenumbers were three times larger than the ground state ones, which independent of other considerations leads to smaller calculated Raman cross sections. Adjusting all the parameters to such a harmonic potential energy diagram model, Williams *et al.* obtained Raman cross sections close to the experimental data. However, the absorption spectrum still could not be modeled exactly. The study of Williams *et al.*[129] showed rather convincingly that the discrepancies between the theoretical analysis and the experimental data lies in the unique shapes of the surfaces of a localized IV-CT system. In contrast, for a delocalized system (**1**$^+$), a very good fit for both absorption and Raman cross sections could be obtained modeling the ground and excited state potential surfaces with equivalent harmonic surfaces.

High displacement parameters were obtained for the vibrational modes in the low wavenumber region. The twisting of the phenyl groups at 257 cm^{-1} and the CNC deformation at 491 cm^{-1} which involves the axial C-N bonds have the highest distortion. However, the displacement of the symmetric C-N stretching along the bridge (Scheme 5.2) is also bigger than one. This mode at 1365 cm^{-1} has the largest displacement of all the stretching modes. The vibrational reorganization energies are proportional to the vibrational wavenumbers (see Eq. 2.56). Therefore, the reorganization energy involved in the symmetric C-N stretching mode is found to be the largest. The sum of the reorganization energies of all symmetrical vibrations that we were able to observe is about 2850 cm^{-1}.

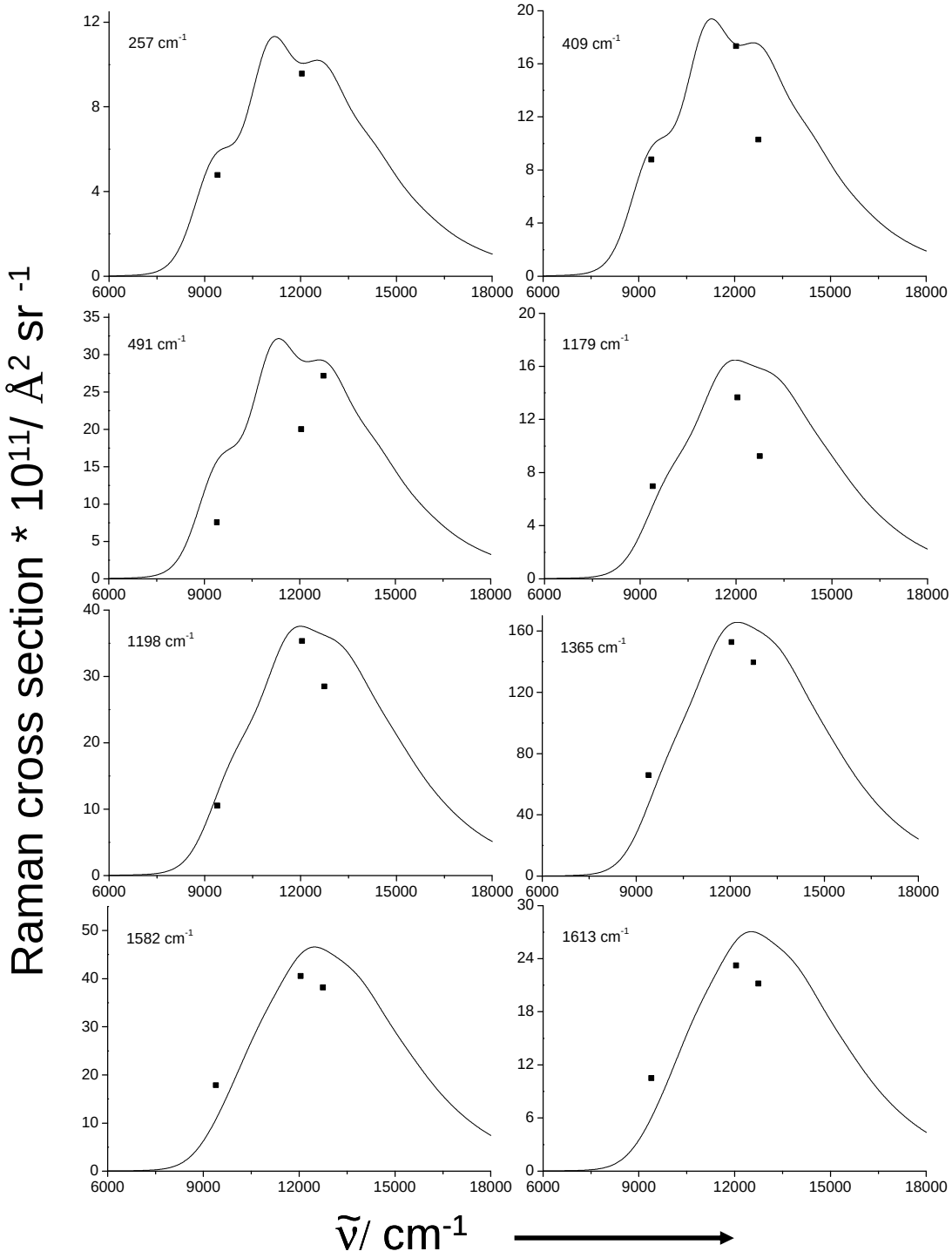

Figure 5.6*. Experimental differential Raman cross sections and the calculated resonance Raman excitation profiles for the eight vibrational modes that are most enhanced.*

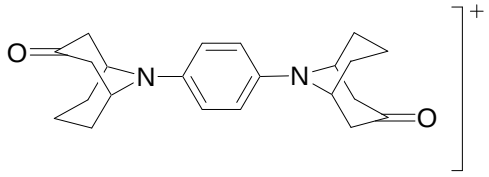

2$^+$

These results can be compared with those recently obtained by Bailey *et al.* for a strongly coupled *p*-phenylenediamine **2**$^+$ radical cation derivative.[116] In contrast to **1**$^+$ the radical cation **2**$^+$ shows an absorption band with strong vibrational progression. For system **2**$^+$ the C=C stretch motion coupled with N-Ar-N stretching at 1620 cm^{-1} has the largest vibrational reorganization energy (see Table 5.2). In our system the symmetric C=C stretching is split into two modes at 1613 and 1582 cm^{-1}. The sum of the vibrational reorganization energies of these two modes is ca. 390 cm^{-1}, which corresponds to the 335 cm^{-1} value obtained in this vibrational region by Bailey *et al.*[116] for the corresponding mode. Much in contrast, the C-N stretching mode at 1365 cm^{-1} along the bridge shows the largest displacement and the largest contribution to l_v in **1**$^+$ but has much less intensity in the *p*-phenylenediamine derivative **2**$^+$ probably due to substituent effects. The minimal total vibrational reorganization energy for **1**$^+$ is, however, a factor of two larger than for the *p*-phenylenediamine derivative reported by Bailey *et al.*

The fit of the resonance Raman and the absorption cross sections obtained within this studies yields $l_v \approx 2850$ cm^{-1} and $l_s \approx 630$ cm^{-1}, which are the total vibrational reorganization energy and the solvent reorganization[23] energy, respectively. The sum of these reorganization energies ($\hat{=}$ 3480 cm^{-1}) compares very well with the reorganization energy L = 4080 cm^{-1} of the symmetric mode obtained from the Marcus-Hush analysis carried out in the group of Prof. Lambert. Together with E_{00} (= 8300 cm^{-1}) the sum of λ_v and λ_s (= 11780 cm^{-1}) agrees very well with the optical transition energy ($\tilde{\nu}_{max}$ = 11580 cm^{-1}):

$$\tilde{\nu}_{max} = E_{00} + l_v + l_s . \qquad (5.1)$$

Furthermore, the solvent reorganization energy obtained from the analysis of the observed resonance Raman intensities is quite small. The obtained value of $l_s \approx 630$ cm^{-1} is an upper limit and is more properly labeled as the classical reorganization energy since it may contain contributions from low-wavenumber vibrational modes that were not observed in the resonance Raman spectra. Such a mode at 205 cm^{-1} due to the out-of-plane deformation

of the phenylene ring could be noticed in the spectrum recorded at 1064 nm. Barbara *et al.*[124] determined from resonance Raman data the classical reorganization energy for localized inorganic mixed-valence compounds in deuterated glycerol and water. The results of Barbara *et al.*[124,145] showed that the solvent induced broadening of the absorption band is significant if the dipole moment of the solute changes upon optical excitation. The classical reorganization energy for localized MV systems obtained from RR data was in the range of 3300-3700 cm^{-1}, which is considerably higher than the value obtained for $\mathbf{1}^+$. The small contribution of the solvent to the reorganization energy and its small influence on the charge transfer process is again a strong evidence for a delocalized system.

A theoretical analysis of Talaga and Zink about the effects of bond length changes and electronic coupling on the intensities of the symmetric and asymmetric modes in absorption and resonance Raman[121] spectra has shown that the symmetric mode intensity increases with increasing D_{coup} which is equivalent to the linear coupling constant l_y of the averaged symmetrical mode considered in the Marcus-Hush analysis. This parameter is a measure of the change in coupling as the molecule vibrates along the symmetric coordinate. Starting from a coordinate-displaced model for the potentials of interacting electronic states for a localized system, Talaga and Zink showed that as the sites move close together, the coupling increases. Talaga and Zink concluded that when the coupling (D_{coup}) is even larger in the direction of increasing valence delocalization, the symmetric modes become the most intense and their contribution to the spectra is more important. This behaviour has also been found in the study of Bailey *et al.*[116] for a strongly delocalized system $\mathbf{2}^+$.

Within the framework of a dynamic vibronic model[118] developed by Coropceanu *et al.* to describe the CT electronic spectra it could be shown that the diagonal coupling elements of the vibronic Hamiltonian lead to displacements of the ground vs. excited state adiabatic potentials along symmetric modes. The effect of symmetric vibrational modes on the absorption band shape of delocalized mixed-valence systems was also recognized previously by Hush,[146,147] Piepho,[148] Schatz *et al.*,[102,149] and Ondrechen.[150,151] In the strong coupling limit, the absorption lineshape is *controlled* by the symmetric modes. Our resonance Raman data in connection with the crystal structure analysis and DFT calculations for $\mathbf{1}^+$ are in agreement with the prediction made by Hush[146] that in general more than one symmetric vibration is involved into the electronic transition, and that the primary symmetric mode was that formed by coupling the donor-bridge and bridge-

acceptor stretch modes. Such a mode provides an apparent vibration in the donor-acceptor separation, and was identified as the symmetric C-N stretch at 1365 cm^{-1} in the case of $\mathbf{1}^+$ (Scheme 5.2). Nevertheless, for $\mathbf{1}^+$ several symmetric vibrational modes are involved in the CT transition. This can probably be explained by an additional coupling of the monosubstituted benzene rings to the electronic transition. Therefore, a closer examination of the molecular orbitals of $\mathbf{1}^+$ is important to understand the charge transfer process and the vibrational modes involved.

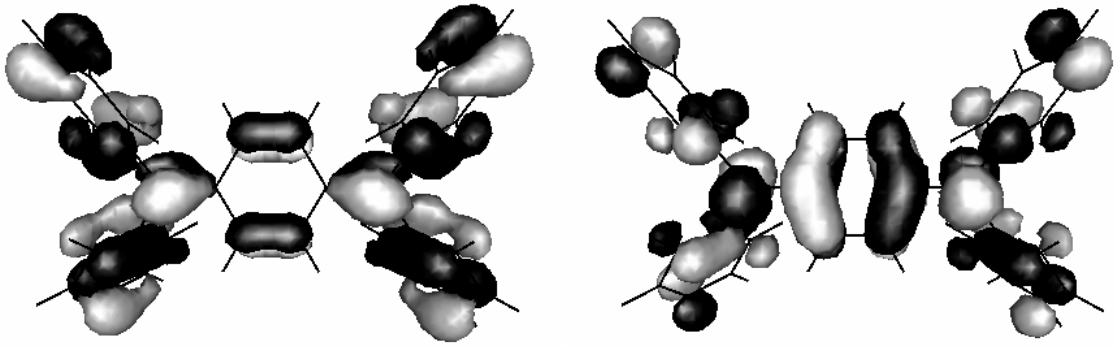

HOMO−1 (B_u) SOMO (B_g)

Figure 5.7*. Contour plot of the molecular orbitals HOMO-1 and SOMO of* $\mathbf{1}^+$ *and their symmetries for a centrosymmetric molecular structure.*

Theoretical calculations performed by Coropceaunu *et al.*[152] within the framework of a single configuration interaction for *N,N,N',N'*-tetrakis(4-methoxyphenyl)phenylenediamine showed that the CT transition is dominated by a HOMO−1 → SOMO electron excitation. In the case of $\mathbf{1}^+$, the HOMO−1→ SOMO transition involves an excitation of an electron from a CN bonding to an antibonding orbital (see Fig. 5.7) leading to a lengthening of the CN bond caused by the N-Ar-N stretch vibration observed around 1370 cm^{-1}. The fact that this vibrational mode presents a very high displacement parameter indicates a significant geometrical change of this bond in the excited state. Furthermore, the orbital coefficients of the phenyl units are bigger in the HOMO−1 orbital than in the SOMO. This indicates that vibrational modes involving the phenyl units are also coupled to the electronic transition.

As described in Chapter 3.3, the dimensionless displacements can be converted into bond length and angle changes (see Eq. 3.14). However, the high number of vibrational modes involved into the charge resonance transfer makes it difficult to determine the

effective bond length changes.[16,17,48] However, taking into account the considerations given above, the sign of the displacement parameters, which result in the lengthening or the shortening of the bonds, can be deduced. The mode at 1365 cm^{-1} induce alone a lengthening of 0.038 Å of the axial N-C (d) bonds.

The difficulty in converting the dimensionless displacement parameters in bond length and angle changes consists, however, not only in their signs but also in selecting the vibrational mode coordinates. In the case of the C=C stretch 5 sets of calculated coordinates could be taken into consideration for the two experimental Raman bands. Nevertheless, similar bond changes were obtained if the 1593 cm^{-1} or 1595 cm^{-1} vibrations were considered for the 1582 cm^{-1} band. Hence, the calculation of the bond changes led to a lengthening of the axial N-C bonds by 0.05 Å, a shortening of the C1-C2 bonds by 0.018 Å and a lengthening of the C2-C3 bonds by 0.015 Å. A significant change of the N-C7 bonds has been determined (0.021 Å). Changes of the phenyl ring bonds of less than 0.01 Å are predicted upon optical excitation.

Conclusion

The resonance Raman experiments showed that at least eight vibrational modes are strongly coupled to the optical charge resonance band. With the help of a DFT based vibrational analysis, these modes were assigned mainly to symmetric vibrations. The resonance Raman intensity analysis allowed us to obtain mode-specific information about the excited-state potential energy surface even if the direct electronic absorption spectrum of $\mathbf{1}^+$ is completely diffuse. The vibrational reorganization energies for symmetrical modes were also quantified and the bond length changes upon optical excitation have been evaluated. The contribution of the symmetric vibrational modes to the reorganization energy is dominant. These findings are in agreement with the conclusions from the simple two-state two-mode Marcus-Hush analysis. In particular, quantitative agreement between the reorganization energy of the symmetric modes was obtained from both analyses. However, in contrast to the analysis of the resonance Raman data the asymmetric mode is also essential for a proper description of the absorption spectrum within the Marcus-Hush treatment. Nevertheless, according to this semiclassical analysis the ET barrier is tiny. The excellent agreement of the X-ray crystal structure analysis and the DFT computed molecular structure of $\mathbf{1}^+$ on the one hand as well as the solvent and solid state IR spectra and the DFT calculated IR active vibrations on the other hand prove $\mathbf{1}^+$ to adopt a

symmetrical delocalized Class III structure both in the solid state and in solution. Despite close structural resemblance of $\mathbf{1}^+$ and of $\mathbf{2}^+$ their absorption spectra are quite different; while $\mathbf{1}^+$ shows a broad asymmetric band that of $\mathbf{2}^+$ displays a distinct vibrational progression. This difference can be traced back to a different degree of mode contribution to the absorption spectra.

Chapter 6

The Ground and Excited State Molecular Structure of a Thiophene Derivative, Solvent Effects

*This chapter reports on a vibrational spectroscopic study of a model organic photorefractive thiophene derivative synthesized in the group of Prof. Würthner, 2-(diethylamino)-5-(2',2'-dicyanovinyl)-thiophene (**1**). Such a push-pull chromophore exhibits a significant solvatochromic effect. Quantum chemical calculations for the ground and excited state structure were carried out. The optimization of the excited state structure using the configuration interaction with single excitations method showed that the contribution of the zwitterionic species is increasing with respect to that of the neutral form. Raman and resonance Raman spectra of (**1**) were recorded and the vibrational assignment was carried out based on DFT and PED calculations. Several modes are Franck-Condon active. These are mainly corresponding to stretching modes along the bonds connecting the donor and acceptor moieties; however the S-C stretching mode is also enhanced. Further theoretical analysis is required to determine the experimental displacement parameters as a function of solvent polarity in order to understand the dependence of the excited state on the solvent environment.*

Motivation

Photorefractive materials have large applicability in telecommunications, optical computing, data storage and optical signal processing. The photorefractive effect (optical modulation of the index of refraction) consists in the persistent but reversible spatial modulation of the refractive index due to the charge redistribution in an optically nonlinear material. The effect arises when charge carriers, photogenerated by a spatially modulated light intensity, separate by drift or diffusion processes and become trapped to produce a non uniform space-charge distribution[153]. The internal space-charge electric field resulting due to Gauss' law, modulates the refractive index to create a phase grating which can diffract a light beam.

The development of organic materials with large second–order nonlinear optical (NLO) response raised significant interest since 1990, when the first doped nonlinear organic crystal was grown[154], because the use of organic systems may present several advantages over inorganic crystals. For organic materials, the nonlinearity is a molecular property arising from the asymmetry of the electronic charge distributions in the ground and excited states, while for inorganic systems it is caused by the large ionic polarizability. As a consequence, a higher performance for organic photorefractive materials (crystals and polymers) is expected. On the other hand, polymeric materials can be easily doped with various molecules and the technical processing of polymers is much easier than the treatment of crystals[153,155-157].

Organic photorefractive compounds are characterized by a photoionizable charge generator, a transporting medium, trapping sites, and a dependence of the index of refraction upon space-charge field[153]. These requirements are accomplished in typical organic NLO compounds by bridging a donor and an acceptor moiety by a *p*-conjugated linker[158]. Polyenes and polyynes show low thermal and chemical stabilities. Therefore, aromatic and heteroaromatic rings are preferred as linking bridges[48,153,155,157,159-163]. In particular, thiophene derivatives[156,158,164-167] have attracted widespread interest because their linear and nonlinear optical properties are superior to those of the corresponding aryl analogues. Several theoretical and experimental studies report on the nonlinear properties of thiophene ring containing donor-acceptor systems[156,158,164-167].

In second-order NLO materials, there is a charge transfer from the donor to the acceptor moiety across the *p*-bridge. For donor-acceptor derivatives or so called "push-

pull" chromophores, the ground and lowest excited states are often described as a linear combination of a neutral structure having zero or small formal charges on the donor and acceptor units[48], and a zwitterionic species. In general, the ground state predominantly corresponds to the neutral form, while the lowest excited state is zwitterionic. The lowest electronic transition corresponds to the charge-transfer process between these states. The aromatic delocalization energy (ADE) of the aromatic or heteroaromatic bridge influences the mixing of the ground and charge transfer states. Decreasing aromatic delocalization energy results in increased mixing of the two states, leading to increased polarizability and hyperpolarizability. The aromatic delocalization energy of thiophene is lower than the ADE of benzene (54 kJ/mol versus 67 kJ/mol)[168]. Therefore, the mixing of the neutral and zwitterionic states in thiophene derivatives is expected to be larger than for the benzene analogues.

The mixing of the neutral and zwitterionic states and consequently the nonlinear properties of the material depend on the local environment of the system. The electronic absorption maxima of push-pull chromophores strongly shifts with increasing polarity and polarizability of the solvent. Furthermore, for technical applications, the NLO materials are embedded into polymers[153]. Therefore, it is of interest to investigate the specific changes in the properties of model photorefractive systems as a function of the solvent environment. In general, the electronic absorption and fluorescence spectra of such systems are completely diffuse. Hence, it is difficult to extract information on the excited state from absorption and fluorescence measurements. Resonance Raman spectroscopy proved to be an adequate method to investigate charge transfer systems in order to gain mode specific information on the charge transfer process. Moreover, a quantitative analysis of the Raman intensities in conjunction with the absorption data allows one to determine the solvent contribution to the reorganization energy[17,18,24]. Several inorganic and a few organic intervalence charge transfer (IV-CT) systems have been studied[16]. Myers Kelley and coworkers investigated aromatic push-pull chromophores and charge-transfer systems in different solvent environments and quantified the vibrational and solvent reorganization energies upon photoexcitation[47,48,141,142].

In this study, a detail structural and vibrational analysis of 2-(diethylamino)-5-(2',2'-dicyanovinyl)-thiophene (**1**) by means of Raman and resonance Raman spectroscopy and quantum chemical calculations is presented. The ground state molecular structure was calculated with DFT methods and the excited state geometry was optimized at the CIS

level of theory. The Franck Condon parameters were determined from theoretical calculations. The vibrational analysis of (**1**) was carried out based on potential energy distribution calculations. Resonance Raman spectra in several solvents were recorded using excitation lines within the charge-transfer band and a quantitative intensity analysis by means of time-dependent propagation methods of these data is currently being under progress.

The calculated ground and excited state molecular structures

The theoretical calculations showed that at least two conformers correspond to minima on the ground state potential surface. Scheme 6.1 depicts the structure of these two conformers, as well as two resonance forms of (**1**) corresponding to the neutral species and the zwitterionic one. The negative charge is probably delocalized on the acceptor dicyanovinyl group. ZINDO calculations[158] showed that the molecular hyperpolarizability b of (**1**) is about 1.6 times larger than that of the corresponding aryl derivative. On the other hand, derivatives where the acceptor group is a dicyanovinyl unit have a higher hyperpolarizability than the corresponding NLO compounds with a nitro group as acceptor. The calculated maximum of the electronic absorption for the gas phase[158], of $l_{max} = 407$ nm, approaches the experimental value measured in cyclohexane solution (449 nm) (see Fig. 6.1). In more polar and polarizable solvents, the maximum of the absorption spectrum of (**1**) shifts toward higher wavelengths, since the ground state geometry of (**1**) becomes more polar. With an increasing contribution of the zwitterionic form to the ground state, the ground and excited states are more alike and the energy difference between the states is decreasing. Moreover, while the absorption spectrum of (**1**) measured in cyclohexane shows a weak vibronic structure, the spectrum recorded in dichloromethane is completely featureless. However, the solubility of (**1**) in cyclohexane is much lower than in dioxane or dichloromethane indicating that the ground state of (**1**) in cyclohexane is also quite polar and that the mixing of the neutral and zwitterionic species in the ground state is significant. This is in agreement with the fact that thiophene has a lower ADE than benzene (see above) and therefore a strong mixing between the states is expected. The charge transfer process for (**1**) is characterized by a very high molar extinction coefficient (ca. 80000 L mol^{-1} cm^{-1}).

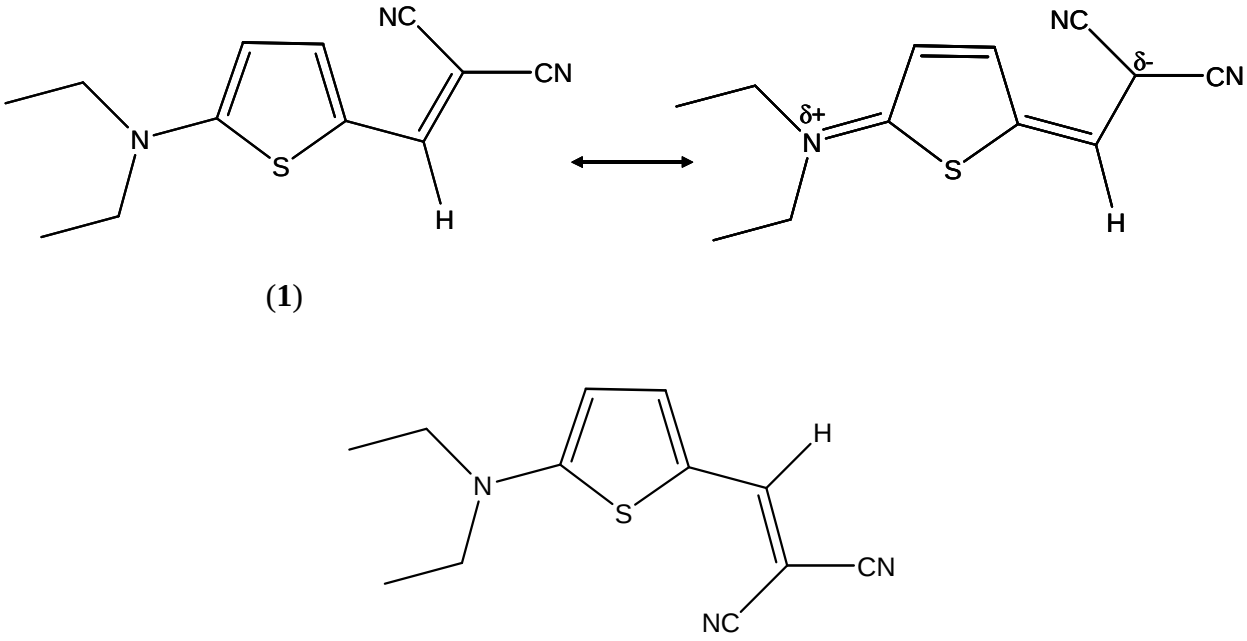

Scheme 6.1. *Neutral and zwitterionic structures of 2-(diethylamino)-5-(2',2'-dicyanovinyl)-thiophene (**1**). The structures of two conformers (**1**) and (**1'**) are presented.*

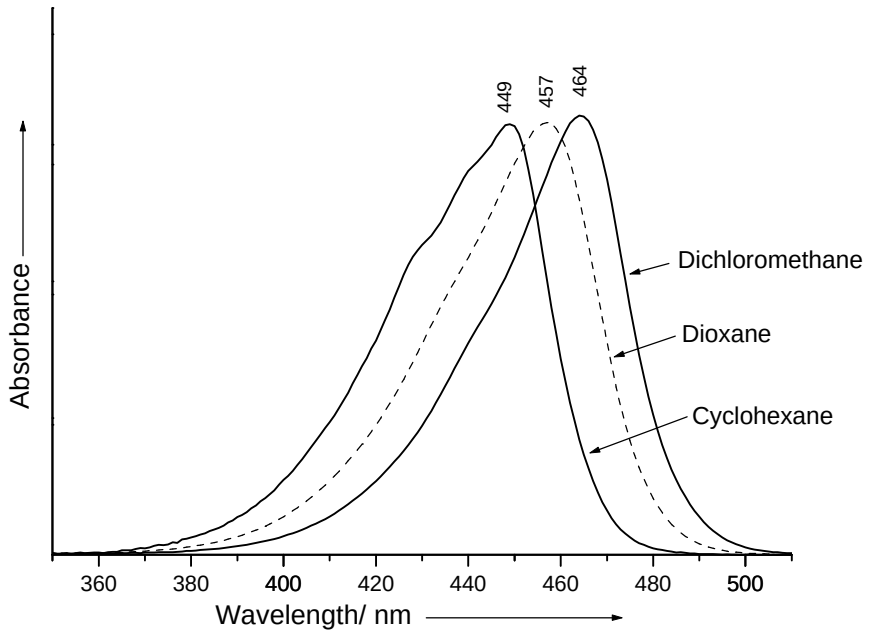

Figure 6.1. *UV-VIS absoption spectra of (**1**) in different solvent environments as indicated.*

In order to get insight into the molecular structure of (**1**), we carried out DFT calculations for its molecular ground state and CIS calculations for the first excited state. Figure 6.2 presents the optimized molecular geometry for the most stable conformer of (**1**) and the corresponding atom numbering. The other conformer (see Scheme 6.1) seems to be stabilized by an intramolecular H-bond, but its π-electron delocalization is probably reduced. The BPW91/6-31+G(d,p) level of theory predicted a very small energy difference between these two conformers, 2.161 kJ/mol for the gas phase. Unfortunately, no crystal structure analysis of (**1**) is available. However, in solution any or possibly both structure may be present.

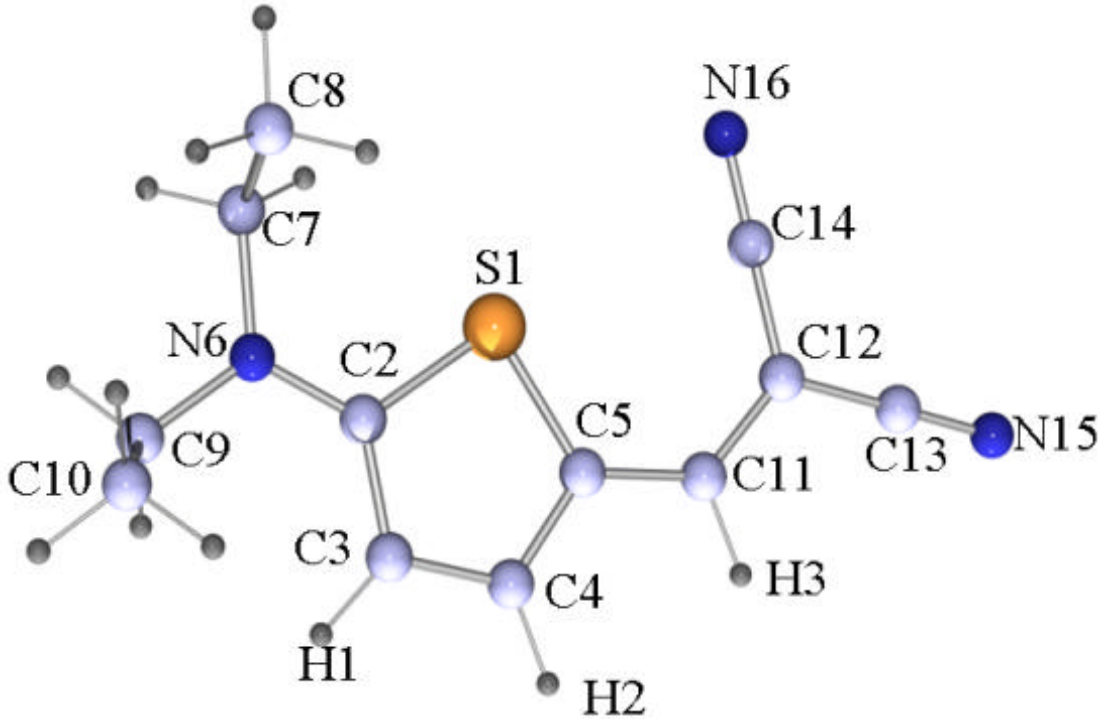

Figure 6.2*. Optimized molecular structure and atom numbering of (**1**).*

Table 6.1 lists selected structural parameters of the most stable conformer. Theoretical calculations for the other species are currently under way. The ground state structure was optimized using several functionals and basis sets (BPW91 and B3LYP, 6-31G(d,p), 6-31+G(d,p) and 6-311+G(d,p). The bond lengths obtained with the BPW91 functional are slightly larger than those predicted by the B3LYP functional. The ground state parameters obtained for a related dithiophene derivative, 5-dimethylamino-5'-nitro-2,2'-dithiophene[169], are also included. The calculated bond lengths of (**1**) are comparable to those of the related dithiophene. Moreover, the crystal structure analysis showed the

dithiophene to be almost planar and the theoretical calculations carried out in this study also predicted derivative (**1**) to adopt an almost planar structure. Interestingly, when a planar geometry was constrained, the calculations predicted two imaginary wavenumbers indicating a minimum of higher order. The imaginary modes correspond to the out-of-plane deformation of the Et_2N moiety suggesting, that this group and most of all the sp^3 hybridization of the N-atom is responsible for the non-planarity. Nevertheless, the dihedral angle C7N6C2C3 (see Fig. 6.2) deviates only slightly from planarity (by ca. 3 degrees depending on the applied level of theory). However, the most interesting results concern the molecular changes between the ground and excited state structures.

*Table 1. Selected parameters of the optimized ground and excited state molecular structures of **(1)**. d corresponds to the difference between the calculated excited state parameters and the ground state data obtained at the B3LYP/6-31+G(d,p) level of theory. * denotes the corresponding bond lengths obtained for the crystal structure analysis of a related bithiophene derivative.*

Bond length (pm)	Ground				Excited	
	BPW91		B3LYP		CIS	δ
	31+Gd,p	311+Gd,p	31Gd,p	31+Gd,p	6-31Gd,p	(pm)
S1-C2	176.5	176.3	175.9	176.0	176.6	+0.6
S1-C5	177.9	177.8	177.4	177.4	177.5	+0.1
C2-C3	141.2	140.9	140.4	140.2	140.5	+0.3
C2-N6	**136.3**	**136.0**	**135.7**	**135.8**	**134.1**	**-1.7**
C3-C4	**140.1**	**139.8**	**139.8**	**139.7**	**137.9**	**-1.8**
C4-C5	**140.6**	**140.2**	**139.6**	**139.3**	**141.9**	**+2.6**
C5-C11	**141.3**	**141.0**	**141.1**	**141.1**	**139.3**	**-1.8**
N6-C7	147.3	147.1	146.9	146.8	146.3	-0.5
N6-C9	147.3	147.2	146.9	146.8	146.1	-0.7
C7-C8	153.8	153.6	153.4	153.3	152.9	-0.4
C9-C10	153.8	153.6	153.4	153.3	152.9	-0.4
C11-C12	**139.6**	**139.1**	**138.3**	**138.1**	**140.1**	**+2.0**
C12-C13	142.9	142.5	142.9	142.8	142.5	-0.3
C12-C14	142.7	142.2	142.6	142.6	142.0	-0.6
C13-N15	**117.9**	**117.0**	**116.6**	**116.5**	**114.1**	**+2.4**
C14-N16	**117.9**	**117.1**	**116.6**	**116.6**	**114.3**	**+2.3**

* C2-C3 138.3, C2-N6 135.6, C3-C4 140.2, C4-C5 137.2 and C5-C’ $^{(Thiophene)}$ 143.8 pm.

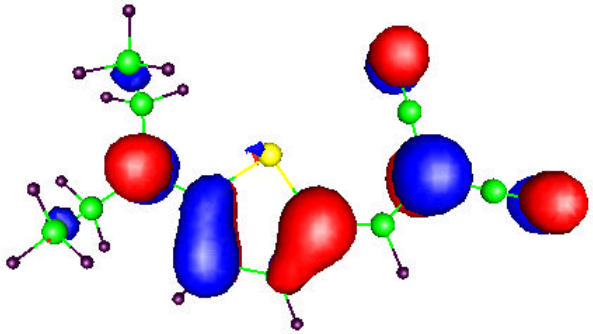

HOMO

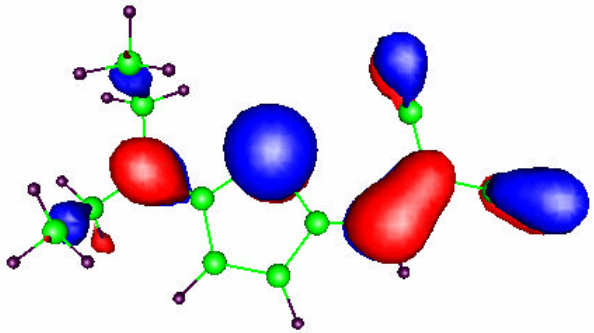

HOMO-1

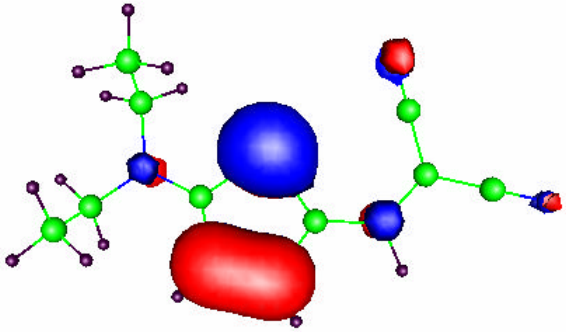

HOMO-2

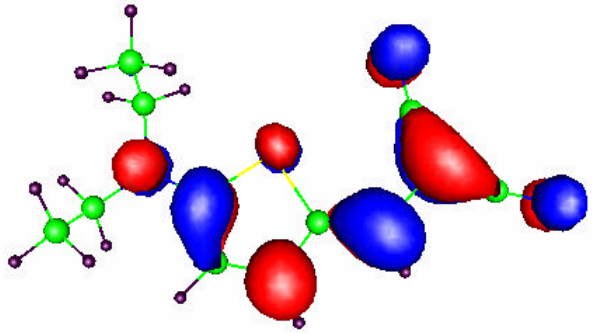

LUMO

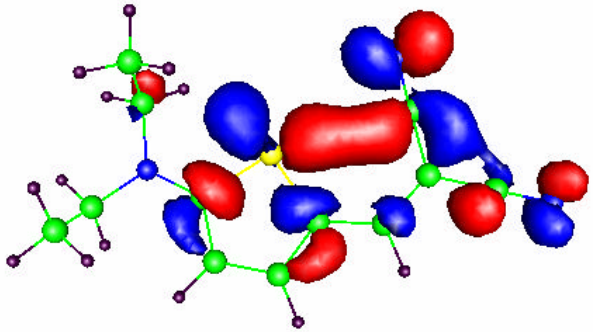

LUMO+1

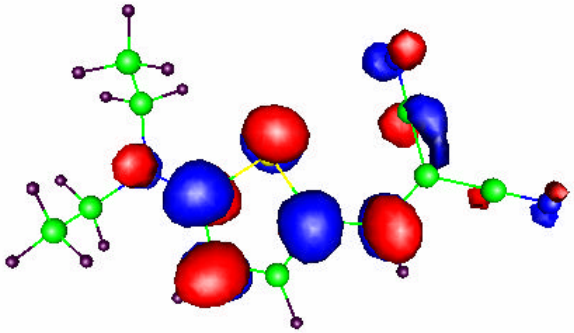

LUMO+2

***Figure 6.3**. Plot of the valence molecular orbitals of (**1**) for an isosurface value -0.05 to +0.05.*

*Table 6.2 Experimental and calculated vibrational wavenumbers (cm^{-1}) of (**1**) and their vibrational assignment. The Franck-Condon parameters obtained through quantum chemical calculations (in parenthesis next to the calculated wavenumbers) are also listed.*

FT-Raman	BPW91		B3LYP	Vibrational Assignment with the calculated PED (%) in parenthesis
	6-31+G(d,p)	6-311+G(d,p)	6-31+G(d,p)	
3114vw	3190 (0.34)	3172 (0.25)	3255 (0.05)	νC4-H2(95)
	3154 (0.05)	3137 (0.02)	3212 (-0.14)	νC3-H1(95)
	3117 (0.17)	3099 (0.13)	3175 (-0.03)	νC11H3(98)
3073vw	3088 (0.19)	3070 (0.22)	3138 (0.12)	$\nu^{as}C10H_3(47) + \nu^{as}C8H_3(47)$
	3086 (-0.52)	3067 (-0.56)	3134 (-0.21)	$\nu^{as}C10H_3(46) + \nu^{as}C8H_3(47)$
	3074 (-0.10)	3056 (-0.05)	3123 (0.22)	$\nu^{as}C10H_3(52) + \nu^{as}C8H_3(47)$
	3072 (1.26)	3054 (1.22)	3120 (1.40)	$\nu^{as}C10H_3(43) + \nu^{as}C8H_3(53)$
3007vw	3039 (0.39)	3024 (0.31)	3100 (0.28)	$\nu^{as}C7H_2(86)$
	3031 (0.05)	3014 (0.01)	3092 (0.08)	$\nu^{as}C9H_3(87)$
2969vw	2996 (-0.84)	2985 (-0.84)	3053 (-0.07)	$\nu^{s}C10H_3(55) + \nu^{s}C8H_3(44)$
	2995 (-0.30)	2984 (-0.17)	3052 (-0.76)	$\nu^{s}C10H_3(44) + \nu^{s}C8H_3(55)$
2939w	2988 (0.37)	2977 (0.31)	3050 (0.35)	$\nu^{s}C7H_2(95)$
	2981 (0.18)	2970 (0.16)	3049 (-0.05)	$\nu^{as}C9H_2(96)$
2203ms	2232 (0.82)	2231 (0.73)	2321 (0.6)	νC13-N15(63) + νC14-N16(25) (in-phase)
2192vs	2210 (0.30)	2209 (0.24)	2302 (0.23)	νC13-N15(25) + νC14-N16(61) (out-of-phase)
1577vs	1577 (-0.08)	1572 (-0.07)	1619 (-0.11)	νC12-C11(30) + νC11-C5(28) + νC5-C4(7) + δCC-H3
1517m	1523 (0.27)	1517 (0.13)	1554 (-0.03)	νC2-N6(35) + νC4-C5(17) + νC11-C12(9)
1484vw	1496 (0.03)	1488 (0.14)	1535 (0.21)	νring(61) + δCC-H1(18) + νC11-C12(8)
sh	1471 (-0.15)	1466 (-0.13)	1511 (0.16)	$\delta^{as}CH_3(41(C8),19(C10)) + \delta^{scis}C7H_2(16)$
	1463 (0.58)	1458 (0.58)	1508 (0.66)	$\delta^{as}CH_3(43(C10),18(C8)) + \delta^{scis}CH_2(14(C9),12(C7))$
	1460 (0.07)	1454 (0.02)	1502 (-0.10)	$\delta^{as}CH_3(30(C8),41(C10)) + \delta^{scis}C7H_2(17)$
1448w	1456 (-0.11)	1449 (-0.09)	1498 (0.25)	$\delta^{scis}C7H_2(41) + \delta^{as}CH_3(19(C8),17(C10)) + \delta^{scis}C9H_2(6)$
1441m	1451 (-0.23)	1446 (-0.27)	1493 (-0.10)	$\delta^{as}CH_3(54(C8),30(C10)) + \delta^{scis}C9H_2(5)$
	1444 (-0.17)	1439 (-0.16)	1490 (-0.06)	$\delta^{scis}C9H_2(64) + \delta^{as}C10H_3(15) + \delta^{scis}C7H_2(8)$
1400w	1400 (0.20)	1395 (0.20)	1439 (0.02)	$\nu ring(46) + \delta^{in}CC\text{-}H2(20) + \nu C2\text{-}N6(8) + \nu C11\text{-}C12(5)$

1385vw	1375 (0.65)	1368 (0.64)	1421 (0.60)	$\delta^{s}CH_3$(52(C8),31(C10), in-phase)
1379vw	1370 (0.60)	1363 (0.68)	1416 (0.53)	$\delta^{s}CH_3$(53(C10),30(C8), out-of-phase)
	1350 (0.74)	1348 (0.60)	1396 (-0.82)	$\delta^{wag}CH_2$(34(C7),34(C9), in-phase) + νring
1350sh	1342 (-0.10)	1339 (0.02)	1385 (-0.50)	νC11=C12-C13(21) + νC2-C3(7) + νN6-C7(6) + $\delta^{twist}C9H_2$(14) + δ^{in}CC-H3(13) + $\delta^{wag}C7H_2$(9)
1342w	1335 (-1.21)	1333 (-1.19)	1381 (-1.27)	$\delta^{wag}CH_2$(46(C9),36(C7), out-of-phase)
1302ms	1314 (-0.21)	1312 (-0.26)	1353 (-0.07)	δ^{in}CC-H3(22) + $\delta^{twist}C9H_2$(21) + νC12-C13(8) + δ^{in}N6C2S1(6)
1287 w	1294 (0.08)	1293 (0.06)	1330 (0.28)	$\delta^{twist}C7H_2$(59) + νring breathing + νC7-N6-C9
	1271 (-0.15)	1266 (-0.14)	1307 (-0.11)	νC5-C11(25) + δ^{in}CC-H3(19) + νS1-C5(7) + δ^{in}ring(9)
1252 m	1249 (-0.47)	1245 (-0.42)	1284 (-0.19)	ν^{s}ring(15) + $\delta^{twist}C9H_2$(18) + δ^{in}CC-H3(11) + νC2-N6(6)
1233 vw	1217 (-0.33)	1213 (-0.38)	1257 (-0.38)	δ^{in}CC-H1(16) + δ^{in}CC-H3(9) + δ^{in}CC-H2(7) + νC12-C13(6) + νN6-C7(5)
1148sh	1169 (-0.24)	1164 (-0.22)	1205 (-0.38)	νN6-C9(16) + νN6-C7(7) + νC4-C5(9) + $\delta^{rock}C7H_2$(19) + $\delta^{rock}C8H_3$(15)
1138ms	1137 (0.17)	1134 (0.17)	1168 (0.16)	ν^{as}C14-C12-C13(36) + νC2-C3(10) + δ^{in}CC-H3(12) + δ^{in}CC-H2(12) + δ^{in}C5-C11-C12(8)
	1132 (0.04)	1127 (-0.04)	1166 (0.26)	νS1-C2-C3(14, trig) + $\delta^{rock}CH_2$(15(9),13(7)) + δ^{in}ring(8)
1079 w	1080 (0.38)	1077 (0.38)	1114 (0.44)	ν^{as}C7-N6-C9(23) + $\delta^{rock}CH_3$(10(C8),10(C10)) + $\delta^{rock}CH_2$(8(C7),8(C9)
1073 w	1069 (0.49)	1067 (0.45)	1102 (0.25)	$\delta^{rock}CH_3$(26,(C8),11(C10)) + νC9-C10(10) + δ^{scis}C8C7N6(18) +
	1066 (-0.26)	1061 (-0.19)	1094 (-0.27)	νC3-C4(13) + δ^{in}CC-H1(22) + δ^{in}CC-H2(24)
	1055 (-0.74)	1052 (-0.76)	1084 (-0.85)	νC7-C8(22) + νC9-C10(12) (out-of-phase) + $\delta^{rock}C10H_3$(22)
1002vw	996 (0.04)	993 (0.05)	1016 (0.04)	νC7-C8(31) + νC9-C10(23) (in-phase) + ν^{s}C7-N6-C9(27)
930 vw	909 (-0.68)	908 (-0.67)	938 (-0.28)	νC7-C8(33) + νC9-C10(21) (out-of-phase) + $\delta^{rock}CH_3$(10,(C8),17(C10))
899 vw	886 (-0.28)	889 (-0.24)	929 (0.73)	δ^{out}CC-H3(59) + δ^{twist}C13-C12-C14(18) + δ^{out}CC-H2(9) + δ^{out}SC-N6(8)
872 vw	855 (-0.17)	854 (-0.17)	891 (0.70)	νN6-C7(11) + δ^{in}ring(31,C2C3C4) + νS1-C2(9) + νC7-C8(8)
814vw	843 (0.63)	844 (0.63)	877 (0.01)	δ^{out}CC-H2(35), δ^{out}CC-H2(31)^{twist} + δ^{twist}C13-C12-C14(13) + δ^{tors}ring(7,C2C3C4)
792 vw	803 (0.13)	803 (0.11)	823 (0.22)	νC12-C14(23), νC12-C13(8)$^{in\text{-}phase}$ + δ^{in}SC-C11(17)
749 vw	766 (-0.18)	762 (-0.18)	790 (-0.05)	$\delta^{rock}CH_2$(36,(C7),9(C9)) + $\delta^{rock}CH_3$(27,(C8),7(C10))
	765 (-0.08)	762 (-0.08)	789 (-0.01)	$\delta^{rock}CH_2$(6,(C7),36(C9)) + $\delta^{rock}C10H_3$(27)

741 vw	732 (0.88)	732 (0.91)	764 (0.86)	δ^{out}CC-H1(52), δ^{out}CC-H2(12)^{wag} + δ^{tors}ring(10,C2C3C4)
676 vw	725 (0.66)	726 (0.83)	748 (0.12)	$\delta^{in,trig}$ring(25,C2C3C4) + νS1-C2(11) + δ^{rock}CC-H3(22)
663 s	**659** (0.77)	**659 (0.69)**	**678 (0.85)**	νS1-C2(21) + $\delta^{in,trig}$ring(16,C3C4C5) + νN6-C9(7) + δ^{rock}CC-H3(9)
	645 (-0.49)	643 (-0.37)	660 (-0.17)	νS1-C5(58) + δ^{in} C5C11C12 (8)
	616 (0.16)	618 (0.11)	639 (0.13)	δ^{out}C11=C12C13C14(65) + δ^{out}N16C14C12C11(17), δ^{out}N15C13C12C11(10)$^{in\text{-}phase}$
614vw	595 (0.50)	602 (0.41)	612 (0.44)	δ^{in}N16C14C12C11(18), δ^{in}N15C13C12C11(14)$^{in\text{-}phase}$ + δ^{in}C14C12C11C5(17), δ^{in}C13C12C11C5(12)$^{in\text{-}phase}$ + νC14C12C13(25)
593m	583 (0.03)	584 (0.10)	606 (-0.02)	δ^{out}S1C2-N6(37) + δ^{tors}ring(42,C2C3C4C5)
554w	553 (-0.04)	552 (0.01)	569 (-0.14)	δ^{in}ring(16,S1C2C3C4C5) + δ^{in}C7-N6C2-C9(28)$^{in\text{-}phase}$
513w	519 (-1.55)	520 (-1.52)	535 (-1.55)	δ^{out}S1C5-C11(47) + δ^{tors}ring(26,S1C5C4)
465w	470 (-0.88)	471 (0.97)	485 (1.10)	δ^{in}C7-N6C2-C9(56)$^{out\text{-}of\text{-}phase}$ + δ^{in}S1C2-N6(9)
457vw	457 (0.41)	459 (0.12)	473 (0.07)	δ^{in}N6C2-C9(16) + δ^{out}C12C13-N15(13) + δ^{tors}ring(14)
429w	448 (0.29)	452 (-0.41)	462 (-0.29)	δ^{in}N16C14-C12-C13N15(23)$^{out\text{-}of\text{-}phase}$ + δ^{tors}ring(9)
403vw	426 (0.24)	426 (0.27)	440 (0.05)	δ^{tors}ring(21) + δ^{in}C7-N6C2-C9(36)$^{in\text{-}phase}$ + δ^{out}S1C5-C11(16)
383 vw	404 (0.01)	404 (-0.07)	417 (-0.06)	δ^{in}N6C2-C7(21) + δ^{rock}C5C11-H3(18) + δ^{in}S1C5-C11(12)
348vw	373 (-0.56)	375 (-0.58)	387 (-0.62)	δ^{twist}C14-C12C11-C13(29) + δ^{out}S1C5-C11(26) + δ^{out}C5C11-C12(11)
312w	322 (0.65)	321 (0.48)	333 (0.49)	δ^{in}S1C5-C11(21) + δ^{in}N6C2-C9(17) + δ^{in}ring(13)
	306 (-0.28)	305 (-0.30)	315 (-0.30)	δ^{in}N6C7-C8(30), δ^{in}N6C9-C10(29)$^{out\text{-}of\text{-}phase}$
268vw	259 (0.02)	258 (-0.01)	269 (0.09)	δ^{in}C2N6-C7(22), δ^{in}C2N6-C9(6)$^{out\text{-}of\text{-}phase}$ + δ^{out}S1C5-C11(9) + δ^{in}S1C2-N6(8)
	245 (-0.23)	248 (-0.18)	252 (-0.15)	
	212 (-0.08)	208 (-0.10)	219 (0.02)	
	188 (-0.14)	186 (-0.16)	195 (-0.10)	
167m	169 (0.56)	168 (0.55)	174 (0.42)	δ^{tors}ring(40) + δ^{wag}C14-C12C11-C13(26)

Abbreviations: vw: very weak, w: weak, m: medium, ms: medium strong, s: strong, vs: very strong, sh: shoulder;
o.p. : out-of-plane, i.p. : in-plane, o.phase. : out-of-phase, i.phase. : in-phase; str. : stretching, def. : deformation, wag. : wagging

The CIS calculations clearly indicate that the zwitterionic resonance structure depicted in Scheme 6.1 has a higher contribution to the excited state of (**1**) than to the ground state. The changes in the bond lengths upon electronic excitation (highlighted in Table 6.1) are following the differences between the resonance structures (see Scheme 6.1). The N6-C2 single bond in the neutral species becomes a double bond in the zwitterions. According to this, the calculations predicted a significant shortening of this bond. The C3-C4 bond also shortens in accordance with its change from a single into a double bond. The C4-C5 bond lengthens because it corresponds to a single bond in the zwitterions, but a single in the neutral species. The C5-C11 bond shortens, while the C11-C12 one lengthens as expected. The lengthening of the C≡N bonds indicates that these bonds have a partial double bond character in the excited state and that the negative charge is highly localized on the nitrogen atoms.

The calculations do not predict significant changes for the C2-C3 bond. On the other hand, the S-C2 bond presents a larger modification than the S-C5 bond. Moreover, the S-C2 bond of the neutral species is shorter than the S-C5 bond. Hence, it seems that the free electrons of the S-atom are also involved in the electronic transition.

The CIS calculations predicted a dominant contribution of the HOMO→LUMO electron transition (0.68), but the HOMO-1→LUMO+2 transition is also involved in the electronic excitation. Taking a closer examination of the valence orbitals of (**1**) (see Fig. 6.3) one can observe that the HOMO→LUMO transition leads to the transformation of the bonding orbital on the C4-C5 atoms into an anti-bonding one. Moreover, the C5-C11 orbital of the LUMO corresponds to a bonding orbital, while the C11-C12 orbital is an anti-bonding one. These changes correlate with the bond length changes discussed above. The transition of an electron from a bonding (C4-C5) into an anti-bonding orbital (C4-C5 and C11-C12) leads to an elongation of the corresponding bonds (see Table 6.1), whereas the increase of electron density in the bonding C5-C11 orbital of the LUMO determines the double bond character of the C5-C11 bond in the excited state. Moreover, the contribution of the HOMO-1 orbital to the electron transfer, where the C11-C12 and the C≡N orbitals were bonding (see Fig. 6.3), leads to an increase of these bonds according to the bond length changes. The change of the orbital coefficients on the S-atom (see HOMO-1) suggests that the free electron pair also contributes to the electronic transition.

However, these theoretical investigations were carried out for the gas phase and, as Fig. 6.1 indicates, the solvent environment influences the electron transfer process from the

amino moiety toward the cyano units significantly. Therefore, resonance Raman measurements in unpolar and polar solvents were carried out and the analysis of the RR spectra is being under progress. Moreover, a complete understanding of the vibrational characteristics of (**1**) is indispensable. In the following, the Raman spectra of the crystalline compound will be discussed based on DFT and PED calculations and the preliminary results of the resonance Raman measurements will be finally presented.

Vibrational analysis

The FT-Raman spectrum of crystalline (**1**) in comparison with the calculated Raman intensities for the conformer shown in Fig. 6.1 at the BPW91/6-311+G(d,p) level of theory is depicted in Fig. 6.4. Table 6.2 lists the observed and calculated wavenumbers together with the vibrational assignment based on PED calculations.

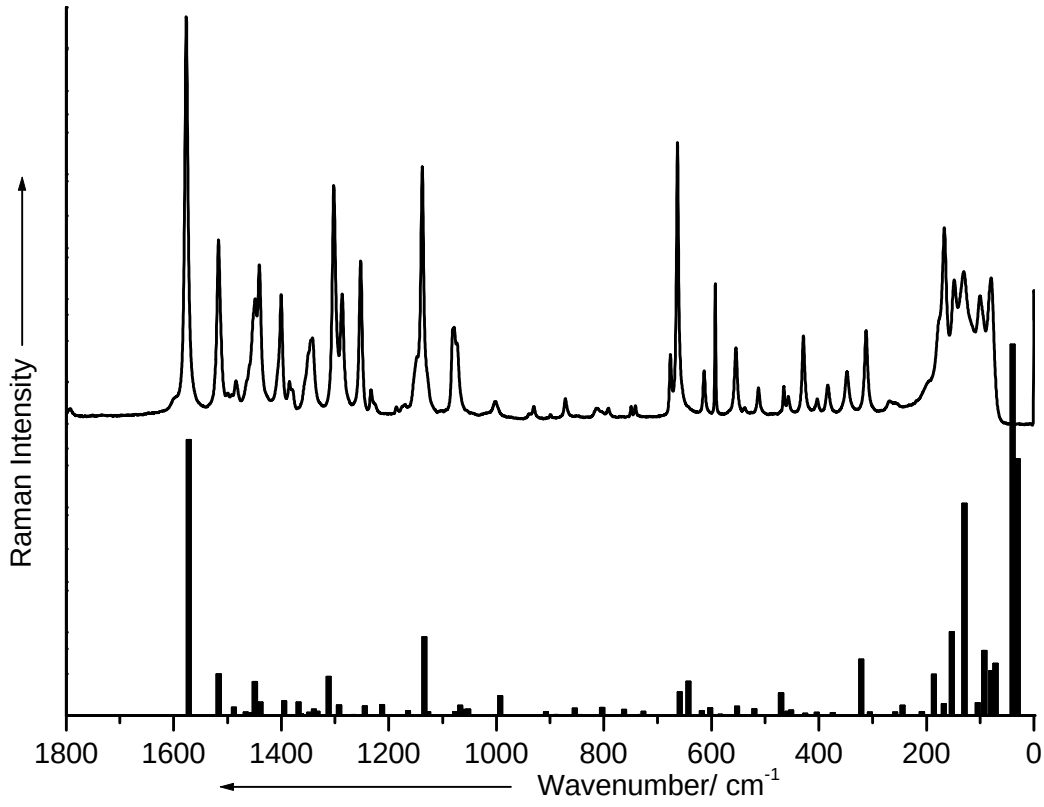

***Figure 6.4**. FT-Raman spectrum of crystalline (**1**) and the theoretical Raman intensities of the gas phase computed at the BPW91/6-311+G(d,p) level of theory presented as bar lines.*

In the high wavenumber region, two very strong bands corresponding to the in-phase and out-of-phase C≡N stretching modes arising at significantly lower wavenumbers (at 2203 and 2192 cm^{-1}) than usually cyano groups are expected to be observed. The reason for the relative low wavenumbers of these C≡N stretching modes is due to their strong electron conjugation with the C=C bond and thiophene ring. Moreover, the amino substituent of the thiophene ring acts as a very strong electron donor and additionally substantiates a partial double bond character for the C≡N bonds.

Figure 6.5

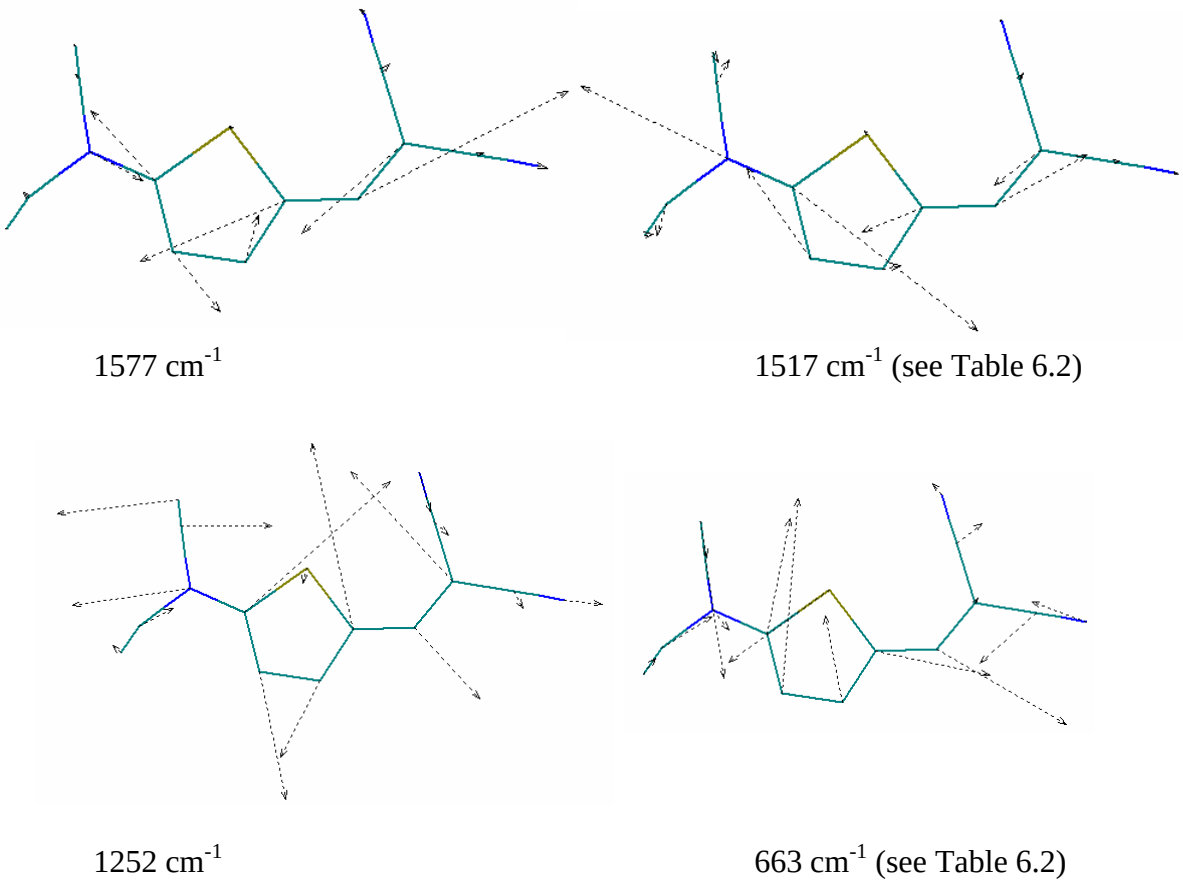

***Figure 6.5**. Representative vibrational modes of (**1**).*

Although the calculated Raman intensities do not match the experimental ones as well as in the case of the intramolecular proton transfer system presented in Chapter 4, a reasonable correspondence can be still found. The very strong mode at 1577 cm^{-1} mainly corresponds to the antisymmetric C12-C11-C5 stretching mode. This vibration is depicted in Fig. 6.5. The C2-N6 stretching mode arising at rather high wavenumbers and thus

reflecting the double bond character of the C2-N6 bond was assigned to the band at 1517 cm^{-1} and is also shown in Fig. 6.5. In contrast, the stretching modes localized on the N6-C7 and N6-C9 single bonds contribute to bands of weak intensity at 1287, 1233, 1148 and 872 cm^{-1}. Hence, the Raman wavenumber positions of the above mentioned different C-N stretching modes reflect the bond length differences (see Table 6.1). The C13-N15 and C14-C16 distances are the shortest and arise at the highest wavenumbers. The C2-N6 bond approaches a double bond length, whereas the N6-C7 and N6-C9 bonds are the longest.

The CH_3 antisymmetrical deformation modes coupled with the CH_2 scissoring modes (see Table 6.1) give rise to the medium strong band at 1441 cm^{-1} (Fig. 6.4). The symmetrical CH_3 deformation mode and the wagging and twisting modes of the CH_2 units exhibit only weak or very weak intensities in the FT-Raman spectrum of (**1**).

The thiophene ring stretching modes usually also involve the dicyano moiety or the C2-N6 bond. Several stretching modes of the thiophene C-C bonds were predicted in the 1500-1000 cm^{-1} region (see Table 6.2), while the S-C stretching vibrations were calculated around 660 cm^{-1}. The strong band at 663 cm^{-1} (see Fig. 6.4) was assigned to the S1-C2 and probably S1-C5 stretching mode.

The skeletal in-plane and out-of-plane deformation modes give rise to several bands of weak intensity below 1000 cm^{-1}.

Resonance Raman data

Figure 6.6 presents the FT-Raman spectrum of crystalline (**1**) compared with the spectrum recorded under preresonant conditions at 514.5 nm excitation, in dioxane solution c_M = 1.5 mM. The solvent spectrum is also depicted. Only a few bands can be clearly recognized in the preresonant spectrum. Some vibrations show a preresonant enhancement when excited with 514.4 nm (see Figs. 6.1 and 6.6) e.g. the bands at 800 and 666 cm^{-1} exhibit stronger intensity relative to the band at 1577 cm^{-1} in the preresonance Raman spectrum.

In this study, resonance Raman spectra in dichloromethane, dioxane and cyclohexane were recorded. The RR bands were sitting on a strong fluorescence background which was subtracted. The concentration of the solution was reduced by a factor of 20 to 100, when going from preresonant to resonant excitation wavelengths. It is noteworthy, that the resonance Raman spectra were recorded at the same concentration as the adsorption spectra where the light path length was 1 cm. This indicates that several

modes are exceedingly enhanced. The quantitative analysis of the resonance Raman intensities in order to determine the displacement parameters is currently under progress. Nevertheless, several features of the resonance Raman spectra are noteworthy.

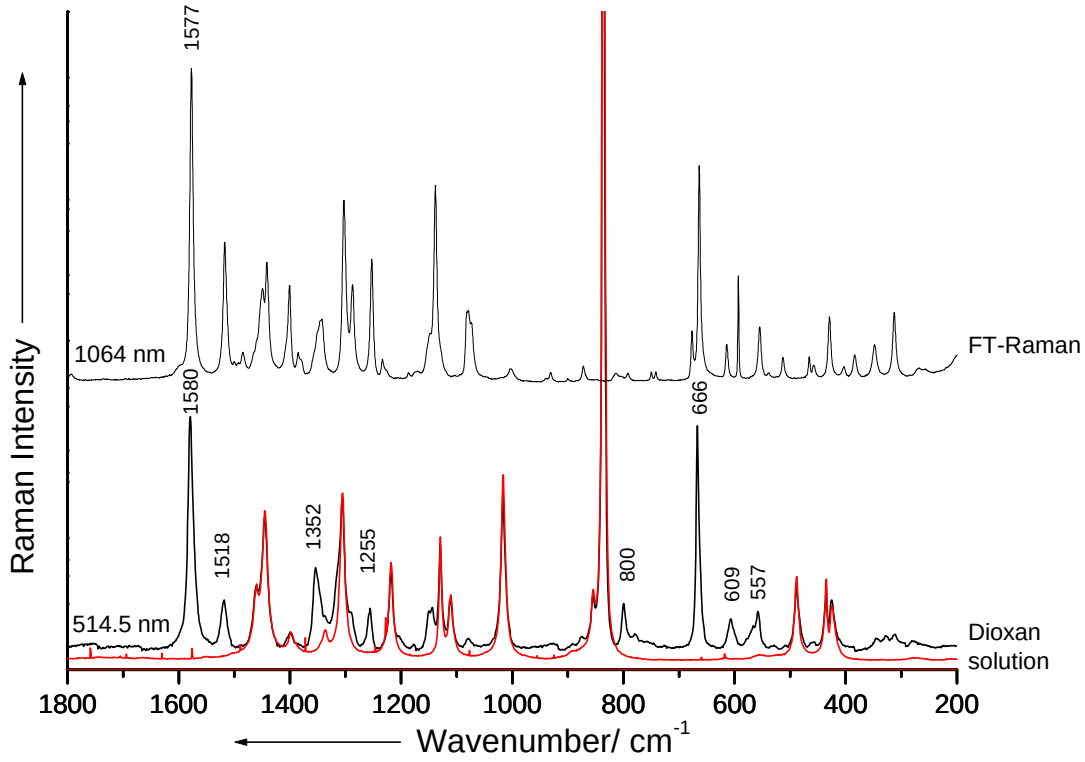

Figure 6.6*. FT-Raman spectrum of (**1**) in comparison with the Raman spectrum recorded under pre-resonant conditions (514 nm) in dioxane solution. The solvent spectrum is also given as a thin line.*

The RR spectra measured in dioxane for several excitation wavelengths are depicted in Fig. 6.7. The solvent lines are marked by an asterisk. The 458.5 nm excitation corresponds to the maximum of the absorption band in dioxane solution. In general, the strongest RR intensities were observed for excitation wavelengths lying in the maximum of the adsorption band. The relative RR intensities of (**1**) are much higher than the intensity of the solvent band at 834 cm^{-1}, although the concentration of the probe was much lower than for the preresonance spectrum shown in Fig. 6.6. Only a few bands of (**1**) are resonantly enhanced and can be therefore seen in the RR spectrum. The band at 666 cm^{-1} exhibits the highest intensity. Nevertheless, the bands at 2203, 1579, 1518, 1354, 1256, 800, 606 and

558 cm^{-1} are also enhanced. These modes are depicted bold in Table 6.2. The band at 800 cm^{-1} has relatively higher intensity compared to the band at 666 cm^{-1} when excited at 501 nm. Similar properties were observed in cyclohexane and dichloromethane.

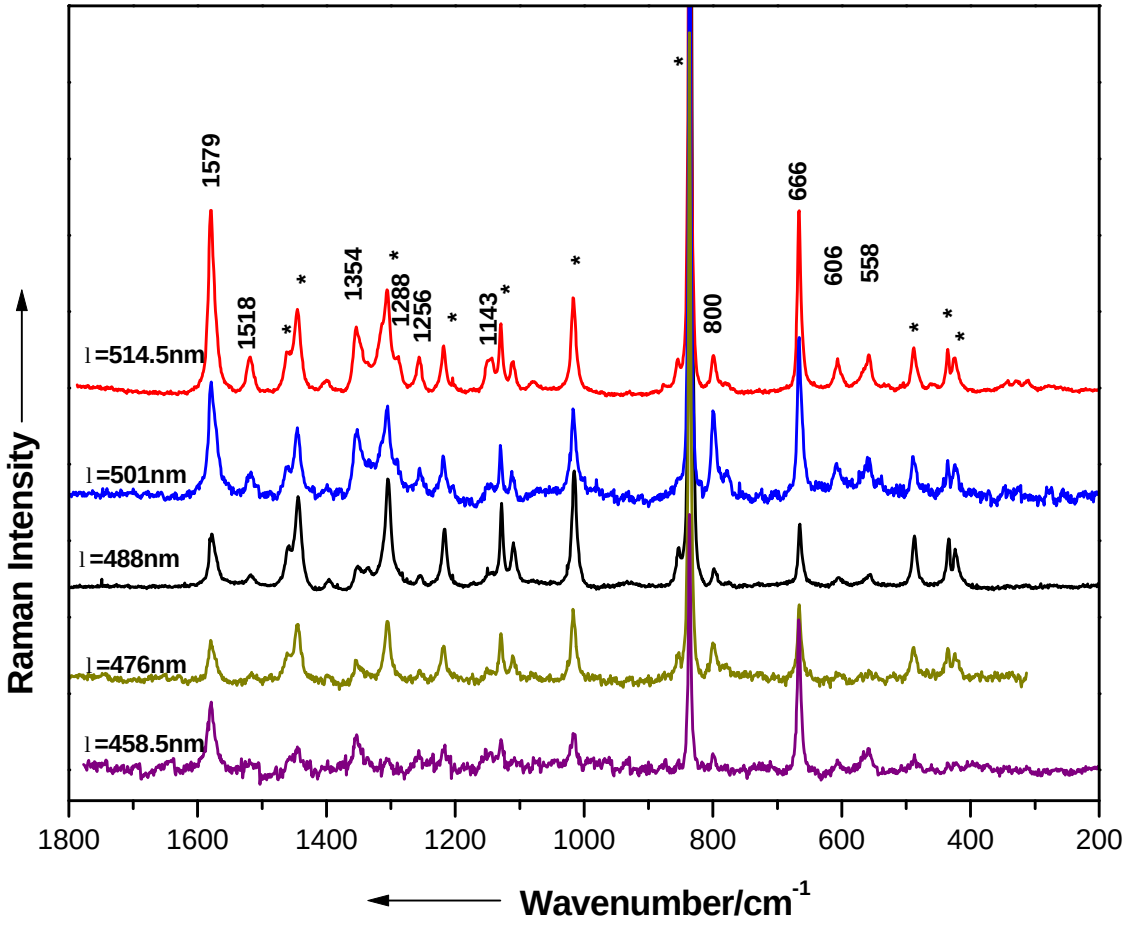

Figure 6.7*. The resonance Raman spectra of* ***(1)*** *recorded in dioxane solution. The solvent bands are marked by *.*

The most enhanced band at 666 cm^{-1} corresponding to the S1-C2 stretching coupled with ring deformation mode (see Table 6.2) is depicted in Fig. 6.5. A significant displacement parameter is expected for this mode indicating that the excited state geometry significantly changes along the S1-C2 bond. The assignment of the other selectively enhanced vibrations (see Table 6.2) indicates that the excited state potential is distorted along the bonds connecting the acceptor and donor groups.

The displacement parameters were theoretically calculated from the CIS coordinates of the excited state and the parameters of the ground state optimized at different levels of theory. The *D*s determined according to Eq. 3.17 are listed in Table 6.2 next to the calculated wavenumbers in paranthesis. The calculated FC parameters with the BPW91 fucntional often differ significantly from those calculated with the B3LYP functional. Furthermore, the observed RR bands do not show the highest theoretical parameters. Several out-of-plane and ethyl deformation modes are predicted to have very high displacement parameters, although these modes cannot be observed in the RR spectra. An explanation could be that: 1) the Duschinsky rotation of the normal mode coordinates (see Chapter 2.2) was not taken into consideration, 2) the CIS level of theory predicted a higher deviation from planarity and therefore the displacement of the out-of-plane modes is larger, or 3) the contribution of the other conformer in solution is also important. Hence, further theoretical analysis is necessary.

Conclusions

The ground and excited state of a push-pull chromophore thiophene derivative was analyzed by means of quantum chemical calculations. DFT methods were applied to optimize the ground state geometry, while the excited state was determined with the CIS method. These calculations proved that the contribution of the zwitterionic structure to the excited state is significantly higher than in the ground state.

Raman and resonance Raman spectra of (**1**) were recorded and the vibrational assignment was carried out based on DFT and PED calculations. Several modes are Franck-Condon active. These are mainly corresponding to stretching modes along the bonds connecting the donor and acceptor moieties, but the S-C stretching mode is also enhanced.

Further theoretical analysis is required to determine the experimental displacement parameters as a function of solvent polarity in order to understand the dependence of the excited state on the solvent environment.

Chapter 7

Hydrogen Bonding in Aziridinyl Peptide, a Cysteine Protease Inhibitor

This chapter reports about the vibrational analysis of an aziridine ring containing tripeptide derivative with two glycine amino acid units. FT-Raman spectroscopy of the tripeptide and its electrophilic building block in combination with DFT calculations were applied to obtain information about the molecular structure and the hydrogen bonding pattern in the crystalline form of the title compound. Furthermore, an epoxide ring containing peptide analogon was also investigated as well as deuterated derivatives. The Raman spectra of the crystalline aziridine peptide proved that the aziridine NH as well as the amide NH bonds are involved in strong to moderately strong hydrogen bonding, respectively.

Motivation

In the last years the interest in inhibitors of cysteine proteases has increased significantly[170-172]. Since these proteases play essential roles in various pathological processes low molecular weight inhibitors could be useful therapeutic agents. One class of inhibitors comprises peptides containing an epoxide[173-177] or aziridine[178-183] ring. These three-membered heterocycles act as electrophilic "war heads" which can be attacked by the cysteine residue of the enzyme's active site thus leading to irreversible enzyme alkylation and inactivation (see Scheme 7.1). Until now little attention was given to peptides containing the aziridine-2,3-dicarboxylic acid as amino acid equivalent, neither do information about the structure of enzyme-inhibitor-complexes exist[184]. This in contrast to the oxygen analogon of these inhibitors, the epoxysuccinyl peptides, for which a variety of 3D-structures of enzyme-inhibitor-complexes have been solved. To understand the different binding modes of these related inhibitor types the preferred conformations have to be known. In addition, the knowledge of inter- and intramolecular hydrogen bonding motifs can contribute to a better understanding of structure-activity-relationships.

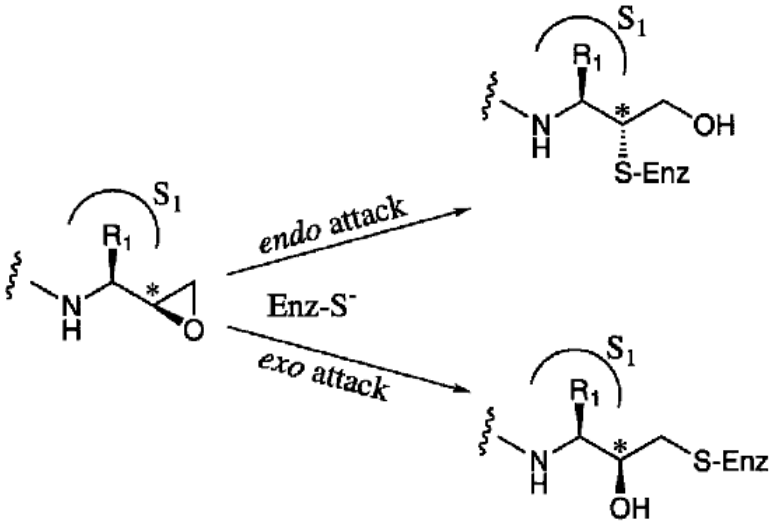

Scheme 7.1. *Enzyme alkylation by the epoxide active agent.*

It is well established that the carbonyl stretching wavenumber is a measure of the hydrogen bonding interaction since strong hydrogen bonding leads to a decrease in its wavenumber[185]. Moreover, the position of the NH stretching modes in vibrational spectra also reflects the H-bonding strength. Furthermore, since an indepth understanding of the

structure sensitive amide bands is of highly interest[15,186-190], a detailed vibrational analysis of the title compound and its electrophilic building block drawing special attention to the contribution of the atomic displacements to the normal mode coordinates was performed. The chemical structure of the investigated aziridine ring containing derivatives (EtO-Azi-OEt (**1**) and EtO-Azi-Gly-Gly-OBN (**2**)) is presented in Scheme 7.2. Moreover, for a reliable vibrational assignment and for a more exact estimate of the hydrogen bonding interactions, a related epoxide derivative (**3**) has been also investigated by means of Raman spectroscopy (see Scheme 7.2). These compounds were synthesized in the group of Prof. Schirmeister.

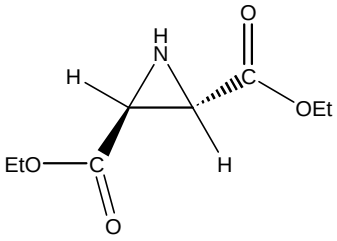

EtO-Azi-OEt (**1**)

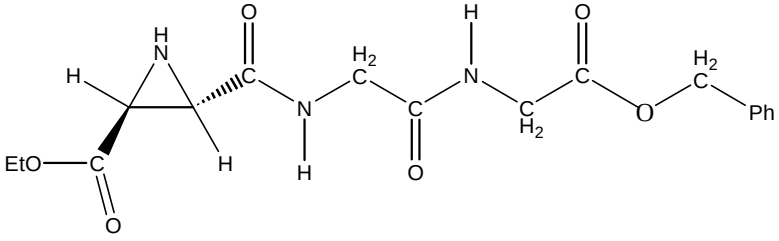

EtO-Azi-Gly-Gly-OBn (**2**)

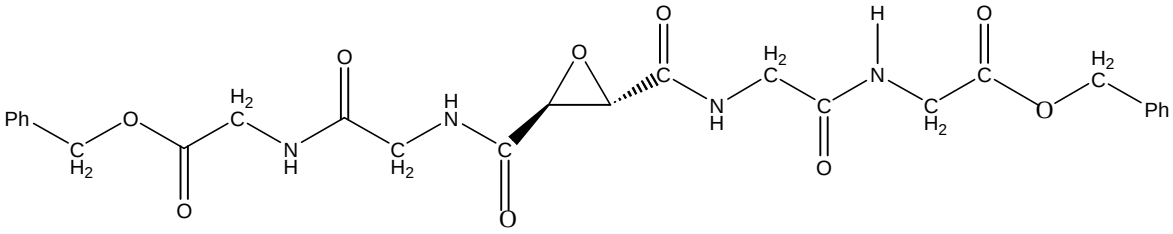

BnO-Gly-Gly-Epo-Gly-Gly-OBn (**3**)

Scheme 7.2*. Molecular structures of the aziridinyl building block (**1**), the aziridinyl peptide (**2**) and the related epoxide peptide derivative (**3**).*

The electrophilic building block (**1**) is a yellow liquid at room temperature, while the peptide derivatives (**2**) and (**3**) are crystalline. The crystal structure of (**2**) was determined in the group of Prof. Stalke and a conformational analysis of a single molecule both in the gas phase and medium to strong polar solvents was performed in the group of Prof. Engels. Strong intermolecular hydrogen bonds were found to be responsible for a zigzag arrangement of the aziridnyl peptide in the crystal.

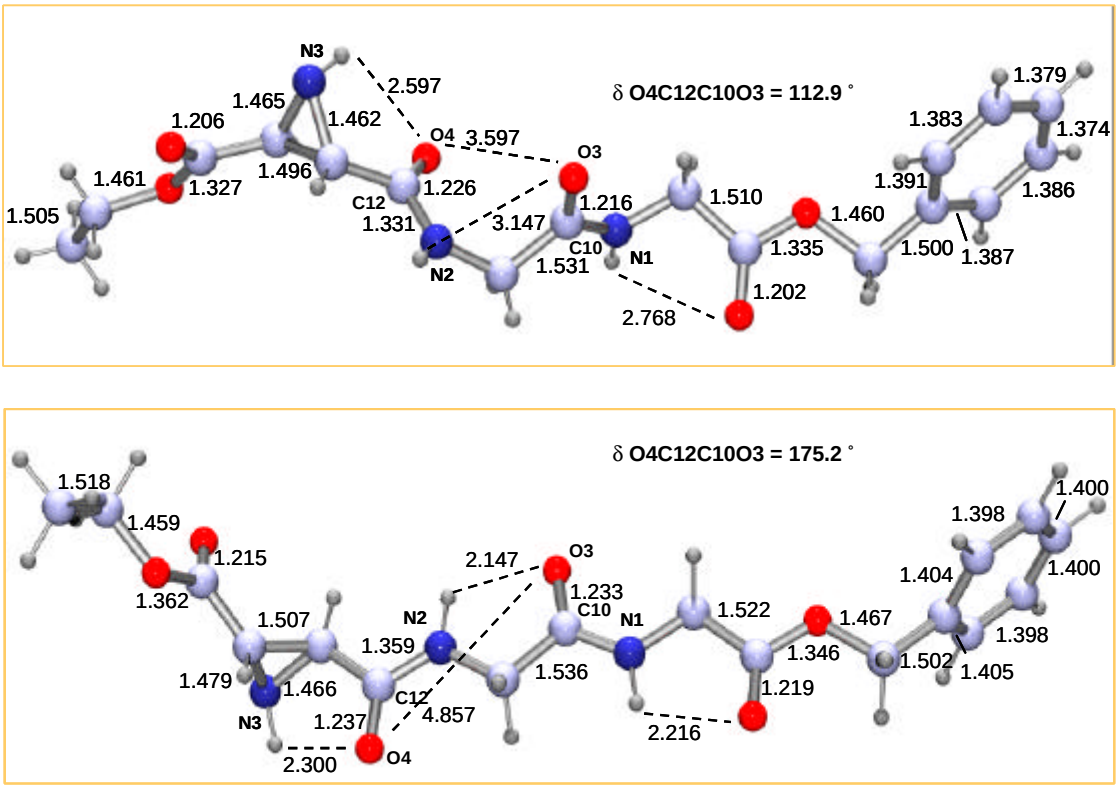

Figure 7.1. *Comparison of the X-ray of (**2**) (top) with the DFT optimization of the isolated molecule (bottom) at the BPW91/6-311G(d,p) level of theory.*

The molecular geometry of the tripeptide (**2**) in the crystalline phase is depicted in Fig. 7.1. The optimized molecular geometry derived from the crystal structure is presented for comparison. A very good agreement between the calculated bond lengths and the experimental ones can be observed, with deviations from the X-ray data of about 0.01 Å. However, the DFT predicted conformation of (**2**), does not correspond to the crystalline form. The calculated backbone of the tripeptide unit is almost planar, probably because the DFT calculations overestimated the electron delocalization of the amide bonds. Hence, the calculated intramolecular H-bonds are much shorter than the experimental ones.

Nevertheless, the conformation analysis carried out in the group of Prof. Engels led to a bent structure for an isolated molecule and in medium to strong polar environments. In the more polar environment the strength of the intramolecular hydrogen bonding interactions is significantly weakened. Unfortunately, the solubility of (**2**) was not sufficiently high to obtain vibrational spectra in solution.

Vibrational analysis of the electrophilic building block

A detailed vibrational analysis of the crystalline aziridine containing peptide (**2**) and its building block (**1**) was performed in order to investigate the hydrogen bonding patern. The FT-Raman spectra of (**1**) and (**2**) were recorded and the vibrational assignment of the bands was achieved with the help of theoretical calculations as well as the investigation of the deuterated compounds and the epoxide analogue peptide (**3**) containing two Gly-Gly-OBn residues bound to the heterocycle. The vibrational wavenumbers and Raman scattering activities were calculated subsequently to the optimization of the molecular structure within the Gaussian98[56] program. Several functionals (BPW91, B3LYP and B3PW91) and different basis sets (6-31+G(d), 6-311++G(d,p)) were applied to calculate the vibrational wavenumbers of (**1**). Since the best agreement between the calculated and experimental wavenumbers was obtained with the BPW91 functional, the latter combined with the 6-311G(d,p) was used in the calculations of (**2**). The calculated vibrational modes were visualized with the HyperChem program. Moreover, the potential energy distribution (PED) for each normal mode was calculated[62], which allowed a better understanding of the contribution of the displacement coordinates to the normal modes in terms of internal coordinates.

Figures 7.2 and 7.3 depict the FT-Raman spectrum of (**1**) in comparison with the spectrum of the deuterated form, where the aziridin H atom (NH) is substituted. Several vibrational modes are sensitive to the exchange of an hydrogen atom by a deuterium atom. A detailed vibrational assignment of (**1**) and (**D1**) is given in Table 7.1. The calculated vibrational wavenumbers obtained applying three different functionals for (**1**) are also listed. The vibrational shifts upon deuteration are emphasized. It is worth noting that the calculations predicted several vibrational modes which cannot be clearly identified in the Raman spectrum. This is due to the fact that (**1**) is a liquid at room temperature and therefore the Raman bands are broadened, or due to the fact that (**1**) contains two identical residues and altough the compound is not symmetrical the corresponding modes of the EtCOO-units arise at nearly the same wavenumber position.

The NH stretching mode is well separated from the CH stretching vibrations arising at 3283 cm^{-1}. Upon deuteration this mode is shifted by 850 cm^{-1} to 2435 cm^{-1} (see Fig. 7.2). However, the aziridine NH stretching vibration arises usually at higher wavenumbers (about 3350 cm^{-1} in unassociated molecules but around 3250 cm^{-1} in hydrogen bounded

species[4]. Therefore, in the case of (**1**) a medium strong intramolecular hydrogen bond between the aziridine hydrogen and one of the carbonyl groups is most likely to exist.

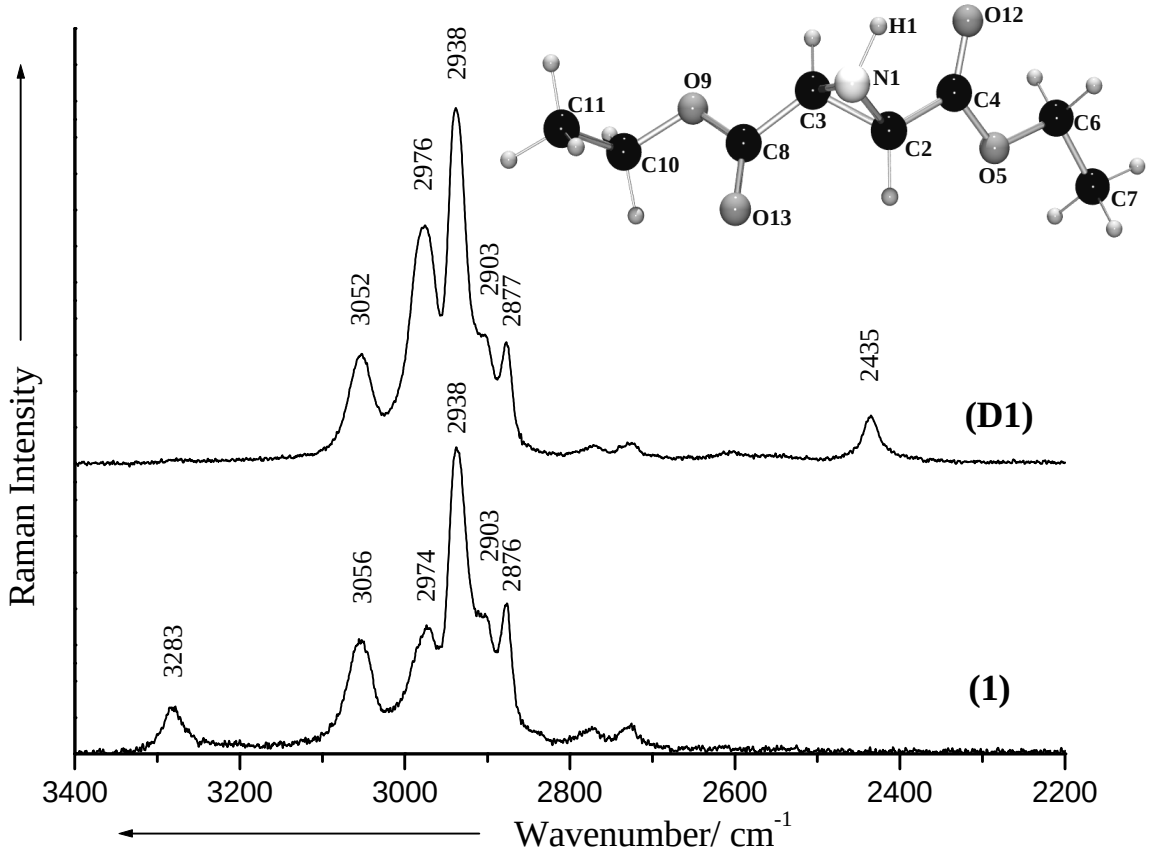

***Figure 7.2**. FT-Raman spectrum of (**1**) (bottom) in comparison with the FT-Raman spectrum of the deuterated form (**D1**) (top). The insert presents the atom numbering of (**1**).*

The CH stretching vibrations of the aziridine ring give rise to a broad band at 3052 cm^{-1}, while the asymmetric and symmetric CH_2 and CH_3 stretching modes are very strong bands and appear at 2976, 2938 and 2903, 2877 cm^{-1}, respectively.

The two ester carbonyl groups of (**1**) overlap and only one characteristic C=O band can be observed in the FT-Raman spectrum (Fig. 7.3). Nevertheless, the DFT calculations predicted two C=O stretching modes corresponding to the broad band at 1737 cm^{-1}. The vibration of the carbonyl group involved into the hydrogen bridge is calculated at lower wavenumbers (Table 7.1). However, the calculations predicted no change at all for the

C=O force constants (Table 7.1) due to the mass effect, since the theoretical wavenumbers of the C=O stretching modes for (**D1**) are equal to those for (**1**). This is in agreement with the fact that no shift of the carbonyl band could be observed upon deuteration.

The prominent band at 1453 cm^{-1} corresponds to the CH_2 scissoring and CH_3 antisymmetric bending modes. The symmetric bending modes (1392, 1337 cm^{-1}) have very low intensity in the Raman spectrum.

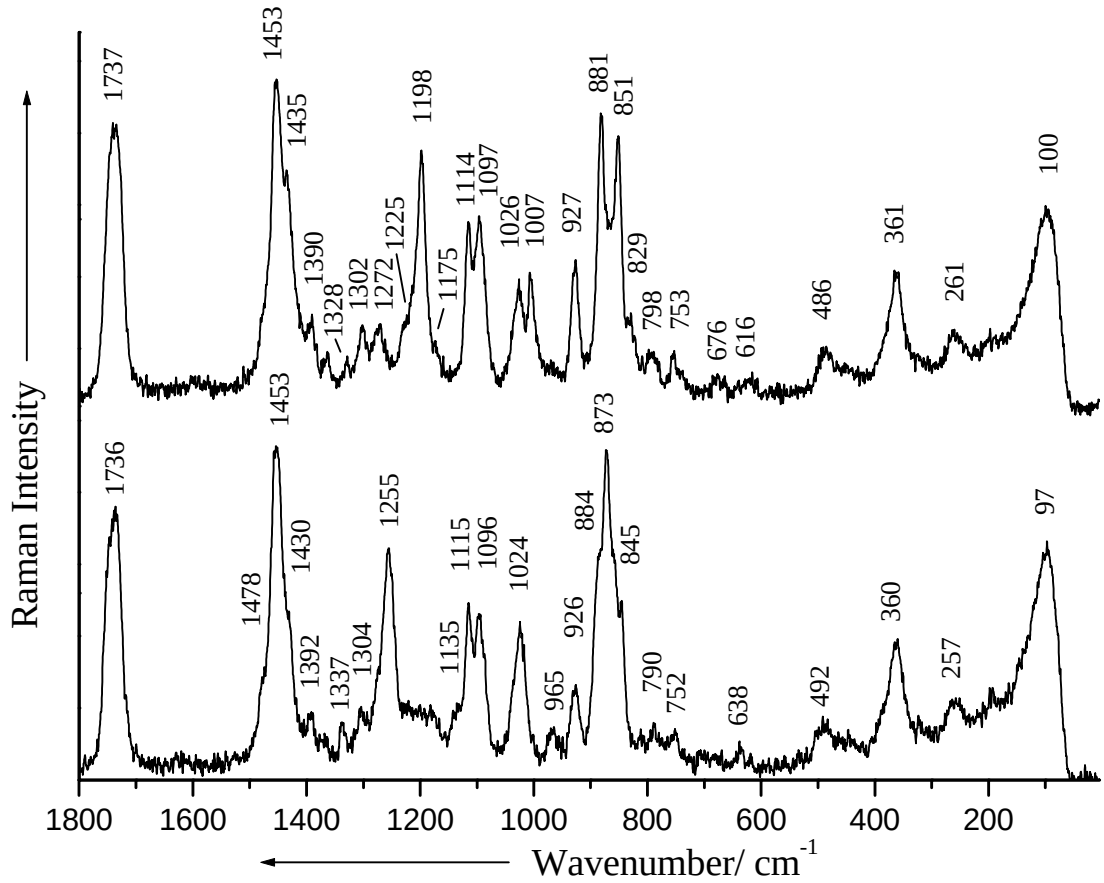

Figure 7.3*. FT-Raman spectrum of* ***(1)*** *(bottom) in comparison with the FT-Raman spectrum of the deuterated form* ***(D1)*** *(top).*

The ring breathing mode with strong contribution from the symmetric NH bending vibration at 1255 cm^{-1} is very sensitive to mass effects and shifts upon deuteration to 1198 cm^{-1}. Moreover, the deuterated species presents a band of medium intensity at 1007 cm^{-1} which can be assigned to the bending of the CND and CCH groups according to the

calculations. The vibration, from which this band for (**D1**) is derived, is probably corresponding to the shoulder at 1135 cm^{-1} in the Raman spectrum of (**1**). Another CND and CCH deformation mode, namely a twist mode between the two groups, has been predicted by the calculations around 913 cm^{-1}, but only the enhanced band at 927 cm^{-1} can be observed in the Raman spectrum of (**D1**) in this spectral region, while the band at 1026 cm^{-1} drops in intensity (see Fig. 7.3). Striking changes upon deuteration reveal the aziridine symmetric ring stretching mode which can be found at 873 cm^{-1} in the Raman spectrum of (**1**) and is shifted to 851 cm^{-1} in the spectrum of (**D1**). The close lying shoulder at 845 cm^{-1} involves also a symmetric aziridine stretching mode, but combined with the carbonyl groups which show unequal deformation modes. The other vibrational modes, which do not involve directly the aziridine ring, present no changes at all in the Raman spectra due to the mass effect.

The very weak band at 1304 cm^{-1} originates from the CH_2 wagging and C-C ring stretching mode. The band at 1272 cm^{-1} (see Fig. 7.3 **D1**) corresponding to the (O=)C-O stretching mode of the carboxylate moiety has very low Raman intensity and can be only observed upon deuteration since it is overlapped by the much stronger aziridine ring breathing vibration coupled to the NH bending mode. The C-C stretching mode of the ethyl units gives rise to the weak band at 1115 cm^{-1}. The band at 1094 cm^{-1} is due to the asymmetric deformation of the aziridine ring where the aziridine CH bending is also involved. The band at 1026 cm^{-1} can be assigned to the O-C(H_2) stretching mode. The calculations predicted the in-phase stretching vibration of the two groups at somewhat lower wavenumbers, but they can not be differentiated in the Raman spectrum.

In the lower wavenumber region (under 800 cm^{-1}) several out-of-plane deformation modes arise, however, with weak intensity. The OC=O out-of-plane deformation modes at 790, 752 and at 638 cm^{-1} have much lower intensity than the in-plane OC=O deformation mode at 360 cm^{-1}.

The in-plane C-C-O deformation vibration coupled to carbonyl and ring deformation modes gives rise to the weak band at 492 cm^{-1}, while the band at 257 cm^{-1} corresponds to the out-of-plane deformation mode of this group. Several out-of-plane deformation modes are predicted to correspond to the broad band at 97 cm^{-1}.

Table 7.1. *Experimental and calculated vibrational wavenumbers (in cm^{-1}) of (**1**) and (**D1**) and their vibrational assignment. The calculated Raman scattering activities are given in parentheses for the calculations at the BPW91/6-31+G(d,p) level. Calculations with the B3PW91 or B3LYP functionals and the 6-31+G(d,p) basis set led to similar data. The calculated PED values are given in parentheses for each mode.*

Observed		BPW91/1+G(d,p)		B3PW91/	B3LYP/	Vibrational assignment
(1)	**(D1)**	**(1)**	**(D1)**	1+G(d,p)	1+G(d,p)	
3283	**2435**	3366	**2462**	3492	3471	νN1-H1(100)
3052		3139	3138	3214	3204	νC2-H(98)
		3137	3117	3193	3185	νC3-H(98)
2976		3094	3095	3166	3150	$\nu^{as}CH_3(67) + \nu^{as}CH_2(32)$
		3086	3086	3156	3137	$\nu^{as}CH_3(86) + \nu^{as}CH_2(13)$
2938		3075	3075	3146	3129	$\nu^{as}CH_3(99)$
		3074	3074	3146	3124	$\nu^{as}CH_3(54) + \nu^{as}CH_2(43)$
		3068	3068	3139	3118	$\nu^{as}CH_3(73) + \nu^{as}CH_2(26)$
		3052	3052	3125	3112	$\nu^{as}CH_2(85) + \nu^{as}CH_2(13)$
2903		3019	3019	3093	3085	$\nu^{as}CH_2(100)$
		3006	3006	3078	3071	$\nu^{as}CH_2(97)$
2876		2996	2996	3063	3051	$\nu^{s}CH_3(99)$
		2993	2993	3060	3049	$\nu^{s}CH_3(100)$
1736w		1748(26.7)	1748	1872	1804	νC8=O13(81)
		1715(27.4)	1715	1795	1773	νC4=O12(80)
		1475(1.18)	1475	1516	1520	$\delta^{as}C7H_3(31) + \delta^{scis}C6H_2$ (56)
		1468(4.1)	1468	1506	1510	$\delta^{as}C23H_3(84)$
1478sh		1461(12.6)	1461	1498	1503	$\delta^{as}C7H_3(45) + \delta^{scis}C6H_2$ (46)
		1452(8.3)	1452	1495	1497	$\delta^{as}C11H_3(83)$
		1451(11.5)	1451	1486	1491	$\delta^{as}C7H_3(91)$
1453m		1447(39.1	1447	1488	1492	$\delta^{scis}C10H_2(79)$
1430sh		1424(85.4)	**1411**	1485	1476	δ^{out}C5-H(26) + νC2-C4 (13) + νC3-C8 (12) + δ^{out}C2-H(10)

1392vw		1386(5.8)	1385	1433	1433	$\delta^{s}C7H_3(55) + \nu C6\text{-}C7\ (13) + \delta^{wag}C6H_2(19)$
		1377(3.6)	1377	1423	1425	$\delta^{s}C11H_3(53) + \nu C10\text{-}C11(10) + \delta^{wag}C10H_2(26)$
1368vw		1357(3.3)	1357	1402	1406	$\delta^{s}CH_3(40,both) + \delta^{wag}C6H_2(38,both)$
1337vw		1350(1.2)	1349	1393	1398	$\delta^{wag}CH_2(61,both) + \delta^{s}CH_3(27,both)$
1304vw		1317(11.9)	1306	1366	1365	$\delta^{wag}C2H,C5H(38) + \nu C2\text{-}C4(9) + \delta^{wag}C6H_2(20)$
	1272	1289(7.5)	1289	1333	1331	$\delta^{twist}C10H_2(87)$
1255w	**1198**	1257	**1216**	1304	1293	νring breathing(36) + δ^{in}N1-H(27)
		1254	1254	1295	1296	$\delta^{twist}C10H_2(82) + \delta^{rock}C11H_3(10)$
		1197	1179	1266	1251	$\nu C4\text{-}O5\ (30) + \delta^{in}$N1-H(14) + δ^{in}C-O5-C(7) + $\nu C8\text{-}O9\ (8)$
		1183	1082	1233	1225	δ^{twist}N1-H,C3-H(49)+ $\nu C4\text{-}O5\ (15)$
		1160	1161	1206	1191	$\delta^{in}C11\text{-}C10\text{-}O9(23)\ \delta^{rock}C10H_2(22) + \delta^{rock}C11H_3(17) + \nu C8\text{-}O9\ (11)$
		1145	1145	1190		$\nu C8\text{-}O9(23) + \delta^{out}C3\text{-}H(23) + \nu C3\text{-}C8(12) + \delta^{rock}C6H_3(7)$
		1138	1138	1175	1177	$\delta^{rock}C6H_2(49) + \delta^{rock}C7H_3(36)$
	1007	1125(4.5)	**992**	1161	1163	δ^{wag}C2-H,N1-H(69)
1115w		1104(6.9)	1104	1140	1136	$\nu C6\text{-}C7\ (23) + \delta^{rock}C7H_3(30) + \delta^{in}$O5-C6-C7(30)
		1085(4.6)	1085	1120	1116	$\delta^{scis}C11\text{-}C10\text{-}O9(40) + \nu C10\text{-}C11\ (15)+ \delta^{rock}C23H_3(24)$
1096w		1077(13.2)	1077	1116	1118	δ^{wag}C2-H,C3-H(73)
1024w		1019(4.0)	1018	1071	1053	$\nu O5\text{-}C6(23) + \nu O9\text{-}C10(15)$ (o.p) + $\nu C6\text{-}C7(12) + \nu C10\text{-}C11(10)$
		1008(3.1)	1010	1056	1034	$\nu O9\text{-}C10(14) + \nu O9\text{-}C10(14)$ (i.p) + $\nu C10\text{-}C11(13) + \nu C6\text{-}C7(18)$
		1002(16.2)	913	1038	1040	δ^{twist}N1-H,C2-H,C3-H(62) + $\nu O9\text{-}C10\text{-}C11(20)$
965vw		953(11.0)	955	994	978	$\nu C2\text{-}C4(22) + \nu$N1-C2,3(19) + $\nu C6\text{-}C7(12)$
926vw		908(3.1)	867	946	936	$\nu C3\text{-}C8(17) + \delta^{out}$N1-C2-C4(9) + δ^{out}N1-C3-C8(9) + νN1-C2(9)
884sh	**881**	870	**855**	914	898	νring(33) + δN1-C3-C8(18)
873m	**851**	856	**817**	900	884	νring(35) + $\nu O5\text{-}C6(8) + \delta^{out}$N1-H(8)
845sh	**829**	842	**836**	884	870	$\nu O5\text{-}C6(24) + \nu$ring(26) + $\delta^{rock}C7H_3(12)$
812vw		834	834	876	860	$\nu O9\text{-}C10(30) + \nu$N1-C2(13) + $\delta^{rock}C11H_3(10)$
790vw		790	789	814	815	$\delta^{rock}CH_3(44,both) + \delta^{rock}CH_2(45,\ both)$
		787	768	808	811	$\delta^{rock}CH_3(51,both) + \delta^{rock}C10H_2(17)$
752vw		741	668	774	769	$\delta^{out}OC{=}O(38,\ both) + \delta^{in}$N1-C2-C4(12) + δ^{in}N1-C3-C8(8)

	728	728	763	755	δ^{out}OC=O(25, both) + νC2-C3(12)
	689	713	720	716	δ^{out}N1-C2-C4(21) + δ^{out}OC=O(26, both)
	655	643	682	678	δ^{out}N1-C3-C8(27) + νC3-C8(9) + δ^{in}C11-C10-O9(9)
492vw	468	466	484	481	δC11-C10-O9(80)
	425	420	441	438	δ^{scis}C11-C10-O9(34) + δ^{scis}C7-C6-O5(19) + δ^{in}C4-O5-C6(14)
360w	366	361	379	376	δ^{scis}C7-C6-O5(21) + δ^{scis}C11-C10-O9(20) + δ^{in}C4-O5-C6(13)
	343	342	355	352	δ^{scis}CCO(35, both) + δ^{in}C7-C6-O5(16) + δ^{in}OC8=O(10)
	332	326	345	345	δ^{scis}C11-C10-O9(29) + δ^{in}N1-C2-C4(16) + δ^{in}N1-C3-C8(14) + δ^{in}OC4=O(9)
	313	312	323	321	δ^{in}C11-C10-O9-C8(51) + δ^{in}C10-O9-C8(18)
257vw	254	253	263	262	τC7H_3(41) + δ^{out}N1-C2-C4(17)
	248	247	256	256	δ^{out}N1-C2-C4(16) + δ^{in}OC4=O(14)
	226	226	231	229	τC11H_3(26) + δ^{in}OC8=O(11)
	174	174	180	179	δ^{in}C7-C6-O5-C4(24) + δ^{in}C11-C10-O9-C8(17)
	168	168	173	172	δ^{in}C10-O9-C8-C3(34) + δ^{in}C6-O5-C4-C3(31)
	126	126	130	129	δ^{in}C7-C6-O5-C4(37)
97	89	89	93	93	δ^{in}C11-C10-O9-C8(55)

ν *stretching*, δ *deformation*, τ *torsion*, as *asymmetric*, s *symmetric*, in *in-plane*, out *out-of-plane*, ip *in-phase*, op *out-of-phase*.

Vibrational analysis of the aziridinyl and epoxid peptides

Figures 7.4 and 7.5 depict the FT-Raman spectrum of (**2**) in comparison with the spectrum of the deuterated form.

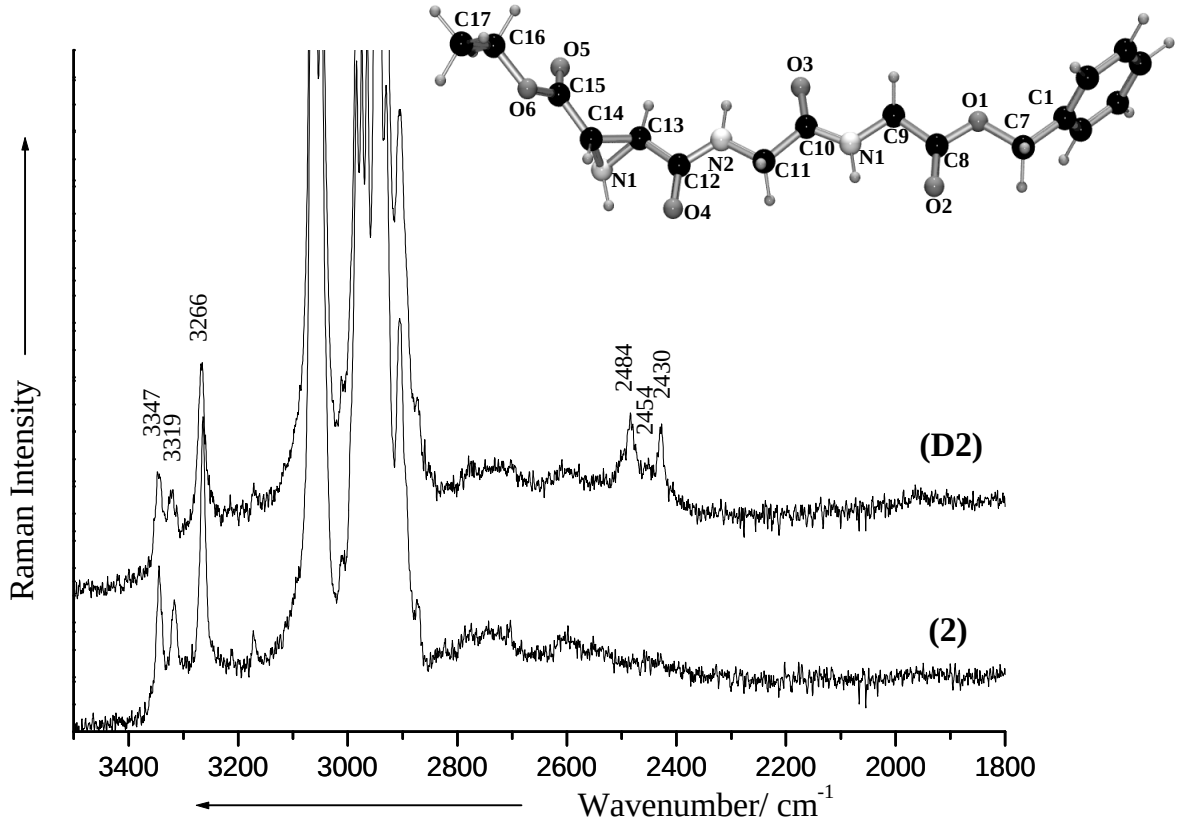

Figure 7.4*. FT-Raman spectrum of (**2**) in comparison with the FT-Raman spectrum of the deuterated form (**D2**). The insert presents the atom numbering of (**2**).*

Unfortunately, the NH hydrogen atoms could not be replaced completely by the deuterium isotope. Nevertheless, the ND stretching modes can be clearly recognized at lower wavenumbers (Fig. 7.4). The NH aziridine stretching was assigned in analogy to (**1**) to the band at 3266 cm^{-1} and is shifted to 2430 cm^{-1} in the spectrum of the deuterated species. Two amide NH stretching modes arise at higher wavenumbers (3347 cm^{-1} and 3319 cm^{-1}, respectively) in the Raman spectrum of (**2**). Although, in the spectrum of (**3**) (not shown here) only one broad band at 3287 cm^{-1} can be observed. The amide NH stretching mode arises at 3288 cm^{-1} in α-glycylglycine and at 3277 cm^{-1} in its

hydrochloride[191], whereas in Poly(Gly)[15] the amide NH stretching vibration arises at 3301 cm^{-1}. Hence, the hydrogen bonding of the aziridine peptide amides is significantly weaker than the hydrogen bonding in the epoxide analogon or the polypeptide. Nevertheless, the bonding interaction of the aziridine NH in the peptide is stronger than in the electrophilic building block (**1**), since it arises at lower wavenumbers by about 17 cm^{-1} (see Figs. 7.2 and 7.3). In the region of skeletal vibrations, however, only changes in intensity can be observed upon deuteration. A detailed vibrational analysis of (**2**) is given in Table 7.2.

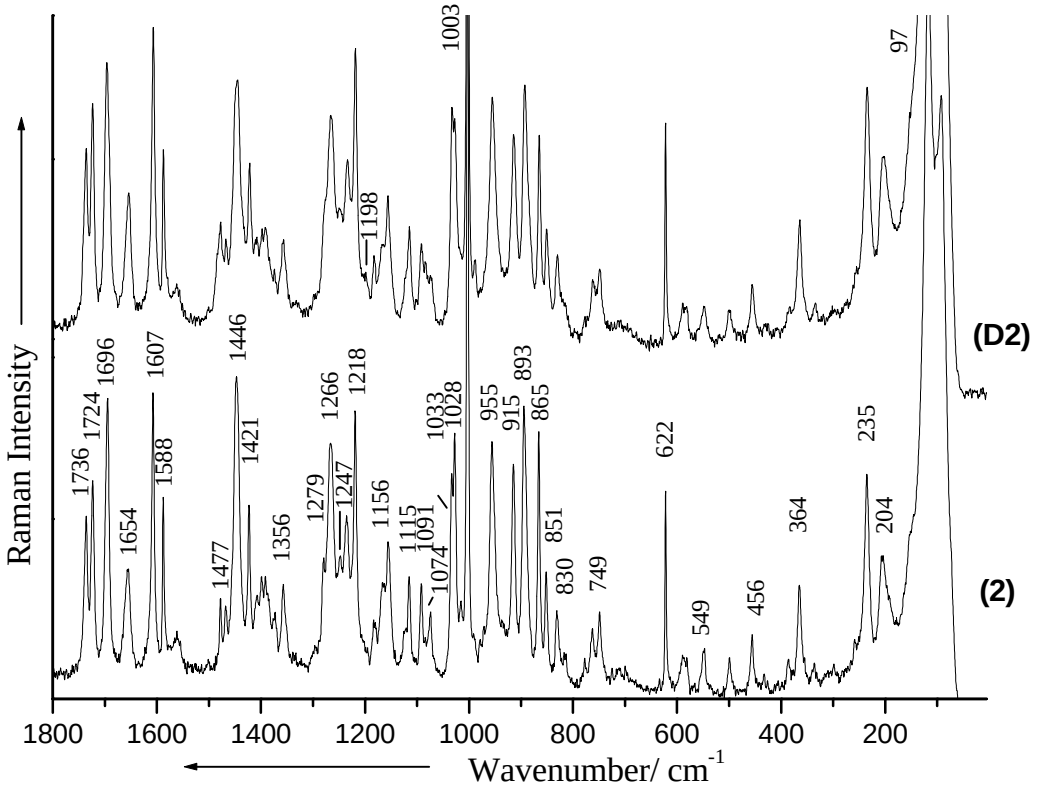

***Figure 7.5**. FT-Raman spectrum of (**2**) in comparison with the FT-Raman spectrum of the deuterated form (**D2**).*

In the case of (**2**) the carbonyl stretching vibrations are well differentiated, and four bands can be observed in the FT-Raman spectrum (see Fig. 7.5) of this derivative corresponding to its four carbonyl groups. The carboxylate moieties give rise to the bands at higher wavenumbers. The ethyl ester arises at 1736 cm^{-1} and the benzyl ester at 1724 cm^{-1}, respectively. The latter slightly couples to the adjacent amide carbonyl. However, the relative low wavenumbers at which the ester carbonyl bands arise tend towards a notable

hydrogen bonding. The corresponding band in the spectrum of (**1**), as discussed previously, arises at 1737 cm^{-1}. The ester carbonyl of the epoxide appears at 1744 cm^{-1} and is probably not involved in any hydrogen bonding. Nonetheless, as mentioned, the amide NH stretching modes of (**3**) indicate much stronger hydrogen bonding than (**2**). Therefore, the differences in the hydrogen bonding pattern of the two peptide derivatives is important to be investigated in more detail.

Table 7.2. *Experimental and calculated vibrational wavenumbers (in cm^{-1}) of (**2**) and their vibrational assignment. The calculations were done at the BPW91/6-311G(d,p) level. The calculated PED values are given in parentheses for each mode.*

FT-Raman cm^{-1}	Calc cm^{-1}	Vibrational assignment, (PED %)
3344	3486	νN1-H(99)
3317	3461	νN2-H(99)
3264	3331	νN3-H(100)
3064	3133	νPhH(93)
	3123	νPhH(99)
	3113	νPhH(99)
3048	3105	νC14-H(97)
	3103	νPhH(99)
	3101	νPhH(100)
	3088	νC13-H(97)
2984	3065	$\nu^{as}CH_3$(87) + $\nu^{as}C16H_2$(12)
	3057	$\nu^{as}CH_3$(99)
2975	3056	$\nu^{as}C7H_2$(100)
2964	3027	$\nu^{as}C16H_2$(87) + $\nu^{as}CH_3$(12)
	3005	$\nu^{s}C7H_2$(99)
2948	3004	$\nu^{as}C9H_2$(99)
	2989	$\nu^{as}C11H_2$(96)
2930	2989	$\nu^{s}C16H_2$(95)
	2984	$\nu^{s}CH_3$(99)
2906	2979	$\nu^{s}C9H_2$(94)
	2953	$\nu^{s}C11H_2$(96)
1736	1751	νC15=O5(75) + ν14-C15(6)
1724	1738	νC8=O2(77) + νO1-C8(6)
1696	1703	νC10=O3(64) + νN1-C10(10) + νC12=O4(7)
1654	1677	νC12=O4(64) + νC12-N2(11) + νC10=O3(8)
1607	1607	νPhenyl(58)(e_{2g}^{a}) + δ^{in}PhenylH(12) + δ^{in}Phenyl(7)
1588	1587	νPhenyl(70)(e_{2g}^{b}) + δ^{in}PhenylH(9) + δ^{in}Phenyl(7)
1562	1501	ν^{as}C10-N1-C9(39) + νC11-C10(7) + νN2-C12(6) + δ^{in}CN1-H(24) + δ^{in}CN2H(5)
	1489	νPhenyl(37)(e_{1u}^{a}) + νC1-C7(7) + δ^{in}PhenylH(56)

1477	1485	νN2-C12(31) + νC11-N2(10) + νN1-C10(8) + δ^{in}CN2-H(22) + νC12-C13(7)
1468	1476	$\delta^{scis}C16H_2$(54) + $\delta^{as}CH_3$(34)
	1459	$\delta^{scis}C7H_2$(93)
1447br	1458	$\delta^{as}CH_3$(73) + $\delta^{scis}C16H_2$(10)
	1454	$\delta^{scis}C11H_2$(84)
	1446	νPhenyl(26)($e_{1u}{}^{b}$) + δ^{in}PhenylH(45)
	1445	$\delta^{as}CH_3$(90)
1423	1445	$\delta^{scis}C9H_2$(83)
1407	1413	ν^{as}C15-C14-C13(30) + ν^{s}C14-N3-C13(12)+ δCC14-H(25) + δ^{in}CN3-H(8)
1399	1378	$\delta^{s}CH_3$(58) + $\delta^{wag}C16H_2$(12) +νC16-C17(12)
1392	1367	$\delta^{wag}C7H_2$(48) + νC9-C8(11) + νC8-O1(6) + νC7-C1(6)
1373	1349	$\delta^{wag}C16H_2$(47) + $\delta^{s}CH_3$(21)
1356	1346	νPhenyl(84)(b_{2u})
	1338	$\delta^{wag}CH_2$(amide, Bn)+ νC11-C10(6)
	1322	$\delta^{wag}C9H_2(20^{+})$ + δCC13-H(14) + νC9-C8(5)
	1316	δ^{in}PhenylH(81)(a_{2g})
1279sh	1291	$\delta^{wag}C11H_2$(33) + δCC13-H(12)
1266	1261	νazi(30)(breathing) + δCN3-H(22) + δCC14-H(12)
1247	1256	$\delta^{twist}C16H_2$(92) + $\delta^{rock}CH_3$(6)
1235	1212	δCN1-H(21) + νC8-O1(10) + νC10-N1-C9(13) + $\delta^{twist}C7H_2$(13)
1218	1209	νC7-C1(39) + δ^{in}PhenylH(11) + νPhenyl(6)
	1208	$\delta^{twist}C7H_2$(74)
	1203	δCN3-H(44), δCC14-H(14)^{scis} + νC15-O6(7) + δC13C14-C15(9)
1183	1196	$\delta^{twist}C11H_2$(71) + δCN2-H(8) + νN2-C11(7)
	1191	$\delta^{twist}C11H_2$(33) + $\delta^{twist}C9H_2$(16) + δCN2-H(14) + νN2-C11(7)
	1189	$\delta^{twist}C9H_2$(79)
1166	1178	νO1-C8(22) + $\delta^{twist}C9H_2$(33) + δCN1-H(10)
	1171	δPhenylH(59)($e_{2g}{}^{a}$) + νO1-C8(8)
1156	1157	δPhenylH(81)(b_{2u}) + νPhenyl(11)
	1142	νC15-O6(25) + $\delta^{rock}C16H_2$(15) + $\delta^{rock}CH_3$(7) + δCC14-H(5) + νC11-N2(5)
	1139	$\delta^{rock}C16H_2$(46) + $\delta^{rock}CH_3$(18) + νC15-O6(8)
1126sh	1134	δCC14-H(24), δCN3-H(8)^{twist} + νC15-O6(10) + νN2-C11(8) + νN1-C9(6) + νC14-C15(6)
1115	1120	δCC13-H(21), δCN3-H(9)^{wag} + νN1-C9(18) + ν^{s}C12-N2-C11(13)
1091	1104	νC16-C17(28) + $\delta^{rock}CH_3$(44)
1084	1085	νPhenyl(42)($e_{1u}{}^{b}$) + δPhenylH(36)($e_{1u}{}^{b}$)
1074	1077	νN2-C11(26) + νN1-C9(22) + νC10-N1(6)
1074	1074	δCC13-H(51), δCC14-H(10)^{wag}
1033	1028	νPhenyl(55)($e_{1u}{}^{a}$) + δPhenylH(17)($e_{1u}{}^{a}$)
1028	1018	ν^{as}C17-C16-O6(58) + $\delta^{rock}CH_3$(8) + δCC14-H(6)
1016	1009	δCC13-H(23), δCC14-H(18), δCN1-H(9) + δCC-C12(10)
1003	991	νPhenyl(86)(trig breathing)
	981	$\delta^{rock}C11H_2$(20) + $\delta^{rock}C9H_2$(11) + νC13-C12(6)

	978	$\delta^{rock}C9H_2(40) + \delta^{out}OC{=}O2(7)$
	972	δ^{out}PhenylH(69)
	971	$\delta^{rock}C11H_2(15) + \delta^{rock}C9H_2(10) + \nu C9\text{-}C8(6) + \delta^{out}OC{=}O3(6)$
955	962	$\nu C13\text{-}C12(9) + \delta^{rock}C11H_2(19) + \delta^{out}OC{=}O3(7)$
	946	δ^{out}PhenylH(81)
	944	$\delta^{rock}C7H_2(64)$
	932	$\nu C14\text{-}C15(12) + \nu N3\text{-}C13(7) + \nu C11\text{-}C10(5) + \delta^{out}$PhenylC(5)
	923	δ^{out}PhenylC(15) + δ^{out}PhenylH(14) + $\nu O1\text{-}C7(7) + \nu C14\text{-}C15(7)$
915	915	$\nu O1\text{-}C7(29) + \nu C9\text{-}C8(8) + \nu C11\text{-}C10(7)$
893	885	$\nu O1\text{-}C7(29) + \delta^{out}$PhenylH(53)
865	873	$\nu N3\text{-}C13(26) + \delta CC\text{-}C12(7) + \delta^{rock}CH_3(6)$
851	861	$\nu N3\text{-}C14(36) + \nu C13\text{-}C14(18) + \delta CC\text{-}C15(18) + \delta^{out}OC{=}O5(7)$
830	843	$\nu O6\text{-}C16(33) + \nu N3\text{-}C13(16) + \delta^{rock}CH_3(16)$
817	828	δ^{out}PhenylH(100)
814	816	$\nu C7\text{-}C1(21) + \nu C9\text{-}C8(9) + \nu$Phenyl(16) + δPhenyl(7)
778	790	$\delta^{rock}CH_3(30) + \delta^{rock}C16H_2(55)$
763	756	$\delta^{out}CC\text{-}C12(41) + \delta^{out}OC{=}O4(14)$
749	747	δ^{out}Phenyl(31) + δ^{out}PhenylC(27) + δ^{out}PhenylH(23)
	713	$\delta^{out}CC\text{-}C12(14) + \delta^{out}OC{=}O5(11)$, $\delta^{out}OC{=}O4(9)^{in\text{-}phase}$
	697	$\delta^{out}CC\text{-}C15(21) + \delta^{out}CC\text{-}C4(12) + \delta^{out}OC{=}O4(7)$
	691	δ^{out}Phenyl(47) + δ^{out}PhenylH(24) + δ^{out}PhenylC(12)
	674	$\delta CC\text{-}C12(15) + \delta CC\text{-}C15(17)$
	637	δ^{in}amide(46)
622	618	δ^{in}Phenyl(86)
590	604	$\delta^{out}CN1\text{-}H(15) + \delta^{out}OC{=}O3(11) + \delta^{rock}C11H_2(24)$
	569	δ^{out}PhenylC(10) + δPhenyl(9) + $\delta^{out}OC{=}O2$
	565	$\delta^{out}OC{=}O2(11) + \delta^{twist}C9H_2(22) + \delta^{out}O1C8C9(15)$
	562	$\delta^{out}CN2\text{-}H(33) + \delta^{out}CCC12(15) + \delta^{out}C12N2C11(8)$
549	547	$\delta^{in}N2C11C10(=O3)N1(28)$ + δPhenyl(9)
499	497	δ^{out}PhenylC(31) + δPhenyl(14) + $\delta^{in}N2C11C10(5)$
456	433	$\delta^{in}C16O6C15{=}O5(31) + \delta CC\text{-}C12(10)$
	401	$\delta^{in}C16O6C15{=}O5(23) + \delta^{out}$PhenylC(8) + δ^{out}Phenyl(9)
386	398	δ^{out}Phenyl(86)
364	354	$\delta^{out}(O{=})C15C14C13C12(=O)N2(73)$
	246	$\delta C15CC\text{-}C12(36) + \delta^{in}OC{=}O5(13)$
235	221	$\delta C15CC\text{-}C12(34)$
204	204	$\delta^{out}C12N2C11C10(30)$

ν *stretching*, δ *deformation*, τ *torsion*, as *asymmetric*, s *symmetric*, in *in-plane*, out *out-of-plane*, ip *in-phase*, op *out-of-phase*.

Due to the electron delocalization in the amide backbone, the amide carbonyl bands are shifted usually to lower wavenumbers. The band at 1696 cm^{-1} corresponds to the C10=O3 stretch vibration, whereas the band at 1654 cm^{-1} corresponds to the carbonyl moiety (C12=O4) adjacent to the aziridine ring. The DFT computed wavenumbers of the

optimized molecular structure of (**2**) (see Table 7.2) are in good agreement with the experimental data. Nevertheless, the band at 1654 cm^{-1} (see Fig. 7.6) is predicted at higher wavenumbers by about 20 cm^{-1}, whereas the other carbonyl modes are calculated with a better accuracy. Therefore, the Raman spectrum of the solid probably shows stronger hydrogen bonding interaction (intermolecular one) involving this group than it is predicted by the gas phase optimization.

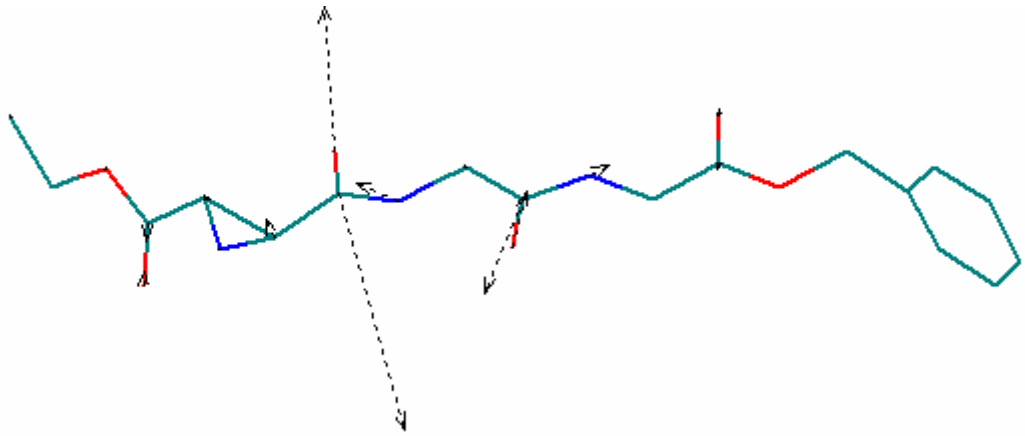

***Figure 7.6**. Carbonyl stretching mode of (**2**) corresponding to the band at 1654 cm^{-1} in the FT-Raman spectrum (see Table 7.2).*

The amide carbonyl stretching modes of the epoxide derivative (**3**) (see Fig. 7.7) arises at 1673 and 1658 cm^{-1}. This indicates that the C10=O3 group of (**2**) is less involved in H-bonding than in the epoxide, since it arises at significantly higher wavenumbers (by 23 cm^{-1}) compared to (**3**), but the C12=O4 group is involved in slightly stronger H-bonding. Moreover, the crystal structure analysis of (**2**) shows stronger H-bonding interaction for the C12=O4, the amide carbonyl adjacent to the aziridine ring, which is in agreement with the experimental Raman data. Furthermore, the C12=O4 bond is the longest carbonyl in the solid state or in the gas phase predicted by the DFT calculations. Comparing (**2**) with the IR and Raman spectra of α-glycylglycine or its hydrochloride[191] or the more recent near-resonance Raman study[190] on single crystal glycylglycine×1.5H_2O, where, however the dipeptide appears as a zwitterion, the same conclusions can be drawn. The amide I bands appear in the IR spectrum of the dipeptide[191] at 1674 and 1661 cm^{-1}, but at 1663 and 1622 cm^{-1} in the Raman spectrum of the single crystal[190] reflecting the much shorter intermolecular O···H bonds (in the range of 1.900 to 2.128 Å)[192] compared with (**2**). The X-ray analysis determined intermolecular H-bonds for (**2**) in the range of 2.05 to 2.56

Å. Sieler et al.[185,188] also reported Raman spectra of the single crystal glycylglycine and in solution and found that the amide bands (at 1665 and 1624 cm^{-1}) in the solid state spectrum[185] are consistent with the data reported by Pajnici et al.[190] Nonetheless, the amide carbonyl modes shift to considerably higher wavenumbers in the case of the solvated molecule[185,188] giving rise to two bands at 1675 and 1692 cm^{-1}. Sieler et al.[185,188] showed that the amide I doublet arises from vibrational mixing with water molecules and ruled out the possibility that the amide I subbands result from peptides with different hydrogen bonding between their CO groups and adjacent water molecules. Poly(L-Gly) shows one amide I band at 1674 cm^{-1} in the Raman spectrum[15], but two bands appear in the IR spectrum at 1685 and 1636 cm^{-1}. Nevertheless, in the case of (**2**) the significant splitting of the amide I band is due to the presence of the two differently H-bonded carbonyl moieties as shown also by the solid state structure. Hence, one carbonyl group is weakly H-bonded, whereas the carbonyl group adjacent to the aziridine ring is involved in both intermolecular H-bonding with the amide NH of a neighboring molecule and intramolecular interactions with the aziridine NH. As shown by the X-ray analysis, the later group is involved also in intermolecular interaction with the benzyl ester carbonyl, and therefore the aziridine NH stretching mode of (**2**) is stronger involved in H-bonding than in (**1**) arising at lower wavenumbers. In contrast to (**2**), both amide carbonyls of (**3**) are involved in strong H-bonding interactions, but the ester carbonyls present no hydrogen bonding, since they arise at 1745 cm^{-1}.

Comparing the FT-Raman spectra of (**2**) and the epoxide analogon, the characteristic modes of the phenyl unit can be easily discerned (see Fig. 7.7). The benzene vibrations do not couple to skeletal vibrations (see Table 7.2). Therefore, these vibrations arise at the same wavenumbers in the Raman spectra of (**2**) and (**3**). The strong bands around 1600 cm^{-1} correspond to the symmetric C=C stretching modes of the phenyl ring, where the degenerate vibrations of benzene are split into their counterparts. The trigonal ring breathing mode gives rise to a very strong band at 1003 cm^{-1}. Other vibrational modes characteristic to the benzene moiety were assigned based on the DFT calculations and comparison with the epoxide derivative (**3**) to the bands at 1356, 1155, 1033 and 622 cm^{-1} (see Table 7.2). Although the DFT optimized structure (see Fig. 7.2), where the optimization started from the crystal structure of (**2**), led to a different conformer, the calculated wavenumbers are in good agreement with the experimental data and the PED information corresponds very well to the experimental data of the investigated compounds

and to those from the literature[15,185,188,189,191]. Nevertheless, the Raman intensities calculated for (**2**) do not match the experimental intensities, probably because of the conformational differences (results not presented here). The agreement between the calculated and the observed wavenumbers is due probably to the fact that the calculated bond lengths for the gas-phase structure are in very good agreement with the crystal structure, even though the dihedral angles present striking discrepancies (see Fig. 7.1).

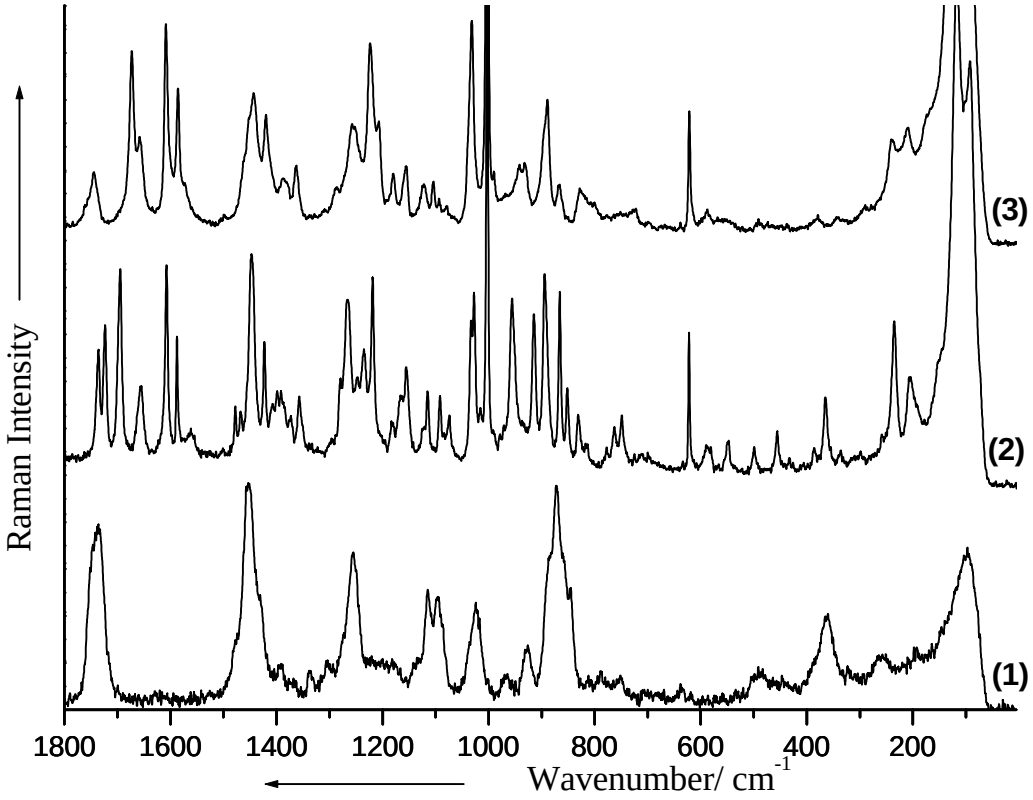

Figure 7.7*. FT-Raman spectra of (**1,2,3**). See text for discussion.*

In the following the backbone vibrations of (**2**) will be briefly discussed (see Table 7.2). The amide II band has usually very low intensity in the Raman spectra if recorded with visible excitation. The FT-Raman spectra of (**2**) and (**3**) present a shoulder at 1561 and 1573 cm^{-1} respectively which could be assigned to this mode. Nevertheless, the calculations predicted two modes corresponding mainly to the CN stretching vibration combined with NH bending mode at 1501 cm^{-1} and 1485 cm^{-1}. In the Raman spectrum the band of weak intensity at 1477 cm^{-1} is most likely to correspond also to an amide II band

involving predominantly the N2-atom. This mode arises usually around 1570 cm^{-1} in model peptides of trans-, but around 1475 cm^{-1} in cis-configuration[193], whereas for Poly(L-Gly)[15] two bands at 1564 and 1515 cm^{-1} can be observed. The amide III band of (**2**) presents medium intensity in the FT-Raman spectrum at 1235 cm^{-1} and corresponds well with assignment of Poly(L-Gly)[2]. The polypeptide presents two amide III bands at 1233 and 1220 cm^{-1}, respectively. The second amide III vibration of (**2**) could be assigned based on the DFT calculations to the band at 1183 cm^{-1}, but however, the contribution of the CH_2 twist vibration to this mode is high. In contrast, the aziridine ring C-N stretching mode which also involves NH bending arises at much lower wavenumbers, namely, at 1266 cm^{-1} for the ring breathing mode (see Fig. 7.8) and in the case of the dominant CN stretching modes at 865 and 851 cm^{-1}. Very often this modes are assigned as a ring deformations[3], but the PED calculations and the atomic displacements showed that a stretching assignment is more proper in terms of internal coordinates. Moreover, an *n*-membered ring presents 3*n*-6 degrees of freedom[194] which are described as *n* stretching modes and 2*n*-6 symmetrized bending and torsional modes. This lead in the case of a 3-membered ring to 3 degrees of freedom corresponding to 3 possible stretching modes.

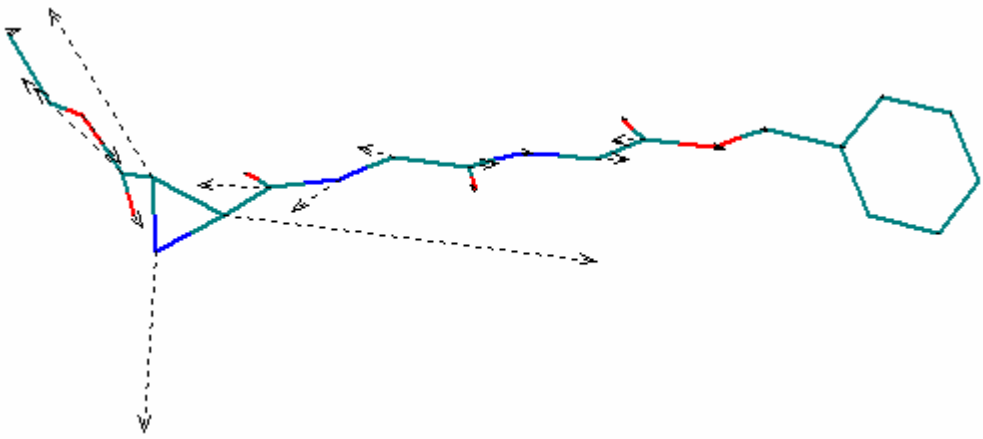

***Figure 7.8**. Aziridine ring breathing mode of (**2**) corresponding to the band at 1266 cm^{-1} in the FT-Raman spectrum (see Table 7.2).*

Several modes corresponding to C-O, N-CH_2 and C-C stretching vibrations arise in the 1400-800 cm^{-1} spectral region. The ester C-O bond is involved into vibrational modes at comparably higher wavenumbers (1166, 1156, 1126 cm^{-1}) than the O-Et, or O-Bn (1028, 915, 893, 830 cm^{-1}) due to its partial double bond character. The N-CH_2 stretching gives

rise to bands at significantly lower wavenumbers (1126, 1115, 1074 cm^{-1}) than the amide II or III modes.

The amide deformation modes have low intensity in the Raman spectrum in the 800-250 cm^{-1} spectral region, but very strong modes can be observed around 100 cm^{-1} where out-of-plane deformation modes probably overlap with lattice vibrations of the crystal unit. Nevertheless, the calculated Raman intensities of the latter modes is also very strong.

Finally, a detailed discussion of the CH_2 and CH_3 bending modes (see Table 7.2) is skipped, but it is worth noting that the strong band at 1447 cm^{-1} corresponds in great amount to the asymmetrical bending of the CH_3 group, since it can be observed in the Raman spectra of (**2**) and (**1**), but with lower intensity in the case of (**3**) where only scissoring modes arise in this spectral region.

Conclusion

A detailed vibrational analysis of an aziridine ring containing tripeptide (**2**) was performed. Therefore, the electrophilic building block (**1**) (EtO-Azi-OEt) and a related epoxide containing peptide were also investigated. The Raman spectra indicate stronger H-bonding of the aziridine NH unit in the solid state of (**2**) than in the electrophilic building block (**1**). The electrophilic building block probably presents only intramolecular interactions, while the aziridine NH of the peptide derivative is also involved in moderately strong intermolecular H-bonding. The amide hydrogen atoms of the aziridine derivative present weaker hydrogen bonding interaction than the related epoxide compound.

The two ester carbonyl groups of (**2**) are found to participate in the hydrogen bonding network, where the carbonyl unit in the vicinity of the benzyl group is more strongly hydrogen bounded than the one next to the ethyl group. In contrast, the ester carbonyls of the epoxide derivative show no hydrogen bonding. The amide carbonyl connecting the aziridine ring shows very strong inter- and intramolecular hydrogen bonding interaction. The second amide carbonyl unit is involved in weak H-bonding. Comparing (**2**) with other glycine peptide derivatives, one can conclude that the aziridine peptide shows moderately strong intermolecular H-bonding. Furthermore, the vibrational modes of the peptide backbone were discussed.

Chapter 8

Adsorption of anti-Leukemia Active Agents on Silver Colloid

Surface enhanced Raman spectroscopy (SERS) has been applied to characterize the interaction of 6-mercaptopurine (6MP) and 6-mercaptopurine-ribose (6MPR), two active drugs used in chemotherapy of acute lymphoblastic leukemia, with a model biological substrate at therapeutical concentrations and as a function of the pH value. Therefore, a detailed vibrational analysis of crystalline and solvated (6MP and 6MPR) based on DFT calculations of the thion and thiol tautomers has been performed. 6MPR adopts the thion tautomeric form in the polycrystalline state while in solution the thiol tautomer was evidenced. The SERS spectra of 6MPR and 6-mercaptopurine (6MP) recorded on silver colloid brought evidence that the ribose derivative shows different adsorption behavior compared with the free base. Under acidic conditions, the adsorption of 6MPR on the metal surface via the N7 and possibly S atoms was proposed with a perpendicular orientation, while 6MP is probably adsorbed through the N9 and N3 atoms. Under basic conditions both molecules are adsorbed through the N1 and possibly S atoms, but 6MP has a more tilted orientation on the silver colloidal surface while 6MPR adopts a perpendicular orientation. The reorientation of the 6MPR molecule on the surface starts at pH 8, while in the case of 6MP the reorientation starts around pH 6. Under basic conditions the presence of the anionic molecular species for both molecules is suggested. The deprotonation of 6MP is completed at pH 8, whereas the deprotonation of the riboside is finished at pH 10. For low drug concentrations under neutral conditions and for pH values 8 and 9, 6MPR interacts with the substrate through both N7 and N1 atoms, possibly forming two differently adsorbed species, while for 6MP only one species adsorbed via N1 was evidenced.

8.1 Adsorption of 6-Mercaptopurine

Motivation

6-Mercaptopurine (6MP), a purine derivative (see Scheme 8.1), is used in the conventional chemotherapy of patients with acute lymphoblastic leukemia (ALL)[195-199]. Variations in the immunosuppressive activity and toxicity of 6MP may be caused, at least in part, by a metabolism depending on individual patients[198,200]. However, poor drug adsorption and compliance may also explain the variable results obtained within orally administered chemotherapy. 6MP, which is administered intravenously, has a short half-life time in plasma and is rapidly eliminated[197,199]. Therefore, the intravenous (i.v.) administration of its derivative, 6-mercaptopurine riboside (6MPR) was recently re-evaluated. The i.v. administration of 6MPR showed less variation with individual cases and the patients undergoing chemotherapy with 6MPR showed high and stable red blood cell levels of active drug.

Although 6MP was extensively investigated by means of theoretical and spectroscopical methods, less attention was devoted to its derivative. Theoretical calculations have been performed to determine the stable tautomers of 6MP and the energy difference between the various species[201,202]. SERS spectra of 6MP adsorbed on gold and on an anodized silver electrode surface have already been reported and the molecular interactions discussed[203]. Metal complexes[204-209] of 6MP and 6MPR have also been investigated, since some of them exhibit antitumor activity, in order to determine the likely coordination sites and binding behavior of these therapeutic agents.

6MP is a pro-drug, undergoing extensive metabolism. The anabolic pathway results in the formation of active 6-thioguanine nucleotides in the erythrocyte cells[197]. The plasma concentration of 6MP varies during the clinical treatment from about 100 $\mu mol \cdot l^{-1}$ immediately after the i.v. administration to undetectable levels after 24 h[197]. The plasma pH value is maintained rigorously by the human body in the range from 7.35 to 7.45. In the human erythrocytes a mean pH value of 7.16 has been determined[210].

During recent years the adsorption of sulfur containing organic molecules has attracted tremendous research interest[211,212]. Widely studied and well-characterized systems include thiols, aliphatic[213-218] as well as aromatic[219-221] derivatives, and disulfides on gold and silver. It has been now well-established that aliphatic as well as aromatic

dithiols adsorb on gold as monothiolates by forming one single metal-S covalent bond. The other thiol group is pendent with respect to the metal surface. Aromatic thiol derivatives containing electron donor atoms are of particular interest because of their electronically and stereochemically versatile binding ability[222-227]. In addition, the adsorption of DNA building blocks and their structural properties is of great importance for understanding different biochemical and biophysical processes.

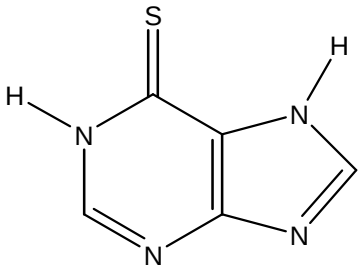

N1-H1, N7-H7

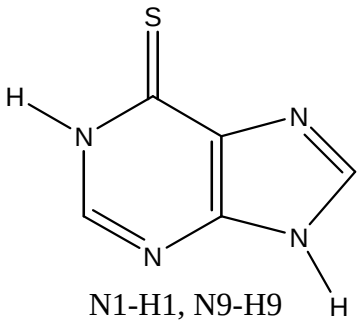

N1-H1, N9-H9

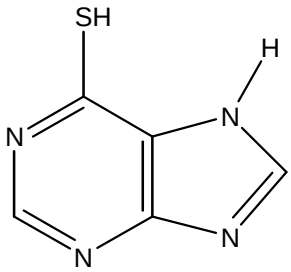

S-H, N7-H7

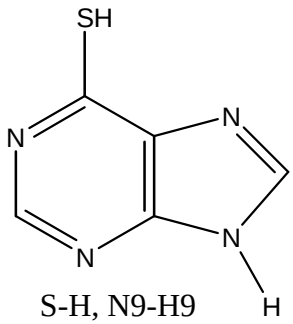

S-H, N9-H9

Scheme 8.1 Tautomeric forms of 6MP.

Extensive investigations of the adsorption mechanism of 6MP and its riboside derivative (6MPR) at physiological concentrations (10^{-4} – 10^{-6} mol·l^{-1}) and as a function of the pH value (3-11) were performed in the current study. Surface enhanced Raman scattering (SERS) spectroscopy (see Chapter 2.1), a versatile technique for providing information on the molecular structure of adsorbed species on metal nanoparticles, was applied to probe the interaction of the title compounds with the substrate. The Lee-Meisel silver colloid[55] served as a model artificial adsorption substrate. SERS spectra were recorded, and the vibrational modes were assigned with the help of DFT calculations[228,229] of the vibrational wavenumbers, Raman intensities, potential energy distribution[60,61,194] (PED) (see Chapter 3.2) and data from the literature[201-209,224,230]. In the first part of this

study, the molecular changes of 6MP and of the adsorbed species on the silver colloid with varying pH values and concentrations will be discussed. The chemical structure of the calculated tautomers is presented in Scheme 8.1. The orientation and the interaction of 6MP with the colloidal substrate were analyzed on the basis of the surface selection rules developed for SERS[52-54] and discussed in Chapter 2.1, and data from the literature for pyrimidine and purine derivatives[224,231-237]. The results obtained for the riboside derivative will be presented in the second part of this study.

Molecular structure

Figure 8.1 presents the optimized molecular structure of the thione and thiol tautomers of 6MP with the corresponding atom numbering. DFT calculations were carried out using the GAUSSIAN98 program[56]. The molecular structures of 6MP thiol and thione tautomers protonated at the N7 or N9 atoms were optimized, and the harmonic vibrational wavenumbers and the Raman scattering activities were calculated. Theoretical calculations for the anionic form of 6MP were also performed. The Becke[238] or the Becke's three-parameter[239] hybrid exchange functionals in combination with the Perdew-Wang 91 gradient-corrected correlation[240] functional were applied. The 6-311++G(d,p) basis set was employed.

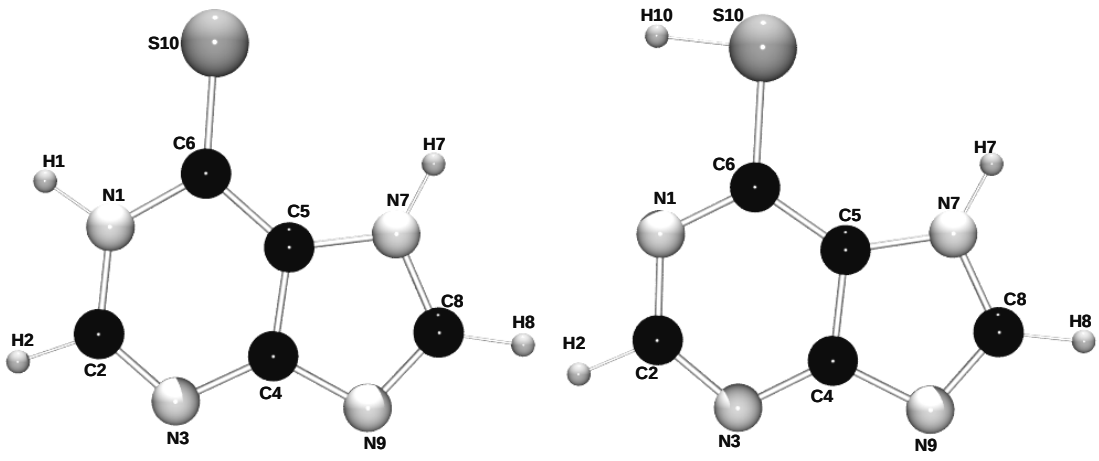

N1-H1, N7-H7 S-H, N7-H7

Figure 8.1 *Optimized molecular geometries of 6-mercaptopurine thione and thiol tautomers with the hydrogen at the N7 atom and the corresponding atom numbering.*

Table 8.1. *Selected structural parameters of 6MP and of the tautomeric forms optimized at the B3PW91/6-311++G(d,p) and BPW91/6-311++G(d,p) (in parentheses) level of theory.*

Bonds (pm)	Exp.		Calculated				
	6MP[58]	**6MP**[57]	**=S, N7-H7**	**=S, N9-H9**	**S-H, N7-H7**	**S-H, N9-H9**	**Anion, N7-H7**
N1-C2	135.8	135.0	136.8 (137.8)	(136.7)	(135.6)	133.9 (135.0)	(135.0)
C2-N3	130.9	130.7	129.4 (130.7)	(131.3)	(133.6)	133.2 (134.5)	(134.7)
N3-C4	136.1	136.4	136.1 (137.0)	(136.0)	(134.5)	132.7 (133.7)	(135.8)
C4-C5	139.4	139.7	139.8 (141.0)	(140.9)	(142.2)	140.1 (141.3)	(140.7)
C5-C6	140.5	139.6	141.0 (141.8)	(143.7)	(140.0)	139.9 (140.8)	(142.1)
N1-C6	137.2	138.4	138.9 (140.3)	(141.7)	(133.9)	133.0 (134.2)	(137.1)
C5-N7	137.3	137.0	136.5 (137.2)	(137.9)	(138.3)	137.7 (138.5)	(137.9)
N7-C8	135.2	134.6	136.3 (137.5)	(131.9)	(138.2)	130.6 (131.9)	(137.5)
C8-N9	133.3	132.6	131.4 (132.6)	(138.4)	(131.7)	137.4 (138.4)	(132.7)
C4-N9	136.0	136.3	136.4 (137.5)	(137.6)	(138.6)	137.2 (138.2)	(139.4)
C6-S	167.9	167.6	166.3 (167.3)	(166.2)	(177.9)	175.4 (176.7)	(172.2)
Angles (°)							
C2-N1-C6	124.7	125.4	125.3 (125.3)	(126.7)	(118.0)	118.6 (118.4)	(118.8)
N1-C2-N3	125.0	125.0	125.3 (125.4)	(124.6)	(128.5)	128.1 (128.4)	(130.9)
C2-N3-C4	113.5	113.0	113.7 (113.5)	(111.6)	(113.4)	111.8 (111.4)	(111.4)
N3-C4-C5	123.9	124.2	123.3 (123.4)	(128.6)	(122.9)	126.6 (126.8)	(122.2)
C4-C5-C6	121.7	121.9	123.4 (123.5)	(119.0)	(118.4)	115.5 (115.4)	(122.7)
C5-C6-N1	111.2	110.4	109.1 (108.8)	(109.5)	(118.7)	119.4 (119.6)	(114.0)
C4-C5-N7	105.8	105.9	105.4 (105.4)	(110.7)	(105.1)	111.1 (111.3)	(105.5)
C5-N7-C8	106.2	106.1	106.2 (106.3)	(104.6)	(106.0)	104.2 (104.1)	(106.5)
N7-C8-N9	113.5	113.6	113.4 (113.4)	(113.1)	(114.0)	113.6 (113.5)	(113.5)
C8-N9-C4	104.2	104.5	104.5 (104.3)	(106.5)	(104.5)	106.6 (106.7)	(104.1)
N9-C4-C5	110.4	109.9	110.4 (110.6)	(105.1)	(110.3)	104.5 (104.4)	(110.3)
S-C6-N1	122.2	122.6	123.1 (123.0)	(120.6)	(119.6)	117.6 (117.5)	(124.7)
S-C6-C5	126.6	127.0	127.8 (128.1)	(129.9)	(121.7)	123.0 (122.9)	(121.4)

Two independent crystal structure analyses[241,242] of 6MP monohydrate showed that the sulfur atom substituted at C6 is rather in the thione than in the thiol form. However, in solution, a tautomeric equilibrium between the two tautomeric forms may exist[201,243]. The crystal structure analyses of 6MP proved additionally the attachment of a hydrogen atom to the N7 atom[241,242]. The N9 substituted thione and thiol tautomers of 6MP are of interest and were also investigated by means of DFT calculations, since in the DNA chain the ribose ring is attached through the nucleosidic N9 substitution of the purine ring. Selected structural parameters of the optimized tautomeric forms and of the anionic 6MP are presented in Table 8.1 together with the corresponding data determined experimentally. The structural differences will be discussed shortly.

The calculated bond lengths of the 6MP, thione N7-H7 tautomer are in very good agreement with the the X-ray data[241,242]. The discrepancy between the calculated bond lengths and angles using the B3PW91 functional and the experimental data is less than 1.7 pm and 1.7°, respectively. The BPW91 functional led to similar results. The good agreement of this data is due to the fact that the N7-H7 thione tautomer is the tautomer observed in the X-ray analysis. Comparing the N7-H7 and N9-H9 optimized tautomers one can observe that the bond lengths N7-C8-N9 differ significantly (ca. 6 pm). Comparing the thiol S-H tautomers with the corresponding thione forms (both with the H-atom at the N7 or N9 position, respectively), major changes of the bond lengths involving the S and C6 atom can be observed (C6-S changes by 10.5 pm and N1-C6 by 7.5 pm). The other bond lengths of the pyrimidine unit vary by about 3 pm, while the imidazole ring bonds remain almost the same. In the case of 6MP the calculated structures possesses C_s symmetry, although the crystal structure analyses assessed a small deviation of the ring atoms from coplanarity.

The structural characteristics of the different tautomeric forms of 6MP will be employed in the following to analyze the vibrational spectra recorded in the solid state and in solution at different pH values in order to investigate the structural changes the title drug compounds undergo in aqueous solution and upon adsorption onto the metal surface.

Vibrational analysis.

Figure 8.2 presents the FT-Raman spectrum of solid 6MP monohydrate and the micro-Raman spectrum recorded in aqueous solution under basic conditions (pH 13). The calculated Raman intensities for the different optimized tautomers[244] are also plotted as

solid lines for comparison. Due to the low solubility of 6MP, only a few bands could be observed in the spectrum recorded under acidic conditions (pH 1). Bands at 436, 1262 (strongest), 1327 cm^{-1} in the spectrum at pH 1 correspond to the bands at 428, 1267 (broad) and 1318 cm^{-1}, respectively, in the spectrum of 6MP in basic solution.

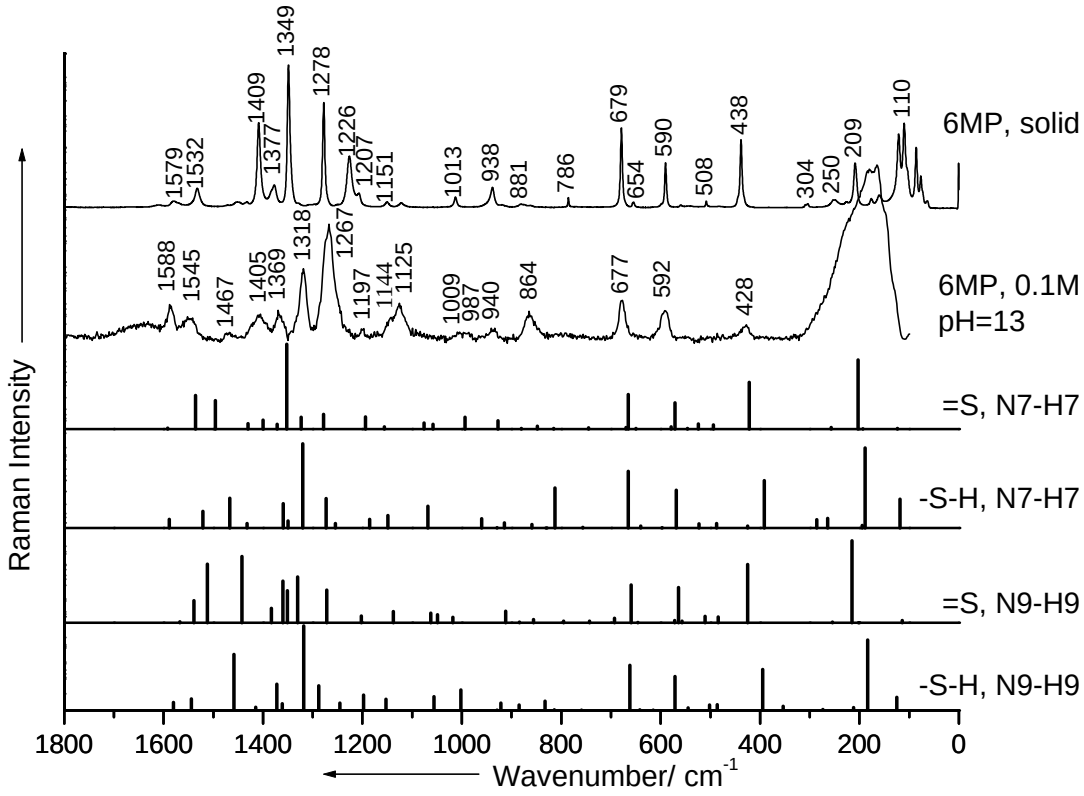

Figure 8.2 *FT-Raman spectrum of polycrystalline 6MP and micro Raman spectrum of 6MP recorded in solution at basic pH value in comparison to the calculated Raman intensities for the different tautomeric forms plotted as lines.*

Lapinski et al.[201] investigated the tautomeric behavior and physicochemical and vibrational properties of 6-mercaptopurine (thiopurine) by means of matrix isolation IR spectroscopy and quantum mechanical calculations. A detailed vibrational analyses was given for the most stable tautomeric forms (thione N1-H, N7-H and thiol N7-H). The IR data presented by Lapinski et al.[201] showed the thione N1-H, N7-H tautomer to be dominant in the solid form, but also the presence, although in minor quantity, of the thiol N9-H tautomer. Nevertheless, the formation of the thiol (N7-H) tautomer was observed

upon optical excitation of the thione N1-H, N7-H tautomer with UV light. The calculations of the vibrational wavenumbers and PED performed in the present study for the 6MP thione N1-H, N7-H and thiol N7-H tautomers are in very good agreement with the data published by Lapinski et al.[201] obtained from HF and DFT calculations and IR spectroscopy. The vibrational assignment for 6MP obtained in this study is also in good agreement with the assignment previously proposed by Vivoni et al.[203].

Nevertheless, in order to understand the complex molecular changes 6MP undergoes upon solvation and to determine the attachment sites of 6MP when it adsorbs to the model silver substrate at different concentrations and pH values, a closer examination of the vibrational characteristics of the tautomeric forms is necessary. Therefore, the experimental Raman and SERS wavenumbers are listed in Tables 8.2 and 8.3 together with the calculated values and their vibrational assignment for the thione N1-H, N7-H and thiol N7-H tautomeric forms. Calculated parameters for the thione and thiol species with a hydrogen atom at the N9 atom can be found in Tables 8.4 and 8.5.

The calculated vibrational wavenumbers at the BPW91 level of theory are in excellent agreement with the experimentally observed data (see Tables 8.2 and 8.3). As can be observed in Fig. 8.2, the calculated Raman intensities below 1000 cm^{-1} are also in good agreement with the experimental spectra. However, at higher wavenumbers the predicted Raman intensities deviate from the experimental intensities probably because of combination modes[201] and/or the high sensitivity of the polarizability derivatives, which are required to evaluate the Raman scattering activities[244] to the level of theory. Nevertheless, a qualitative accordance can be found.

The solubilized molecule (see Fig. 8.2 spectrum 6MP, ca. 0.1 M) presents a different vibrational pattern (wavenumbers and intensities) compared to the spectrum of the solid 6MP. These changes suggest a structural reorganization of the thione tautomer. The shift of the very strong band at 1349 cm^{-1} (Fig. 8.2) while going from the solid form to the aqueous solution presents the most striking difference. This mode was assigned mainly to the stretching of the C4-N9 and C4-C5 bonds (see Table 8.2) for the thione N7H tautomer and was calculated at 1352 cm^{-1} with very strong intensity (see Fig. 8.2, =S, N7-H7). Upon solvation, it is shifted to 1318 cm^{-1}. The DFT calculations predicted for the thiol tautomer the C4-N9 and C4-C5 stretching mode to arise at 1320 cm^{-1}. The strong band at 1409 cm^{-1} in the FT-Raman spectrum of solid 6MP significantly drops in intensity in aqueous solution. This mode could be mainly assigned to the N1-H bending vibration.

Table 8.2. *Experimental FT-Raman vibrational wavenumbers (cm^{-1}) observed for 6MP in crystalline form and the calculated wavenumbers (cm^{-1}) at the B3PW91/6-311++G(d,p) and BPW91/6-311++G(d,p) levels of theory for the thione, =S, N1-H, N7-H form with the calculated PED (%) assignment in parentheses.*

FT-Raman (cm^{-1})	BPW91 (cm^{-1})	Vibrational assignment
	3538	νN7-H(99)
3433vw	3493	νN1-H(99)
3098s	3186	νC8-H(98)
	3114	νC2-H(98)
1609vw	1592	ν(6-ring, (30) C5-C6, (20) C2-N3, (14) C5-N7, (8) C4-C5, (5) N1-C2)
1579vw	1536	νC2-N3(45) + δCN1H1(14) + νC5-C6(9) + νN1-C6(5) + νN3-C4(5)
1532vw	1496	νN3-C4(20) + νC4-C5(13) + νC5-N7(10) + νC8-N9(9) + $\delta^{in,\ 5,6}{}_{ring}$(21)
1432vw	1430	νC8-N9(30) + νN3-C4(14) + νC4-C5(10) + $\delta^{in,\ 5}{}_{ring}$(14)
1409ms	1400	δCN1H1(18) + νN7-C8(15) + νC5-N7(14) + νC8-N9(13) + νN1-C2(9) + δCN7H7(5)
1377w	1372	δCC2H2(25) + νN7-C8(12) + νC5-N7(11) + νC4-C5(9) + νN3-C4(8) + νC2-N3(7)
1349vs	1352	νC4-C5(20) + νC4-N9(20) + νN7-C8(11) + $\delta^{in,\ 5}{}_{ring}$(16) + δCN7H7(7)
1278s	1323	νC4-N9(34) + δCC2H2(29) + νN3-C4(9) + νC5-N7(5) + νN7-C8(5)
1226m	1278	νC8-N9(23) + νC4-N9(13) + νC5-C6(10) + νC5-N7(8) + νC2-N3(8) + νN1-C2(8)
1207sh	1194	δCC8H8(33) + $\delta^{in,\ 6}{}_{ring}$(23) + νC5-N7(10) + νC8-N9(6)
1151vw	1156	νN1-C6(42) + δCNH1(20) + νC6=S(17)
1122vw	1076	νN1-C2(28) + νN7-C8(23) + δCN7H7(17) + νC6=S(7) + δCN1H1(7)
1013vw	1058	νN7-C8(27) + δCN7H7(16) + νN1-C2(12) + νN1-C6(10) + δCC8H8(7)
938vw	994	$\delta^{in,\ 5,6}{}_{ring}$(43) + νC4-N9(15) + νC6=S(11) + δCN7H7(9) + δCC8H8(7)
881?	927	$\delta^{in,\ 5}{}_{ring}$(78) + νC4-C5(9)
786vw	880	δ^{out}CC2H2(87)
	848	$\delta^{in,\ 5,6}{}_{ring}$(62) + νC5-N7(7) + νC6=S(6) + νN3-C4(6)
	815	δ^{out}CC8H8(77) + $\delta^{out,\ 5}{}_{ring}$(18)
	745	$\delta^{out,\ 5,6}{}_{ring}$(91)

	670	δ^{out}CN1H1(69) + δ^{out}CC=S(10) + $\delta^{out,\ 5,6}{}_{ring}$(15)
679ms	665	$\delta^{in,\ 5,6}{}_{ring}$(41) + νN3-C4(22) + νC6=S(6) + νN1-C6(6)
654vw	650	$\delta^{out,\ 5,6}{}_{ring}$(86) + δ^{out}CC=S(7)
590w	579	δ^{out}CC=S(49) + $\delta^{out,\ 5,6}{}_{ring}$(33) + δ^{out}CN7H7(11)
	571	$\delta^{in,\ 5,6}{}_{ring}$(54) + νC5-C6(14) + δCC2H2(9)
560	546	$\delta^{out,\ 5,6}{}_{ring}$(82) + δ^{out}CN7H7(8) + δ^{out}CN1H1(7)
	524	$\delta^{out,\ 5,6}{}_{ring}$(48) + δ^{out}CN7H7(30) + δ^{out}CC=S(13) +
508	494	$\delta^{in,\ 6}{}_{ring}$(42) + δCN7H7(13) + δCC8H8(11)
438m	422	$\delta^{in,\ 6}{}_{ring}$(53) + νC6=S(19) + δCN1H1(8)
	257	$\delta^{butterfly}{}_{ring}$(71) + $\delta^{out,\ 5,6}{}_{ring}$(20)
209w	203	δCC=S(49) + δCN7H7(16) + δCC8H8(9)
	193	$\delta^{out,\ 5,6}{}_{ring}$(72) + δ^{out}CC=S(18)
121ms, 110ms	124	$\delta^{out,\ 5,6}{}_{ring}$(89)

ν *stretching*, δ *deformation*, in *in-plane*, out *out-of-plane*.

Table 8.3. *Experimental Raman vibrational wavenumbers (cm^{-1}) observed for 6MP in aqueous solution at pH 13, SERS data and calculated wavenumbers (cm^{-1}) at the BPW91/6-311++G(d,p) level of theory for the thiol, S-H, N7-H form with the calculated PED (%) assignment in parentheses.*

Raman Solution (cm^{-1})	SERS pH = 5 (cm^{-1})	SERS pH = 10 (cm^{-1})	Calc. (cm^{-1})	Vibrational assignment
			3564	νN7-H(99)
			3176	νC8-H(98)
			3106	νC2-H(98)
			2620	νS-H(99)
1588w	1586m	1571m	1589	νC5-C6(38) - νC5-N7(20) - $\delta^{in,\ 6}{}_{ring}$(12) + νC2-N3(6) + νC8-N9(6) - νN3-C4(6)
1545w	sh	1532w	1521	νN3-C4(34) - νC4-C5(22) - νN1-C2(10) + νN1-C6(6)
1467vw	1474s	1446sh	1467	νC8-N9(55) + $\delta^{in,\ 5}{}_{ring}$(18) - νC5-C6(9) + δNC8H8(9)

	1436w	1432w	1432	δNC2H2(30) - νC2-N3(23) + νN1-C6(16) - νC5-N7(7) + δCN7H7(5) + νN7-C8(5)
1369w	1387m	1387vw	1359	νN7-C8(36) + δCN7H7(25) + $\delta^{in,\ 5}{}_{ring}$(13) - δNC8H8(6)
			1350	νC5-N7(24) + νC2-N3(16) - νC4-C5(15) + δNC2H2(12) - νN3-C4(6) + $\delta^{in,\ 5}{}_{ring}$(6)
1318s	1325vs	1314sh	1320	νC4-N9(45) - νC4-C5(14) + $\delta^{in,\ 6}{}_{ring}$(9) - δNC2H2(9)
1267vs	1282s	1291	1273	νN1-C6(30) - νN1-C2(21) - νN3-C4(11) - δNC2H2(10) + νC4-C5(9) + $\delta^{in,\ 5}{}_{ring}$(5)
	1262sh	1246vw	1254	νC2-N3(26) - νC8-N9(20) + δNC8H8(14) - νC5-C6(9) - νN1-C2(8)
	1235sh			
1197vw	1207w	1209w	1186	δNC8H8(13) + νN1-C2(13) + $\delta^{in,\ 5,6}{}_{ring}$(30) - νC4-N9(9) + νN1-C6(9) - νC6-S(8)
1125w	1139m	1148w	1149	νC5-N7(22) - νN1-C2(18) + δNC8H8(12) + $\delta^{in,\ 6}{}_{ring}$(18) - νN1-C6(6) - νC2-N3(5)
			1068	νN7-C8(54) - δCN7H7(30) + δNC8H8(8)
1009vw	999s	998w	960	νC4-N9(22) + $\delta^{in,\ 5,6}{}_{ring}$ (36) - νC6-S(11) + νC4-C5(7) - δNC8H8(6) - δCSH(5)
940vw	949vw	949w	929	δ^{out}NC2H2(91) + $\delta^{out,\ 6}{}_{ring}$(9)
		918w	915	$\delta^{in,\ 5}{}_{ring}$(71) + νC4-C5(10) + δCN7H7(6)
864w	859s	870m	859	δCSH(43) + $\delta^{in,\ 5,6}{}_{ring}$(23) - νN1-C6(8) - νN1-C2(7)
			831	δ^{out}NC8H8(87)
	790vw	796vw	813	$\delta^{in,\ 5,6}{}_{ring}$(36) - δCSH(19) + νC6-S(11) - νN3-C4(6) - νC5-N7(6)
			757	$\delta^{out,\ 5,6}{}_{ring}$(85) - δ^{out}CCS(6)
677m	680vw	684vw	665	$\delta^{in,\ 5,6}{}_{ring}$(49) - νN3-C4(16) - νC6-S(9)
		625vw	640	$\delta^{out,\ 5,6}{}_{ring}$(81) - δ^{out}CCS(13)
			597	$\delta^{out,\ 5,6}{}_{ring}$(93)
592w	614vw		569	$\delta^{in,\ 5,6}{}_{ring}$(46) + νC5-C6(14) - δNC2H2(8) + νC4-N9(8) + δCSH(6)
	544vw		523	$\delta^{out,\ 5,6}{}_{ring}$(59) - δ^{out}CCS(33)
		487vw	488	$\delta^{in,\ 6}{}_{ring}$(37) - δCSH(14) - δCN7H7(11) - δNC8H8(10) - νC5-N7(6)
			425	δ^{out}CN7H7(69) + $\delta^{out,\ 5}{}_{ring}$(24)
428	433vw	447vw	392	νC6-S(46) + $\delta^{in,\ 6}{}_{ring}$(31) + δ^{in}CCS(6)
broad			286	$\delta^{out,\ 5,6}{}_{ring}$(69) - δ^{out}CSH(26)
			264	$\delta^{butterfly}{}_{ring}$(66) + $\delta^{out,\ 6}{}_{ring}$(17)
			195	$\delta^{out,\ 5,6}{}_{ring}$(32) - δ^{out}NC2H2(15) - δ^{out}CSH(15) + δ^{out}CCS(14) - δ^{out}CN7H7(10)

ν *stretching*, δ *deformation*, in *in-plane*, out *out-of-plane*.

Table 8.4. *Calculated wavenumbers (cm^{-1}) at the BPW91/6-311++G(d,p) level of theory for the thiol, S-H, N9-H form with the calculated PED (%) assignment in parentheses.*

BPW91/ 6-311++G(d,p) (cm^{-1})	Vibrational assignment
3564	νN9-H(99)
3181	νC8-H(98)
3111	νC2-H(98)
2595	νS-H(99)
1580	νN3-C4(36) + νC4-N9(15) + νC4-C5(9) + νN1-C6(7) + νC5-C6(7) + $\delta^{in,\ 6}{}_{ring}$(6)
1544	νC5-C6(31) + νC4-C5(19) + νC2-N3(8) + νN1-C2(8) + $\delta^{in,\ 6}{}_{ring}$(7)
1458	νN7-C8(46) + $\delta^{in,\ 5}{}_{ring}$(22) + δNCH8(9) + νC5-C6(5)
1415	δCCH2(31) + νN1-C6(23) + νC2-N3(9) + νC4-C5(7) + νC4-N9(15)
1372	νC8-N9(33) + δCNH9(25) + δNCH2(15) + νN1-C2(6)
1361	νC4-N9(38) + νC4-C5(10) + $\delta^{in,\ 6}{}_{ring}$(10) + νC5-C6(9) + νC5-N7(8) + νN7-C8(6) + νN3-C4(6)
1318	νC5-N7(29) + νC4-C5(15) + $\delta^{in,\ 5}{}_{ring}$(11) + νN1-C2(8) + νN1-C6(8) + δNCH8(7)
1288	νC2-N3(33) + νN1-C2(27) + νN1-C6(8) + νN3-C4(6) + νC5-C6(6)
1245	δNCH2(15) + νN1-C6(14) + νN7-C8(13) + δNCH8(12) + νN3-C4(9) + δCNH9(9)
1198	δNCH8(22) + $\delta^{in,\ 6}{}_{ring}$(29) + νN1-C2(10) + νC4-N9(7) + νC6-S(7) + νN1-C6(6)
1153	νC5-N7(24) + νN1-C2(14) + νC2-N3(11) + $\delta^{in,\ 6}{}_{ring}$(17) + νN1-C6(9) + δNCH8(9)
1056	νC8-N9(46) + δCNH9(35) + δNCH8(9)
1002	$\delta^{in,\ 5,6}{}_{ring}$(31) + νC4-N9(21) + νC6-S(16) + νC4-C5(8) + δCSH(6) + δNCH8(5)
929	δ^{out}NCH2(91) + $\delta^{out,\ 6}{}_{ring}$(9)
921	$\delta^{in,\ 5}{}_{ring}$(58) + δCSH(25) + νC4-C5(7)
885	$\delta^{in,\ 5,6}{}_{ring}$(46) + δCSH(30) + νN1-C6(6)
833	$\delta^{in,\ 5,6}{}_{ring}$(56) + νC6-S(7) + νN3-C4(6) + νC5-N7(6)
814	δ^{out}NCH8(82) + $\delta^{out,\ 5}{}_{ring}$(7)
759	$\delta^{out,\ 5,6}{}_{ring}$(83) + δ^{out}CCS(9)
662	$\delta^{in,\ 5,6}{}_{ring}$(50) + νN3-C4(13) + νC6-S(8) + νC4-N9(7) + νC5-N7(7)

642	$\delta^{out,\ 5,6}{}_{ring}(91)$
614	$\delta^{out,\ 5,6}{}_{ring}(85) + \delta^{out}CCS(12)$
572	$\delta^{in,\ 5,6}{}_{ring}(42) + \nu C5\text{-}C6(17) + \delta NCH8(8) + \delta^{in}CSH(5)$
545	$\delta^{out,\ 6}{}_{ring}(36) + \delta^{out}CNH9(37) + \delta^{out}CCS(20)$
502	$\delta^{out,\ 5,6}{}_{ring}(42) + \delta^{out}CNH9(44) + \delta^{out}CCS(10)$
486	$\delta^{in,\ 6}{}_{ring}(40) + \delta CNH9(15) + \delta NCH8(10) + \nu C4\text{-}N9(7) + \delta CSH(6) + \delta NCH2(6)$
395	$\nu C6\text{-}S(7) + \delta^{in,\ 6}{}_{ring}(32) + \delta^{in}CCS(6)$
354	$\delta^{out}CSH(94)$
273	$\delta^{butterfly}{}_{ring}(71) + \delta^{out,\ 6}{}_{ring}(11)$
212	$\delta^{out,\ 5,6}{}_{ring}(57) + \delta^{out}CCS(19) + \delta^{out}CSH(9) + \delta NCH8(5)$
183	$\delta^{in}CCS(51) + \delta^{in}CSH(34)$
125	$\delta^{out,\ 5,6}{}_{ring}(88)$

Table 8.5. *Calculated wavenumbers (cm^{-1}) at the BPW91/6-311++G(d,p) level of theory for the thion, =S, N1-H, N9-H form with the calculated PED (%) assignment in parentheses.*

BPW91/ 6-311++G(d,p) (cm^{-1})	Vibrational assignment
3557	$\nu N9\text{-}H(99)$
3479	$\nu N1\text{-}H(99)$
3181	$\nu C8\text{-}H(98)$
3121	$\nu C2\text{-}H(99)$
1567	ν(6-ring, 35 C2-N3, 14 C4-C5, 13 C5-C6, 12 N1-C2) + $\delta^{in?6}{}_{ring}(7) + \delta CCH2(6)$
1539	$\nu N3\text{-}C4(29) + \nu C4\text{-}N9(19) + \nu N7\text{-}C8(12) + \delta^{in,\ 6}{}_{ring}(11) + \nu C2\text{-}N3(8) + \nu C4\text{-}C5(8)$
1512	$\nu C5\text{-}C6(22) + \delta CNH1(20) + \nu C2\text{-}N3(18) + \nu C4\text{-}N9(6) + \nu C4\text{-}C5(6)$
1442	$\nu N7\text{-}C8(34) + \delta^{in,\ 5}{}_{ring}(17) + \nu N3\text{-}C4(13) + \delta CCH8(7) + \nu C8\text{-}N9(6) + \nu C4\text{-}C5(5)$
1383	$\nu C4\text{-}C5(17) + \delta CCH2(14) + \nu N1\text{-}C2(13) + \nu N7\text{-}C8(11) + \nu C4\text{-}N9(8) + \delta CNH1(8)$
1360	$\nu C4\text{-}N9(32) + \nu C4\text{-}C5(13) + \delta CCH2(8) + \nu C8\text{-}N9(7) + \nu N7\text{-}C8(6) + \delta CNH9(6) + \delta^{in,\ 5,6}{}_{ring}(11)$
1351	$\nu C5\text{-}C6(19) + \nu C5\text{-}N7(12) + \delta CNH1(11) + \nu N1\text{-}C2(8) + \nu C2\text{-}N3(8) + \nu C8\text{-}N9(8) + \nu N1\text{-}C6(6)$

1330	νC5-N7(20) + δCCH2(19) + $\delta^{in,\ 5,6}{}_{ring}$(21) + νC4-C5(9) + νC8-N9(9) + νN7-C8(6) + δCNH9(5)
1272	νC5-N7(28) + δCCH2(11) + δCCH8(10) + νN3-C4(9) + δCNH9(8) + νN7-C8(8) + νN1-C2(5)
1202	$\delta^{in,\ 6}{}_{ring}$(37) + δCCH8(30) + νC6=S(9) + νC5-N7(8) + νN1-C2(7) + νN7-C8(7)
1138	δCNH1(31) + νN1-C6(27) + νN1-C2(16) + νC6=S(10)
1062	νN1-C6(24) + νC6=S(18) + νN1-C2(16) + νC5-N7(7) + $\delta^{in,\ 5}{}_{ring}$(5)
1049	νC8-N9(43) + δCNH9(32) + δCCH8(10) + $\delta^{in,\ 5}{}_{ring}$(7)
1018	$\delta^{in,\ 5,\ 6}{}_{ring}$(34) + νC4-N9(16) + νN1-C6(9) + δCCH2(9) + νC6=S(8)
912	$\delta^{in,\ 5}{}_{ring}$(74) + νC4-C5(5)
884	δ^{out}CCH2(92)
856	$\delta^{in,\ 5,6}{}_{ring}$(69) + νN3-C4(7) + νC6=S(6) + νC5-N7(6)
795	δ^{out}CCH8(80) + $\delta^{out,\ 5}{}_{ring}$(8)
743	$\delta^{out,\ 5,6}{}_{ring}$(77) + δ^{out}CC=S(10) + δ^{out}CCH8(7)
693	δ^{out}CNH1(74) + δ^{out}CC=S(7) + $\delta^{out,\ 6}{}_{ring}$(9)
659	$\delta^{in,\ 5,6}{}_{ring}$(40) + νN3-C4(18) + νN1-C6(7) + νC4-N9(6) + νC5-N7(5)
646	$\delta^{out,\ 5,6}{}_{ring}$(94)
572	δ^{out}CC=S(40) + $\delta^{out,\ 5,6}{}_{ring}$(51)
564	$\delta^{in,\ 5,6}{}_{ring}$(50) + νC5-C6(17) + δCCH2(10)
557	$\delta^{out,\ 6}{}_{ring}$(39) + δ^{out}CNH9(39) + δ^{out}CC=S(6)
511	$\delta^{out,\ 5,6}{}_{ring}$(45) + δ^{out}CNH9(39) + δ^{out}CC=S(6)
484	$\delta^{in,\ 6}{}_{ring}$(42) + δCNH9(15) + δCCH8(11) + νC4-N9(6) + νN1-C6(6)
425	$\delta^{in,\ 6}{}_{ring}$(48) + νC6=S(15) + δCNH1(16)
253	$\delta^{butterfly}{}_{ring}$(64) + $\delta^{out,\ 5,6}{}_{ring}$(31)
215	δCC=S(54) + δCNH9(11) + δCCH8(9) + $\delta^{in,\ 6}{}_{ring}$(12)
201	$\delta^{out,\ 5,6}{}_{ring}$(86) + δ^{out}CCH2(9)
113	$\delta^{out,\ 5,6}{}_{ring}$(88)

The calculations for the thione N1-H, N7-H tautomer predicted a very weak mode at 1432 cm^{-1} corresponding to the C8-N9 stretching, while this mode is predicted at 1467 cm^{-1} for the thiol tautomer N7-H. Correspondingly, a band of very weak intensity arises at 1467 cm^{-1} in the aqueous solution spectrum of 6MP. Interestingly, the band at 1278 cm^{-1} becomes a very broad band with the strongest intensity and shifts to 1267 cm^{-1} in the Raman spectrum of the 6MP solution. A reasonable explanation could be that in the case of the thiol N7-H tautomer a new vibrational mode mainly due to the N1-C6 and N1-C2 stretching mode is predicted at 1273 cm^{-1}, while the C8-N9 stretching vibration assigned to the band at 1278 cm^{-1} for the thione form, which was calculated at 1278 cm^{-1} (see Table 8.2) is predicted at 1254 cm^{-1} for the thiol form (see Table 8.3). Moreover, this mode has strong contributions from the C2-N3 stretching vibration. The in-plane bending of the pyrimidine moiety at 1226 cm^{-1} in the solid spectrum is probably shifted to lower wavenumbers upon solvation and corresponds to the very weak mode at 1197 cm^{-1}.

Minor changes between the spectra recorded in solution and solid state can be observed below 1000 cm^{-1}. However, the bands with considerable intensity at 679 and 590 cm^{-1} (see Fig. 8.2) correspond to the same vibrations of the thione and thiol tautomers as shown by the theoretical calculations having strong contributions from the in plane bending of the purine ring. Nevertheless, the band at 864 cm^{-1} can be only observed in the spectrum recorded in solution. The calculations predicted for the thiol N7H form the SH bending mode with contributions from N1-C6 and N1-C2 stretching vibrations at 859 cm^{-1} which probably gives rise to the band at 864 cm^{-1} in the spectrum of the 6MP solution (see Fig. 8.2).

The Raman data of 6MP measured in aqueous solutions together with the DFT calculations indicate the formation of the thiol tautomer or probably the anionic form under basic conditions. The higher solubility of 6MP in basic solution also suggests the formation of $6MP^{-}Na^{+}$ species.

SERS spectra and the adsorption of 6-mercaptopurine

It is well established that SERS spectroscopy allows the determination of the adsorption sites and orientation of biological molecules as a function of the pH value and the concentration on metal surfaces (see Chapter 2.1). 6MP possesses possible binding sites to metals and biological targets at the nitrogen N1, N3, N7, N9 and the sulfur atoms. In previous studies, several metal complexes have been synthesized and characterized to

determine the coordination properties of 6MP[205,209]. Metal complexes show conjugate metal coordination to the S and N7 atoms or only to the S atom[205]. Recently, unusual purine-purine base pairing mostly via strong N(1)-H ··· $N(1)^-$ hydrogen bonding has been reported[209].

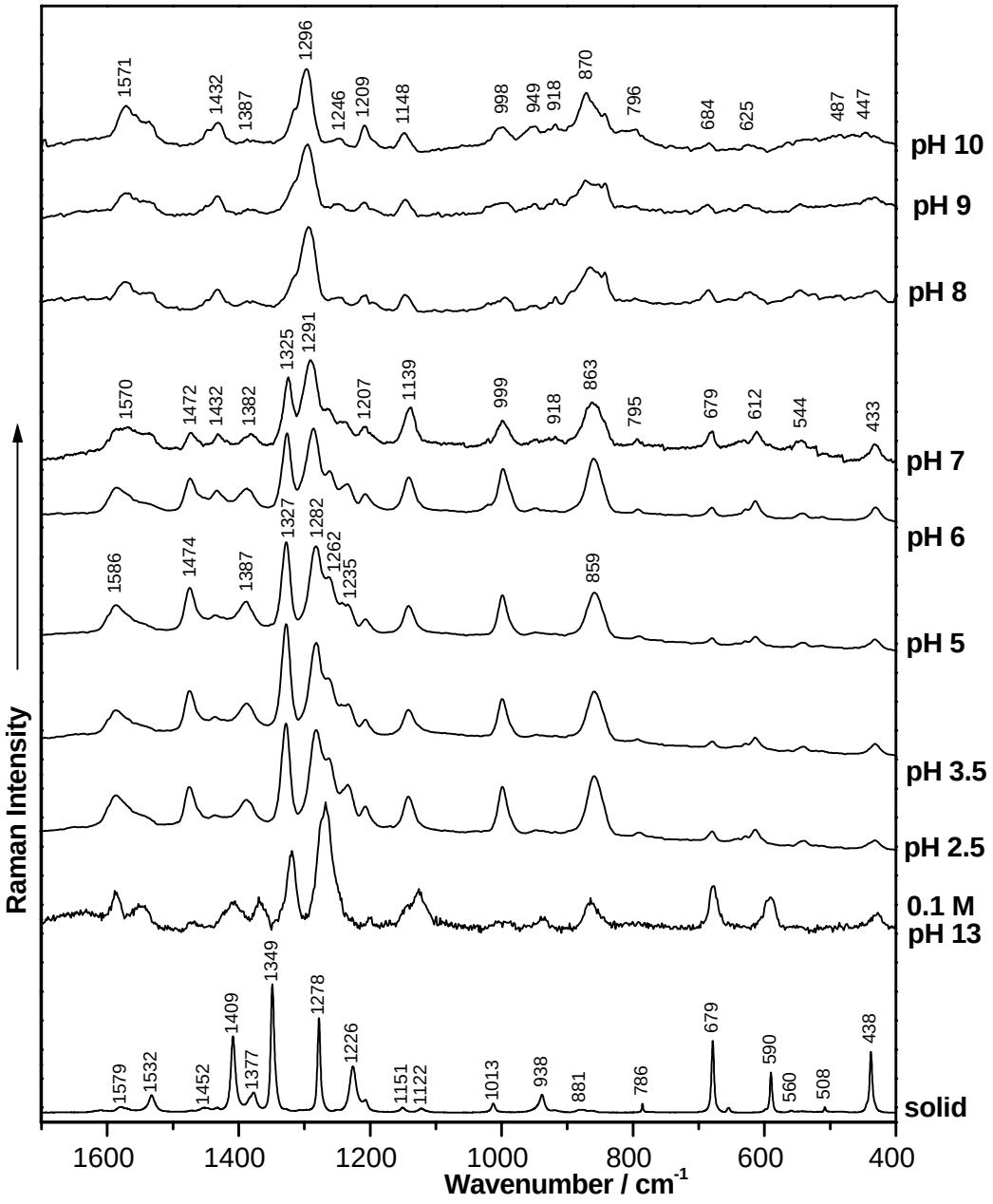

Figure 8.3 *SERS spectra of 6MP recorded at different pH values as indicated in the figure for the 10^{-5} M concentration. The FT-Raman spectrum of solid 6MP and the micro-Raman spectrum recorded in basic solution (0.1M) are plotted for comparison.*

In order to establish the most probable adsorption site of 6MP, the partial atomic charges have been computed via a natural population analysis (NPA). The results obtained for the different investigated tautomeric forms are summarized in Table 8.6. While for the thione tautomers the N1 atom is protonated, this is not the case for the thiol form, therefore N1 is an additional plausible binding site. Moreover, the thiol S-H, N7-H tautomer exhibits the highest negative partial charge on the N1 atom apart from the protonated N7 atom. The unprotonated N3 and N9 atoms in both the thione and thiol N7-H tautomers present similar charges which do not differ significantly between these tautomers. Nevertheless, the N9 atom has a slightly higher negative partial charge compared to the N3 atom (Table 8.6).

Table 8.6. *Selected partial atomic charges (e) obtained from NPA analysis at the BPW91/6-311++G(d,p) level of theory for the different tautomeric forms of 6MP.*

Atom	=S, N7-H	=S, N9-H	-S-H, N7-H	-S-H, N9-H	Anionic
N1	-0.53157	-0.53580	-0.49967	-0.49536	-0.53567
C2	0.26659	0.27497	0.24647	0.25632	0.22026
N3	-0.43878	-0.48113	-0.43829	-0.48008	-0.52198
C4	0.30564	0.30946	0.32490	0.33541	0.28653
C5	0.04580	0.03506	0.03714	0.02195	0.03202
C6	0.00230	0.00430	0.06778	0.08053	0.02496
N7	-0.50054	-0.42491	-0.52564	-0.46991	-0.52629
C8	0.22820	0.21117	0.24647	0.22595	0.18255
N9	-0.45237	-0.51939	-0.45272	-0.52866	-0.50244
S	-0.16311	-0.09943	0.04217	0.10606	-0.39568

Figure 8.3 presents the SERS spectra of 6MP recorded under acidic, neutral and basic conditions (at 10^{-5} M concentration) together with the Raman spectra recorded in the solid state and in aqueous solution (0.1 M). It can be seen that significant changes in the SERS spectra of 6MP when changing from acidic to basic conditions occur. For pH values ≤ 5 the SERS spectra are dominated by the bands at 1327 and 1282 cm^{-1}. The intensity of the band at 1282 cm^{-1} increases toward neutral pH values, at pH 6 it is more intense than the band at 1327 cm^{-1} (see Fig. 8.3). Moreover, it shifts to higher wavenumbers. This mode is found at pH 7 at 1291 cm^{-1}. At basic pH values it becomes the dominant band and is found at 1296 cm^{-1}, while the mode at 1325 cm^{-1} becomes a shoulder. These changes

suggest a gradual reorientation of the molecule with respect to the silver surface and/or the adsorption of 6MP through a different binding site to the substrate.

The spectra of 6MP recorded for basic pH values (8-10, Fig. 8.3) are very similar to the SERS spectrum of 6MP adsorbed on a silver electrode reported by Vivoni et al.[203] The band positions differ by up to 12 cm^{-1}, but the same intensity pattern is observed. The strongest mode at 1285 cm^{-1} in the spectrum of 6MP adsorbed on a silver electrode is found at 1296 cm^{-1} in the basic silver colloidal spectrum. The shoulder at 1310 cm^{-1} correlates to the shoulder at 1314 cm^{-1}, while the bands at 1572, 1532, 1430, 1375, 1233, 1202, 1140, 991, 865, 694 cm^{-1} in the SERS spectrum recorded by Vivoni et al.[203] correspond to the modes at 1571, 1536, 1432, 1387, 1246, 1209, 1148, 998, 870, 684 cm^{-1}, respectively, in the spectra measured in silver sol (see Fig. 8.3). The spectra recorded in the silver colloid show a high signal to noise ratio and a background in the low wavenumber region for basic pH values, which suggests a weaker binding of 6MP to the colloid than to the electrode.

Vivoni et al.[203] characterized the interaction of the adsorbate on the silver electrode being a head-on attachment of 6MP through the N1 position. In the vibrational assignment given by Vivoni et al.[203] the mode at 1285 cm^{-1} was attributed to the C2-N3 stretching mode. This assignment would be in agreement with our calculations for the thiol N9-H tautomeric form where a vibrational mode at 1288 cm^{-1} corresponding to the C2-N3 stretching mode with important contributions from the N1-C2 and N1-C6 stretching was predicted. In contrast, the vibrational analysis performed in this study based on DFT calculations of the thione and thiol tautomers with a hydrogen atom at the N7 position suggested the presence of the thiol form in aqueous solution, or probably of the deprotonated 6MP, S^- anionic form for basic pH values. In this case, the broad band at 1267 cm^{-1} could be assigned to two vibrational modes calculated at 1273 and 1254 cm^{-1} corresponding to the N1-C6 and N1-C2 stretching mode and the C2-N3 stretching with contribution from C8-N9 stretching, respectively. However, it should be mentioned that Vivoni et al.[203] performed their theoretical calculations for the anionic N9-H tautomer. Since the crystal structure analysis and the FT-Raman spectrum unequivocally showed the thione N7-H in the crystalline state, the thiol N7-H tautomer is probably formed upon solvation. Moreover, the DFT calculations of the Raman intensities and vibrational wavenumbers indicate the formation of the S-H, N7-H7 tautomer in solution. The differences in the adsorption and vibrational behaviors of 6MP and 6MPR also suggest the

N7-H7 tautomeric form of 6MP in solution (results presented in the second part of this study).

With the thiol N7-H tautomer present in solution, as presented in the previous section, the most enhanced vibration at 1296 cm^{-1} was assigned to the N1-C6 and N1-C2 stretching vibration (see Fig. 8.4 for the representation of this mode) and not to the C2-N3 streching mode as proposed by Vivoni et al.[203] Comparing the SERS spectra of 6MP recorded for basic pH values to the Raman spectrum in aqueous basic solution, the N1-C2 stretching mode is shifted by about 20 cm^{-1}. This shift indicates an increase in electron density on the N1 atom and thus the coordination via the N1 atom of 6MP to the silver surface. An increase in electron density on the coordinated atom leads to an increase of the vibrational wavenumbers of the modes involving this atom. However, Vivoni et al.[203] also proposed the adsorption of 6MP on a silver electrode via the N1 atom.

Further support for the N1 coordination is the complete absence of the band at 1409 cm^{-1} corresponding to the CN1-H1 bending mode in the SERS spectra recorded for basic pH values. Other vibrational modes involving the N1-C2 stretching mode are also shifted to higher wavenumbers and are enhanced in intensity as compared to the Raman spectrum recorded in aqueous solution. The mode at 1209 cm^{-1} probably corresponds to the weak band at 1197 cm^{-1} in the Raman spectrum of solution 6MP assigned to N1-C2 stretching and purine ring deformation (see Table 8.3, Fig. 8.3, basic pH). The neighboring band at 1148 cm^{-1} can be assigned to the C5-N7 and C1-N2 stretching mode and is also enhanced in the SERS spectrum. In the low wavenumber region the most prominent band in the SERS spectra recorded for basic pH values is the mode at 870 cm^{-1}, which was assigned to a deformation mode combined with the N1-C6 and N1-C2 stretching vibrations.

The band at 1318 cm^{-1} corresponding to C4-N9 stretching mode in the solution spectrum is shifted to lower wavenumbers at 1314 cm^{-1} in the SERS spectrum indicating a decrease of the electron density on the imidazole unit. The same is valid for the C6-C5-N7 stretching mode at 1588 cm^{-1} (Fig. 2) which is shifted to 1571 cm^{-1} in the SERS spectrum (see Fig. 3). The weak band at 1246 cm^{-1} in the SERS spectrum is probably due to the C2-N3 and C8-N9 stretching modes.

Hence, the vibrational analysis of the SERS spectra of 6MP recorded for basic pH values indicates that the adsorption of 6MP on the silver colloid under basic conditions occurs via the N1 atom similarly to the adsorption of 6MP on silver electrode suggested by Vivoni et al.[203] The calculations of the partial charges also substantiate this finding, since

the N1 atom has the highest negative charge among the unprotonated nitrogen atoms in the case of the thiol form (see Table 8.6).

In contrast, the SERS spectra recorded for acidic and neutral conditions (see Fig. 8.3, pH 2.5-7) present a different vibrational pattern and much lower signal to noise ratio than the spectra recorded under basic conditions. Moreover, several modes corresponding to ring stretching vibrations are significantly enhanced. Therefore, the interaction of 6MP with the colloidal substrate at acidic pH is stronger than under basic conditions and probably occurs through many binding sites. The strongest mode arises at 1327 cm^{-1} corresponding to the C4-N9 stretching vibration. As previously mentioned, this mode drops gradually in intensity and is shifted to lower wavenumbers toward neutral pH values. The band at 1282 cm^{-1} assigned to the N1-C2 and N1-C6 stretching mode also possesses very strong intensity. The bands at 1474 and 999 cm^{-1}, showing weak intensity in the solid state and aqueous solution Raman spectra (see Figs. 4 and 2), appear exceedingly pronounced. The band at 1474 cm^{-1} has been assigned to the C8-N9 stretching of the thiol form (Table 3), while the band at 999 cm^{-1} is due to the C4-N9 stretching and ring deformation mode. Moreover, the broad band at 1262 cm^{-1} in the solution spectrum is well resolved and two shoulders at 1262 and 1235 cm^{-1} can be observed in the SERS spectra. The mode at 1262 cm^{-1} involves the C2-N3 stretching vibration, while the band at 1235 cm^{-1} is probably due to the in-plane bending of the pyrimidine moiety.

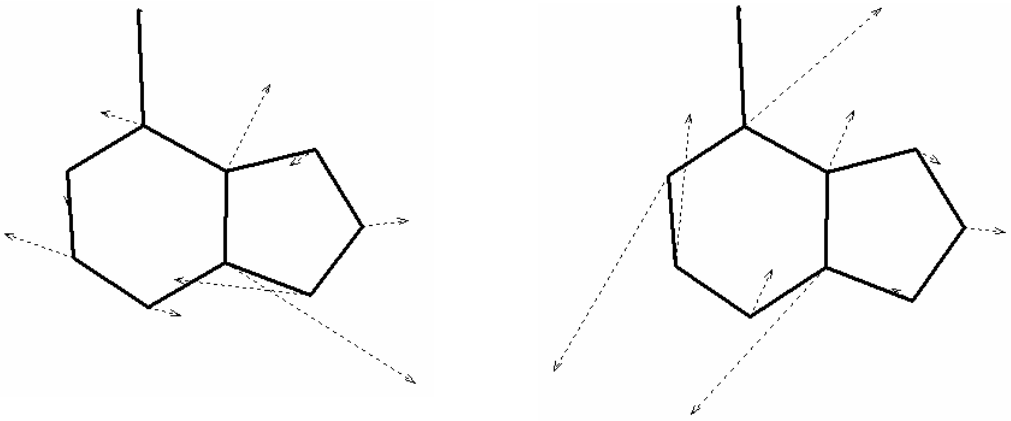

1320 cm^{-1} (1318 cm^{-1}, see Fig. 2) 1273 cm^{-1} (1267 cm^{-1}, see Fig. 2)

Figure 8.4 *Representative vibrational modes of 6MP (BPW91/6-311++G(d,p) level). Experimental wavenumbers are given in parentheses.*

The high enhancement of the ring vibrational modes mainly involving the stretching modes of the N9 atom indicate the coordination of the molecule to the silver surface through the N9 atom. In addition, interaction through the N3 atom of the 6MP molecules with the substrate is also likely. Based on the surface selection rules[52-54] discussed in Chapter 2.1, a perpendicular orientation of 6MP is proposed for acidic pH values. The ring stretching modes show large changes of the polarizability components in the *z*-direction when the molecule is adsorbed perpendicular on the substrate. Moreover, in the case of a perpendicular orientation of the molecule on the metal surface via the N9 and N3 atoms, the N1-C2 stretching vibration at 1282 cm^{-1} (see Figs. 8.3, pH 5 and 8.4) undergoes changes of the polarizability tensor components along the *z*-direction, which is in agreement with its significant enhancement under acidic conditions.

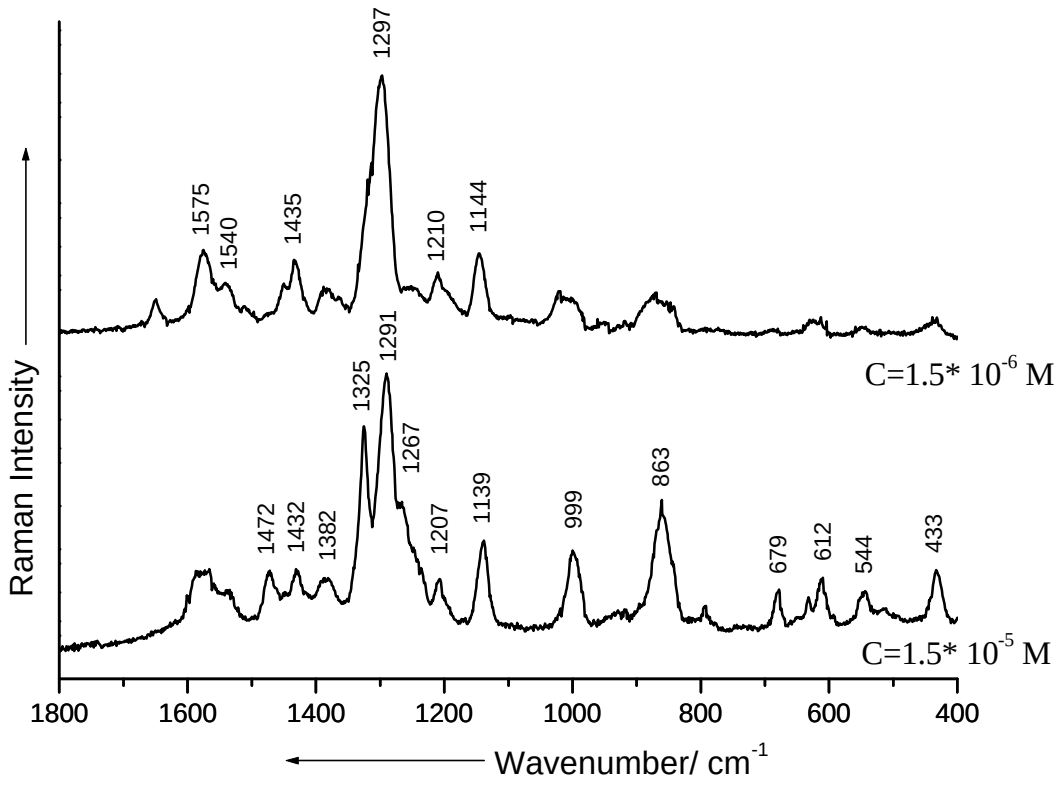

Figure 8.5 *SERS spectra of 6MP recorded at different concentrations as indicated under neutral conditions.*

A precise determination of the adsorption orientation of 6MP on the colloidal Ag surface under basic conditions is quite difficult. The spectra recorded for different concentrations at neutral pH value are presented in Fig. 8.5. For 10^{-6} M concentration the SERS spectrum resembles the SERS spectra recorded under basic conditions. The general decrease in intensity of the ring stretching modes suggests a tilted orientation of the adsorbate to the silver surface at lower concentrations and basic pH values. The increase in wavenumber of the band at 863 cm^{-1} (at pH = 7, Fig. 3) to 870 cm^{-1} (pH =10) also indicates a tilted orientation (see vide-infra).

Moreover, the fact that the band intensities corresponding to ring stretching modes decrease gradually from pH 5 to 8 (see Fig. 8.3) indicates that the molecule reorients gradually on the surface. A possible explanation for the reorientation of the adsorbed molecules toward basic pH values could be that the concentration of adsorbed molecules decreases[217] when NaOH is added. The pH value, at which a decrease of the adsorption of 6MP seems to start, is at about pH = 6. Between pH = 8 and 10 the SERS spectra of 6MP do not change significantly. Similar pH dependence of the adsorption strength was reported for adenine. The strongest interaction of adenine with silver colloid has been observed[236] around pH = 4.

In order to understand the activity of the 6MP drug in the treatment of leukaemia, it is reasonable to compare the adsorption behavior of 6MP with hypoxanthine, the purine derivative with a C6=O substituent, and adenine, the derivative with an amino group at the C6 atom. In the case of adenine several studies have been reported[233-235,237] and the proposed interaction mechanisms are often contradictory. A recent study based[232] on DFT calculations and vibrational analysis of the deuterated analogues proposes the adsorption of the adenine molecule via the N7 atom with additional interaction through the amino group. An almost perpendicular orientation has been determined. In the study of Giese and McNaughton[232] no concentration dependence of the SERS spectra has been observed. Nevertheless, Kim et al.[237] observed a concentration dependent shift of the ring breathing mode toward higher wavenumbers and proposed the reorientation of the adenine molecule on silver colloid from perpendicular to almost parallel. A pH dependent SERS study[235] on a silver electrode revealed no significant changes of the SERS spectra. At pH = 3, protonation of the adenine molecule has been observed, but the vibrational wavenumbers and band intensities remained basically unchanged. In contrast, the SERS spectra of 6MP in the present study indicate several changes for different pH values. While the SERS

spectra of adenine are dominated by the ring breathing mode[235], the SERS spectra of 6MP are dominated by ring stretching modes around 1300 cm^{-1}.

Hypoxanthine also exists[231,243] in two tautomeric forms, namely keto- and enol-forms. The keto tautomer has been identified in the solid state, while at alkaline pH the enol form predominates[231]. Nevertheless, in hypoxanthine and adenine the N9 atom is hydrogen substituted and not the N7 atom as in the case of 6MP. Hypoxanthine, adenine and other purine derivatives and DNA bases present a characteristic ring breathing mode of the pyrimidine unit around 720 cm^{-1}. The ring breathing mode is also a marker band in the SERS spectra of these compounds. The ring breathing mode could also be observed for caffeine, a methylated xanthine derivative[245]. In contrast, such a mode has not been observed in the case of 6MP either in the thione or in the thiol tautomers. However, 6MP thiol present a stretching mode coupled with deformation vibration of the pyrimidine unit at 864 cm^{-1} (see Fig. 8.2), which is also present in our SERS spectra (Fig. 8.3).

The SERS spectra of hypoxanthine[231], at acidic and neutral conditions, is dominated, similar to the spectra of 6MP, by ring stretching modes. Toward basic pH values, their relative intensities drop substantially. Concomitantly, the shift of the ring breathing mode to higher wavenumbers has been observed.

For an acidic pH value, a perpendicular orientation of hypoxanthine has been proposed, where the molecule is adsorbed through the N3 atom[231]. In contrast, the SERS spectra recorded in the present study indicate the adsorption of 6MP through the N9 and possibly the N3 atoms under acidic conditions. The interaction of 6MP through the N9 atom with the silver colloid is further supported by the differences between the SERS spectra recorded in an acidic medium for the base and its riboside derivative, where the N9 atom is substituted. These data are presented in the second part of this study. For basic pH values the hypoxanthine molecule is oriented nearly parallel on the metal surface via nonbonding electrons of N1 and O6[231]. The ring breathing mode of hypoxanthine is shifted by 22 cm^{-1} when going from acidic to basic conditions, when the molecule changes from a perpendicular to a parallel orientation. In the case of 6MP, the shift of the band at 859 cm^{-1} for an acidic pH value toward basic conditions is about 11 cm^{-1} suggesting that the 6MP molecule is significantly tilted under basic conditions. Another reason for the vibrational shift and decrease in intensity of this mode could be the deprotonation of the thiol moiety at basic pH values. Nevertheless, Vivoni et al.[203] proposed a head-on orientation of adsorbed 6MP (via N1) on a silver electrode. However, in the SERS spectra reported by

Vivoni et al.[203] the band at 865 cm^{-1} is well resolved and has the strongest intensity except for the band at 1285 cm^{-1}, but for a basic colloidal silver it is shifted to 870 cm^{-1} (see Fig. 3). The spectra recorded at different concentrations at neutral pH also indicate a tilting of the adsorbed molecule.

Conclusion

In this subchapter a detailed vibrational analysis of 6-mercaptopurine was carried out. The Raman spectra of the crystalline form and of the solvated molecule in aqueous solution at basic pH values were recorded and analyzed with the help of DFT calculations for the thione and thiol tautomeric forms. Raman spectroscopy, in conjunction with DFT calculations, proved to be adequate to distinguish between the different tautomeric forms of 6MP, which the molecule adopts in the solid state and in solution. In the crystalline form, the thione (N1-H, N7-H) tautomer is present, but in solution the thiol form (S-H, N7-H) is present. The adsorption behavior of 6MP at physiological concentrations and as a function of the pH value was investigated by means of SERS spectroscopy. Significant changes in the SERS spectra occurred for different pH values and concentrations. Under acidic conditions stronger interaction of 6MP with the substrate was observed probably through the N9 and N3 atoms with a perpendicular orientation of the molecule on the substrate. From pH 6 toward pH 8 a reorientation of the adsorbate occurs with spectral modifications similar to the changes observed in the spectra recorded for different concentrations. Therefore, a decrease in the concentration of the adsorbed molecules on the silver substrate for basic pH values is proposed. At low concentrations and basic pH values the molecule is adsorbed via the N1 atom with a tilted orientation relative to the substrate.

8.2 Adsorption of 6-Mercaptopurine-Riboside

Motivation

As described in Chapter 2.1 and the previous subchapter, surface enhanced Raman spectroscopy is a highly sensitive and selective technique to obtain structural information on molecules at aqueous/ solid interfaces. As many biophysical processes take place at interfaces, SERS spectroscopy became a widely used technique in the field of biophysics. Special interest has been accorded to the adsorption of DNA bases and related derivatives[203,224,227,231-237,245-247], sulfur containing derivatives able to form self-assembled monolayers[211,215,220,221,225,226], etc. Moreover, SERS spectroscopy allows the determination of the adsorption sites of molecules and their orientation on metal surfaces.

6-mercaptopurine (6MP) and its derivatives are used in the conventional chemotherapy of patients with acute lymphoblastic leukemia (ALL)[195-200,230]. However, the adsorption of 6MP is rather poor, and therefore the intravenous (i.v.) administration of its riboside derivative (6MPR) has been re-evaluated[200]. The i.v. administration of 6MPR showed less interindividual variation and higher red blood cell level in children undergoing cancer chemotherapy. The application of 6MPR yields stable blood levels of active drug. Moreover, 6MP is a prodrug requiring intracellular activation to thiopurine nucleotides to exert antileukemic effect.

In this part, an attempt to determine the adsorption similarities and differences between 6MPR and the free purine base on a Ag surface was undertaken by means of SERS spectroscopy. In the previous section (see Chapter 8.1) a detailed analysis of the adsorption behavior of 6-mercaptopurine (6MP) on colloidal silver was expantiated. In the current subchapter, the interaction of 6MPR with the silver colloid at physiological concentrations[197] (10^{-4} – 10^{-6} M) and as a function of pH value (3-11) is analyzed. First, a comparison of the optimized molecular structure of 6MPR with the crystal structure is presented. Furthermore, the structural changes 6MPR undergoes upon solvation in basic and acidic media are investigated. The vibrational modes of the title molecule were assigned with the help of DFT calculations and data from the literature for related nucleosides[248,249] as well as the comparison of 6MPR with 6-mercaptopurine[201,203] and D-ribose[249,250]. Finally, the SERS spectra of 6MPR were presented and the adsorption mechanism analyzed. The active molecular site was proposed and the orientation of the

molecule on the silver colloid was determined based on the SERS[52-54,233] "surface selection rules" (see Chapter 2.1). The effect of the ribose ring on the adsorption behavior of the mercaptopurine moiety on the silver colloid was discussed.

Molecular structure

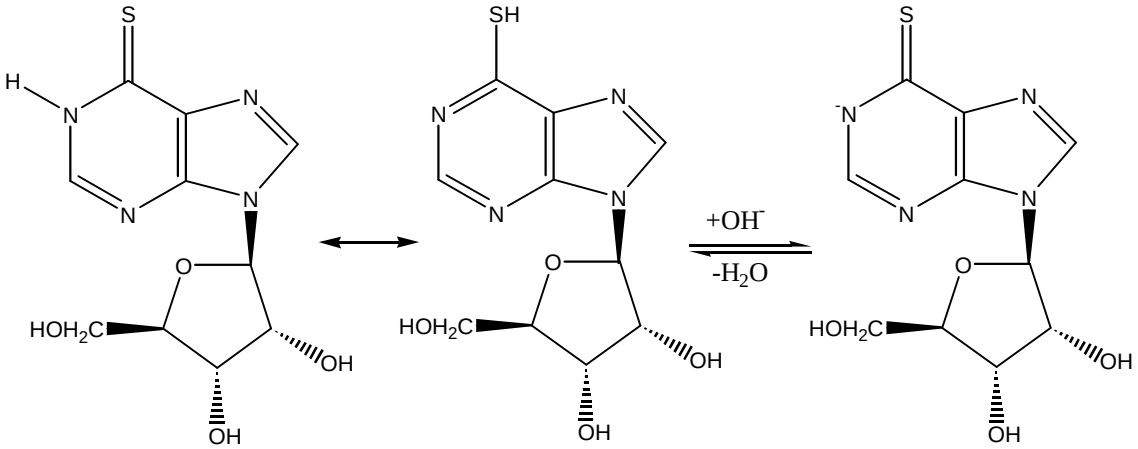

thion 6MPR thiol 6MPR anionic 6MPR

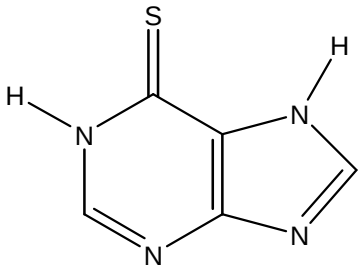

6MP, N1-H, N7-H

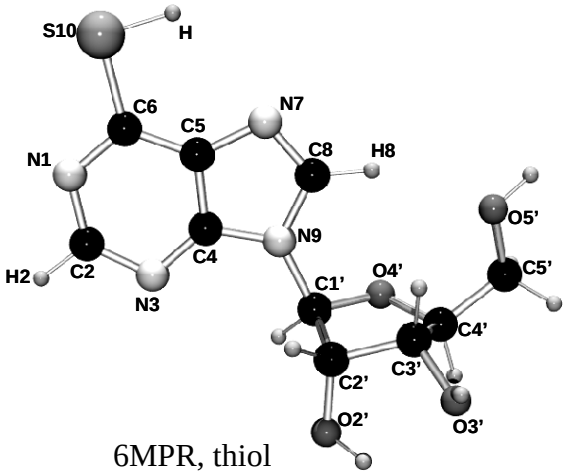

6MPR, thiol

Figure 8.6 *Molecular structures of the thion and thiol tautomers and anionic species of 6MPR and of the thion 6MP tautomer. The atom numbering is given for the optimized structure of the 6MPR thiol tautomer.*

Figure 8.6 presents the molecular structure of the thion and thiol tautomers and anionic species of 6MPR, and also the thion form of crystalline 6MP for comparison. The

optimized molecular structure of the thiol tautomer is also included with the corresponding atom numbering. Selected structural parameters of the calculated tautomeric forms and of the experimentally determined parameters of the crystalline compounds[251] are given in Table 8.7. The X-ray analysis of 6MPR showed two unique molecules in the crystal[251] which are involved in a complex intra- and intermolecular hydrogen bonding network. Similarly to the parent purine base 6MP[241,242] (see Chapter 8.1), 6MPR can be also found in the thione form in the crystal unit. The discrepancy between the experimentally determined structure and the calculated molecular structure of the corresponding thione tautomer are similar to those obtained in the case of 6MP[252]. The bond lengths deviate by up to 1.9 pm and the bond angles by 2° (Table 8.7). Moreover, the calculated bond lengths at the B3PW91/6-311++G(d,p) level generally lie in between the values of the two corresponding parameters of the 6MPR molecules found in the crystal packing. Interestingly, if one compares the calculated structural parameters of the 6MPR tautomers with the parameters of the 6MP tautomers with a hydrogen bond to the N9 atom, almost the same parameters for the purine ring bonds and angles can be found (see Table 8.7) indicating that the gas phase molecular structure of the purine backbone of 6MPR does not depend considerably on the ribose substituent. Nevertheless, as will be presented in the next section, the vibrational modes of the purine unit are affected by the ribose substituent through vibrational coupling which has also been observed for other nucleosides[248,253].

The crystal structure analyses showed the purine ring of both 6MP[241,242] and 6MPR[251] to be almost coplanar. The DFT calculations determined a very small deviation of the purine ring atoms from planarity in the case of 6MPR, but determined a C_s symmetrical molecule in the case of 6MP.

Nevertheless, the conformation of the computed structure does not correspond to the conformation found in the solid state. In the solid state strong intramolecular hydrogen bonding between the O5'-H-atom and the N3 atom was found[251] while for the optimized structure the ribose ring is rotated with respect to the purine ring, and the optimized structure corresponds to the *anti* rotamer, whereas both 6MPR molecules observed in the crystal structure adopt the *syn* conformation. Nevertheless, the majority of X-ray structural analyses of purine nucleosides show a preference for the *anti*-conformation in the solid state[251]. Theoretical calculations for adenosine[248] and guanosine[253] also led to the *anti*-conformer in the gas phase similarly to the calculations for 6MPR.

Table 8.7. *Selected structural parameters of 6MP and 6MPR and of the tautomeric forms optimized at the B3PW91/6-311++G(d,p) and BPW91/6-311++G(d,p) level of theory (in parantheses). The structural X-ray data 6MP and two 6MPR molecules found in the polycrystalline unit are also listed.*

Bonds	Exp.		Calculated			
(pm)	**6MP**	**6MPR***	**6MP, =S, N9-H9**	**6MP, S-H, N9-H**	**6MPR, =S**	**6MPR, S-H**
N1-C2	135.8	136.5 (134.9)	(136.7)	133.9 (135.0)	135.8 (136.7)	133.9 (135.0)
C2-N3	130.9	128.5 (131.8)	(131.3)	133.2 (134.5)	130.0 (131.3)	133.2 (134.5)
N3-C4	136.1	134.8 (135.9)	(136.0)	132.7 (133.7)	135.3 (136.1)	132.8 (133.8)
C4-C5	139.4	138.3 (138.1)	(140.9)	140.1 (141.3)	139.7 (141.0)	140.2 (141.3)
C5-C6	140.5	141.4 (144.0)	(143.7)	139.9 (140.8)	142.8 (143.5)	139.8 (140.7)
N1-C6	137.2	138.3 (138.1)	(141.7)	133.0 (134.2)	140.2 (141.7)	133.1 (134.2)
C5-N7	137.3	136.8 (138.8)	(137.9)	137.7 (138.5)	136.9 (137.8)	137.5 (138.3)
N7-C8	135.2	133.1 (131.9)	(131.9)	130.6 (131.9)	130.8 (132.1)	130.9 (132.2)
C8-N9	133.3	136.6 (137.7)	(138.4)	137.4 (138.4)	138.0 (139.0)	137.9 (138.9)
C4-N9	136.0	139.1 (137.4)	(137.6)	137.2 (138.2)	136.7 (138.0)	137.5 (138.7)
C6-S	167.9	167.1 (166.7)	(166.2)	175.4 (176.7)	165.5 (166.5)	175.6 (176.9)
N9-C1’		143.7 (146.8)			146.1 (147.2)	146.0 (147.2)
C1’-C2’		152.8 (151.0)			153.5 (154.4)	153.4 (154.4)
C2’-C3’		151.6 (151.7)			153.6 (154.7)	153.6 (154.7)
C3’-C4’		155.4 (151.5)			152.9 (153.9)	152.9 (153.8)
C4’-C5’		149.2 (153.8)			151.2 (152.0)	151.1 (152.0)
C2’-O2’		140.5 (140.3)			140.8 (142.2)	140.7 (142.2)
C3’-O3’		142.2 (143.5)			141.8 (143.6)	141.8 (143.5)
C4’-O4’		145.6 (144.5)			142.9 (144.5)	142.9 (144.5)
C1’-O4’		140.9 (141.0)			140.9 (142.6)	141.0 (142.6)
C5’-O5’		143.9 (140.2)			142.0 (143.6)	142.1 (143.7)

Angles (°)								
C2-N1-C6	124.7	124.1 (126.8)		(126.7)	118.6 (118.4)		126.5 (126.6)	118.5 (118.3)
N1-C2-N3	125.0	125.5 (123.9)		(124.6)	128.1 (128.4)		124.5 (124.5)	128.1 (128.3)
C2-N3-C4	113.5	112.2 (112.7)		(111.6)	111.8 (111.4)		112.1 (111.9)	111.9 (111.6)
N3-C4-C5	123.9	127.9 (126.5)		(128.6)	126.6 (126.8)		128.1 (128.3)	126.5 (126.7)
C4-C5-C6	121.7	118.7 (119.5)		(119.0)	115.5 (115.4)		119.0 (119.1)	115.4 (115.4)
C5-C6-N1	111.2	111.6 (110.5)		(109.5)	119.4 (119.6)		109.8 (109.7)	119.6 (119.7)
N3-C4-N9	125.7	127.1 (127.5)		(126.3)	128.9 (128.7)		126.2 (126.1)	121.5 (128.4)
C6-C5-N7	132.5	129.0 (129.5)		(130.3)	133.4 (133.3)		130.6 (130.4)	133.6 (133.5)
C4-C5-N7	105.8	112.3 (111.0)		(110.7)	111.1 (111.3)		110.4 (110.6)	111.0 (111.1)
C5-N7-C8	106.2	103.1 (103.6)		(104.6)	104.2 (104.1)		104.8 (104.7)	104.3 (104.2)
N7-C8-N9	113.5	114.1 (113.7)		(113.1)	113.6 (113.5)		113.2 (113.3)	113.7 (113.7)
C8-N9-C4	104.2	105.0 (105.7)		(106.5)	106.6 (106.7)		105.8 (105.8)	106.0 (106.0)
N9-C4-C5	110.4	105.0 (106.0)		(105.1)	104.5 (104.4)		105.7 (105.6)	105.0 (105.0)
S-C6-N1	122.2	121.7 (122.1)		(120.6)	117.6 (117.5)		120.5 (120.4)	117.6 (117.5)
S-C6-C5	126.6	126.7 (127.3)		(129.9)	123.0 (122.9)		129.7 (130.0)	122.8 (122.7)
C4-C9-C1’		129.1 (129.2)					126.0 (125.9)	125.8 (125.8)
C8-C9-C1’		124.6 (124.1)					128.2 (128.3)	128.1 (128.2)
C9-C1’-C2’		114.0 (133.6)					113.1 (113.3)	113.3 (113.4)
C9-C1’-O4’		110.1 (108.4)					108.9 (108.9)	108.8 (108.9)
O4’-C1’-C2’		105.7 (106.1)					107.0 (107.2)	107.0 (107.1)

* parameters of the second molecule in parenthesis.

The structural characteristics of the different tautomeric forms of 6MPR will be employed in the following to analyze the vibrational spectra recorded in solid state and in solution for different pH values in order to get information on the structural changes the title molecule undergoes in aqueous solution.

Vibrational analysis

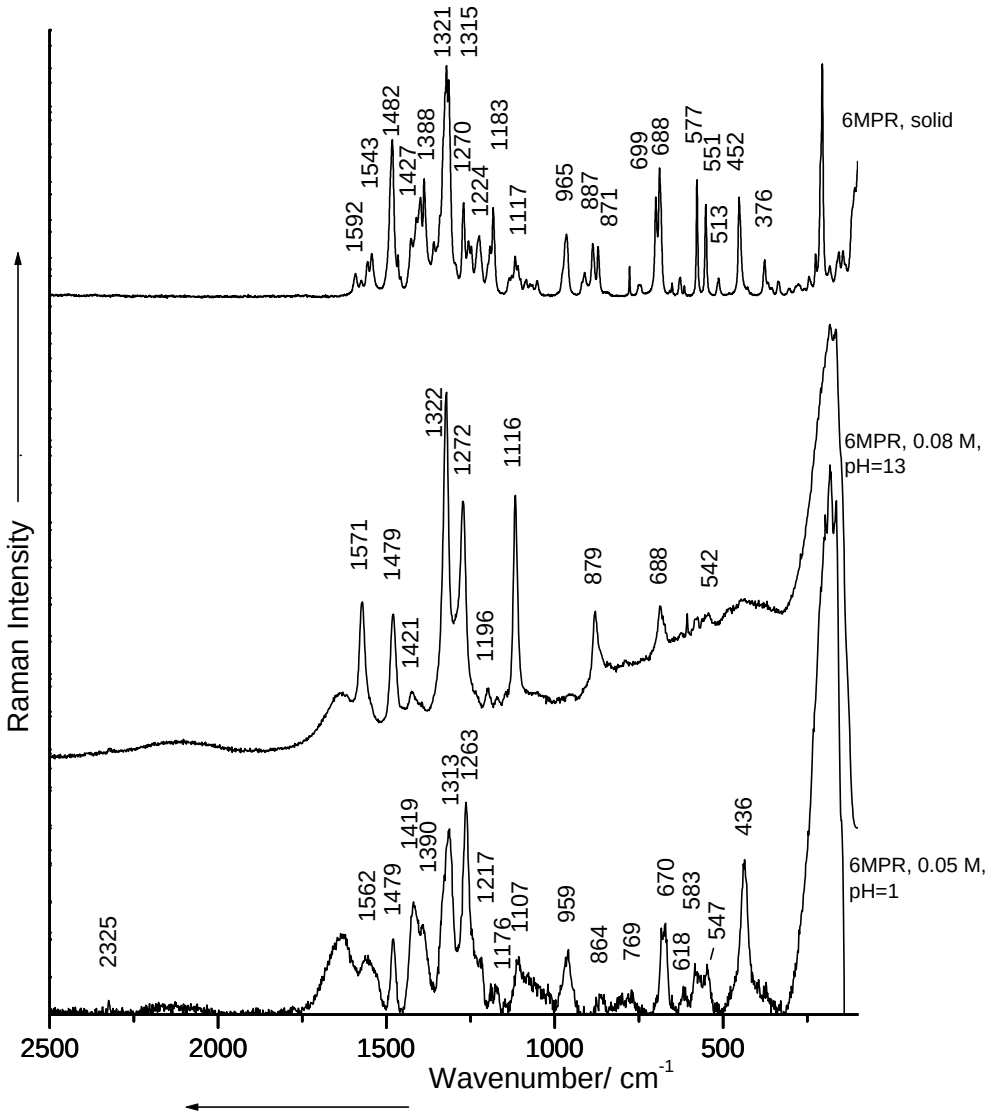

Figure 8.7. *FT-Raman spectrum of 6MPR and micro Raman spectra recorded in solution at basic and acidic pH values.*

Figure 8.7 shows the Raman spectra of the 6MPR derivative recorded in the solid state and in aqueous solution for the pH values 1 and 13. Major changes can be observed upon solvation. For pH = 1 a band of very low intensity can be observed at 2325 cm^{-1} corresponding to the S-H stretch vibration demonstrating the formation of the thiol tautomer or the protonation of 6MPR at the sulphur atom. Nevertheless, the S-H stretching mode arises at significantly lower wavenumbers compared with other thiol derivatives[217] indicating that the hydrogen atom is involved in strong hydrogen bonding interaction with the neighboring N1 atom or possibly with water molecules. Moreover, due to the very low intensity of the S-H stretching vibration an equilibrium between the two tautomers (Fig. 8.6) cannot be excluded.

Tables 8.8 and 8.9 summarize the experimental and calculated vibrational wavenumbers together with the vibrational assignment of 6MPR in the solid and aqueous solutions, respectively. In the high wavenumber region, several intense bands due to C-H and O-H stretching modes are observed in the FT-Raman spectrum of the polycrystalline form (spectra not shown here, see Table 8.8). Since no S-H stretching mode is observed in the FT-Raman spectrum of solid 6MPR (see Fig. 8.7), an N-H stretching mode is expected. Nevertheless, the N-H stretching vibration usually gives rise to bands of low intensity and in the high wavenumber region of the FT-Raman spectrum only a weak shoulder at 3393 cm^{-1} can be observed which probably corresponds to the N1-H stretching mode. The N-H stretching vibration of 6MP arises at 3433 cm^{-1}, and therefore it seems that the intramolecular hydrogen bonding between N1-H ··· S is stronger in the case of 6MPR. The stretching modes of the O-H groups of the ribose unit give rise to the bands around 3100 cm^{-1}. The gas phase calculations predicted these modes at much higher wavenumbers (see Table 8.8), but strong intermolecular hydrogen bonding shifts the O-H stretching modes significantly toward the region of the C-H stretching vibrations of the purine ring. A similar feature was observed in the case of adenosine[248]. The C-H stretching modes of the sugar ring arise between 2900 and 3000 cm^{-1}.

Table 8.8. *Experimental FT-Raman and calculated wavenumbers (cm^{-1}) at the B3PW91/6-311++G(d,p) level for 6MPR thion tautomer.*

Raman (cm^{-1})	Calc. (cm^{-1})	Tentative vibrational assignment (PED %)
3393vw	3586	νN1H1(99)
3122m	3885	νO5'H(100)
3105w	3889	νO3'H(100)
3084w	3773	νO2'H(100)
3070w	3249	νC8H8(98)
	3193	νC2H2(99)
2966m	3105	νC1'H(98)
	3088	νC3'H(97)
2930vs	3062	ν^{as}C5'H_2(99)
	3040	νC2'H(96)
	3035	νC4'H(86) + νC5'H_2(7)
2895w	3011	ν^{s}C5'H_2(90) + νC4'H(9)
1592vw	1635	νC2-N3(42) + νC5-C6(12) + νN1-C2(11) + νC4-C5(6) + δ^{6}_{ring}(6) + δC2H2(6)
1573vw	1584	νN3-C4(28) + νC4-C5(14) + νC4-N9(12) + νN7-C8(9) + δ^{6}_{ring}(9) + νC2-N3(7) + δN1H1(6)
1555vw	1565	νN7-C8(16) + νC5-C6(15) + νC4-N9(13) + νC2-N3(12) + δN1H1(11) + δ^{5}_{ring}(7)
1543w	1505	δ^{6}_{ring}(21) + νN7-C8(19) + νN3-C4(18) + νC4-C5(9) + δN1H1(5) + νC8-N9(5)
1482s	1494	δ^{sciss}C5'H_2(98)
	1451	δC3'H(34) + νC3'-C4'(9) + νC4-N9(7) + δC3'H(7) + νN7-C8(6) + δC3'H(26)
1465sh	1447	νC4-N9(30) + νN7-C8(19) + νC4-C5(11) + δC3'H(6) + νN9-C1'(6)
1457sh	1444	δ^{wag}C5'H_2(46) + νC4'-C5'(18) + δO5'H(13) + δC4'H(7)
1427w	1434	δC1'H(36) + νC8-N9(8) + δC2'H(6) + νC5-N7(5) + νN1-C2(5)
1411w	1413	νC5-C6(17) + νN1-C2(13) + δN1H1(10) + νC5-N7(8) + δC1'H(5)
1398w	1400	δC4'H(27) + δC1'H(9) + δO2'H(7) + νC8-N9(6) + δ^{wag}C5'H_2(7)
1388m	1387	δC2H2(28) + νC5-N7(25) + δ^{6}_{ring}(10) + νN7-C8(8) + νC2-N3(8) + νC4-C5(7)
	1380	δC2'H(21) + δO2'H(21) + δC4'H(17) + νC1'-C2'(6)

1359w	1372	δC1'H(23) + δC2'H(26) + δC3'H(10) + δO2'H(9)
1340sh	1350	δC4'H(18) + νC5-N7(10) + δC2H2(8) + δC1'H(7) + δO2'H(6)
1325sh	1339	δC4'H(24) + δC2'H(18) + νC5-N7(10) + δC1'H(8) + δC2H2(6)
1321	1321	δC1'H(30) + δC3'H(26) + δC2'H(7) + νC1'-C2'(6)
1315	1303	δC1'H(17) + δC4'H(15) + δC3'H(12) + δC2'H(17) + δO3'H(9) + δO2'H(6)
	1284	$\delta^{twist}C5'H_2(60)$ + $\delta^{out}C4'C5'(11)$ + δC4'H(7)
1270m	1272	νC8-N9(19) + δC1'H(16) + νN9-C1'(11) + νC5-N7(6) + νN1-C2(5)
1256w	1262	δO5'H(18) + δO3'H(11) + δC3'H(20) + $\delta^{wag}C5'H_2(6)$ + $\delta^{out}C4'C5'(6)$
1247w	1247	δC8H8(40) + $\delta^{5,6}{}_{ring}(16)$ + νN9-C1'(7) + νN7-C8(5)
1224br	1211	δC2'H(23) + δO2'H(14) + δO3'H(13) + νC2'-C3'(5)
1191w	1189	νN1-C6(26) + δN1H1(24) + νC6=S(18) + νN1-C2(8) + $\delta^{6}{}_{ring}(6)$
1183m	1182	δO5'H(34) + δC3'H(11) + δC4'H(8) + $\delta^{wag}C5'H_2(8)$
	1173	νC2'-O2'(11) + $\delta^{5}{}_{ring}(9)$ + νC8-N9(6) + δC2'H(6) + νN9-C1'(6)
	1154	νC5'-O5'(17) + νC4'-C5'(14) + νC2'-O2'(9) + νC4'-O4'(8) + νC1'-O4'(8) + $\delta_{riboside}(8)$
1134vw	1137	νC4'-O4'(17) + νC2'-O2'(16) + νC8-N9(7) + $\delta^{rock}C5'H_2(7)$ + νC2'-C3'(6)
1128vw	1124	νC3'-O3'(26) + νC5'-O5'(15) + νC2'-O2'(8) + νC2'-C3'(5) + νC4'-C5'(5) + νC3'-C4'(5)
1117w	1106	νC3'-O3'(20) + $\delta^{rock}C5'H_2(17)$ + νC2'-O2'(11) + δC3'O3'(7) + δC4'C5'(7) + νC4'-O4'(6)
sh	1101	νN1-C6(29) + νN1-C2(20) + δC2H2(9) + $\delta^{6}{}_{ring}(7)$ + νC5-N7(7) + νC6=S(5)
1084vw	1066	νC1'-O4'(22) + νC1'-C2'(12) + νC5'-O5'(11) + νC3'-O3'(11) + δC4'H(6)
1052vw	1050	δC4'C5'(23) + νC5'-O5'(10) + νC1'-O4'(9) + $\delta^{rock}C5'H_2(7)$ + νC3'-C4'(7) + δO3'H(6)
	1016	νC1'-C2'(20) + $\delta^{5}{}_{ring}(11)$ + $\delta^{rock}C5'H_2(9)$ + δC2'H(8)
976sh	991	$\delta^{5,6}{}_{ring}(45)$ + δN9C1'(9) + νC6=S(6) + νC4-N9(5)
965br	966	νC2'-C3'(14) + νC5'-O5'(13) + δC2'O2'(10) + νC4'-C5'(9) + νC1'-O4'(7)
910vw	928	$\delta^{out}C8H8(88)$
	900	$\delta^{5,6}{}_{ring}(45)$ + νC5-N7(9) + νN3-C4(8) + νC6=S(6)
	898	$\delta^{out}C8H8(32)$ + $\delta^{rock}C5'H_2(18)$ + νC4'-O4'(14) + δN9C1'(6)
887w	895	$\delta^{out}C8H8(47)$ + $\delta^{rock}C5'H_2(12)$ + νC4'-O4'(9)
	871	$\delta^{out}C4'C5'(25)$ + $\delta^{out}C3'$-O3'(14) + νC2'-C3'(11) + νC5'-O5'(7) + $\delta^{out}{}_{ribose}(5)$ + νC2'-O2'(6)
871w	827	$\delta^{5,6}{}_{ring}(20)$ + $\delta^{out}N9C1'(18)$ + $\delta^{out}{}_{ribose}(10)$ + $\delta^{out}C2'$-O2'(9) + νN9-C1'(6) + νC8-N9(6)

777vw	776	$\delta^{out,\ 5,6}{}_{ring}(76) + \delta^{out}N9C1'(7) + \delta_{ribose}(6)$
745vw	770	$\delta^{out,\ 5,6}{}_{ring}(32) + \delta^{out}N9C1'(14) + \delta_{ribose}(9)$
699m	717	$\nu C4'\text{-}C5'(10) + \delta C2'\text{-}O2'(15) + \delta C4'C5'O5'(9) + \delta_{ribose}(5) + \delta C3'\text{-}O3'(6) + \nu C2'\text{-}C3'(5)$
	712	$\delta^{out}N1H1(76) + \delta^{out,\ 6}{}_{ring}(10)$
688ms	682	$\delta^{out,\ 5,6}{}_{ring}(31) + \delta^{out}N9C1'(11) + \nu N3\text{-}C4(11)$
651vw	670	$\delta^{out,\ 5,6}{}_{ring}(71)$
627br	634	$\delta C4'C5'O5'(29) + \delta_{ribose}(7) + \delta^{\ 6}{}_{ring}(5)$
615vw	624	$\delta C4'C5'O5'(35) + \delta^{\ 5,6}{}_{ring}(20) + \nu C5\text{-}C6(5)$
577ms	599	$\delta^{out,\ 5,6}{}_{ring}(66) + \delta^{out}C6S(24)$
	571	$\delta^{out,\ 6}{}_{ring}(20) + \delta_{ribose}(18) + \delta N9C1'(9) + \delta^{out}C6S(8) + \delta C3'\text{-}O3'(7)$
	554	$\delta^{out,\ 5,6}{}_{ring}(52) + \delta^{out}C6S(7) + \delta^{out}N1H1(8)$
551m	549	$\delta^{5,6}{}_{ring}(40) + \delta C2H2(11) + \nu C5\text{-}N7(6) + \nu N1\text{-}C6(6) + \nu C5\text{-}C6(5)$
513vw	495	$\delta^{out}O2'H(76) + \delta^{out}O3'H(8)$
452m	440	$\delta^{5,6}{}_{ring}(51) + \nu C6{=}S(16) + \delta N1H1(8)$
	430	$\delta N9C1'(16) + \delta C3'\text{-}O3'(20) + \delta C4'C5'(26) + \delta^{out,\ 5,6}{}_{ring}(6)$

ν *stretching*, δ *deformation*, in *in-plane*, out *out-of-plane*

Table 8.9. *Selected experimental and calculated wavenumbers (cm^{-1}) at the BPW91/6-311++G(d,p) level for 6MPR thiol tautomer.*

Raman pH 13 (cm^{-1})	Raman pH 1 (cm^{-1})	SERS pH 10 (cm^{-1})	SERS pH 5 (cm^{-1})	Calc	Tentative vibrational assignment (PED %)
	2325vw			2593	νSH(99)
1571m	1562br	1574	1574	1559	νN3-C4(31) + νC5-C6(12) + νC4-N9(10) + νN1-C6(9) + νC5-N7-C8(15) + δ^{6}_{ring}(15)
		1532		1544	νC5-C6(24) + νC4-C5(24) + νN1-C2(9) + νN3-C4(8) + νC2-N3(7) + δ^{5}_{ring}(7)
1479m	1479m		1485	1462	νN7-C8(34) + δ^{5}_{ring}(25) + δC8H8(12) + νC5-C6(6) + νC8-N9(6)
				1452	$\delta^{sciss}C5'H_2$(93)
1421vw	1419ms	1433	1435	1411	δC2H2(38) + νN1-C6(23) + νC2-N3(10) + νC4-C5(6) + νC4-N9(6)
	1390m			1399	$\delta^{wag}C5'H_2$(30) + δC3'H(26) + δO3'H(7) + νC3'-C4'(6)
				1393	$\delta^{wag}C5'H_2$(27) + δC3'H(16) + νC4'-C5'(15) + δO5'H(11) + δC4'H(9) + νC3'-C4'(5)
		1379		1383	δC1'H(47) + νC8-N9(13) + δC2'H(8) + νN7-C8(7)
				1371	νC4-N9(32) + νN7-C8(11) + νC4-C5(6) + νN9-C1'(5)
				1353	δC4'H(28) + δO2'H(14) + δC1'H(7) + νC4-N9(5)
				1337	δO2'H(33) + δC4'H(21) + δC3'H(9) + δO3'H(7) + δC2'H(5)
1313vs	1322vs	sh	1338	1326	νC5-N7(26) + νC4-C5(14) + δC2H2(9) + νN1-C6(8) + νN1-C2(8) + δC2'H(6) + δ^{6}_{ring}(6)
				1322	δC2'H(35) + δC1'H(16) + νC5-N7(6)
				1301	δC4'H(33) + δC2'H(9) + $\delta^{twist}C5'H_2$(7) + δO2'H(6)
		1290		1294	νN1-C2(24) + νC2-N3(24) + νN1-C6(12) + νN3-C4(8) + νC5-C6(6)
1272ms	1263vs			1284	δC1'H(17) + νC2-N3(14) + δC2H2(13) + δC2'H(7) + δC8H8(6)
			1265	1275	δC1'H(35) + δC3'H(20)
				1263	δC4'H(16) + δC1'H(15) + δC3'H(18) + δC2'H(19) + δO3'H(10)
				1242	$\delta^{twist}C5'H_2$(62) + $\delta^{out}C4'C5'O5'$(12) + δC4'H(6)
				1227	δO5'H(21) + δO3'H(11) + δC3'H(20) + $\delta^{wag}C5'H_2$(8) + $\delta^{out}C4'C5'$(5)
				1210	δC8H8(26) + $\delta^{5,6}_{ring}$(25) + νN1-C2(10) + νN9-C1'(8)
1196w		1207	1206	1198	νC8-N9(23) + δC1'H(13) + νN9-C1'(8) + νN1-C6(8)
		1145	1136	1155	νC5-N7(26) + νN1-C2(16) + νC2-N3(13) + νN1-C6(10) + δC8H8(6)

				1147	δO5'H(26) + δC3'H(16) + δC4'H(9) + δ^{wag}C5'H_2(8) + δC2'H(8)
1116ms	1107br			1120	νN9-C1'(11) + $\delta^{5,6}{}_{ring}$(23) + νC2'-O2'(7) + νC4-C5(6)
				1097	νC4'-C5'(18) + νC5'-O5'(15) + νC2'-O2'(8) + $\delta_{riboside}$(7)
				1055	νC3'-O3'(40) + δC3'O3'(10) + νC5'-O5'(6) + δ^{out}C4'C5'(6)
				1007	νC1'-C2'(15) + νC5'-O5'(14) + νC1'-O4'(13) + νC3'-O3'(12)
				1003	νC1'-O4'(15) + δ^{rock}C5'H_2(9) + δ^{out}C4'C5'(9) + νC5'-O5'(6) + δC4'C5'O5'(12)
				974	νC1'-C2'(14) + δ^{rock}C5'H_2(10) + $\delta^{5}{}_{ring}$(9) + νC1'-O4'(9) + δC2'H(6)
	959m	994		954	$\delta^{5}{}_{ring}$(29) + δCSH(12) + δN9C1'(8)
				925	νC5'-O5'(16) + νC2'-C3'(15) + δC2'O2'(9) + νC1'-O4'(9) + νC4'-C5'(9)
				924	δ^{out}C2H2(91)
		868	877	891	$\delta^{5,6}{}_{ring}$(29) + δCSH(40) + νN1-C6(6)
				867	δ^{out}C8H8(86) + $\delta^{out,\ 5}{}_{ring}$(6)
				856	δ^{rock}C5'H_2(22) + νC4'-O4'(20) + δN9C1'(8)
			842	848	$\delta^{6}{}_{ring}$(28) + νC5-N7(8) + νC4-C5(7) + νN3-C4(6) + νC6-S(6) + νC4'-O4'(5)
				836	δ^{out}C4'C5'(23) + δ^{out}C3'-O3'(13) + νC2'-C3'(11) + νC5'-O5'(9) + $\delta^{out}{}_{ribose}$(8)
				793	$\delta^{5,6}{}_{ring}$(27) + δ^{out}N9C1'(15) + δ^{out}C2'-O2'(9) + $\delta^{out}{}_{ribose}$(8) + νN9-C1'(6)
				765	$\delta^{out,\ 5,6}{}_{ring}$(78) + δ^{out}C6S(12)
				742	δ^{out}N9C1'(23) + δ_{ribose}(20) + δC1'H(7) + νC1'-O4'(6)
688br	sh			691	νC4'-C5'(10) + δC2'-O2'(15) + δC4'C5'O5'(8) + δ_{ribose}(7) + δC3'-O3'(6) + νC2'-C3'(6)
	670m	683	681	659	$\delta^{5,6}{}_{ring}$(36) + δ^{out}N9C1'(13) + νN3-C4(9) + νC6-S(6)
				638	$\delta^{out,\ 5,6}{}_{ring}$(79) + δN9C1'(5)
				620	$\delta^{out,\ 5,6}{}_{ring}$(59) + δ^{out}C6S(11)
		620	630	614	$\delta^{6}{}_{ring}$(15) + δ_{ribose}(12) + δC4'C5'(14)
				604	δC4'C5'(42) + δC4'H(6) + $\delta^{6}{}_{ring}$(5)
542vw			542	547	δ_{ribose}(24) + δN9C1'(10) + $\delta^{out,\ 6}{}_{ring}$(10) + δC3'-O3'(9) + νC3'-O3'(7) + δ^{out}C6S(6)
				538	$\delta^{6}{}_{ring}$(36) + δSH(9) + νC5-N7(8) + νC5-C6(8) + δC2H2(7) + δC8H8(5)
				416	δN9C1'(16) + δC3'-O3'(19) + δC4'C5'(28) + $\delta^{out,\ 5,6}{}_{ring}$(6)
	436m	430	433	397	νC6-S(41) + $\delta^{6}{}_{ring}$(32)

ν *stretching*, δ *deformation*, in *in-plane*, out *out-of-plane*

In the 1600-900 cm^{-1} wavenumber region several modes due to stretching vibrations of the purine and ribose rings can be observed in the Raman spectra of the solid as well as the solvated 6MPR (Fig. 8.7 and Tables 8.8 and 8.9). Nevertheless, PED calculations showed that deformation modes of the CH_2 group and CCH and COH units contribute significantly to the vibrational modes in this wavenumber region. The identification of the original ribose and mercapto-purine vibrations contributing to combined modes is hardly possible because of the strong vibrational coupling[253]. Moreover, the vibrational bands generally overlap, and therefore an exact vibrational assignment becomes difficult.

The purine ring stretching modes are free of deformation modes of the sugar unit around 1550 cm^{-1}. Below 1500 cm^{-1} several purine ring stretching modes are predicted by the DFT calculations (see Table 8.8). The C4-N9 stretching mode is predicted at higher wavenumbers than the C5-N7 stretching vibration. The C5-N7 stretching mode was assigned to the band at 1388 cm^{-1}. This mode has also important contributions to the strong band around 1320 cm^{-1}. The C8-N9 stretching mode arises at 1270 cm^{-1}. Since the N1-C6 and N1-C2 stretching modes couple with a C=S stretching mode in the thion tautomer, these modes arise below 1200 cm^{-1} in the FT-Raman spectrum of polycrystalline 6MPR. The ribose ring C'-O' stretching modes are predicted also below 1200 cm^{-1}, while the C'-C' stretching modes arise at lower wavenumbers around 1000 cm^{-1}. By comparing the FT-Raman spectrum of 6MPR with the spectrum of 6MP and according to the DFT calculations[201,252] the prominent band at 1482 cm^{-1} is assigned to the scissoring mode of the sugar CH_2 group. Two bands were observed in the spectrum of solid D-ribose around 1460 cm^{-1} and assigned to the CH_2 deformation mode[249,250]. Below 1000 cm^{-1} several deformation modes of the purine and ribose rings can be observed (see Table 8.8).

Table 8.9 summarizes the Raman wavenumbers of 6MPR in aqueous basic and acidic solutions together with the calculated wavenumbers for the thiol tautomer. The Raman spectra of 6MPR recorded in aqueous solution resemble the FT-Raman spectrum reported for polycrystalline adenosine[248] related to 6MPR. Although similarities between the micro-Raman spectra of 6MPR for pH 13 and pH 1 and with the micro-Raman spectrum of 6MP recorded under basic conditions can be found with respect to the band positions and relative intensities, the Raman bands observed for the aqueous 6MP[252] and D-ribose solutions[249,250] cannot be found directly in the spectra of aqueous 6MPR. Therefore, the cleavage of the glycosidic N9-C1' bond in 0.1 N NaOH or HCl probably

does not occur. Moreover, in the Raman spectrum of 6MPR (see Fig. 8.7) recorded for pH 13 a strong band at 1116 cm^{-1} can be observed, while under acidic conditions a broad band at 1117 cm^{-1} arises. These bands probably involve the N9-C1' stretching vibration as predicted by the theoretical calculations for the thiol tautomer (calculated at 1120 cm^{-1}, Table 8.9). A strong band around 1120 cm^{-1} is also common in the vibrational spectra of ribonucleosides[249]. Nevertheless, an intense band can be also observed in the spectra of D-ribose[249,250] at 1120 cm^{-1} assigned to the C2'-O2' stretching vibration. The theoretical calculations performed within this study also showed an important contribution of the C2'-O2' stretching mode to the vibration at 1116 cm^{-1}. The intensity difference is probably due to the high conformational sensitivity of the marker bands of nucleic acids[253].

The purine ring stretching vibrations predicted for the thiol tautomer differ from those predicted for the thione tautomer mainly for the vibrations involving the pyrimidine unit. In the solution Raman spectra of 6MPR (see Fig. 8.7) a medium intense band at 1571 cm^{-1} (pH 13) and 1562 cm^{-1} (pH 1), respectively, corresponds to the stretching mode of the pyrimidine moiety. The very strong band at 1322 cm^{-1} in the Raman spectrum of 6MPR recorded for pH 13 and the band at 1313 cm^{-1} in the spectrum recorded for pH 1, respectively, could be assigned to the C5-N7 stretching mode. The stretching vibrations involving the N1 atom are predicted to appear at higher wavenumbers for the thiol tautomer than in the case of the thione tautomer. The very strong band at 1263 cm^{-1} in the Raman spectrum recorded for acidic conditions and the band at 1272 cm^{-1} for basic conditions, respectively, probably involves the N1-C2 and N1-C6 stretching modes (see Table 8.9), but also deformation modes of the sugar moiety. In the Raman spectrum recorded for acidic conditions, two medium strong bands around 1400 cm^{-1} can be observed. The mode at 1419 cm^{-1} is probably due to stretching modes of the pyrimidine unit while the band at 1390 cm^{-1} probably involves the imidazole moiety.

Below 1000 cm^{-1} several deformation modes of the purine and ribose rings are predicted (see Table 8.9, Fig. 8.7). In the Raman spectrum recorded for acidic pH values, the band at 959 cm^{-1} possibly involves also bending modes of the S-H thiol group. Under basic conditions the 6MPR molecule is probably deprotonated, and therefore this mode is absent in the spectrum recorded for pH 13.

SERS and the absorption of 6-mercaptopurine-ribose

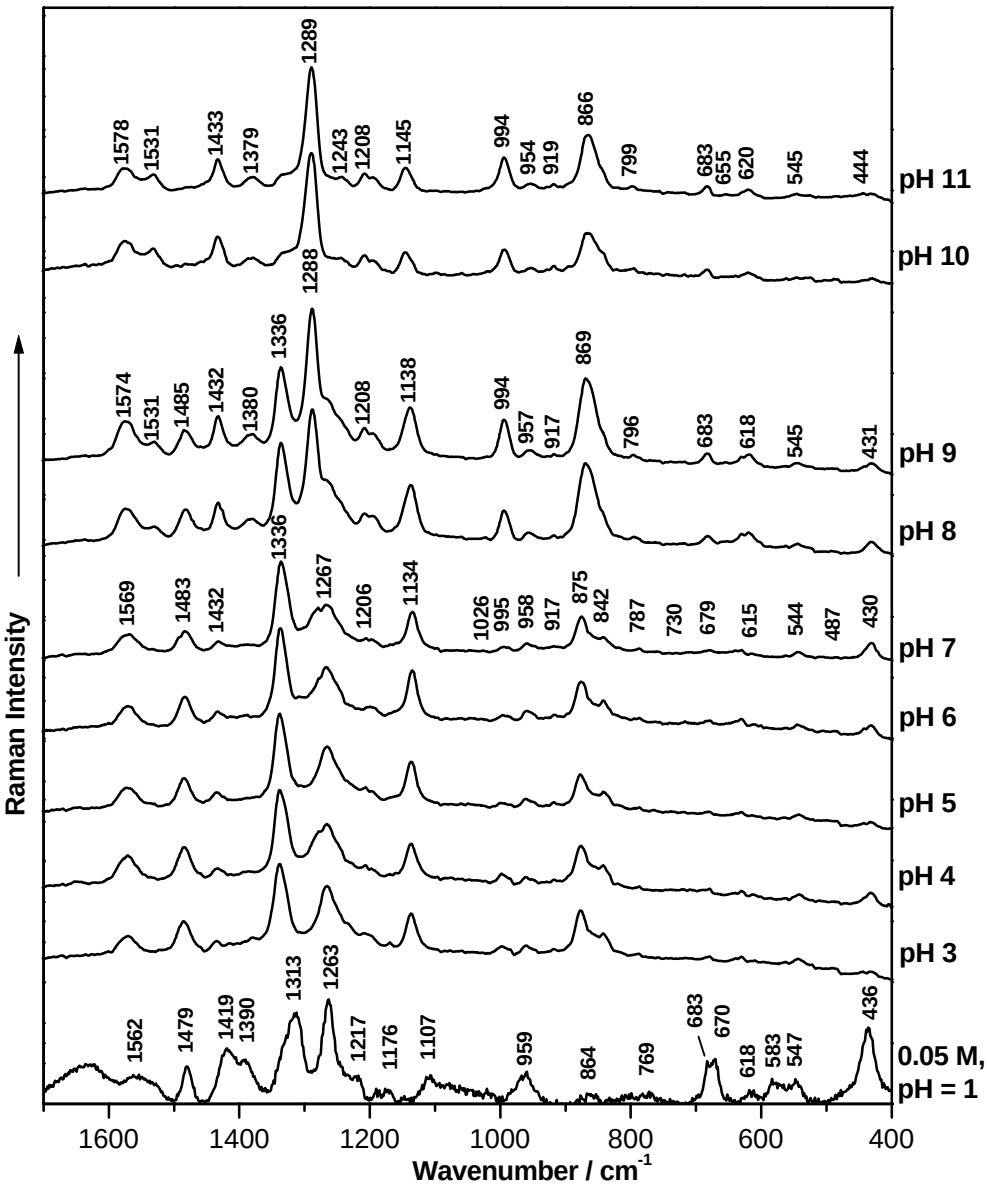

Figure 8.8. *SERS spectra of 6MPR recorded at different pH values. The micro-Raman spectrum recorded in solution (0.05 M) under acidic conditions (pH=1) is plotted for comparison.*

Figure 8.8 presents the SERS spectra of 6MPR recorded for different pH values in comparison with the micro-Raman spectrum recorded under acidic conditions. Well resolved SERS spectra could be obtained under acidic as well as basic conditions. Around pH 8 the rearrangement of the adsorbed molecule on the colloidal substrate begins.

Although the sugar unit could also interact with the silver colloid via the O atoms, SERS studies of DNA nucleosides[234,235,246,247] revealed that the lone electron pairs of the N atoms of the DNA bases are the preferable binding sites. Moreover, SERS studies of aldoses determined a low binding affinity of sugar rings to silver or gold particles.

In order to determine the most probable adsorption site of 6MPR on a metal surface, the partial atomic charges were calculated for both the thiol and thion tautomers. Selected atomic charges are listed in Table 8.10 together with the data obtained for the N9-H substituted 6MP tautomers. The thiol 6MPR tautomer shows a significant increase in negative charge on the N7 atom with respect to the thion tautomer. Comparing the 6MPR tautomers with those of 6MP, similar partial charges can be observed. Nevertheless, the N7 atom of 6MPR is more negatively charged than the N7 atom of the free purine, while the N9 atom is more positively charged because of the glicosidic bonding. Nonetheless, in the case of the thiol 6MPR the N1, N3 and N7 atoms present very similar partial charges, and each atom could act as a plausible adsorption site. In the following, the SERS spectra of 6MPR will be compared with the data obtained for 6MP and discussed.

Table 8.10. *Selected atomic charges (e^-) obtained from NPA analysis at the BPW91/6-311G(d,p) level of theory for the different tautomeric forms of 6MPR and 6MP with substitution at the N9 atom.*

	6MP			6MPR	
Atom	=S, N9-H	-S-H, N9-H		=S, N9-C1’	-S-H, N9-C1’
N1	-0.53671	-0.50499		-0.53764	-0.50639
C2	0.29003	0.27621		0.28820	0.27253
N3	-0.49305	-0.49673		-0.49919	-0.50201
C4	0.32997	0.35518		0.34072	0.36549
C5	0.03736	0.02106		0.04107	0.02693
C6	0.01618	0.10405		0.01621	0.10123
N7	-0.43846	-0.48618		-0.44313	-0.49344
C8	0.22705	0.24224		0.22894	0.24520
N9	-0.52929	-0.53797		-0.40598	-0.41572
S	-0.12708	0.08240		-0.14055	0.07111

At pH 10 and 11, the SERS spectra of 6MPR are similar to the SERS spectra of 6MP recorded under basic conditions (see Fig. 8.9) and to the SERS spectrum reported by Vivoni et al.[203] recorded on a silver electrode. Moreover, the band positions in the SERS spectra of 6MPR at pH 10 and 11 differ only by up to 4 cm^{-1} from the band positions observed in the study of Vivoni el al.[203] for 6MP, while the band positions in the SERS spectra of 6MPR and of 6MP both adsorbed on a silver colloid differ by about 12 cm^{-1}. It is also noteworthy, that the signal to noise ratio in the SERS spectra of 6MPR on a silver colloid is much lower than in the case of 6MP on the same colloid.

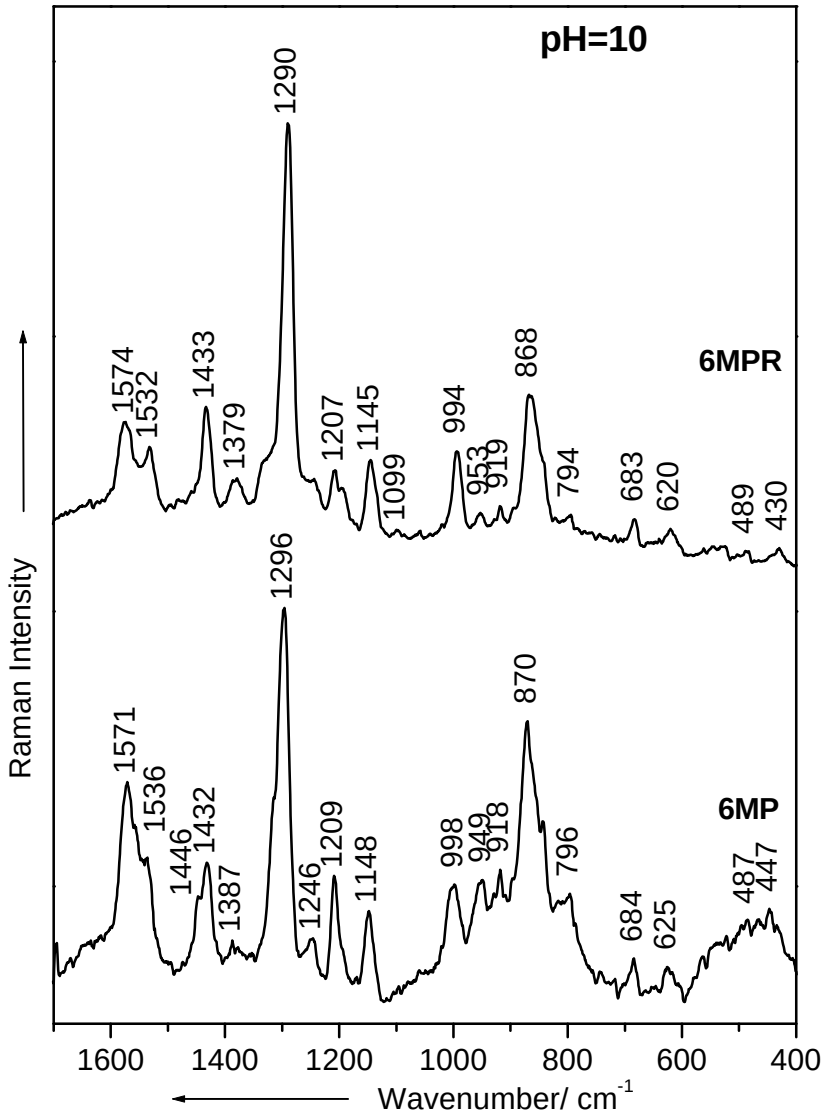

Figure 8.9. *The SERS spectra of 6MPR and 6MP recorded under basic conditions.*

The most enhanced band arises at 1290 cm^{-1} in the SERS spectrum of 6MPR recorded for pH 10. The theoretical calculations predicted for the 6MPR thiol tautomer, the N1-C2 stretching mode to appear at 1294 cm^{-1} (see Table 8.9) originating from the pyrimidine stretching mode of 6MP. The coupled N1-C2 and N1-C6 stretching mode of 6MP gives rise to the band at 1296 cm^{-1} in the SERS spectrum recorded for basic conditions (see Chapter 8.1). In the SERS spectrum of 6MPR recorded for basic pH values the band at 1433 cm^{-1} probably also involving the N1-C2 and N1-C6 stretching modes is considerably enhanced. Important contributions from the stretching modes of N1-C2 and N1-C6 can be attributed also to the bands at 1207, 1145 and 868 cm^{-1}. Hence, the adsorption of 6MPR on the silver colloid for basic pH values takes also place through the N1 atom as has been proposed in the case of 6MP[203,252] (see Chapter 8.1).

The 6MPR molecular orientation on the silver substrate seems to be perpendicular, while 6MP probably has a more tilted orientation under basic conditions. The ring stretching modes around 1550 cm^{-1} are well resolved. The mode at 1532 cm^{-1} corresponds mainly to the C5-C6 stretching mode. This mode would present significant changes of the polarizability tensor components in the *z*-direction in the case of a perpendicular orientation of the 6MPR molecule on the surface. Such a perpendicular orientation is also substantiated by the fact that the SERS spectra of 6MPR at pH 10 and 11 are almost identical with the spectrum of 6MP on silver electrode[203] where a perpendicular arrangement was indicated.

The similarities between the SERS spectra of 6MPR and 6MP for basic pH values might be due to the cleavage of the glycosidic N9-C1' bond upon adsorption of the molecule on the metal colloid. Another explanation is that the 6MPR is oriented perpendicular on the colloidal surface, while for the 6MP molecule a tilted orientation on the colloidal surface was proposed for basic pH values (as discussed in the previous subchapter). In this case the ribose unit leads to a repulsion from the metal surface of the imidazole moiety favoring the perpendicular orientation. Moreover, a perpendicular orientation of 6MPR allows an increase of the concentration of adsorbed molecules on the metal surface, and therefore would explain the lower signal to noise ratio in the case of 6MPR under basic conditions. In the case of an interaction via the N1 atom of the 6MPR molecule with the Ag substrate and a perpendicular orientation of the molecule on the silver substrate, the ribose unit is further away from the colloidal surface, and therefore its vibrational modes are not enhanced. Nevertheless, the presence of the ribose unit leads to a

stronger interaction of the mercaptopurine ring with the metal particles under basic conditions.

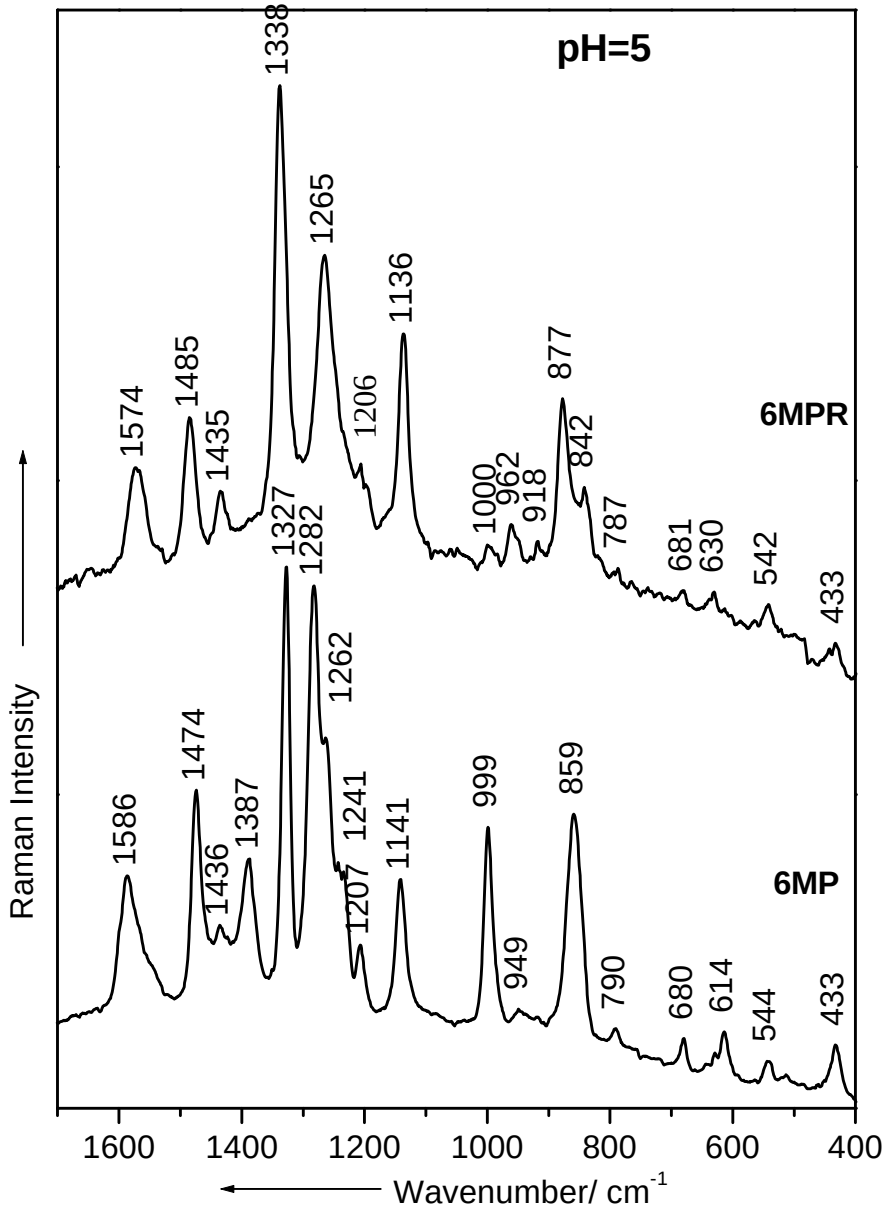

Figure 8.10 *The SERS spectra of 6MPR and 6MP recorded under acidic conditions.*

Figure 8.10 presents the SERS spectra of 6MPR and 6MP recorded for an acidic pH value of 5. A completely different vibrational and intensity pattern between the two compounds can be observed indicating a different binding of the riboside on the silver surface compared with the free purine base. In the spectrum of solvated 6MPR recorded

under acidic conditions, the most prominent band arises at 1336 cm^{-1}. This mode can be assigned based on DFT calculations (see Table 8.9) to a purine ring stretching vibration with strong contribution from the C5-N7 stretching mode. In the FT-Raman spectrum of the polycrystalline 6MPR thion tautomer the C5-N7 stretching mode has contributions to the very strong band around 1320 cm^{-1} (Table 8.8) as shoulders at 1325 and 1340 cm^{-1} (see Table 8.8). Theoretical calculations performed for the thiol form predict a purine ring stretching at 1326 cm^{-1} (Table 8.9). The shift of the C5-N7 stretching mode toward higher wavenumbers indicates an increase of the electron density on the N7 atom. The broad band at 1265 cm^{-1} (see Fig. 8.10) probably corresponds to several vibrational modes. As mentioned previously, a purine ring stretching mode is predicted at 1294 cm^{-1} corresponding to a stretching mode of the pyrimidine unit mainly involving the N1-C2 bond. Another mode, calculated at 1284 cm^{-1}, corresponds to the C2-N3 stretching mode combined with a C'-H bending vibration. Several modes corresponding to C'-H and O'-H bending vibrations were predicted at lower wavenumbers (at 1275, 1263 and 1242 cm^{-1}, see Table 8.9). Therefore, it seems that bending modes of the ribose ring are also present in the SERS spectrum of 6MPR recorded for acidic conditions. The band at 1485 cm^{-1} can be assigned to the N7-C8 stretching mode, but the CH_2 scissoring mode could also contribute to this band.

Hence, an interaction of 6MPR with the metal colloid through the N7 atom is proposed under acidic conditions. The enhancement of the band at 1574 cm^{-1} indicates a perpendicular orientation of the molecule on the substrate.

Figure 8.11 presents the SERS spectra of 6MPR recorded for three different concentrations under neutral conditions. For low concentrations of 6MPR ($1.5 \cdot 10^{-6}$) the reorientation of the molecule can be observed as indicated by the changes in the SERS spectra as compared to those obtained for higher concentrations ($1.5 \cdot 10^{-4}$ and $1.5 \cdot 10^{-5}$) which are almost identical. The spectrum recorded for 10^{-6} M concentration under neutral conditions resembles the SERS spectra recorded for pH 8 and 9 (see Figs 8.8 and 8.11). The band at 1292 cm^{-1} corresponding to the N1-C2 and N1-C6 stretching mode arises at low concentrations indicating an interaction of 6MPR through both the N7 and N1 atoms and probably a tilted orientation of the molecule in the metal colloid. Nevertheless, the existence of two differently adsorbed species is also possible. This involves the adsorption of the thiol tautomer through the N7 atom and the presence of the anionic structure adsorbed through the N1 atom according to an equilibrium between these two species (see

Fig. 8.6). The strong intensity of the band around 870 cm^{-1} is probably due to the overlap of several bands of the two adsorbed species.

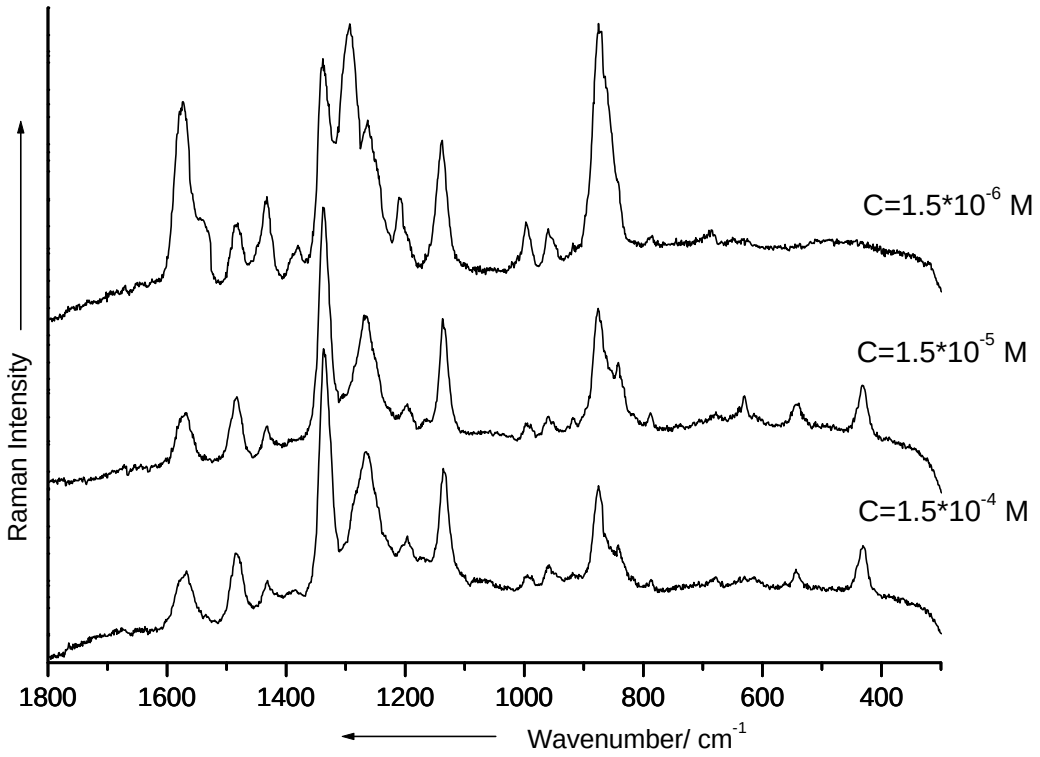

Figure 8.11. *SERS spectra of 6MP recorded at different concentrations under neutral conditions.*

For neutral conditions, where most of the biological processes occur, the 6MPR species adsorbed through the N7 atom dominates, while in the case of 6MP the species adsorbed through the N1 atom exhibits an important contribution to the SERS spectrum[252]. The intensity of the band at 1288 cm^{-1} in the SERS spectra of 6MPR for pH values 8 and 9 increases gradually while the intensity of band at 1336 cm^{-1} decreases. Nevertheless, the vibrational modes characteristic for the species adsorbed under acidic conditions via the N7 atom and the bands characteristic to the species adsorbed through the N1 atom are both present. This indicates that probably two species with different interaction sites are adsorbed on the metal surface for slightly basic conditions. The deprotonation of 6MPR seems to be completed around pH 10, while in the case of 6MP the deprotonation is already completed around pH 8. The effect of the ribose ring on the tautomeric equilibrium

is to act as a buffer hindering the deprotonation of 6MPR and those favoring the adsorption of 6MPR on the metal surface through the N7 atom.

Previously, in order to determine the most probable coordination site of 6MPR several metal complexes were synthesized and the coordination through the N7 and S atoms was determined[205-207]. The SERS study of azathioprine[230,254] a mercaptopurine derivative also used in chemotherapy, with a nitro-imidazole substituent at the S atom, on a silver electrode evidenced an attachment via the N3 atom of the purine ring on the metal surface. The voluminous substituent seems to hinder the adsorption through the N1 atom, as in the case of 6MP on silver electrode or through the N7 atom in the case of 6MPR. Moreover, the formation of the anionic species is also blocked through the substituent at the S atom. Similarly, in the case of 6MP adsorbed on colloidal silver for acidic pH values (see Chapter 8.1), an attachment via the N9 and N3 atoms was indicated[252].

SERS studies of adenine and adenosine[232,234,235,246,247] also indicated the N7 atom of these DNA components as the most probable molecular interaction site with silver surfaces. Recently, Jang[246] reported a SERS study for guanosine, cytidine and tymidine derivatives on gold particles. Nevertheless, previous SERS studies indicated that the ribose unit reduced the adsorption affinity of the latter nucleotides, and no SERS signal could be obtained on a silver surface[234,246]. In the present study, well resolved SERS spectra of 6MPR could be recorded on a silver colloid. The adsorption behavior of 6MPR under acidic and neutral conditions is similar to the adenosine molecule, thus probably favoring the adsorption of the drug molecules into the red blood cells, while 6MP showed a different adsorption behavior.

Conclusions

The calculated structural parameters of 6MPR are in very good agreement with the experimentally determined polycrystalline data. The 6MPR molecule exists as the thion tautomer in the solid state. However, the thiol species could be evidenced unequivocally in solution for acidic conditions, while under basic conditions the anionic form is probably present. A detailed vibrational analysis for the 6MPR thiol and thion tautomers by means of DFT calculations was presented paying much attention to the vibrational coupling between the ribose and purine base rings. The SERS spectra of 6MPR were recorded at physiological concentrations and as a function of the pH value.

For acidic to neutral conditions, the 6MPR molecule adsorbs on the metal substrate via the N7 atom with a perpendicular orientation, similarly to adenosine, while for 6MP an attachment via the N9 and N3 atoms was evidenced under acidic conditions. For pH values 10 and 11, the attachment of 6MPR through the N1 atom was proposed, as in the case of the free mercaptopurine base. Nevertheless, while 6MP probably adopts a more tilted orientation on the Ag colloid, the riboside has a perpendicular orientation as in the case of 6MP adsorbed on a silver electrode. For pH values 8 and 9 an interaction of 6MPR with the colloid through both N1 and N7 atoms with a tilted orientation is possible or the formation of an equilibrium between two adsorbed species might be the case. The concentration of the species adsorbed through N1 is increasing toward basic pH values, while the concentration of the species adsorbed through N7 decreases. Nevertheless, in the case of 6MPR the molecular reorientation starts around pH 8 and is completed at pH 10, while in the case of 6MP begins around pH 6. The ribose moiety hinders the formation of the anionic 6MPR and those favors the adsorption through the N7 atom. These findings are of interest for the elucidation of the adsorption and action of the title drug in cancer therapy. Therefore, further research is required, giving the reason to progress in understanding the action of modified bases when embedded in the DNA sequence.

Chapter 9

Summary // Zusammenfassung

The present thesis reports about vibrational and quantum chemical investigations on model systems undergoing photochemical processes and pharmaceutically active compounds, respectively. Infrared (IR) and Raman spectroscopy were applied for the characterization of the ground state molecular structure. Moreover, resonance Raman (RR) spectra contain additional information about the resonantly enhanced excited state molecular structure. A quantitative resonance Raman intensity analysis in conjunction with the simultaneous simulation of the absorption spectra by means of *time-dependent* propagation methods was accomplished in order to extract valuable information about the excited state molecular structures of the investigated systems. Surface enhanced Raman scattering (SERS) allows one to determine the interaction and adsorption site of active agents on a metal substrate. Furthermore, density functional theory (DFT) and potential energy distribution (PED) calculations were carried out for an exact assignment of the vibrational spectra. Complete active space self consistent field (CASSCF) and configuration interaction (CI) calculations for some model systems were also performed to assess the experimental results on the excited state potential surfaces.

The first chapter introduces the general topic of the thesis. The various projects are related to recent research developments in the respective chapters. This chapter is concluded by discussing the connection between various projects being presented later in the thesis.

Chapter 2 summarizes the basic theoretical principles of the applied spectroscopical techniques and quantum chemical methods. A short survey about the basic principles of vibrational spectroscopy introduces the IR and Raman spectroscopic methods. Special attention was paid to the advantages and disadvantages of these, often complementary,

techniques. Furthermore, the fundamentals of resonance Raman spectroscopy are treated in detail, describing the physical processes and emphasizing the theoretical methodologies which allow one to obtain the information about the resonantly excited state via an RR intensity analysis. The Brownian oscillator model to determine the solvent reorganization energy is briefly presented. Furthermore, the SERS enhancement mechanisms and selection rules to determine the orientation of the molecules adsorbed on the metal substrate are discussed. In the second part of this chapter, the Hartree-Fock approach to calculate the ground state geometry is expatiated, and the basic characteristics of the CI and CASSCF calculations are specified. The chapter ends with a short description of the DFT theory.

Chapter 3 shortly presents the various experimental setups for the absorption, Raman, RR and SERS measurements and provides an overview about the computational strategies of the quantum chemical and PED calculations. Finally, the handling of the experimental and theoretical data to determine the displacement parameters and the geometry of the resonantly excited state is presented.

Chapter 4 deals with the investigation of the excited state intramolecular proton transfer of the model system, 1-hydroxy-2-acetonaphthone (HAN). In doing so, the non resonant FT-Raman spectrum of polycrystalline HAN was analyzed based on DFT and PED calculations and by comparison with related derivatives. The vibrational wavenumbers and Raman intensities predicted for the enol tautomer at the BPW91/6-31+G(d,p) level of theory are in excellent agreement with the measured spectrum. In order to determine the Franck-Condon (FC) active modes and FC (dimensionless) parameters, resonance Raman measurements and in particular an analysis of the RR intensities via a time-dependent formalism were carried out. Moreover, CASSCF optimizations and natural population analyses of the ground and first excited states were accomplished to calculate the displacement parameters and charge distribution. A very good agreement between the experimental and theoretical displacement parameters was obtained indicating that the predicted excited state geometry is a reliable picture of the structural changes upon photo excitation. About eighteen vibrational modes were found to be involved in the initial dynamics of HAN. The vibrations showing the highest displacement parameters correspond to stretching and in-plane deformation modes of the naphthalene ring and the

conjugated carbonyl group, while the OH stretching mode exhibits no observable enhancement. The cooperative effect of the skeletal vibrations reduces the distance between the carbonyl and hydroxyl oxygen atoms in accordance with a general electron density redistribution. Hence, the leading force in the proton transfer process is the increase in electron density on the carbonyl group and the decrease of the negative charge on the hydroxyl oxygen.

In chapter 5 the structural and vibrational characteristics of the organic mixed valence system N,N,N',N'-tetraphenylphenylenediamine radical cation ($\mathbf{1}^+$) are discussed. Such optoelectronic systems are characterized by a broad and rather strong absorption band in the near infrared region corresponding to an intervalence charge transfer (IV-CT) band in the case of localized (Class II) systems or charge resonance transfer band for delocalized (Class III) systems. The DFT optimized structural parameters of ($\mathbf{1}^+$) are in very good agreement with the results of the crystal structure analysis. Two stable conformers with D_2 and C_{2h} symmetries were predicted by the DFT calculations for the gas phase, whereas the C_{2h} species showing an inversion center was found in the crystalline state. A detailed vibrational assignment of the IR and Raman spectra of ($\mathbf{1}^+$) based on DFT calculations and by comparison with the vibrational modes of benzene derivatives was accomplished. Resonance Raman measurements with excitation lines in the near infrared region were performed. These experiments showed that at least eight vibrational modes are strongly coupled to the optical charge transfer process in ($\mathbf{1}^+$). These Franck-Condon active modes were assigned to symmetric vibrations. Their displacement parameters and vibrational reorganization energies were determined via a quantitative time-dependent resonance Raman intensity analysis. The most enhanced band corresponds to the symmetric stretching mode along the N-phenylene-N unit and exhibits the largest vibrational reorganization energy. Nevertheless, symmetric stretching modes of the phenylene and phenyl units as well as deformation modes are also coupled to the electronic process. The total vibrational reorganization energy of these symmetrical modes is dominant, while the solvent induced broadening and reorganization energy are found to be small. The resonance Raman data are in agreement with the results of a simple two-state two-mode Marcus-Hush analysis, yielding a tiny electron transfer barrier. Hence, ($\mathbf{1}^+$) adopts a symmetrical delocalized Robin-Day Class III structure in the ground state. Furthermore,

the dimensionless displacement parameters were converted into bond length changes. A significant lengthening of the axial N-C bonds was predicted upon photo excitation.

Chapter 6 reports about a vibrational spectroscopic investigation of a model organic photorefractive thiophene derivative, 2-(N,N-diethylamino)-5-(2',2'-dicyanovinyl)-thiophene (**T**). The geometry of the first excited state were optimized and the FC parameters were calculated using the configuration interaction with single excitations method (CIS/6-31G(d,p)). These calculations show that the contribution of the zwitterionic structure to the excited state is significantly higher than in the ground state. The resonance Raman spectra indicate that several stretching modes along the bonds connecting the donor and acceptor moieties as well as the S-C stretching vibrations are enhanced.

Chapter 7 presents the vibrational analysis of an aziridinyl tripeptide, a cysteine protease inhibitor active drug. In doing so, detailed Raman investigations of the electrophilic building block (EtO-Azi-OEt) (**1**), aziridine ring containing tripeptide (EtO-Azi-Gly-Gly-OBn) (**2**) and a related peptide derivative with an epoxide ring (BnO-Gly-Gly-Epo-Gly-Gly-OBn) (**3**) were carried out. Additional measurements for deuterated species of (**1**) and (**2**) were performed. The calculated bond lengths of (**2**) are in very good agreement with the crystal structure parameters; however a different conformational species was predicted. Nevertheless, the calculated vibrational wavenumbers of (**2**) match the experimental ones. The vibrational analysis reveals stronger H-bonding of the aziridine NH unit in the solid state of (**2**) than in the liquid electrophilic building block, indicating medium strong intermolecular H-bond interactions in the crystal unit. The amide hydrogen atoms of (**2**) are involved in weaker H-bonds than in the investigated epoxide analogon. The amide carbonyl unit connected to the aziridine ring is involved in strong inter- and probably intramolecular hydrogen bonding interaction than the second amide carbonyl unit of (**2**) or the corresponding amide C=O group in (**3**). Moreover, the amide carbonyl of (**2**) adjacent to the ester moiety and the ester carbonyls are involved in weak H-bonding. Nevertheless, (**2**) shows weaker hydrogen bonding interactions than glycine peptide derivatives. Furthermore, the characteristic vibrational modes of the peptide backbone were discussed.

Chapter 8 reports on the adsorption mechanism of two related anti-leukemia active agents, 6-mercaptopurine (6MP) and 6-mercaptopurine-ribose (6MPR) on a silver colloid. First, the structural and vibrational characteristics of 6MP were discussed in the solid state and aqueous solutions based on DFT and PED calculations for different tautomers. The thione tautomer can be found in the solid state, while the thiol or anionic species is probably formed in aqueous solution. Furthermore, the SERS spectra of 6MP as a function of the pH value and concentration were presented and discussed. The ribose derivative is in the focus of the second part of this chapter. The thione tautomer of 6MPR was also evidenced in the polycrystalline form, whereas in acidic aqueous solution the presence of the thiol (S-H) species could be identified. The SERS spectra of 6MPR were finally discussed in comparison with the spectra of 6MP. Both molecules adsorb through the N1 and possibly S atom on the metal surface under basic conditions. However, 6MP adopts a more tilted orientation on the surface while 6MPR adopts a perpendicular orientation. The SERS spectra recorded for acidic pH values showed that the ribose derivative exhibits a different adsorption behavior compared to the free base. 6MP probably adsorbs on the silver sol through the N9 and N3 atoms, while 6MPR interacts with the surface via the N7 and probably S atoms. Interestingly, the reorientation of the 6MP molecules on the surface starts around pH 6, whereas the ribose derivative reorients first around pH 8. Under strong basic conditions, the presence of the anionic species for both molecules is suggested. Nevertheless, it seems that the deprotonation of 6MP is completed at pH 8, while the deprotonation of 6MPR is finished at pH 10. Around critical biological concentrations and pH values i.e. at low concentrations and almost neutral condition (pH 7-9), 6MPR interacts with the substrate through both N7 and N1 atoms, possibly forming two differently adsorbed species, while for 6MP only the species adsorbed via N1 was evidenced. These findings are of interest for the elucidation of the adsorption and action of the title drugs in cancer therapy, since 6MP shows poor drug adsorption.

The experiments and results presented in this thesis demonstrate that vibrational spectroscopy in conjunction with quantum chemical calculations have a large applicability for the investigation of the molecular structure. In particular, resonance Raman spectroscopy proved to be a valuable method to obtain information about the initial dynamics and excited state structure of photochemically active systems. Moreover, Raman and SERS spectroscopy brought an important contribution in the understanding of the structure-activity relationship of several pharmaceuticals.

Zusammenfassung

In der vorliegenden Arbeit wurden schwingungsspektroskopische und quantenchemische Untersuchungen an unterschiedlichen Modellsystemen, die an photochemischen Prozessen beteiligt sind, und an verschiedenen Pharmazeutika durchgeführt. Die Methoden der Infrarot- (IR) und Raman-Spektroskopie wurden für die Charakterisierung der Grundzustandsgeometrie verwendet. Darüber hinaus konnten aus Resonanz-Raman- (RR) Spektren zusätzliche Informationen über den elektronisch angeregten Zustand erhalten werden. Diese aufschlussreichen Aussagen über die elektronisch angeregten Zustände der untersuchten Systeme wurden durch die simultane quantitative Analyse der Resonanz-Raman-Spektren und des Absorptionsspektrums gewonnen. Die Anregungsprofile für die Resonanz-Raman-Streuung und die Absorptionsquerschnitte wurden mittels zeitabhängiger Propagationsmethoden berechnet. Oberflächen-verstärkte Raman-Streu- (SERS *Surface Enhanced Raman Scattering*) Experimente ermöglichten die Charakterisierung der Wechselwirkungen und Adsorptionsbindungsstellen von Wirkstoffen an Metalloberflächen. Des Weiteren wurden Dichtefunktionaltheorie- (DFT *Density Functional Theory*) und PED-Rechnungen (PED *Potential Energy Distribution*) durchgeführt, um eine genaue Zuordnung der Schwingungsspektren zu gestatten. CASSCF- (*Complete Active Space Self Consistent Field*) und CI-Rechnungen (*Configuration Interaction*) wurden in einzelnen Fällen durchgeführt, um sie mit den experimentellen Ergebnissen für die Potenzialhyperfläche des angeregten Zustands vergleichen zu können.

Im ersten Kapitel wurde eine kurze Einführung in die Thematik der vorliegenden Arbeit gegeben. Ein Bezug der einzelnen Projektteile zu aktuellen Forschungsergebnissen wurde in den entsprechenden Kapiteln ausführlich hergestellt.

Das zweite Kapitel fasst die theoretischen Grundlagen der verwendeten spektroskopischen Techniken und quantenchemischen Methoden zusammen. Ein kurzer Überblick über die Grundsätze der Schwingungsspektroskopie führte die IR- und Raman-spektroskopische Methoden ein. Hierbei wurden die Vor- und Nachteile dieser oft komplementären Techniken betrachtet. Die Grundlagen der Resonanz-Raman-Spekroskopie wurden ausführlich diskutiert. Dabei wurden die physikalischen Prozesse beschrieben und die mathematischen Techniken, die die Bestimmung der Parameter des angeregten Zustands durch die RR-Intensitätsanalyse ermöglichen, hervorgehoben. Das

Modell des Brownian-Oszillators für die Ermittlung der Lösungsmittel-Reorganisationsenergie wurde kurz beschrieben. Weiterhin wurden die SERS Verstärkungsmechanismen und Auswahlregeln diskutiert. In dem zweiten Teil dieses Kapitels wurde der Hartree-Fock-Ansatz zur Berechnung des Grundzustandes sowie die CI- und CASSCF-Methoden erläutert. Das Kapitel endete mit einer kurzen Beschreibung der Grundlagen von DFT-Rechnungen.

Im dritten Kapitel wurden der jeweilige experimentelle Aufbau, der bei den Absorptions-, Raman-, Resonanz-Raman- und SERS-Messungen angewendet wurde, und die Strategien der quantenchemischen und PED-Rechnungen vorgestellt. Schließlich wurde die Datenverarbeitung zur Bestimmung der *Displacement*-Parameter und der Geometrie des elektronisch angeregten Zustands angegeben.

Im vierten Kapitel wurden die Untersuchungen an einem Modell-Systems (1-hydroxy-2-acetonaphthone HAN), das einen Protonentransferprozess im angeregten Zustand zeigt, dargestellt. Das FT-Raman-Spektrum des kristallinen HAN wurde anhand von DFT- und PED-Rechnungen bzw. Literaturdaten für ähnliche Verbindungen analysiert. Die berechneten Schwingungswellenzahlen und Raman-Intensitäten für das Enol-Tautomer unter der Anwendung des BPW91/6-31+G(d,p) Funktionals/Basissatzes sind in ausgezeichneter Übereinstimmung mit dem experimentellen Spektrum. Um die Franck-Condon (FC) aktiven Moden zu identifizieren und die dimensionslosen FC-Parameter zu bestimmen, wurden Resonanz-Raman-Intensitätsmessungen und deren Analyse mittels zeitabhängiger Propagationsmethoden durchgeführt. Des Weiteren wurden CASSCF-Optimierungen und NPA-Rechnungen (Natural Population Analysis) des Grund- und des angeregten Zustandes ausgeführt, um zusätzlich die Verschiebungsparameter quantenchemisch zu bestimmen und die Elektronendichteverteilung zu ermitteln. Die sehr gute Übereinstimmung zwischen den experimentellen und theoretischen *Displacement*-Parametern zeigt, dass die berechnete Geometrie des angeregten Zustands eine zuverlässige Ermittlung der strukturellen Änderungen aufgrund der optischen Anregung erlaubt. Es wurden etwa achtzehn Moden gefunden, die zu der Anfangsdynamik des Systems beitragen. Die Streck- und Deformationsmoden des Naphthalinrings und der konjugierten Carbonylgruppe weisen die größten *Displacement*-Parameter auf, während die O-H-Streckschwingung keine Resonanz-Verstärkung erfährt. Diese Gerüst-

schwingungsmoden verringern den Abstand zwischen den Carbonyl- und Hydroxyl-Sauerstoffatomen, was mit einer generellen Umverteilung der Elektronendichte einhergeht. Daher wird der Protonentransferprozess durch die Zunahme der Elektronendichte auf dem Carbonylsauerstoffatom und der gleichzeitigen Abnahme der negativen Ladung auf dem Hydroxylsauerstoffatom gesteuert.

Im fünften Kapitel wurden die strukturellen und vibronischen Eigenschaften eines organischen gemischtvalenten Systems, des N,N,N',N'-tetraphenylphenylenediamine Radikalkations (**1**$^+$), untersucht. Derartige optoelektronische Systeme weisen eine breite und relativ intensive Absorptionsbande im nahen Infrarot auf. Diese Bande entspricht einer Intervalenz-Ladungstransferbande (IV-CT, *Intervalence Charge Transfer*) für den Fall eines lokalisierten Systems (*Class* II) oder der sogenannten Resonanz-Ladungstransferbande für ein delokalisierten Systems (*Class* III). Die DFT-optimierten Geometrieparameter von (**1**$^+$) zeigen eine sehr gute Übereinstimmung mit den Ergebnissen der Kristallstrukturanalyse. Die DFT-Rechnungen lieferten zwei stabile Konformere mit D_2- bzw. C_{2h}-Symmetrie für den gasförmigen Zustand, während in der kristallinen Phase das C_{2h}-Konformer mit einem Inversionszentrum vorliegt. Die IR- und Raman-Spektren von (**1**$^+$) wurden mittels DFT-Rechnungen und über einen Vergleich mit Schwingungsspektren einiger Benzolderivate analysiert. Resonanz-Raman-Spektren wurden mit Anregungswellenlängen im nahen Infrarot aufgenommen. Diese Experimente zeigten, dass mindestens acht Schwingungsmoden stark an den optischen Ladungstransferprozess gekoppelt sind. Diese Franck-Condon aktiven Moden wurden vornehmlich symmetrischen Moden zugeordnet. Außerdem wurden die *Displacement*-Parameter und die entsprechenden Schwingungsreorganisationsenergien der Resonanz-verstärkten Moden mittels einer quantitativen zeitabhängigen Resonanz-Raman-Intensitätsanalyse bestimmt. Die am meisten verstärkte Mode entspricht der symmetrischen Streckschwingung entlang der N-Ar-N-Achse. Jedoch sind auch symmetrische Streckschwingungsmoden der Phenyl- und Phyenylen-Gruppen und Deformationsmoden an dem elektronischen Prozess beteiligt. Ferner konnte gezeigt werden, dass der Beitrag dieser symmetrischen Moden zur Reorganisationsenergie dominiert, während die Lösungsmittelreorganisationsenergie nur sehr gering ist. Die Resonanz-Raman-Daten stimmen mit den Ergebnissen einer Zwei-Zustands-Zwei-Moden-(*two-state two-mode)* Analyse, welche eine kleine Energiebarriere des Elektronentransfers

voraussagt, überein. Die erhaltenen Ergebnisse beweisen, dass es sich hier um ein symmetrisches delokalisiertes Robin-Day-*Class*-III-System handelt. Darüber hinaus wurden die Änderungen der Bindungslängen aus den dimensionslosen *Displacement*-Parametern ermittelt.

Das sechste Kapitel beschäftigt sich mit einer schwingungsspektroskopischen Analyse eines organischen photorefraktiven Thiophen-Derivat-Modellsystems, 2-(N,N-diethylamino)-5(2',2'-dicyanovinyl)-thiophen (**T**). Die Geometrien des Grund- und ersten angeregten Zustands wurden optimiert und die FC Parameter unter Anwendung der CI („*configuration interaction*")- Methode (CIS/6-31G(d,p)) berechnet. Diese Rechnungen ergaben, dass der Anteil der zwitterionischen Struktur im angeregten Zustand dominiert. Die Resonanz-Raman-Spektren zeigten, dass mehrere Streckschwingungsmoden entlang der Bindungen, die die Donor- und Akzeptor-Einheiten verknüpfen, und die S-C Streckschwingungsmoden verstärkt wurden.

Das siebte Kapitel behandelt die schwingungsspektroskopische Analyse eines Aziridinyl-Tripeptids, ein Wirkstoff gegen Cystein-Proteasen. Dafür wurden ausführliche Raman-Untersuchungen der elektrophilen Baueinheit (EtO-Azi-OEt) (**1**), des Aziridinring enthaltenden Tripeptids (EtO-Azi-Gly-Gly-OBn) (**2**) und eines ähnlichen Peptids, das einen Epoxidring enthält, (BnO-Gly-Gly-Epo-Gly-Gly-OBn) (**3**) durchgeführt. Zusätzlich wurden Raman-Messungen der deuterierten Spezies der Verbindungen (**1**) und (**2**) vorgenommen. Obwohl die berechneten Bindungslängen von (**2**) sehr gut mit den Parametern der Kristallstruktur übereinstimmen, wurde das Vorliegen eines anderen Konformers vorhergesagt. Jedoch stimmen die berechneten Wellenzahlen mit den experimentellen Daten überein. Die Schwingungsanalyse ergab eine stärkere Wasserstoffbrückenbindung der Aziridin NH-Gruppe des Moleküls (**2**) im festen Zustand als in der flüssigen Verbindung (**1**). Die Wasserstoffatome der Amidgruppen des Tripeptids (**2**) sind an schwächeren Wasserstoffbrückenbindungen als die des Epoxid-Analogons beteiligt. Die Amid-Carbonylgruppe, welche am Aziridinring gebunden ist, weist eine stärkere inter- und möglicherweise auch intramolekulare Wasserstoffbrücken-bindung auf als die zweite Amid C=O Gruppe des Derivats (**2**) oder die entsprechende Gruppe der Verbindung (**3**). Die zur Esthergruppe benachbarte Amid Carbonylgruppe und die Esther C=O Gruppen des Derivats (**2**) zeigen nur schwache Wechselwirkungen mit

Wasserstoffatomen. Weiterhin weist die Verbindung (**2**) schwächere Wasserstoffbrückenbindung als Glycin-Peptidderivate auf. Darüber hinaus wurden die charakteristischen Gerüstschwingungsmoden des Tripeptids diskutiert.

Im vorletzten Kapitel wurde der Adsorptionsmechanismus von zwei verwandten Anti-Leukämie-Wirkstoffen, 6-Mercaptopurin (6MP) und 6-Mercaptopurin-ribose (6MPR) diskutiert. Der erste Teil dieses Kapitels beschreibt die Struktur- und Schwingungs-charakteristika des 6MP-Moleküls im festen Zustand und in wässriger Lösung. Dafür wurden DFT- und PED-Rechnungen an mehreren Tautomeren durchgeführt. Im kristallinen Zustand liegt das Thion-Tautomer vor, während in wässriger Lösung wahrscheinlich die Thiol- oder anionische Spezies vorkommt. Anschließend wurden die SERS-Spektren, welche als Funktion des pH-Werts und der Konzentration aufgenommen wurden, diskutiert. Das Ribose-Derivat steht im Mittelpunkt des zweiten Teils dieses Kapitels. Dieses Derivat liegt ebenso wie (6MP) als Thion-Spezies in polykristalliner Form vor, während die Existenz des Thiol-Tautomers in sauerer wässriger Lösung nachgewiesen wurde. Schließlich wurden die SERS-Spektren des 6MPR-Derivats im Vergleich mit den SERS-Spektren des Mercaptopurins diskutiert. Unter basischen Bedingungen adsorbieren beide Moleküle über die N1- und möglicherweise S-Atome an der Metalloberfläche. Während das 6MP-Molekül eine ziemlich geneigte Orientierung an der Oberfläche einnimmt, ist das 6MPR-Molekül senkrecht auf der Oberfläche orientiert. Die SERS-Spektren, aufgenommen unter saueren Bedingungen, zeigen, dass das Ribose-Derivat ein unterschiedliches Adsorptionsverhalten im Vergleich zum freien Purin besitzt. Wahrscheinlich adsorbiert das 6MP-Molekül an dem Silberkolloid über die N9- und N3-Atome, wobei beim Ribose-Derivat eine Wechselwirkung mit dem Substrat durch das N7- und möglicherweise S-Atom vorliegt. Interessanterweise beginnt die Umorientierung des 6MP-Moleküls an der Oberfläche bei pH 6, während im Falle der Ribose-Verbindung das Adsorptionsverhalten sich erst bei pH 8 ändert. Unter basischen Bedingungen wurde die Bildung des Anions für beide Moleküle an der Metalloberfläche vorgeschlagen. Jedoch scheint die Deprotonierung des 6MP-Derivats bei etwa pH 8 vollendet zu sein, während die Deprotonierung der 6MPR-Verbindung erst bei pH 10 abgeschlossen ist. Für biologisch kritischen Konzentrationen und pH-Werten, d.h. für nahezu neutrale Bedingungen (pH-Wert 7-9) und eine geringe Konzentration, wurde festgestellt, dass das 6MPR-Molekül mit dem Substrat sowohl über das N7- als auch N1-Atom wechselwirkt,

wobei wahrscheinlich zwei unterschiedlich adsorbierte Spezies vorhanden sind. Im Gegensatz dazu weist das 6MP-Molekül nur eine über das N1-Atom adsorbierte Spezies auf. Diese Ergebnisse sind von großem Interesse für die Erklärung der Adsorption und Wirkung dieser Pharmazeutika in der Krebstherapie, besonders da der 6MP-Wirkstoff eine geringe Adsorption während klinischer Untersuchungen zeigte.

Die Experimente und Ergebnisse, die in dieser Arbeit vorgestellt wurden, veranschaulichen, dass Schwingungsspektroskopie in Zusammenhang mit quantenchemischen Rechnungen eine breite Anwendbarkeit zur Untersuchung der molekularen Struktur und molekularen Aktivität besitzen. Dabei nimmt die Resonanz-Raman-Spektroskopie eine besondere Stellung ein, da sie eine wertvolle Methode zur Untersuchung des angeregten Zustands und der Anfangsdynamik photochemisch aktiver Systeme darstellt. Nicht zuletzt lieferten Raman- und SERS-Spektroskopie einen wichtigen Beitrag für das Verständnis der Struktur-Wirkungs-Zusammenhänge einiger Pharmazeutika.

References

(1) Wilson, B., E.; Decius, J. C.; Cross, P. C. *Molecular Vibrations, The Theory of Infrared and Raman Vibrational Spectra*; Dover Publications Inc.: New York, 1980.

(2) *Raman Spectroscopy, Theory and Practice*; Szymanski, H. A., Ed.; Plenum Press: New York, 1967.

(3) Lin-Vien, D.; Colthup, N. B.; Fateley, W. G.; Grassetti, J. G. *The Handbook of Infrared and Raman Characteristics Frequencies of Organic Molecules*, 1991.

(4) Dollish, F. R.; Fateley, W. G.; Bentley, F. F. *Characteristic Raman Frequencies of Organic Compounds*, 1973.

(5) Kiefer, W.; Long, D. A. *Non-linear Raman Spectroscopy and Its Chemical Applications*; D. Reidel: Dordrecht, 1982.

(6) Kiefer, W. In *Infrared and Raman Spectroscopy*; Schrader, B., Ed.; VCH: Weinheim, 1995; pp 465.

(7) Kiefer, W. In *Infrared and Raman Spectroscopy*; Schrader, B., Ed.; VCH: Weinheim, 1995; pp 162.

(8) Polavarapu, P. L. *Vibrational Spectra, Principals and Applications with Emphasis on Optical Activity*; Elsevier: Amsterdam, 1998.

(9) Raman, C. V.; Krishnan, K. S. *Nature* **1928**, *121*, 501.

(10) Smekal, A. *Zeitsch. Physik* **1925**, *32*, 241.

(11) Hamaguchi, H.-o. The Resonance Raman Effect and Depolarization in Vibrational Raman Scattering. In *Advances in Infrared and Raman Spectroscopy*; Clark, R. J. H., Hester, R. E., Eds.; Wiley: Heyden, 1985; Vol. 12.

(12) *Biological Applications of Raman Spectroscopy*; Spiro, T. G., Ed.; Wiley & Sons: New York, 1987-1988.

(13) Ziegler, L. D.; Myers, A. B. *Special Issue on Raman Resonances in Ultrafast Spectroscopy. [In: J. Raman Spectrosc., 1995; 26(7)]*, 1995.

(14) Myers, A. B.; Mathies, R. A. Resonance Raman Intensities: A Probe of Excited-State Structure and Dynamics. In *Biological Applications of Raman Spectroscopy*; Spiro, T. G., Ed.; Wiley & Sons: New York, 1987; Vol. 2.

(15) Tu, A. T. *Raman Spectroscopy in Biology: Principles and Applications*, 1982.

(16) Zink, J. I.; Shin, K. S. K. *Advances in Photochem.* **1991**, *16*, 119.

(17) Myers, A. B. Excited Electronic State Properties from Ground-State Resonance Raman Intensities. In *Laser Techniques in Chemistry*; Myers, A. B., Rizzo, T. R., Eds.; John Woley & Sons: New York, 1995; Vol. XXIII; pp 325.

(18) Myers, A. B. *Chem. Rev.* **1996**, *96*, 911.

(19) Albrecht, A. C. *J. Chem. Phys.* **1961**, *34*, 1476.

(20) Albrecht, A. C.; Hutley, M. C. *J. Chem. Phys.* **1971**, *55*, 4438.

(21) Tang, J.; Albrecht, A. C. In *Raman Spectroscopy*; Szymanski, H. A., Ed.; Plenum: New York, 1970; Vol. 2.

(22) Kiefer, W.; Ganz, M.; Vogt, P.; Schmitt, M. *J. Mol. Struct.* **1995**, *347*, 229.

(23) Mukamel, S. Principles of nonlinear optical spectroscopy. In *Oxford Series in Optical and Imaging Sciences*; Lapp, M., Nishizawa, J.-I., Snavely, B. J., Stark, H., Tam, A. C., Wilson, T., Eds.; Oxford University Press: New York, 1995; Vol. 6; pp 209.

(24) Myers, A. B. *Annu. Rev. Phys. Chem.* **1998**, *49*, 267.

(25) Chang, R. K.; Furtak, T. E. *Surface Enhanced Raman Scattering*; Plenum Press: New York, 1982.

(26) Creighton, J. A. The Selection Rules for Surface-Enhanced Raman Spectroscopy. In *Spectroscopy of Surfaces*; Clark, R. J. H., Hester, R. E., Eds.; John Wiley & Sons: Chichester, 1998; Vol. 16; pp 37.

(27) Cotton, T. M. The Application of Surface-Enhanced Raman Scattering to Biological Systems. In *Spectroscopy of Surfaces*; Clark, R. J. H., Hester, R. E., Eds.; John Wiley & Sons: Chichester, 1998; Vol. 16; pp 91.

(28) Hehre, W. J.; Radom, L.; Schleyer, v. R. P.; Pople, J. A. *Ab initio Molecular Orbital Theory*; Wiley: New York, 1986.

(29) Jensen, F. *Introduction to Computational Chemistry*; Wiley & Sons: Chichester, 1999.

(30) Koch, W.; Holthausen, M. C. *A Chemist's Guide to Density Functional Theory, 2nd Edition*, 2001.

(31) Fogarasi, G.; Fulay, P. *Vibrational Spectra and Structure* **1985**, *14*, 125.

(32) Haarer, D.; Spiess, H. W.; Editors *Spectroscopy of Amorphous and Crystalline Solids*, 1995.

(33) Long, D. A. *Raman Spectroscopy*; McGrow Hill: New York, 1977.

(34) Porezag, D.; Pederson, M. R. *Phys. Rev. B* **1996**, *54*, 7830.

(35) Shorygin, P. P. *J. Phys. Chem. (U.S.S.R.)* **1947**, *21*, 1125.

(36) Kelley, A. M. *J. Phys. Chem. A* **1999**, *103*, 6891.

(37) Myers, A. B.; Mathies, R. A.; Tannor, D. J.; Heller, E. J. *J. Chem. Phys.* **1982**, *77*, 3857.

(38) Lee, S.-Y.; Heller, E. J. *J. Chem. Phys.* **1979**, *71*, 4777.

(39) Heller, E. J. *Acc. Chem. Res.* **1981**, *14*, 368.

(40) Heller, E. J.; Sundberg, R.; Tannor, D. *J. Phys. Chem.* **1982**, *86*, 1822.

(41) Hoskins, L. C.; Pham, A. X.; Rutt, G. C. *J. Raman Spectrosc.* **1990**, *21*, 543.

(42) Lu, H. M.; Page, J. B. *J. Chem. Phys.* **1989**, *90*, 5315.

(43) Frosch, T.; Kuestner, B.; Schluecker, S.; Szeghalmi, A.; Schmitt, M.; Kiefer, W.; Popp, J. *J. Raman Spectrosc.* **2004**, *35*, 819.

(44) Sando, G. M.; Spears, K. G.; Hupp, J. T.; Ruhoff, P. T. *J. Phys. Chem. A* **2001**, *105*, 5317.

(45) Myers, A. B.; Trulson, M. O.; Mathies, R. A. *J. Chem. Phys.* **1985**, *83*, 5000.

(46) Peteanu, L. A.; Mathies, R. A. *J. Phys. Chem.* **1992**, *96*, 6910.

(47) Li, B.; Johnson, A. E.; Mukamel, S.; Myers, A. B. *J. Am. Chem. Soc.* **1994**, *116*, 11039.

(48) Moran, A. M.; Kelley, A. M. *J. Chem. Phys.* **2001**, *115*, 912.

(49) Myers, A. B. *Chem. Phys.* **1994**, *180*, 215.

(50) Marin, T. W.; Homoelle, B. J.; Spears, K. G.; Hupp, J. T.; Spreer, L. O. *J. Phys. Chem. A* **2002**, *106*, 1131.

(51) Kerker, M.; Wang, D.-S.; Chew, H. *Appl. Opt.* **1980**, *19*, 4159.

(52) Moskovits, M. *J. Chem. Phys.* **1982**, *77*, 4408.

(53) Moskovits, M.; Suh, J. S. *J. Phys. Chem.* **1984**, *88*, 5526.

(54) Moskovits, M.; Suh, J. S. *J. Phys. Chem.* **1984**, *88*, 1293.

(55) Lee, P. C.; Meisel, D. *J. Phys. Chem.* **1982**, *86*, 3391.

(56) Frisch, M. J.; Trucks, G. W.; Schlegel, H. B.; Scuseria, G. E.; Robb, M. A.; Cheeseman, J. R.; Zakrzewski, V. G.; Montgomery, J. A.; Stratmann, R. E.; Burant, J. C.; Dapprich, S.; Millam, J. M.; Daniels, A. D.; Kudin, K. N.; Strain, M. C.; Farkas, O.; Tomasi, J.; Barone, V.; Cossi, M.; Cammi, R.; Mennucci, B.; Pomelli, C.; Adamo, C.; Clifford, S.; Ochterski, J.; Peterson, G. A.; Ayala, P. Y.; Cui, Q.; Morokuna, K.; Malick, D. K.; Rabuck, A. D.; Raghavachari, K.; Foresman, J. B.; Cioslowski, J.; Ortiz, J. V.;

Baboul, A. G.; Stefanov, B. B.; Liu, G.; Liashenko, A.; Piskorz, P.; Komaromi, I.; Gomperts, R.; Martin, R. L.; Fox, D. J.; Keith, T.; Al-Laham, M. A.; Peng, C. Y.; Nanayakkara, A.; Gonzalez, C.; Challacombe, M.; Gill, P. M. W.; Johnson, B.; Chen, W.; Wong, M. W.; Andres, J. L.; Gonzales, C.; Head-Gordon, M.; Reploge, E. S.; Pople, J. A. *Gaussian 98 Revision A.7.*; Gaussian Inc.: Pittsburg PA, 1998.

(57) Stirling, A. *J. Chem. Phys.* **1996**, *104*, 1254.

(58) Johnson, B. G.; Florian, J. *Chem. Phys. Lett.* **1995**, *247*, 120.

(59) Laaksonen, L. *J. Mol. Graph.* **1992**, *10*, 33.

(60) Pulay, P.; Fogarasi, G.; Pang, F.; Boggs, J. E. *J. Am. Chem. Soc.* **1979**, *101*, 2550.

(61) Pulay, P.; Fogarasi, G.; Pongor, G.; Boggs, J. E.; Vargha, A. *J. Am. Chem. Soc.* **1983**, *105*, 7037.

(62) Martin, J. M. L.; Van Alsenoy, C. *GAR2PED* **1995**, University of Antwerp.

(63) Trulson, M. O.; Mathies, R. A. *J. Chem. Phys.* **1986**, *84*, 2068.

(64) FORTRAN code to calculate absolute differential Raman cross sections was obtained by courtesy of Prof. Anne Myers Kelley at the Univeristy of California.

(65) Orlandi, G.; Zerbetto, F.; Zgierski, M. Z. *Chem. Rev.* **1991**, *91*, 867.

(66) Weller, A. *Z. Elektrochem.* **1952**, *56*, 662.

(67) Douhal, A.; Lahmani, F.; Zehnacker-Rentien, A. *Chem. Phys.* **1993**, *178*, 493.

(68) Douhal, A.; Lahmani, F.; Zewail, A. H. *Chem. Phys.* **1996**, *207*, 477.

(69) Lochbrunner, S.; Riedle, E. *Recent Res. Devel. Chem. Phys.* **2003**, *4*, 31.

(70) Lochbrunner, S.; Schultz, T.; Schmitt, M.; Shaffer, J. P.; Zgierski, M. Z.; Stolow, A. *J. Chem. Phys.* **2001**, *114*, 2519.

(71) Lochbrunner, S.; Stock, K.; Riedle, E. *J. Mol. Struct.* **2004**, *700*, 13.

(72) Lochbrunner, S.; Wurzer, A. J.; Riedle, E. *J. Phys. Chem. A* **2003**, *107*, 10580.

(73) Schwartz, B. J.; Peteanu, L. A.; Harris, C. B. *J. Phys. Chem.* **1992**, *96*, 3591.

(74) Barbara, P. F.; Walsh, P. K.; Brus, L. E. *J. Phys. Chem.* **1989**, *93*, 29.

(75) Chudoba, C.; Riedle, E.; Pfeiffer, M.; Elsaesser, T. *Chem. Phys. Lett.* **1996**, *263*, 622.

(76) McMorrow, D.; Kasha, M. *J. Phys. Chem.* **1984**, *88*, 2235.

(77) Myers, A. B. *Ann. Rev. Phys. Chem.* **1998**, *49*, 267.

(78) Marzocchi, M. P.; Mantini, A. R.; Casu, M.; Smulevich, G. *J. Chem. Phys.* **1998**, *108*, 534.

(79) Pfeiffer, M.; Lau, A.; Lenz, K.; Elsaesser, T. *Chem. Phys. Lett.* **1997**, *268*, 258.

(80) Pfeiffer, M.; Lenz, K.; Lau, A.; Elsaesser, T. *J. Raman Spectrosc.* **1995**, *26*, 607.

(81) Pfeiffer, M.; Lenz, K.; Lau, A.; Elsaesser, T.; Steinke, T. *J. Raman Spectrosc.* **1997**, *28*, 61.

(82) Lenz, K.; Pfeiffer, M.; Lau, A.; Elsaesser, T. *Chem. Phys. Lett.* **1994**, *229*, 340.

(83) Luiz, M.; Biasutti, A.; Soltermann, A. T.; Garcia, N. A. *Polymer Degrad. Stab.* **1999**, *63*, 447.

(84) Catalan, J.; del Valle, J. C. *J. Am. Chem. Soc.* **1993**, *115*, 4321.

(85) Catalan, J.; Palomar, J.; De Paz, J. L. G. *Chem. Phys. Lett.* **1997**, *269*, 151.

(86) Catalan, J.; Palomar, J.; de Paz, J. L. G. *J. Phys. Chem. A* **1997**, *101*, 7914.

(87) Organero, J. A.; Garcia-Ochoa, I.; Moreno, M.; Lluch, J. M.; Santos, L.; Douhal, A. *Chem. Phys. Lett.* **2000**, *328*, 83.

(88) Organero, J. A.; Moreno, M.; Santos, L.; Lluch, J. M.; Douhal, A. *J. Phys. Chem. A* **2000**, *104*, 8424.

(89) Tobita, S.; Yamamoto, M.; Kurahayashi, N.; Tsukagoshi, R.; Nakamura, Y.; Shizuka, H. *J. Phys. Chem. A* **1998**, *102*, 5206.

(90) Lu, C.; Hsieh, R. M. R.; Lee, I. R.; Cheng, P. Y. *Chem. Phys. Lett.* **1999**, *310*, 103.

(91) Sobolewski, A. L.; Domcke, W. *Phys. Chem. Chem. Phys.* **1999**, *1*, 3065.

(92) Sobolewski, A. L.; Domcke, W. *J. Phys. Chem. A* **1999**, *103*, 4494.

(93) Sobolewski, A. L.; Domcke, W. *Chem. Phys. Lett.* **1999**, *300*, 533.

(94) Pascal, R. A., Jr. *J. Phys. Chem. A* **2001**, *105*, 9040.

(95) Crutchley, R. J. *Adv. Inorg. Chem.* **1994**, *41*, 273.

(96) Creutz, C. *Progr. Inorg. Chem.* **1983**, *30*, 1.

(97) Sutin, N. *Progr. Inorg. Chem.* **1983**, *30*, 441.

(98) Launay, J.-P. *Chem. Soc. Rev.* **2001**, *30*, 386.

(99) Barbara, P. F.; Meyer, T. J.; Ratner, M. A. *J. Phys. Chem.* **1996**, *100*, 13148.

(100) Nelsen, S. F.; Ismagilov, R. F.; Trieber, D. A. *Science* **1997**, *278*, 846.

(101) Robin, M. B.; Day, P. *Adv. Inorg. Chem. Radiochem.* **1967**, *10*, 247.

(102) Wong, K. Y.; Schatz, P. N. *Progr. Inorg. Chem.* **1981**, *28*, 369.

(103) Brunschwig, B. S.; Creutz, C.; Sutin, N. *Chem. Soc. Rev.* **2002**, *31*, 168.

(104) Badger, B.; Brocklehurst, B. *Trans. Faraday Soc.* **1970**, *66*, 2939.

(105) Braun-Sand, S. B.; Wiest, O. *J. Phys. Chem. B* **2003**, *107*, 9624.

(106) Ito, T.; Hamaguchi, T.; Nagino, H.; Yamaguchi, T.; Washington, J.; Kubiak, C. *Science* **1997**, *277*, 660.

(107) Demadis, K. D.; Hartshorn, C. M.; Meyer, T. J. *Chem. Rev.* **2001**, *101*, 2655.

(108) Nelsen, S. F. *Chem. Eur. J.* **2000**, *6*, 581.

(109) Lambert, C.; Nöll, G. *J. Am. Chem. Soc.* **1999**, *121*, 8434.

(110) Lindeman, S. V.; Rosokha, S. V.; Sun, D.; Kochi, J. K. *J. Am. Chem. Soc.* **2002**, *124*, 843.

(111) Roeder, J. C.; Meyer, F.; Hyla-Kryspin, I.; Winter, R. F.; Kaifer, E. *Chem. Eur. J.* **2003**, *9*, 2636.

(112) Demadis, K. D.; Neyhart, G. A.; Kober, E. M.; White, P. S.; Meyer, T. J. *Inorg. Chem.* **1999**, *38*, 5948.

(113) Rocha, R. C.; Toma, H. E. *Inorg. Chim. Acta* **2000**, *310*, 65.

(114) Stadler, C.; Daub, J.; Koehler, J.; Saalfrank, R. W.; Coropceanu, V.; Schuenemann, V.; Ober, C.; Trautwein, A. X.; Parker, S. F.; Poyraz, M.; Inomata, T.; Cannon, R. D. *J. Chem. Soc., Dalton Trans.* **2001**, 3373.

(115) Londergan, C. H.; Rocha, R. C.; Brown, M. G.; Shreve, A. P.; Kubiak, C. P. *J. Am. Chem. Soc.* **2003**, *125*, 13912.

(116) Bailey, S. E.; Zink, J. I.; Nelsen, S. F. *J. Am. Chem. Soc.* **2003**, *125*, 5939.

(117) Nelsen, S. F.; Tran, H. Q.; Nagy, M. A. *J. Am. Chem. Soc.* **1998**, *120*, 298.

(118) Coropceanu, V.; Malagoli, M.; Andre, J. M.; Bredas, J. L. *J. Am. Chem. Soc.* **2002**, *124*, 10519.

(119) Utz, N.; Koslowski, T. *Chem. Phys.* **2002**, *282*, 389.

(120) Hupp, J. T.; Williams, R. D. *Acc. Chem. Res.* **2001**, *34*, 808.

(121) Talaga, D. S.; Zink, J. I. *J. Phys. Chem. A* **2001**, *105*, 10511.

(122) Watson, D. F.; Bocarsly, A. B. *Coor. Chem. Rev.* **2001**, *211*, 177.

(123) Doorn, S. K.; Hupp, J. T. *J. Am. Chem. Soc.* **1989**, *111*, 4704.

(124) Tominaga, K.; Kliner, D. A. V.; Johnson, A. E.; Levinger, N. E.; Barbara, P. F. *J. Chem. Phys.* **1993**, *98*, 1228.

(125) Doorn, S. K.; Hupp, J. T.; Porterfield, D. R.; Campion, A.; Chase, D. B. *J. Am. Chem. Soc.* **1990**, *112*, 4999.

(126) Petrov, V.; Hupp, J. T.; Mottley, C.; Mann, L. C. *J. Am. Chem. Soc.* **1994**, *116*, 2171.

(127) Lu, H.; Petrov, V.; Hupp, J. T. *Chem. Phys. Lett.* **1995**, *235*, 521.

(128) Williams, R. D.; Petrov, V. I.; Lu, H. P.; Hupp, J. T. *J. Phys. Chem. A* **1997**, *101*, 8070.

(129) Williams, R. D.; Hupp, J. T.; Ramm, M. T.; Nelsen, S. F. *J. Phys. Chem. A* **1999**, *103*, 11172.

(130) Strohriegl, P.; Grazulevicius, J. V. *Adv. Mater.* **2002**, *14*, 1439.

(131) Koene, B. E.; Loy, D. E.; Thompson, M. E. *Chem. Mater.* **1998**, *10*, 2235.

(132) Blackstock, S. C.; Selby, T. D. Polyradical cations of high spin. In *Magnetic Properties of Organic Materials*; Lahti, P. M., Ed.; Marcel Dekker: New York, 1999; pp 165.

(133) Bushby, R.-J. Triarylmethyl and amine radicals. In *Magnetism: Molecules to Materials II*; Miller, J. S., Drillon, M., Eds.; Wiley-VCH: Weinheim, Germany, 2001; pp 149.

(134) Szeghalmi, A. V.; Erdmann, M.; Engel, V.; Schmitt, M.; Amthor, S.; Kriegisch, V.; Noell, G.; Stahl, R.; Lambert, C.; Leusser, D.; Stalke, D.; Zabel, M.; Popp, J. *J. Am. Chem. Soc.* **2004**, *126*, 7834.

(135) Brown, G. M.; Freeman, G. R.; Walter, R. I. *J. Am. Chem. Soc.* **1977**, *99*, 6910.

(136) Sobolev, A. N.; Bel'skii, V. K.; Romm, I. P.; Chernikova, N. Y.; Guryanova, E. N. *Acta Crystallogr. C.* **1985**, *41*, 967.

(137) Low, P. J.; Paterson, M. A. J.; Puschmann, H.; Goeta, A. E.; Howard, J. A. K.; Lambert, C.; Cherryman, J.; Tackley, D. R.; Leeming, S.; Brown, B. *Chem. Eur. J.* **2003**, *in press*.

(138) Jones, G. A.; Carpenter, B. K.; Paddon-Row, M. N. *J. Am. Chem. Soc.* **1999**, *121*, 11171.

(139) Blomgren, F.; Larsson, S.; Nelsen, S. F. *J. Comput. Chem.* **2001**, *22*, 655.

(140) Schluecker, S.; Szeghalmi, A.; Schmitt, M.; Popp, J.; Kiefer, W. *J. Raman Spectrosc.* **2003**, *34*, 413.

(141) Egolf, D. S.; Waterland, M. R.; Kelley, A. M. *J. Phys. Chem. B* **2000**, *104*, 10727.

(142) Lilichenko, M.; Tittelbach-Helmrich, D.; Verhoeven, J. W.; Gould, I. R.; Myers, A. B. *J. Chem. Phys.* **1998**, *109*, 10958.

(143) Baranovski, V. I.; Lubimova, O. O.; Makarov, A. A.; Sizova, O. V. *Chem. Phys. Lett.* **2002**, *361*, 196.

(144) Shriver, D. F.; Dunn, J. B. R. *Appl. Spectrosc.* **1974**, *28*, 319.

(145) Kambhampati, P.; Son, D. H.; Kee, T. W.; Barbara, P. F. *J. Phys. Chem. A* **2000**, *104*, 10637.

(146) Reimers, J. R.; Hush, N. S. *Chem. Phys.* **1996**, *208*, 177.

(147) Hush, N. S. In *Mixed Valence Compounds151*; Brown, D. B., Ed.; D. Reidel Publishing Comp.: Dordercht, Holland, 1980; pp 151.

(148) Piepho, S. B. *J. Am. Chem. Soc.* **1988**, *110*, 6319.

(149) Schatz, P. N. Vibronic coupling models of mixed valency: relation of the PKS and MO models for one- and two-electron systems. In *Mixed Valency Systems: Applications in Chemistry, Physics and Biology*; Prassides, K., Ed.; Kluwer Academic Publishers, 1991; pp 7.

(150) Root, L. J.; Ondrechen, M. J. *Chem. Phys. Lett.* **1982**, *93*, 421.

(151) Ko, J.; Ondrechen, M. J. *J. Am. Chem. Soc.* **1985**, *107*, 6161.

(152) Coropceanu, V.; Malagoli, M.; Andre, J. M.; Bredas, J. L. *J. Chem. Phys.* **2001**, *115*, 10409.

(153) Moerner, W. E.; Silence, S. M. *Chem. Rev.* **1994**, *94*, 127.

(154) Sutter, K.; Guenter, P. *J. Opt. Soc. Am. B* **1990**, *7*, 2274.

(155) Rao, V. P.; Jen, A. K. Y.; Chandrasekhar, J.; Namboothiri, I. N. N.; Rathna, A. *J. Am. Chem. Soc.* **1996**, *118*, 12443.

(156) Wong, K. Y.; Jen, A. K. Y.; Rao, V. P.; Drost, K. J. *J. Chem. Phys.* **1994**, *100*, 6818.

(157) Beckmann, S.; Etzbach, K.-H.; Kramer, P.; Lukaszuk, K.; Matschiner, R.; Schmidt, A. J.; Schuhmacher, P.; Sens, R.; Seybold, G.; Wortmann, R.; Wurthner, F. *Adv. Mater.* **1999**, *11*, 536.

(158) Breitung, E. M.; Shu, C.-F.; McMahon, R. J. *J. Am. Chem. Soc.* **2000**, *122*, 1154.

(159) Albert, I. D. L.; Marks, T. J.; Ratner, M. A. *J. Am. Chem. Soc.* **1997**, *119*, 6575.

(160) Albert, I. D. L.; Morley, J. O.; Pugh, D. *J. Phys. Chem.* **1995**, *99*, 8024.

(161) Kelley, A. M.; Leng, W.; Blanchard-Desce, M. *J. Am. Chem. Soc.* **2003**, *125*, 10520.

(162) Wurthner, F.; Wortmann, R.; Matschiner, R.; Lukaszuk, K.; Meerholz, K.; DeNardin, Y.; Bittner, R.; Brauchle, C.; Sens, R. *Angew. Chemie* **1998**, *36*, 2765.

(163) Leng, W.; Wuerthner, F.; Kelley, A. M. *J. Phys. Chem. B* **2004**, *108*, 10284.

(164) Wurthner, F.; Thalacker, C.; Matschiner, R.; Lukaszuk, K.; Wortmann, R. *Chem. Com.* **1998**, 1739.

(165) Wuerthner, F.; Vollmer, M. S.; Effenberger, F.; Emele, P.; Meyer, D. U.; Port, H.; Wolf, H. C. *J. Am. Chem. Soc.* **1995**, *117*, 8090.

(166) Effenberger, F.; Wuerthner, F. *Angew. Chemie* **1993**, *105*, 742.

(167) Wuerthner, F.; Effenberger, F.; Wortmann, R.; Kraemer, P. *Chem. Phys.* **1993**, *173*, 305.

(168) Gilchrist, T. L. *Heterocyclic Chemistry*; Wiley & Sons: New York, 1985.

(169) Effenberger, F.; Wuerthner, F. *Angew. Chem.* **1993**, *105*, 742.

(170) Otto, H.-H.; Schirmeister, T. *Chem. Rev.* **1997**, *97*, 133.

(171) Schirmeister, T.; Klockow, A. *Mini-Rev. Med. Chem.* **2003**, *3*, 585.

(172) Powers James, C.; Asgian Juliana, L.; Ekici Ozlem, D.; James Karen, E. *Chem. Rev., 102*, 4639.

(173) Albeck, A.; Kliper, S. *Biochem. J.* **2000**, *346*, 71.

(174) Eilon, G. F.; Gu, J.; Slater, L. M.; Hara, K.; Jacobs, J. W. *Cancer Chemother. Pharmacol.* **2000**, *45*, 183.

(175) Gour-Salin, B. J.; Lachance, P.; Plouffe, C.; Storer, A. C.; Menard, R. *J. Med. Chem.* **1993**, *36*, 720.

(176) Matsumoto, K.; Mizoue, K.; Kitamura, K.; Tse, W. C.; Huber, C. P.; Ishida, T. *Biopolymers* **1999**, *51*, 99.

(177) Meara, J. P.; Rich, D. H. *J. Med. Chem.* **1996**, *39*, 3357.

(178) Schirmeister, T. *Arch. Pharm.* **1996**, *329*, 239.

(179) Schirmeister, T. *Peptide Sci. Present and Future* **1999**, 634.

(180) Schirmeister, T. *J. Med. Chem.* **1999**, *42*, 560.

(181) Schirmeister, T.; Peric, M. *Bioorg. Med. Chem.* **2000**, *8*, 1281.

(182) Morodor, L.; Musiol, H. J.; Scharf, R.; Moroder, L. *FEBS Letters* **1992**, *299*, 51.

(183) Martichonok, V.; Plouffe, C.; Storer, A. C.; Menard, R.; Jones, J. B. *J. Med. Chem.* **1995**, *38*, 3078.

(184) Shao, H.; Jiang, X.; Gantzel, P.; Goodman, M. *Chem. Biol.* **1994**, *1*, 231.

(185) Sieler, G.; Schweitzer-Stenner, R.; Holtz, J. S. W.; Pajcini, V.; Asher, S. A. *J. Phys. Chem. B* **1999**, *103*, 372.

(186) Schweitzer-Stenner, R. *J. Raman Spectrosc.* **2001**, *32*, 711.

(187) Herrebout, W.; Clou, K.; Desseyn, H. O.; Blaton, N. *Spectrochim. Acta A* **2003**, *59A*, 47.

(188) Sieler, G.; Schweitzer-Stenner, R. *J. Am. Chem. Soc.* **1997**, *119*, 1720.

(189) Holtz, J. S. W.; Li, P.; Asher, S. A. *J. Am. Chem. Soc.* **1999**, *121*, 3762.

(190) Pajcini, V.; Chen, X. G.; Bormett, R. W.; Geib, S. J.; Li, P.; Asher, S. A.; Lidiak, E. G. *J. Am. Chem. Soc.* **1996**, *118*, 9705.

(191) Destrade, C.; Dupart, E.; Joussot-Dubien, M.; Garrigou-Lagrange, C. *Can. J. Chem.* **1974**, *52*, 2590.

(192) Schirmeister, T.; Breuning, A.; Murso, A.; Stalke, D.; Mladenovic, M.; Engels, B.; Szeghalmi, A.; Schmitt, M.; Kiefer, W.; Popp, J. *J. Phys. Chem. A* **2004**, *108*, 11398.

(193) Song, S.; Asher, S. A.; Krimm, S.; Shaw, K. D. *J. Am. Chem. Soc.* **1991**, *113*, 1155.

(194) Fogarasi, G.; Zhou, X.; Taylor, P. W.; Pulay, P. *J. Am. Chem. Soc.* **1992**, *114*, 8191.

(195) Dervieux, T.; Medard, Y.; Verpillat, P.; Guigonis, V.; Duval, M.; Lescoeur, B.; Suciu, S.; Vilmer, E.; Jacqz-Aigrain, E. *Leukemia* **2001**, *15*, 1706.

(196) Dervieux, T.; Chu, Y.; Su, Y.; Pui, C.-H.; Evans, W. E.; Relling, M. V. *Clin. Chem.* **2002**, *48*, 61.

(197) Jacqz-Aigrain, E.; Nafa, S.; Medard, Y.; Bessa, E.; Lescoeur, B.; Vilmer, E. *Eur. J. Clin. Pharmacol.* **1997**, *53*, 71.

(198) Nishida, A.; Kubota, T.; Yamada, Y.; Higashi, K.; Kitamura, K.; Nakahara, K.; Iga, T. *Clin. Chim. Acta* **2002**, *323*, 147.

(199) Zimm, S.; Collins, J. M.; Riccardi, R.; O'Neill, D.; Narang, P. K.; Chabner, B.; Poplack, D. G. *N. Engl. J. Med.* **1983**, *308*, 1005.

(200) Mawatari, H.; Unei, K.; Nishimura, S.-I.; Sakura, N.; Ueda, K. *Pediatr. Intern.* **2001**, *43*, 673.

(201) Lapinski, L.; Nowak, M. J.; Kwiatkowski, J. S.; Leszczynski, J. *J. Phys. Chem. A* **1999**, *103*, 280.

(202) Stepanenko, T.; Lapinski, L.; Nowak, M. J.; Kwiatkowski, J. S.; Leszczynski, J. *Spectrochim. Acta A* **2001**, *57A*, 375.

(203) Vivoni, A.; Chen, S.-P.; Ejeh, D.; Hosten, C. M. *Langmuir* **2000**, *16*, 3310.

(204) Domazetis, G.; Magee, R. J.; James, B. D. *J. Organometal. Chem.* **1980**, *197*, 39.

(205) Katsaros, N.; Grigoratou, A. *J. Inorg. Biochem.* **1985**, *25*, 131.

(206) Buncel, E.; Kumar, R.; Norris, A. R. *Can. J. Chem.* **1986**, *64*, 442.

(207) Hadjiliadis, N.; Theophanides, T. *Can. J.Spectrosc.* **1977**, *22*, 51.

(208) Szorcsik, A.; Nagy, L.; Gajda-Schrantz, K.; Pellerito, L.; Nagy, E.; Edelmann, F. T. *J. Radioanal. Nucl. Chem.* **2002**, *252*, 523.

(209) Cini, R.; Corsini, M.; Cavaglioni, A. *Inorg. Chem.* **2000**, *39*, 5874.

(210) Buettner, D.; Buettner, J. *Clin. Chem. Lab. Med.* **1998**, *36*, 757.

(211) Ulman, A. *Chem. Rev.* **1996**, *96*, 1533.

(212) Kim, H. S.; Lee, S. J.; Kim, N. H.; Yoon, J. K.; Park, H. K.; Kim, K. *Langmuir* **2003**, *19*, 6701.

(213) Porter, M. D.; Bright, T. B.; Allara, D. L.; Chidsey, C. E. D. *J. Am. Chem. Soc.* **1987**, *109*, 3559.

(214) Bain, C. D.; Troughton, E. B.; Tao, Y. T.; Evall, J.; Whitesides, G. M.; Nuzzo, R. G. *J. Am. Chem. Soc.* **1989**, *111*, 321.

(215) Bryant, M. A.; Pemberton, J. E. *J. Am. Chem. Soc.* **1991**, *113*, 3629.

(216) Himmelhaus, M.; Eisert, F.; Buck, M.; Grunze, M. *J. Phys. Chem. B* **2000**, *104*, 576.

(217) Kudelski, A. *Langmuir* **2003**, *19*, 3805.

(218) Ko, B. S.; Babcock, B.; Jennings, G. K.; Tilden, S. G.; Peterson, R. R.; Cliffel, D.; Greenbaum, E. *Langmuir* **2004**, *20*, 4033.

(219) Jung, H. H.; Won, Y. D.; Shin, S.; Kim, K. *Langmuir* **1999**, *15*, 1147.

(220) Han, S. W.; Lee, S. J.; Kim, K. *Langmuir* **2001**, *17*, 6981.

(221) Joo, S.-W. *Chem. Lett.* **2004**, *33*, 60.

(222) Gui, J. Y.; Lu, F.; Stern, D. A.; Hubbard, A. T. *J. Electroanal. Chem.* **1990**, *292*, 245.

(223) Caldwell, W. B.; Campbell, D. J.; Chen, K.; Herr, B. R.; Mirkin, C. A.; Malik, A.; Durbin, M. K.; Dutta, P.; Huang, K. G. *J. Am. Chem. Soc.* **1995**, *117*, 6071.

(224) Tripathi, G. N. R.; Clements, M. *J. Phys. Chem. B* **2003**, *107*, 11125.

(225) Di Felice, R.; Selloni, A. *J. Chem. Phys.* **2004**, *120*, 4906.

(226) Kirk, J. S.; Bohn, P. W. *J. Am. Chem. Soc.* **2004**, *126*, 5920.

(227) Sandstroem, P.; Aakerman, B. *Langmuir* **2004**, *20*, 4182.

(228) Parr, R. G.; Yang, W. *Density-functional Theory of Atoms and Molecules*, 1989.

(229) Parr, R. G. *Density-Functional Theory of Atoms and Molecules*, 1995.

(230) Vivoni, A.; Chen, S.-P.; Qiao, Z.; Hosten, C. M. *J. Raman Spectrosc.* **2001**, *32*, 866.

(231) Chowdhury, J.; Mukherjee, K. M.; Misra, T. N. *J. Raman Spectrosc.* **2000**, *31*, 427.

(232) Giese, B.; McNaughton, D. *J. Phys. Chem. B* **2002**, *106*, 101.

(233) Suh, J. S.; Moskovits, M. *J. Am. Chem. Soc.* **1986**, *108*, 4711.

(234) Otto, C.; de Mul, F. F. M.; Huizinga, A.; Greve, J. *J. Phys. Chem.* **1988**, *92*, 1239.

(235) Otto, C.; Hoeben, F. P.; Greve, J. *J. Raman Spectrosc.* **1991**, *22*, 791.

(236) Thornton, J.; Forcé, R. K. *Appl. Spectrosc.* **1991**, *45*, 1522.

(237) Kim, K. S.; Joo, T. H.; Suh, S. W.; Kim, M. S. *J. Raman Spectrosc.* **1986**, *17*, 381.

(238) Becke, A. D. *Phys. Rev. A* **1988**, *38*, 3098.

(239) Becke, A. D. *J. Chem. Phys.* **1993**, *98*, 5648.

(240) Perdew, J. P.; Burke, K.; Wang, Y. *Phys. Rev. B* **1996**, *54*, 16533.

(241) Sletten, E.; Sletten, J.; Jensen, L. H. *Acta Cryst. B* **1969**, *25*, 1330.

(242) Brown, G. M. *Acta Cryst. B* **1969**, *25*, 1338.

(243) Lichtberger, D.; Bergmann, F.; Neimann, Z. *J. Chem. Soc.* **1971**, *C*, 1676.

(244) Porezag, D.; Pederson, M. R. *Phys. Rev. B: Condensed Matter* **1996**, *54*, 7830.

(245) Pavel, I.; Szeghalmi, A.; Moigno, D.; Cinta, S.; Kiefer, W. *Biopolymers* **2003**, *72*, 25.

(246) Jang, N. H. *Bull. Chem. Soc.* **2002**, *23*, 1790.

(247) Demers, L. M.; Oestblom, M.; Zhang, H.; Jang, N.-H.; Liedberg, B.; Mirkin, C. A. *J. Am. Chem. Soc.* **2002**, *124*, 11248.

(248) Bailey, L. E.; Navarro, R.; Hernanz, A. *Biospect.* **1997**, *3*, 47.

(249) Carmona, P.; Molina, M. *J. Raman Spectrosc.* **1990**, *21*, 395.

(250) Mathlouthi, M.; Seuvre, A. M.; Koenig, J. L. *Carbohydr. Res.* **1983**, *122*, 31.

(251) Shefter, E. *J. Pharmaceut. Sciences* **1968**, *57*, 1157.

(252) Szeghalmi, A.; Leopold, L.; Cînta Pînzaru, S.; Chis, V.; Silaghi-Dumitrescu, I.; Schmitt, M.; Popp, J.; Kiefer, W. *J. Mol. Struct.* **2004**, *in press*.

(253) Pelmenschikov, A.; Hovorun, D. M.; Shishkin, O. V.; Leszczynski, J. *J. Chem. Phys.* **2000**, *113*, 5986.

(254) Chen, S.-P.; Qiao, Z.; Vivoni, A.; Hosten, C. M. *Spectrochim. Acta A* **2003**, *59A*, 2905.

Acknowledgment

I would like to express my gratitude to Prof. Kiefer for the opportunity to continue my studies here in Germany and his continuous support. The fascinating and diversified projects of this thesis were highly motivating. The possibility to participate in numerous conferences always brought me a step farther.

Additionally, I would like to express appreciation and gratitude to my major advisor, Dr. Michael Schmitt, who provided remarkable assistance and support throughout this project, and over the course of my doctoral research. His frankness and openness have made it a pleasure to have him as major advisor. This time during the PhD was not always easy and I would like to thank him for his support in those hard hours.

I would like to recognize Prof. Lambert, Prof. Schirmeister and Prof. Popp for having introduced me to very interesting topics. I highly appreciate their support to accomplish many of the research tasks. I also thank Prof. Würthner, Prof. Quast, Prof. Engel, Prof. Engels, Prof. Bringmann, Prof. Stalke, Prof. Zgierski, Prof. Hu, Conf. Dr. Pînzaru, Conf. Dr. Anca Silvestru and all of the professors from Germany and Romania, who opened the doors of knowledge in the fascinating realm of chemistry and physics for me.

I thank Prof. Myers Kelley and Dr. Andy Moran for their help with the computational demands. Dear Andy, thank you for one very special happy day during my PhD.

I would like to thank Dr. Champ for his very helpful and instructive advices.

And without the strong hand of Mrs. Wirth during the English classes, it would have been more difficult to write these sentences. Without Frau Müller the time during my PhD wouldn’t have gone off without a hitch.

I would like to thank Marco Erdmann, Stephan Amthor, Volker Kriegisch, Gilbert Nöll, Rainer Stahl, Alexander Heckmann, Dirk Leusser, Alexander Breuning, Alexander Murso, Milena Mladenovic, Ute Neugebauer, Torsten Frosch and Sebastian Schlücker for the very nice cooperation and not only.

I would like to thank Belinda Leimeister, Peter Popp, Melanie Grom and the super people from the mechanics and electronics workshops as well as the staff from the computer center for all their support.

Dear Loredana, Minewer and Katharina, I hope that the time you spent in AK Kiefer was interesting. Thank you for the work you did and the nice time together.

Dear Björn, thank you for taking the time to help me with a lot of problems, for the driving lesson nearby the Main and for many small, but very important things. I wish you all the best with your PhD.

Dear Benjamin, Joachim, Raman and Berny, I will always remember the laughing in the Mensa, Cafeteria, coffee breaks, sometimes Kneipen or movie theaters, thank you for being there whenever I just needed. Dear Benjamin and Berny, I probably won't be there for your "Promotionskolloquium", I am so, sorry!!!

Dear Stefi, Nicola, Marion, Katrin, Daiva, Roland, Damian, Petra, Jan, Torsten, Barbara, Krisztina, Nicu, Danny, Monica, Lucian, Claudiu, Horea and Nicoleta, thank you for everything.

Dear Ionela and Rainer, I will remember with great pleasure the time we spent in Szeged.

Dear Patrick and Bettina, I am happy that I met you. You and Jochen, I would like to thank for somehow making me a better person.

Dear Daniel, Ioana Pavel and Bernd Giese, I would like to thank you for the numerous discussions we have had, you made me always stronger.

Dear Mrs Sabine, thank you.

Dear Emi, Ileana, Diana, Iuliana, Nona, Ralu, Andrea, Andrei, Bianca, Ovidiu, Petrica, Petre, although you were far away, you helped me often.

Dragi parinti, va iubesc mult mult. I would like to thank my family, my aunts, uncles, my cousins.

And finally, I wish to acknowledge the financial support of the Graduiertenkolleg 690 *Electron Density – Theory and Experiment* and the Sonderforschungsbereich SFB 630 TP C1 as well as of the Fonds der Chemischen Industrie and the Deutsche Forschungsgemeinschaft DFG which made this research project possible.

Resume

SZEGHALMI ADRIANA VIORICA

Date of Birth	17.02.1979
Place of Birth	Oradea, Romania
Nationality	Romanian
Present Address	Ziegelaustrasse 4, D-97080 Würzburg, Germany
Address	Matei Corvin 80 RO-3700, Oradea, Romania

Education

07.2001-now	PhD student at the Institute of Physical Chemistry (Prof. Dr. Dr. hc Kiefer), University of Würzburg, Germany Title of PhD thesis: "The Ground and Excited State Molecular Structure of Model Systems Undergoing Photochemical Processes and the Characterization of Active Agents by means of Vibrational Spectroscopy and Theoretical Calculations"
06.2001	Diploma *Licentiate in Chemistry* Title of Diploma thesis: "Raman und Oberflächen-vestärkte Raman Streung an Koffein: Theoretische DFT Rechnungen und Experimentelle Untersuchungen"
09.1997-06.2001	Student at the Faculty of Chemistry and Chemical Engineering of the Babes-Bolyai University, Cluj-Napoca, Romania
04.2000-03.2001	Exchange student at the University of Würzburg, Germany *Socrates* Fellowship and Fellowship of the *Bavarian Ministry of Art, Science and Researc*h
07.1997	High school diploma
09.1993-06.1997	Mihai Eminescu High School Oradea. Participation at the National Chemistry Olympiad 1994 III, 1995 I, 1996 III award, 1997 mention

Work Experience

07.2001-now	Research assistant, supervision of students, diploma students
04.2004-06.2004	Internship at BASF, The Chemical Company, Ludwigshafen

Skills

Language:	Romanian, Hungarian: mother tongue German: fluently *DSH Diploma*; English: fluently *Anglikum Diploma* French: good
EDV:	Windows, Unix, Word, PowerPoint, Excel, Adobe, Corel, Origin, Gaussian, Fortran, etc.
Hobbies:	Traveling, swimming, reading